ISBN 978-82-326-1296-3 (printed version)
ISBN 978-82-326-1297-0 (electronic version)

Doctoral theses at NTNU, 2015:320

Birgitte Hjelmeland McDonagh

# Multifunctional Nanoparticles for Bioimaging

NTNU
Norwegian University of
Science and Technology

Doctoral Thesis

Birgitte Hjelmeland McDonagh

Doctoral theses at NTNU, 2015:320

NTNU

**NTNU**
Norwegian University of
Science and Technology
Faculty of Natural
Sciences and Technology
Department of Chemical Engineering

NTNU
Norwegian University of
Science and Technology

Birgitte Hjelmeland McDonagh

# Multifunctional Nanoparticles for Bioimaging

Thesis for the degree of Philosophiae Doctor

Trondheim, December, 2015

Norwegian University of Science and Technology
Faculty of Natural
Sciences and Technology
Department of Chemical Engineering

NTNU
Norwegian University of
Science and Technology

**NTNU**
Norwegian University of Science and Technology

Thesis for the degree of Philosophiae Doctor

Faculty of Natural
Sciences and Technology
Department of Chemical Engineering



ISBN 978-82-326-1296-3 (printed version)
ISBN 978-82-326-1297-0 (electronic version)

Doctoral theses at NTNU, 2015:320

Printed by Skipnes Kommunikasjon as

# Preface

This thesis is submitted in partial fulfillment of the requirements for the degree of Philosophiae Doctor (Ph.D) at the Norwegian university of Science and Technology (NTNU) and consists of five papers. The work presented herein was mainly performed at the Ugelstad Laboratory at the Department of Chemical Engineering, at the stem cell lab at the Department of Circulation and Medical Imaging, and at the NTNU NanoLab. The project has been funded by research and development funds from NTNU, and support from MyFab/NorFab. The work has been supervised by Professor II Dr. Wilhelm Robert Glomm, and co-supervised by Dr. Ioanna Sandvig and MD, PhD Axel Sandvig.

I completed my Master of Science in Biotechnology with a spcialization in biochemistry and biopolymer chemistry at the Department of Biotechnology at NTNU in June 2012. I was accepted as a PhD candidate at the Ugelstad Laboratory, Department of Chemical Engineering in August 2012.

# Acknowledgements

Although it is my name that adorns the front page of this thesis, the work I present here has culminated from a great collaboration with my exceptional colleagues that I have been very fortunate to work with during these last three years.

First and foremost, a huge thank you goes to Wilhelm. I would have never started a PhD if it wasn't for you; it did not fully cross my mind until you urged me to apply. You have been the best supervisor a PhD candidate can ask for; guiding when needed, and pushing when appropriate. Thank you for guiding me to become a scientist, thank you for letting me get the opportunity to teach, and thank you for involving me in all levels of the project. Thank you for your enthusiasm and support. I have really enjoyed these three years. You have taught me so much, and I will be forever grateful for that.

One great supervisor is more than a PhD candidate can ask for, however, I was fortunate enough to get two additionally great co-supervisors as well. Ioanna and Axel at the Dept. of Neuroscience have brought new ideas and perspectives to the project, and have been invaluable in planning and performing experiments *in vitro* and *in vivo*. They have as such brought our nanoparticles into the *real* world. A special thanks to Ioanna for putting in a lot of effort in teaching me how to work *in vitro* and *in vivo*, for organizing the Journal Club's, for praise, dinner, coffee and biscuits, and for always having a funny story to tell.

A special thank you to my group members, Sina, Sondre, Sulalit, and Gurvinder, for all the practical and theoretical help, as well as being awesome co-authors and co-workers. Thank you to Marte and Manuel for joining our group, for interesting discussions, for cake and coffee breaks. Thank you to Sjoerd, for investing a lot of time by the MR scanner, for helping in data interpretation, MatLab, and of course for being a great colleague. Thank you to Ingrid for all the laughs, cinnamon buns, for *in vivo* work, and for staying with me throughout the long hours at the MR scanner. Thank you to all my co-authors for collaborating and making the manuscripts better.

Thank you, Professor Johan Sjøblom, for including me in social events at the Ugelstad Laboratory, and for providing a well-equipped laboratory. To Lisbeth who is the oracle of IKP, to Arne for getting my chemicals, and to all my wonderful colleagues at Ugelstad for beer, cake, lunch and coffee. Thank you to Susana Gonzalez who spent endless hours with my samples on the Mass Spectrometry. I would also like to thank NanoLab and NorFab for allowing me to work in excellent laboratory facilities, as well as providing financial support.

To all of my friends for making everything better! Thank you!

To my family; those who are here and those who are not. Thank you, Mamma, Pappa, Kirsten and Magnus for being patient, interested, proud and supportive. I would also like to express my gratitude to my extended family; Beth, Kristian, Bjørg, Ida, Pål, Elisabeth, Hedda and Hennie (…pluss Barolo and Ebba) for support, interest and acceptance. You are great!

Last but not least, to my beloved Atle, who during these last three years has acquired knowledge in nanobiotechnology equivalent to a Bachelor's degree. Thank you for listening, for rubber-ducking, for your long-winded, and sometimes extraterrestrial patience. Nothing is worth it unless I can come home to you. I love you.

# No Small Matter

*The human body is a fortress*
*wreathed in a red vortex*
*of wriggling insatiable crocodile cells*

*A hostile place for a nanoparticle.*
*Getting by,*
*is* no small matter.

*The human cell is fortified*
*braided in garland forests*
*of branched glycosylated protein trees*

*the viscous fluid-like membrane protecting its holy grail:*
*the intracellular space.*

*A tremendous jungle for a nanoparticle*
*Getting in,*
*is* no small matter.

# Abstract

Bioimaging is a broad term that covers all processes in which biological tissues are imaged. It can range from single-cell visualization with fluorescence microscopy, to imaging of brain structures in living human beings with magnetic resonance imaging. As such, the term is not only interesting from a researcher's point of view, but also to existing medical technologies.

Imaging living organisms is mainly based on existing tissue densities between blood, brain, cartilage, and bone. However, in some cases these differences are not sufficient to separate *e.g* pathological tissue from healthy tissue. In these instances, a contrast agent may be administered to alter the contrast in the region of interest. Bioimaging of excised tissue usually involve staining with a dye that binds specifically to a cellular organelle or membrane, making it easier to separate intracellular structures from each other. Bioimaging of living and excised tissue both involves an external probe that enhances the available information in the image. Such probes must be synthesized from materials that are likely to improve the acquisition of the image, and must also have few toxic side-effects.

Nanomaterials are in the size-range of molecules and proteins, and can potentially traverse cellular membranes as well as being systemically administered. Nanoparticles are described as multifunctional because they can show a range of optical responses, carry drugs and vibrate in response to heat. The nanomaterials in this thesis were chosen based on their plasmonic and magnetic properties, as well as their biocompatibility.

The aim of this thesis is twofold. The first aim is to fully characterize and synthesize plasmonic nanomaterials of gold with biomineralization from proteins and from chemical synthesis. The second aim is synthesis and characterization of magnetic nanomaterials of iron and manganese. Characterization in this sense refers not only to physical description of the nanoparticles or nanoconstructs, but involves describing how these nanomaterials interact with biological tissues *in vitro* or *in vivo*, to assess their potential for bioimaging, hyperthermia and drug delivery.

A plethora of methods have been used to characterize the nanomaterials synthesized in this thesis. The nanomaterials of gold synthesized from proteins were described with a range of optical techniques such as UV-visible and steady state spectroscopy, and time-correlated single-photon counting. Size and shape was assessed with dynamic light scattering, scanning transmission electron microscopy and high resolution transmission electron microscopy. The surface charge was determined with zeta potential measurements. The crystalinity and composition of nanoparticles were characterized with X-ray diffraction spectroscopy, and surface composition was described with X-ray photoelectron spectroscopy. Interactions between protein-stabilized nanomaterials and model membranes were described with Langmuir-trough studies and atomic force microscopy. Magnetic nanomaterials were characterized with magnetic resonance imaging and zero field cooling. Further, nanomaterials were co-incubated with human cancer and/or rodent cells to assess their *in vitro* uptake or cytotoxicity. The methods for *in vitro* assays involved fluorescence microscopy and a cytotoxicity assay. Finally, ultramicrotome sectioning and scanning transmission electron microscopy was used to describe cellular uptake as a function of time.

The main findings in the first part of this thesis are that fluorescent protein-gold nanoconstructs show membrane interactions radically different from the native protein. We also describe how protein-directed self-assembly of fluorescent gold nanoclusters and plasmonic nanoparticles can be tuned to yield different optical gold nanostructures. In the second part of this thesis, the main findings are size, - and shape-dependent uptake of novel

plasmonic and magnetic nanoparticles *in vitro*, as well as cell actuation in a magnetic field. The final part of this thesis culminates in synthesis of a nanoparticle system that can give dual contrast in magnetic resonance imaging while at the same time release a drug.

# List of publications

**Paper I**

McDonagh, B.H., Volden, S. Lystvet, S. M., Singh, G., Ese, M., Ryan, J.A., Lindgren, M., Sandvig, A., Sandvig, I., Glomm, W.R. **Self-assembly and characterization of transferrin–gold nanoconstructs and their interaction with bio-interfaces**. *Nanoscale* 2015; Volume 15. p. 8062-8070, **DOI:** 10.1039/C5NR01284H

**Paper II**

McDonagh, B.H., Singh, G., Bandyopadhyay, S., Lystvet, S. M., Ryan, J.A., Volden, S., Kim, E., Sandvig, I., Sandvig, A., Glomm, W.R. **Controlling the self-assembly and optical properties of gold nanoclusters and gold nanoparticles biomineralized with Bovine Serum Albumin.** *RSC. Adv.,* 2015; Volume 5, p. 101101-101109, **DOI:** 10.1039/C5RA23423

**Paper III**

Bandyopadhyay, S., McDonagh, B.H., Singh, G., Sandvig, I., Sandvig, A., Glomm, W.R. ***Makura*-shaped gold nanostructures show high cytotoxicity in cancer cells.**

*Manuscript in preparation*

**Paper IV**

McDonagh, B.H., Singh, G., Peddis, D., Bandyopadhyay, S., Sandvig, I., Sandvig, A., Glomm, W.R. **Pentatwinned iron oxide nanoparticles as glioblastoma-astrocytoma cell actuators.**

*Manuscript in preparation*

**Paper V**

McDonagh, B.H., Singh, G., Hak, S., Bandyopadhyay, S., Augestad, I.L., Peddis, D., Sandvig, I., Sandvig, A., Glomm, W.R. **L-DOPA coated manganese oxide nanoparticles as dual MRI contrast agents and drug delivery vehicles.** *Accepted in SMALL*

# Additional Publications

**Paper VI**

Mørch, Ý., Hansen, R., Berg, S., Åslund, A.K.O., Glomm, W.R., Eggen, S., Schmid, R., Johnsen, H., Kubowicz, S., Snipstad, S., Sulheim, E., Hak, S., Singh, G., McDonagh, B.H., Blom, H., de Lange Davies, C., Stenstad, P.M., **Nanoparticle-stabilized microbubbles for multimodal imaging and drug delivery,** *Contrast Media and Molecular Imaging,* 2015, **DOI**: 10.1002/cmmi.1639

**Paper VII**

Singh, G., McDonagh, B.H., **Synthesis of $Gd_2O_3$ nanodisks and GD-doped iron oxide nanoparticles**

*Manuscript in preparation*

**Paper VIII**

Bandyopadhyay,S., Andersen, M.K., Raju, R., McDonagh, B.H., Glomm, W.R. **Synthesis and property control of pNIPAM-AAc colloidal gels for drug delivery.**

*Submitted to Materials Cheimstry B*

## Posters and conference contributions

**Poster at Nordic Neuroscience**

Title: *L-DOPA-coated manganese oxide nanoparticles as dual MRI contrast agents and potential drug delivery vehicles*
Authors: McDonagh B.H., Singh, G., Hak, S., Bandyopadhyay, S., Augestad,I.L., Sandvig, I., Sandvig, A., and Glomm,W.R.
Date: 10-12th of June 2015
Location: Gløshaugen, NTNU

**Talk at BioNanoMed**

Title: *L-DOPA-coated manganese oxide nanoparticles as dual MRI contrast agents and potential drug delivery vehicles*
Comment: 15 minute talk
Authors: McDonagh B.H., Singh, G., Hak, S., Bandyopadhyay, S., Augestad,I.L., Sandvig, I., Sandvig, A., and Glomm,W.R.
Date: 9th of April 2015
Location: University Hospital, Graz, Austria

**Talk at 10th annual NanoLab symposium**

Title: *Manganese, MRI and Parkinson's*
Comment: 15 minute talk
Authors: McDonagh B.H., Singh, G., Hak, S., Bandyopadhyay, S., Augestad,I.L., Sandvig, I., Sandvig, A., and Glomm,W.R.
Date: 10th of November 2014
Location: Britannia Hotel, Trondheim

**Poster, 10th annual NanoLab symposium**

Title: *Functional Nanomaterials for Theranostic Applications*
Authors: McDonagh B.H., Singh, G., Bandyopadhyay, S., and Glomm,W.R.
Date: 10-11th of November 2014
Location: Britannia Hotel, Trondheim

**Poster, 8th annual NanoLab symposium**
Title: *Functional Nanomaterials for Theranostic Applications*
Authors: McDonagh B.H., Singh, G., Bandyopadhyay,S., and Glomm,W.R.
Date: 12th of November 2013
Location: Lian Restaurant, Trondheim

**Talk at 8th annual NanoLab symposium**
Title: *From Protein to nanocluster to nanoparticle: tailoring the growth of protein-nanogold systems*
Comment: 15 minute talk
Authors: McDonagh,B. H., Singh, G., Lystvet, S.M., Bandyopadhyay, S., Volden, S., and Glomm, W.R.
Date: 12th of November 2013
Location: Lian Restaurant, Trondheim

**Poster at Norfab seminar**
Title: *Staining and cytotoxicity of transferrin gold nanoclusters on cancer cells*
Authors: McDonagh, B.H., Volden, S., Lystvet, S.M., Singh, G., Ese, M.G., Sandvig, I., Sandvig, A., Lindgren, M., and Glomm, W.R.
Date: 17-18th of April 2013
Location: Ångström Laboratory, Uppsala University, Sweden

# Popular science communication

**TV performance**
Program: NRK Newton
Title: *Oppvask, (Eng.: Washing-up)*
Date**:**19th of April 2015
http://tv.nrk.no/serie/newton#t=20m25s

**TV performance**
Program: Schrødingers katt/NRK Viten
Title: *Øyeblikket: Oppvask, (Eng.: Snapshot: Washing-up)*
Date**:** 4th of February 2015
http://tv.nrk.no/serie/oeyeblikket/DMPV73050115/sesong-1/episode-1
http://www.nrk.no/viten/oyeblikket_-oppvasken-1.11992038

**Competition: PhD Grand Prix**
Name of presentation: *Multi-tasking med Nanopartikler (Eng.: Multi-tasking with Nanoparticles)* (4 minutes)
Comment: 1st place out of 7 contestants
Date: 4th March 2015
Location, Gløshaugen, NTNU

**Competition**: **Forsker Grand prix- Trondheim 2014**
Name of presentation: *Magnetiske nanopartikler med magiske egenskaper (Eng.: Magnetic Nanoparticles with Magical Properties)* (4+6 minutes)
Comment: Joint 5th place of 10 contestants
Date: 25th of September 2014

Location: Trondheim, Byscenen
The presentation can be found at NRK website:
*http://tv.nrk.no/serie/kunnskapskanalen/MDFP15002714/20-12-2014 (44:20 min)*

**Invited public talk**
Name of presentation: *Magnetiske Nanopartikler med Magiske Egenskaper (Eng.: Magnetic Nanoparticles with Magical Properties)*
Arranged by: JABB
Date: 29th of October 2014
Location: Digs Baklandet, Trondheim

## Outreach

**Researchers Night: Open University Night**
Title: *Lag ditt eget Nanogull (Eng.:Make your own Nano gold!)*
Arranged by: Samarbeidsforum, NTNU
Description: Stand. Explaining nanotechnology for high school students.
Date: 27th of september 2013
Location: Gløshaugen, NTNU

**Demonstration for primary school students**
Title: *Nanogull i forskning og medisin (Eng.: Nano gold in science and medicine)*
Description: Presentation of our research in protein synthesis of gold nanoparticles to pupils in upper secondary school.
Date: On several occasions in February and March, 2015, 2014 and 2013.
Location: Gløshaugen, NTNU

## Invited talks and blog posts

**Researchers Night: Open University Night**
Title: *Magi med Nanoteknologi (Eng.: Nanotechnology is magic)*
Arranged by: Samarbeidsforum, NTNU
Description: 6 minute inspirational talk to high school students
Date: 25th of september 2015
Location: Gløshaugen, NTNU

**Invited talk for students**
Title: *Forsker Grand Prix- Behind the scenes!*
Arranged by: Linjeforeningen Volvox og alkymisten (Sorority for students studying biology and chemistry)
Date: 19th of November 2014
Location: Gløshaugen, NTNU

**Invited talk for students**
Title: *PhD?*

Arranged by: Høiskolens Chemikerforening (Sorority for students studying chemical engineering)
Date: 7th of November 2014
Location: Gløshaugen, NTNU

**Invited blog post**
Title: *Forsker Grand Prix-klart du kan! (Eng.: Forsker Grand Prix- Yes, you can!),*
Invited by: Faculty of Science and Technology, NTNU
Date: 29th of September 2014
Link: http://blog.nt.ntnu.no/forsker-grand-prix-det-kan-du-vel/

**Lektor 2**
Title: *Nanoteknologi (Eng.: Nanotechnology)*
Comment: 3 hour lecture for pupils
Description: Lektor 2 is a national science initiative funded by the Ministry of Education. Funds are given to upper secondary school/high schools that wish to engage professionals from industry/academia in teaching.
Date: 20th of March 2013
Location: Gauldal Videregående skole, Støren

# Contents

# List of abbreviations

| | |
|---|---|
| AFM | Atomic force microscopy |
| AuNCs | Gold nanoclusters |
| AuNPs | Gold nanoparticles |
| BSA | Bovine serum albumin |
| CAs | Contrast agents |
| CT | Computed tomography |
| DLS | Dynamic light scattering |
| ECM | Extracellular matrix |
| EM | Electromagnetic |
| HOMO-LUMO | Highest – Lowest Occupied Molecular Orbital |
| LSPR | Localized surface plasmon resonance |
| MONPs | Manganese oxide nanoparticles |
| MRI | Magnetic resonance imaging |
| NP/NPs | Nanoparticle/ Nanoparticles |
| SPIONs | Superparamagnetic iron oxide nanoparticles |
| *T1w* | *T1* weighted |
| *T2w* | *T2* weighted |
| TCAA | Hydrogen Tetrachloroaureate (III) |
| TEM | Transmission electron microscopy |
| TCSPC | Time-correlated single-photon counting |
| Tf | Transferrin |
| Trp | Tryptophan |
| UV-vis | Ultra violet-visual |
| XPS | X-ray photoelectron spectroscopy |
| XRD | X-ray diffraction |

# 1 Motivation

*"There's plenty of room at the bottom"*
*- Richard Feynman, 1959*

Colloidal gold has been used for millennia for decoration and glass staining. When glassblowers mixed gold salt into the molten glass, the end-product would give off a beautiful red color. The reason for this color change was not known for a long time. A breakthrough came in the 1850's, when Michael Faraday first synthesized colloidal gold and described that the color of the suspension was caused by interactions between these *miniscule particles of gold* and the incoming ray of light.[1] However, the seed that would eventually grow into a field called nanotechnology was planted by Richard Feynman during a lecture held in 1959. The quotation above sparked the idea of creating and manipulating materials through a bottom-up assembly of atoms. This is the essence of creating atomically scaled materials, or *nanomaterials*, which is one of the main aims of this thesis.

The properties of nanomaterials arise from their size (1-100 nm), which give them remarkably different characteristics compared to their bulk counterparts. For instance, the optical properties of gold change with size and shape: bulk gold is a noble metal with a characteristic metallic yellow color, while nanoparticles (NPs) of gold resonate with light and can be red, purple, blue and orange depending on their size, shape and aggregation state. Bulk gold is chemically inert, in contrast to gold nanoparticles which can have catalytic activity. When gold nanoparticles are below a critical size, they even display molecular fluorescence.

The physical and chemical properties of NPs are advancing a field named *nanobiotechnology*, which can be defined as the use of fabricated nanomaterials in biological systems and applications. Although nanobiotechnology is largely an experimental field, the applications of nanomaterials can be translatable into current medical technologies, particularly in *bioimaging*. This includes diagnostic imaging techniques such as magnetic resonance imaging (MRI), positron emission tomography (PET), computed tomography (CT), ultrasound (US), and in-vivo near-infrared fluorescence (NIRF) imaging that are currently being used to diagnose *e.g* cancer, cardiac diseases, and Alzheimer's disease. Bioimaging not only refers to imaging of internal organs, but also covers imaging down to single cells and excised tissue that has been fixated for observation.

The above mentioned bioimaging techniques often rely on additional contrast agents or probes, that typically are chemical compounds that alter the contrast through *e.g* fluorescence, X-ray scattering or magnetic susceptibility. This allows enhanced information retrieval which can further improve the diagnostic value of the imaging tool. However, current contrast agents typically serve only one function: altering the contrast. Nanoparticles offer the possibility of multifunctionality both by additive and emergent properties which can arise from surface modification with drugs, antibodies or any other biological molecule that serve a therapeutic or improved diagnostic function. For instance, magnetic nanoparticles, such as iron oxide nanoparticles, have magnetic properties that can be induced and thereby controlled by an external magnetic field. This effect can be utilized in modern medical technologies, such as in MRI or hyperthermia applications. If these NPs are combined with a biologically active molecule, such as a drug, they could potentially act as drug delivery vehicles as well. The real potential of nanoparticles is thus fulfilled when they are combined

with biological molecules or drugs which enables a multifunctional probe that can simultaneously be visualized and have a therapeutic function.

Although nanoparticles offer a range of functionalities not seen in today's contrast agents, administering them for diagnostic purposes still involves high risk, and targeting NPs to a site of action still remains a tremendous challenge: NPs should be stable in a range of pH-values, be non-toxic, escape the reticuloendothelial system, and be safely cleared from the body.[2-6] This is the *Pandora's Box* of nanoparticles; introducing them to the body could cause more harm than good. Thus, nanoparticles prepared for bioimaging and therapy must be steered in the direction of biocompatible bioimaging probes that have a significant signal-to-noise ratio and that are safely removed from the body.

In this thesis, the focus has been on synthesizing novel nanomaterials that serve more than one function; several optical properties, magnetic susceptibility, and drug delivery. Additionally, the nanomaterials synthesized herein have been tested in biological systems, not only to investigate their bioimaging function but also to describe their biocompatibility.

Specifically, *this thesis aims at synthesizing and characterizing multifunctional plasmonic and magnetically active biocompatible nanomaterials for bioimaging applications*. The work has been restricted to mainly three elements; gold, iron and manganese. The major reasons being size-tunability and optical and magnetical properties beneficial for bioimaging applications. Different methods were used to synthesize these nanomaterials, and they have been divided into two groups; the hybrid nanomaterials and magnetic nanoparticles. The former group involved synthesis of fluorescent and plasmonic gold nanostructures with two different proteins; Transferrin and bovine serum albumin, while the latter group involved chemical synthesis of gold nanostructures, iron oxide NPs and manganese oxide NPs.

The first part of this thesis aims at contributing to an increased understanding on how transferrin and bovine serum albumin can synthesize gold nanomaterials through characterization, *in vitro* work, and describing how growth of these constructs, and concomitantly the optical properties, can be tuned. The second part of this thesis aims at synthesizing and characterizing superparamagnetic and paramagnetic nanoparticles of different morphologies that are to be used as contrast agents in magnetic resonance imaging and potential drug delivery and hyperthermia applications.

Moreover, all the nanomaterials synthesized herein were assessed either *in vitro* or *in vivo* to increase the understanding of how nanoparticles prepared from different elements and with different shapes interact with cells and living animals. Nanomaterials prepared from iron oxide and manganese were taken to further studies *in vivo* with the aim of investigating their properties as bioimaging probes and potential drug delivery vehicles in a living system.

# 2 Hybrid Nanomaterials

Two classes of nanomaterials are synthesized, characterized and applied in this thesis and are divided into two groups based on their synthetic routes: either biomineralized with proteins or *via* thermal decomposition in organic solvents. The latter group is comprised of magnetically active nanoparticles, which are introduced in the next chapter.

Proteins offer two properties particularly important for synthesis of gold nano species; first, their inherent reduction potential is sufficient to convert ionic gold into solid gold.[I] Secondly; the protein is a steric stabilizer that creates stable suspensions even in buffers. [II]

Nanomaterials synthesized from protein biomineralization are here called *hybrid nanomaterials*, as the final product consists of a metallic structure (gold nanoconstruct) stabilized in a biological molecule (protein). These hybrid nanomaterials will be the focus of this chapter, starting with a basic introduction to proteins. Then, an overview of the optical properties of gold nanoclusters and gold nanoparticles are given. Finally, the applications of these unique hybrid nanomaterials are reviewed.

## 2.1 Proteins

Proteins are the functional expression of which the genetic code is conveyed, and proteins are the basis for all cellular functions. The functional properties of proteins arise from their structure, which governs flexibility, hydrodynamic volume, and hydrophobic pockets that can have catalytic activities. Irrespective of species, all proteins are built up of the same 20 amino acids, and the composition and sequence of these amino acids determine the final structure of the protein. The combined physical and chemical properties of amino acids will ultimately decide the structure of the protein. Some amino acids are hydrophobic, while some are hydrophilic and folding of the polypeptide is largely based on hydrophilic and hydrophobic interactions with water. For instance, water soluble proteins found in the blood stream have their hydrophilic amino acids mainly at the protein surface, while hydrophobic amino acids are forced to the interior part of the protein. In the case of membrane spanning proteins, they are partitioned in the membrane in such a way that hydrophobic domains reside in the interior of the membrane, while hydrophilic domains prefer to stay at the outer part of the membrane. In this way, the loss of entropy from surrounding water molecules is kept to a minimum.

In the cell, proteins are synthesized by cytosolic ribosomes from an mRNA strand. The mRNA is converted into a polypeptide chain that gradually grows and protrudes from the ribosome in an unfolded state. Proteins can contain several domains that can be up to 100 amino acids long, and correct folding of a domain requires a remarkable molecular recognition that was initially hypothesized to be spontaneous. However, correct folding of non-native proteins was later shown to be mediated by an army of proteins named *chaperones*. [7, 8] Misfolded proteins are usually devoid of normal biological activity, and these are normally degraded as they pose a potential threat to the cell. [7] However, if degradation does not occur, they can aggregate or interact with cells in an unwanted manner. [9, 10] For example, in Alzheimer's disease, neurodegeneration is caused by amyloid plaques formed by misfolded β-amyloid protein aggregation, [11, 12] and it is hypothesized that chaperones play a critical role in the development of the disease. [13] Interestingly, some proteins must actually be

[I] Standard reduction potential to reduce $Au^{3+}$ to Au(s) is 1.40 E°(V)
[II] AuNPs crash out in high saline solvents due to reduced thickness of the electrical double layer.

in an unfolded or disordered state to be functional. These proteins comprise approximately 30 % of all proteins and are named *intrinsically disordered proteins.* [14]

Due to the close link between the function and structure of proteins, it is useful to describe their structure in hierarchical levels of complexity. The *primary structure* of a protein is a description of the amino acid sequence and any disulfide bridges (S-S) binding the polypeptide chain together.

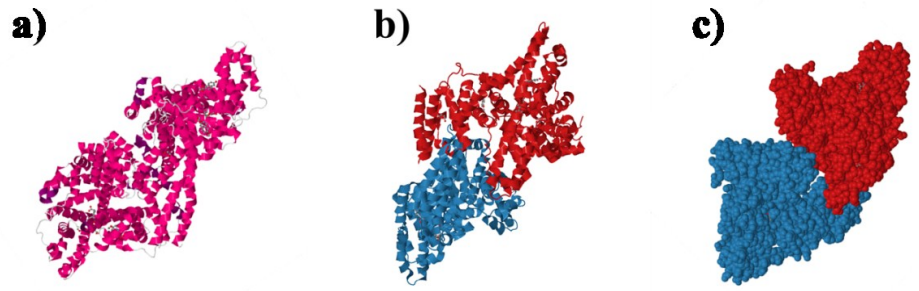


Figure 2.1: The a) secondary, b) tertiary, and c) quaternary structure of bovine serum albumin. [15, 16]

The *secondary structure* of a protein is the three dimensional arrangements of polypeptide chains in α-helixes and β-sheets. These arrangements are mainly governed by hydrogen bonding between amino acids. The *tertiary structure* describes all aspects of the three dimensional folding of a polypeptide. If a protein has several domains or subunits, the *quaternary structure* describes how subunits are oriented in relation to each other. This means that the secondary, tertiary and quaternary structure of proteins describe the spatial arrangements of amino acids and is generally referred to as the *protein conformation*. [17] An example of the secondary, tertiary and quaternary structure of the protein bovine serum albumin (BSA) is shown in Figure 2.1. The hierarchical structure of a protein typically describes a protein in its native (N) state. That is, under optimal pH and temperature conditions. A protein may transit to the unfolded state (U) or the denatured state (D) if it is exposed to elevated temperatures or extreme pH values.

Predicting with computer modeling, and/or experimental work how a protein obtains its three dimensional structure is not only highly complex, but also expensive and time-consuming. Therefore, the structure of a majority of proteins remains to be described. However, one protein that has been extensively studied is BSA, which undergoes several transitions as a function of pH. BSA has a neutral charge at pH=4.7. At neutral pH, BSA obtains its N state, that transit to a basic state (B) at pH 8.0, and an aged state (A) at pH 10.0. [18] The B isomerization is a less rigid molecule compared to the N isomerization, meaning that BSA at basic pH has more degrees of freedom. [19] At pH values above 10.5, tyrosinyl residues becomes deprotonated which can result in the U state. [20] Several proteins have an intermediate state, which has been named the *molten globule (MG)* state. The MG state is described as being an intermediate of the unfolded and the native state. Typically, the tertiary structure is lost, but secondary structural motifs such as α-helixes and β-sheets still prevail. [21] For BSA,

the MG state has been suggested to occur at around pH 11.0. This was investigated by determining the pH-dependent binding interactions between BSA and a hydrophobic fluorescent dye, 8-anilino-1-naphthalene-sulfonate (ANS). At around pH=11, the binding between ANS and BSA is higher compared to any other pH-values, which suggests that hydrophobic residues in BSA are more available for interactions with ANS. [20] Not only the exposure of hydrophobic pockets are an interesting property of BSA, but also that it is stable at very high pH-values. At high pH, BSA becomes negatively charged and can electrostatically attract metallic ions, and in some cases these metals can be reduced and self-assemble into nanostructures aided and stabilized by the protein. This property is further discussed in the next subsection.

## 2.2 Proteins can biomineralize gold

A biomineral is a composite material that consists of a mineral and a biological molecule. The term *biomineralization* thus refers to the process in which these materials are formed. [22] Proteins are particularly interesting in this context, as some have specific structures that have a particular affinity for ions and metals. Some proteins depend on metals for increased activities, and the metal is in such named a *co-factor*. For instance, hemoglobin has a porphyrin ring with a central iron ion that it needs to properly bind and transport oxygen in the blood. Some proteins have been shown to go beyond binding of single-metal ions and perform biomineralization of metals. One such enzyme is bovine serum albumin, which was the first protein described to synthesize nanostructures of gold. [23] BSA does not need co-factors to function properly, and does not biomineralize gold at physiological pH. However, at basic conditions, an increasing amount of amino acids becomes negatively charged, such as tyrosine ($pK_R$=10.07) histidine ($pK_R$=6.00) and cysteine ($pK_R$=8.18). If gold ions are incubated with BSA at pH values above 10.0, the protein will electrostatically attract positively charged gold ions particularly to areas rich in tyrosine, histidine and cysteine. [24] Once at the protein backbone, the gold ions are reduced to atomically sized gold structures, referred to as *gold nanoclusters* (AuNCs). With increased time and concentration of gold ions, these nanoclusters grow into *gold nanoparticles* (AuNPs). At the particular pH, BSA is believed to be in its molten globule state, which was recognized as being a flexible state with exposed hydrophobic residues but with retained secondary motifs.

As hybrid nanomaterials are comprised and stabilized by proteins, the protein structure may change as a result of the incorporated gold nanostructures. It is therefore important to describe any unfolding of the protein backbone. The aromatic amino acids tryptophan, phenylalanine and tyrosine are fluorophores in proteins that can be excited with wavelengths from 260-295 nm, and that have emission maxima from 285-350 nm (Figure 2.2). [25] Using fluorescence spectroscopy, the emission of the protein in the hybrid material can be compared to the native protein emission, and changes in the emission profile is explained as an alteration of the protein conformation due to incorporation of a metallic nanostructure (this is further discussed in subsection 5.2 and 5.3).

Here, the proteins Transferrin (Tf) and BSA were used to synthesize gold nanoclusters and nanoparticles. Apart from being able to reduce gold ions, they were chosen based on availability, water solubility, fluorescence properties and biological function.

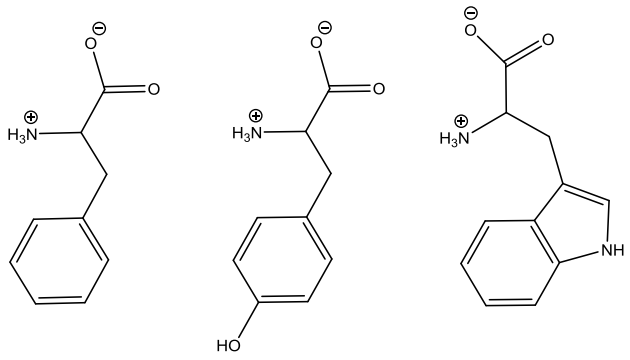


Figure 2.2: The polar fluorescent amino acids in proteins (pH=7.0)

Transferrin is an iron-binding protein that carries iron from the blood and delivers it to cells. Once at the extracellular matrix, Tf is taken up by receptor-mediated endocytosis *via* the transferrin receptor (TfR). Iron is released intracellularly and iron-free Tf (*apo*- Tf) is recycled to the blood. [17] Iron is an important co-factor in many cellular events, particularly in proliferation and mitosis, and the expression of TfR is regulated according to the cell cycle. In highly proliferating cancer cells, the expression of TfR is increased, [26, 27] which means that hybrid nanomaterials created in a Tf scaffold would potentially have a higher probability of targeting cancer cells, assuming that the affinity of Tf towards TfR is unaltered or sufficient.

BSA is very similar to human serum albumin, and is as Tf also a blood protein. However, BSA is less specific than Tf, and can carry a plethora of molecules in the blood, such as drugs and lipids. [28, 29] As was described above, BSA has several states can undergo major conformational changes without denaturation.[18, 30, 31]

The two next subsections will describe the second component of the hybrid nanomaterials, which is comprised of two different structures of gold; the nanoparticles and the nanoclusters.

## 2.3 Optical properties of gold nanoparticles

Michael Faraday (1791-1867) was a remarkable scientist most widely known for his contributions to the theory of electromagnetism. He is perhaps less known for his contributions to modern nanotechnology, as he was the first to synthesize and describe the optical properties of gold nanoparticles approximately 150 years ago:

*"Light has a relation to the matter which it meets in its course, and is affected by it, being reflected, deflected, transmitted, refracted, absorbed, etc. by particles very minute in their dimensions. Gold seemed especially fitted […] because of its development of color both in the reflected and transmitted ray, and because known phenomena appeared to indicate that a mere variation in the size of its particles gave rise to a variety of resultant colors. […] The waves of light are so large compared to the dimensions of the particles of gold which in various conditions can be subjected to a ray, that it seemed probable the particles might come into effective relations to the much smaller vibrations of the ether particles."*

*-M. Faraday* [32]

Today we know that the "*effective relations"* between AuNPs and light occur due to an optical phenomenon called *localized surface plasmon resonance (LSPR)*.

A *plasmon* is the collective plasma oscillation of conducting electrons at the nanoparticle (NP) surface. The conducting electrons have a higher energy level than the valence electrons, and can freely move between atoms. LSPR is initiated by an external electromagnetic wave that displaces the electrons from the NP core (Figure 2.3). This displacement creates an electric field both inside and immediately outside the AuNP in a standing oscillation opposite to the electric field of the incident light. As the EM wave propagates, the electron cloud of the NP oscillates with the same frequency as the incoming beam, but out-of-phase, causing a shift in the dipole moment of the AuNP(indicated with arrows in Figure 2.3). The interactions between the incoming photons and the surface electrons of the AuNP lead to a high absorption coefficient, which is observed as a maximum absorption peak in UV-visible spectroscopy at approximately 520 nm.

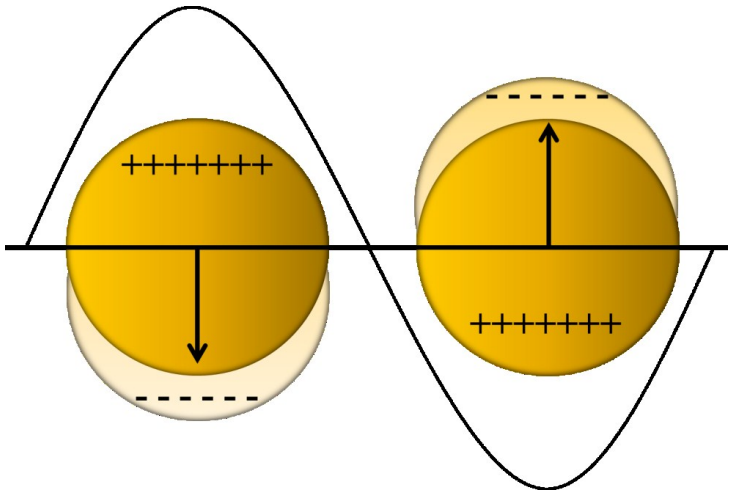

Figure 2.3: Localized surface plasmon resonance of gold nanoparticles. Arrows indicate the dipole moment of the AuNP.

Furthermore, Faraday's observation that the "*mere variation in size […] gave rise to variety of resultant colors"* points to the fact that the optical properties of gold are size-dependent. [33]

Two types of gold nanostructures are described and synthesized in this thesis, and they are separated based on their size and interactions with light. The smallest structures are the gold nanoclusters which are in the size-range of molecules. AuNCs have discrete energy levels, no conduction bands, and can therefore not exhibit LSPR. Instead, excitation of AuNCs causes emission of fluorescence. Gold nanoclusters obtain their molecular properties as their diameter is reduced to sizes comparable to the *de Broglie's* wavelength at the Fermi energy[III] of the metal. [34] For gold, this diameter is approximately 2 nm. [35]

[III] This is also called the *Fermi wavelength*

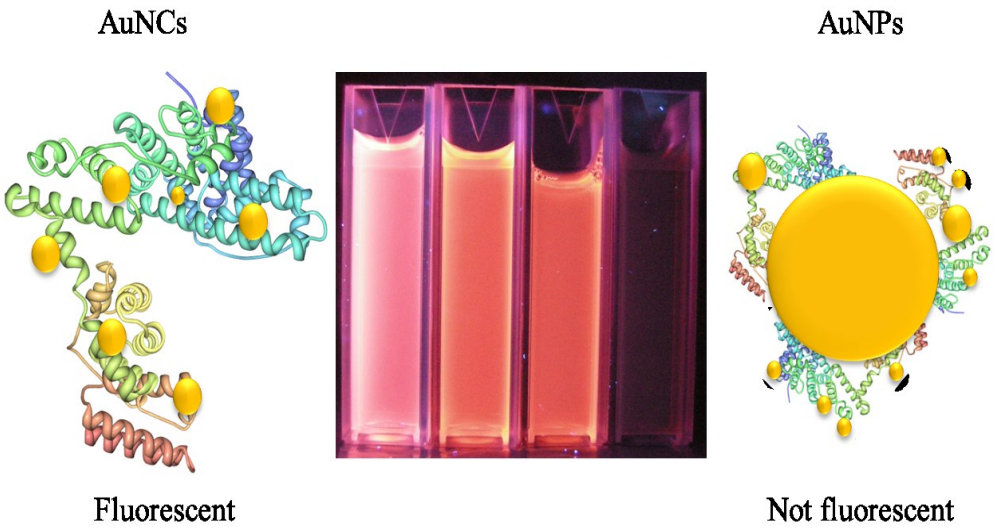


Figure 2.4: Size-dependent fluorescence of BSA-stabilized AuNCs excited with handheld UV-lamp (longwave: 365 nm). The fluorescent cuvettes contain BSA-stabilized AuNCs. The sizes of the AuNCs increase from the left. To the far right, BSA-stabilized AuNPs that quench fluorescence from AuNCs.

AuNPs larger than this do not fluoresce, but absorb light in the visible region of the electromagnetic (EM) spectrum due to LSPR of the conducting electrons. This size-dependent property of gold is illustrated in Figure 2.4, which show AuNCs and AuNPs stabilized in BSA.

In this subsection, the focus is on the optical properties of AuNPs, while the optical properties of AuNCs are the main topic of the next subsection.

The oscillations of the plasmons occur at a specific frequency and wavelength, which depends on the size and aspect ratio of the AuNP, as well as the dielectric constant of the solvent. [25, 36-39] When an incoming beam initiates electron oscillation, the electrons are excited to energy levels above the Fermi level[IV] which raise their chemical potential. The total light that is absorbed by a spherical particle is described by the *Mie theory* in equation 2.1:

$$\sigma_{abs} = \sigma_{ext} - \sigma_{sca} \qquad (2.1)$$

Where $\sigma_{abs}$, $\sigma_{ext}$, and $\sigma_{sca}$ are cross-sections of the absorbance, extinction, and scattering, respectively.[V] For spherical NPs that have a circumference much smaller than the wavelength of the incoming beam ($2\pi R << \lambda$), the magnitude of scattering is proportional to $R^6$, while the absorption is proportional to $R^3$. Thus, small AuNPs have an extinction band that is

[IVIV] The *Fermi level* is the chemical potential of electrons

[V] A *cross-section* is a general term in physics describing the probability of a certain particle-particle interaction, for instance the probability of absorption, scattering or extinction.

dominated by absorption, while scattering dominates with larger AuNPs. [40] If we assume that the nanoparticle diameter (d) is very small compared to the wavelength of the incident beam (d<<λ), we obtain a simplified expression for the extinction and scattering cross sections:

$$\sigma_{ext} = \frac{18\pi\varepsilon_m^{\frac{3}{2}}V}{\lambda}\frac{\varepsilon_2(\lambda)}{\left[\varepsilon_1(\lambda)+2\varepsilon_m\right]^2+\varepsilon_2(\lambda)^2}$$

$$\sigma_{sca} = \frac{32\pi^4\varepsilon_m{}^2V^2}{\lambda^4}\frac{(\varepsilon_1-\varepsilon_m)^2+(\varepsilon_2)^2}{\left[\varepsilon_1+2\varepsilon_m\right]^2+(\varepsilon_2)^2}$$

Where $\varepsilon_1$ and $\varepsilon_2$ are part of the complex dielectric function:

$$\varepsilon = \varepsilon_1 + i\varepsilon_2$$

Further, $\varepsilon_1$ represents the real part and $\varepsilon_2$ the imaginary part of the complex function. $\varepsilon_m$ is the dielectric function of the solvent/medium. The resonance condition is fulfilled when $\sigma_{ext}$ is maximized, that is when $\varepsilon_1(\lambda) = -2\varepsilon_m$.[VI] For instance, AuNPs in water ($\varepsilon_{m,\ water}$ ~1.7) have a maximum absorbance wavelength when $\varepsilon_1 = -2\varepsilon_m$ which corresponds to 520 nm. This wavelength is the LSPR peak, which can be estimated with *Drude's theory*.

The Drude theory describes a frequency-dependent form of $\varepsilon_1$ that can be used to determine the LSPR peak wavelength:

$$\varepsilon_1 = 1 - \frac{\omega_p}{\omega^2+\gamma^2} \qquad (2.2)$$

Where $\omega_p$ is the plasma frequency and $\gamma$ is the damping parameter of the bulk material. From the Drude theory (equation 2.2), the maximum frequency can be expressed as a function of $\omega_p$:

$$\omega_{\max} = \frac{\omega_p}{\sqrt{2\varepsilon_m+1}} \qquad (2.3)$$

However, the maximum wavelength is a more convenient number that can be calculated from the maximum frequency:

$$\lambda_{\max} = \frac{2\pi c}{\omega_{\max}} \qquad (2.4)$$

Equation 2.4 can now be rearranged to equation 2.5:

[VI] $\varepsilon_1$ is negative because the electrons oscillate out of phase with the incoming electromagnetic wave.

$$\frac{\lambda_{\max}}{2\pi c} = \frac{\sqrt{2\varepsilon_m + 1}}{\omega_p} \qquad (2.5)$$

The plasma frequency can be rewritten to yield the plasma wavelength similar to the maximum wavelength (from equation 2.4) which gives:

$$\frac{\lambda_{\max}}{2\pi c} = \frac{\lambda_p}{2\pi c}\sqrt{2\varepsilon_m + 1} \qquad (2.6)$$

By rearranging equation 2.6 and setting the squared refractive index, $n^2$, equal to the dielectric constant

$$\varepsilon_m = n^2$$

We arrive at the final expression for the peak wavelength of LSPR, $\lambda_{max}$[36]:

$$\lambda_{\max} = \lambda_p\sqrt{2n_m{}^2 + 1} \qquad (2.7)$$

The LSPR peak depends on the size and aspect ratio of the AuNP, as well as the dielectric constant of the medium. For instance, AuNPs with a diameter of 10 nm have an LSPR absorption maximum at 520 nm, while AuNPs in the size-range of 80 nm have an absorption maximum at approximately 540 nm. This bathochromic shift of the LSPR peak is because AuNPs with 80 nm diameter have surface oscillating plasmons with lower frequencies. [33] The effect is best seen in gold nanoparticles shaped as rods, which have two plasmon resonances; one in the longitudinal and one in the transverse direction. The transverse plasmon frequency is the same as for spherical AuNPs, while the longitudinal plasmon frequency increases with the length. A change in the refractive index will cause an alteration in the surface oscillations of the AuNP electrons and cause a shift in the LSPR peak. However, the properties of the surface capping agent[VII] is also important as they can locally alter the surface oscillations.[41] This is the basis of sensing applications with AuNPs which will be discussed after the optical properties of AuNCs.

## 2.4 Optical properties of gold nanoclusters

In contrast to LSPR, AuNCs have discrete HOMO-LUMO transitions of a one-electron nature. This results in molecule-like properties such as size-dependent fluorescence. The emission energy depends on the number of atoms, $N$, in each gold nanocluster and the Fermi energy, $E_F$, of bulk gold *via* the relationship

$$\frac{E_F}{N^{1/3}}$$

This indicates that the electronic structure is determined by the AuNCs free electron density and AuNC size. AuNCs that have a diameter below 2 nm does not have LSPR, and have been described as semiconducting materials. [35]

[VII] The capping agent in this thesis is mainly the proteins BSA and Tf.

The threshold at which gold goes from exhibiting LSPR to fluorescence can be estimated based on the free electron theory, by approximating the average spacing of electronic energy levels, $\delta$, to the Fermi energy[VIII], $E_f$, and the number of gold atoms, $N$:

$$\delta \approx \frac{E_f}{N} \qquad (2.8)$$

This equation states that with decreasing size, the average spacing of electronic levels gets larger. Setting the Fermi energy of gold ($E_f$=5.5 eV) into equation 2.8 and using the thermalenergy at room temperature ($T=298\ K$) as a criterion for distinct energy quantization:

$$\delta \geq k_B T$$

We obtain an expression for the amount of gold atoms:

$$N \geq \frac{5.5eV}{k_B 298K}$$

Using Boltzmann constant ($8.6173303\times10^{-5} eV\ K^{-1}$), the critical number of gold atoms in an AuNC is estimated to 200-300 atoms, which corresponds to roughly 2 nm in diameter.[39,42]

The amount of atoms in AuNCs follow a shell model named the *Jellium model* with the corresponding magic numbers 2, 8, 10, 20, 25, 34, 40. An analogy to the Jellium model is the electronic structure of atoms, in which each shell is stable with an optimal amount of electrons. For instance, the noble gases fulfill the octet rule, and are very stable elements not likely to undergo reactions with other atoms. As the stability of an atom is governed by closed valence shells, so is the stability of magic numbered nanoclusters. [43-45]

The size-dependent fluorescence of AuNCs can be measured using steady-state fluorescence spectroscopy. However, the actual origin of fluorescence is not clear, as it can arise from the metal core, or from interactions between the metal core and surface ligands, named *Metal to Ligand* and *Ligand to Metal Charge Transfer* (LMCT and MLCT) transitions. [39] Particularly, electron-rich atoms appear to affect the fluorescence intensity in a positive manner, and is believed to occur either as a charge transfer or as a direct donation of delocalized ligand electrons. [46] Here, the proteins BSA and Tf were used to synthesize and stabilize AuNCs and AuNPs. Proteins offer a plethora of energy donating atoms, such as S, N and O, and can therefore collectively enhance the fluorescence intensity via surface interactions if they are used as capping agents. AuNCs synthesized *via* proteins are excited at 370 nm and generally emit at two different wavelengths ($\lambda_{em}$*=430-450 nm and* $\lambda_{em}$*=560-730 nm*) with different intensities, depending on the diameter and concentration of AuNCs. The emission peak at between 430-450 nm is attributed to populations of smaller AuNCs with magic numbers 8, 10 ($Au_8$, $Au_{10}$), while the peak between 600-700nm is attributed to populations of larger AuNCs ($Au_{25+}$). [23, 47]

The main work on synthesizing the AuNCs were performed with BSA as scaffold and reducing agent, and from this study we were able to describe the growth of AuNCs in the protein backbone. The results were reproducible, and we were able to synthesize different populations of AuNCs and AuNPs by varying the reaction parameters. As the populations of

[VIII] The *Fermi energy* is defined at absolute zero temperature, and is the energy difference between the highest and lowest occupied single- particle states.

AuNCs and AuNPs dictate protein unfolding and optical properties, tuning the sizes of AuNCs/AuNPs is one important factor for their applications, some of which are discussed in the next subsection.

### 2.5 Applications of protein-stabilized AuNPs and AuNCs

AuNPs can be synthesized via a range of methods, and an extensive review of synthesis methods is given in reviews by Saha[37] and Szunerits. [48] AuNPs can be water stabilized by binding of thiol groups to the surface, due to the affinity of thiol groups to gold. [49-51] The low toxicity and surface active electronic structure of AuNPs makes them useful in a range of applications; from cancer therapeutics[52] to catalysis applications. [53] The principle of sensing with AuNCs and AuNPs stems from alteration of the optical properties that occur due to interactions with biological molecules or ions. This can for example be from quenching or enhancement of AuNC fluorescence, or from alterations in the LSPR absorbance of AuNPs.

Techniques for sensing with AuNPs can involve tuned aggregation or changes to the refractive index surrounding the AuNP. Aggregation of AuNPs would be observed as a red-shift in the LSPR peak. The principle of sensing with AuNPs can for instance be done by designing the surface chemistry of AuNPs in such a way that when specific molecules bind, AuNPs aggregate. The aggregation can for instance be driven by folding of a polypeptide chain on the surface. [54, 55] The sensitivity can be tuned towards enzymes such as metalloproteinases,[56] or neurotoxins, [57] by changing the properties of the surface polypeptide or receptor. A complete coverage of applications is beyond the scope of this subsection, and the reader is referred to Daniel *et al* [58] for a review of general applications of AuNPs.

Adsorption of proteins onto AuNPs has been extensively studied, [9, 59-62] but it was not until 2009 that Xie *et al* suggested a bottom-up approach for synthesis of AuNCs, with BSA acting as both a template *and* reducing agent of gold ions. [23] In this thesis, the bottom-up biomineralization approach was used to synthesize AuNPs and AuNCs and the work mainly centered on the synthesis mechanism, characterization and biocompatibility of protein-stabilized gold nanoconstructs. Therefore, the focus of this subsection will be on applications of these nanomaterials rather than applications involving adsorption of peptides/proteins onto separately synthesized AuNPs.

During AuNC and AuNP synthesis the protein backbone unfolds, and depending on the degree of unfolding this may in some cases disrupt biological membranes. [63]

Elevated concentrations of heavy metal ions (*e.g* $Pb^{2+}$, $Hg^{2+}$, $Cd^{2+}$) in biological tissue is toxic and potentially deadly for the host. For instance, high doses of $Hg^{2+}$ are related to neurotoxicology, and heavy metals have been linked to development of Parkinson's and Alzheimer's disease. [64] Sensing of heavy metal ions in blood and in water is important to protect the host and the environment. [65] With BSA-stabilized AuNCs, colorimetric detection assays of heavy metal ions such as $Hg^{2+}$ and $Cu^{2+}$ is possible, due to quenching of the fluorescence. [66,67,68] The basis of sensing $Hg^{2+}$ is that $Hg^{2+}$ can complex with BSA-AuNCs *via* cysteine bonding (Hg-S), and this affects the optical properties of AuNCs. Specifically, excited BSA stabilized AuNCs transfer the excited electron to $Hg^{2+}$ leading to oxidation of $Hg^{2+}$ to $Hg^{+}$. This causes fluorescence quenching which can be observed as a decrease in the intensity of the signal. [69] AuNCs stabilized in proteins can not only detect heavy metals, but also biological molecules such as dopamine, which is relevant in applications towards Parkinson's disease. [70] One major advantage of protein-stabilized AuNCs is that they are more biocompatible compared to the quantum dots (QDs), which are prepared from

semiconductor materials. [66, 71] BSA-stabilized AuNCs can also compete with QDs as they show comparable detection limits, for instance detecting the amino acid cysteine down to 10 nM. [72]

The optical properties of protein-stabilized AuNPs and AuNCs are without a doubt very intriguing, and they appear to have a promising future in biosensing. However, we found that when incubated with typical fluorescent dyes for cell experiments, we observed what appeared to be spectral interactions between the dyes and the AuNCs (See paper I, Figure 6). When the cells were incubated only with protein-AuNCs and no dyes, the emission intensity of AuNCs were too weak to be observed through the fluorescence microscope. This probably was an effect of low concentrations of AuNCs and the high intensity of the inverted beam from the microscope optics that could have photobleached the AuNCs. Because of this, we were unable to determine whether the cells internalized the AuNPs/AuNCs or not, and we decided to not further investigate the internalization with transmission electron microscopy. However, it is worth mentioning that we did test AuNPs as contrast agents in X-ray computerized tomography (CT)[IX]. AuNPs below 100 nm have attracted a lot of attention as potential CT CAs [73-75] and AuNPs stabilized in BSA could be used as contrast agents in CT. [76] BSA-stabilized gold have a remarkable suspension stability, which gives them shelf lives up to one year. This is a very important feature of nanobiomaterials as it increases their applicability. We managed to see a size-dependent attenuation with CT (see paper II, supporting information), but the results were not convincing enough to elaborate on further studies. We therefore shifted our attention to another method for imaging deep tissue, namely magnetic resonance imaging (MRI). In contrast to CT, MRI is based on relaxation of hydrogen nuclei after a radiofrequency pulse. The acquired images separate blood from fat, muscles from bones, and potentially malignant tissue from normal tissue. Contrast agents (CAs) are used in MRI to ease the diagnostics, and must be of materials capable of altering the relaxation of protons. The most commonly used clinical CAs are chelates of $Gd^{3+}$ (*e.g* Gadovist, Magnevist). [77, 78] However, magnetic nanoparticles are emerging as potential CAs in MRI, for several reasons. NPs have longer blood circulation times as compared to chelates, [1] and the large surface-to-volume ratio of NPs results in a greater contact area between magnetically active centers and the tissue. Moreover, the large surface-to-volume ratio allow not only for an altered contrast, but for surface-functionalization with drugs. This creates the possibility of designing multifunctional nanoparticles that can carry drugs as well as signaling its location. The remaining theoretic parts of this thesis will focus on the properties of magnetic nanoparticles, and their possibility for entering eukaryotic cells.

[IX] CT is a diagnostic imaging technique based on different tissue absorptions.

# 3 Magnetic nanomaterials

The previous chapter covered the hybrid nanomaterials that could be synthesized with proteins due to the combined reduction potential of amino acids. However, synthesis of magnetic nanomaterials requires a different approach and here involves thermal decomposition of a metal-oleate complex in organic solvents under high pressure and argon atmosphere. With thermal degradation, the geometry, size, and size distribution of the resultant particles can be fine-tuned by adjusting the rate of nucleation events.

Magnetic nanomaterials were here used for bioimaging with magnetic resonance imaging, and the focus will therefore be on the magnetic properties of nanoparticles that enable contrast in MRI. This chapter starts with an introduction to magnetism and MRI, before the physical properties and applications of contrast agents are described.

## 3.1 Magnetism and Magnetic Resonance Imaging

According to the law of electromagnetism, a moving charge will induce a local magnetic field. As such, magnetism is a fundamental property of the atom that arises from spinning electrons. In the nucleus, the neutrons and protons also spin, but in opposite directions. The sum of the nuclear spins is called the *quantum spin number*, *I,* where a proton has $I = ½$, and a neutron has $I = -½$. If there is an equal amount of neutrons and protons in a nucleus, the total spin is zero ($I=0$). However, when there is an uneven amount of protons and neutrons in the nucleus, for instance in isotopes, the nucleus has a net spin ($I \neq 0$) which is called an *angular momentum*. [79] The $^1$H (protium) is an isotope of hydrogen, with only one proton and no neutrons. As there are no opposite spins from any neutrons, protium has a net nuclear spin ($I = ½$), and therefore an angular momentum. The magnetic moment of the protium is the basis for MRI, which is a diagnostic tool for imaging soft tissues.

When a protium is placed in an external magnetic field, $B_0$, it becomes polarized, meaning that the rotation of electrical charges spin in the direction of the applied force, and a magnetic dipole moment, $\mu$, is produced in a direction perpendicular to the applied force. [X] The magnetic moment describes the direction and magnitude of the produced field. As $^1$H is abundant in biological tissue, it provides a relatively large magnetic moment that is sufficient to acquire an MR signal. [78]

MR images are collected by an MR scanner which provides an external magnetic field, $B_0$. This causes the protium in a tissue to align with the field (Figure 3.1). Depending on the thermal energy of the different protiums, they will be oriented either as spin-up or spin-down. Spin-up nuclei are low energy nuclei that align parallel to $B_0$, while spin-down nuclei are high energy nuclei that align antiparallel to $B_0$. The *net magnetization vector (NMV)* is the vector sum of the spin-up and spin-down nuclei (Figure 3.1). Once aligned, all the magnetic moments of $^1$H spin around the field lines of $B_0$ in a precessional path. The speed of precession is the precessional frequency, or Larmor frequency, $\omega_0$, which is related to $B_0$ as described by the *Larmor equation*:

$$\omega_0 = B_0\gamma$$

Where $\gamma$ is the gyromagnetic ratio. [80]

[X] According to the right-hand rule

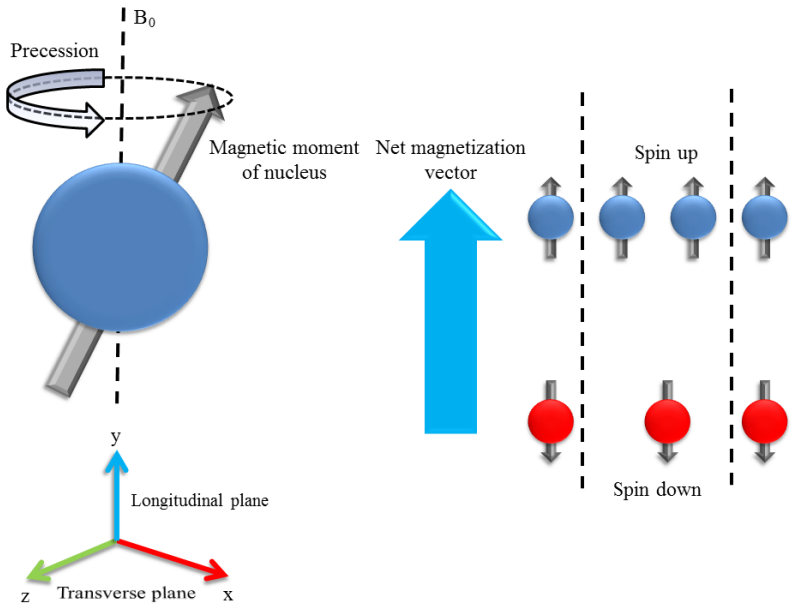


Figure 3.1: Precession of hydrogen nuclei ($^1$H) and parallel and antiparallel spin. [78]

The MR signal is acquired by applying a radiofrequency (RF) pulse to the sample. The RF pulse has the same frequency as the Larmor frequency of the protium. The low energy spin-up nuclei absorbs the energy of the RF pulse and becomes high energy spin-down nuclei. This causes the NMV to move out of alignment with $B_0$. Depending on the length of the RF pulse, the NMV takes up an angle to $B_0$ in the longitudinal plane, called a flip angle (FA). A FA of 90° brings the NMV all the way down to the transverse plane. After the RF pulse is switched off, the NMV will relax back to its original position. This leads to magnetic field fluctuations that induce an electrical voltage in a receiver coil. The magnetically induced electrical current is the MR signal that is converted to an MR image *via* Fast Fourier Transformation. The NMV relaxes in a three dimensional rotating coordinate system. The NMV can therefore be decomposed into a transverse and a longitudinal component, and the MR signal is collected in either of these planes. Relaxation in the longitudinal plane is named the *T1 relaxation time,* while relaxation in the transverse plane is named the *T2 relaxation time.* The *T1* relaxation time is defined as the time it takes for 63% of the longitudinal magnetization to recover, while the *T2* relaxation time reflects the time it takes to recover 37% of the transverse magnetization.

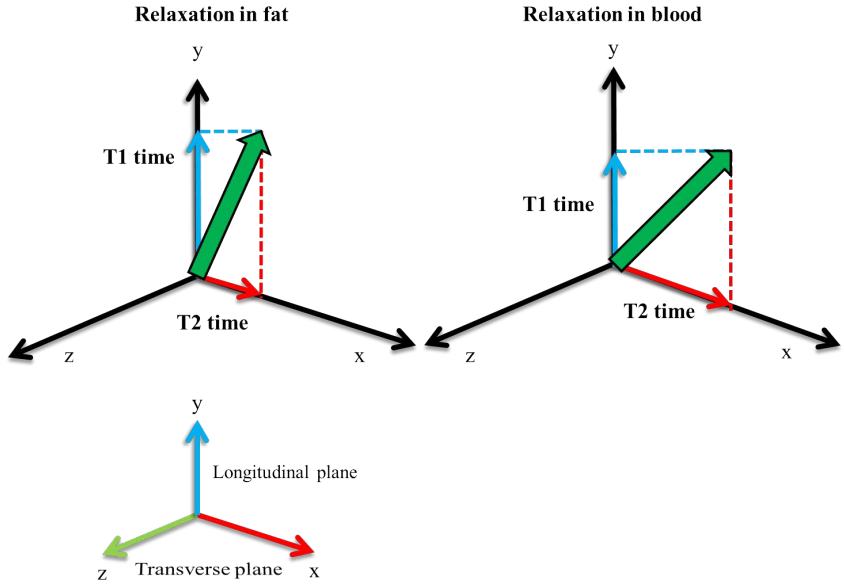


Figure 3.2: Longitudinal and transverse relaxation of fat and water after an RF pulse.

MR images can be weighted to depict tissue differences in the *T2* or the *T1* time, and these images are called *T1* weighted (*T1w*) or *T2* weighted (*T2w*) images, respectively. [78] Both relaxation times are affected by three factors, but to a different degree[78]:

1. *Spin-lattice interactions*. Relaxation of the protium involves thermal interaction with surrounding molecules, named the *lattice*. If the lattice contains macromolecules that can absorb energy from the spinning protium, then the energy transfer and relaxation is more efficient. Thus, protiums in fat are in close proximity to a large lattice of macromolecules, and therefore have an efficient relaxation, while protiums in water have a less structured lattice, making spin-lattice relaxation less efficient.
2. *Density of molecules.* Densely packed protiums have faster dephasing of the magnetic moments, as they have a higher probability of interactions with neighboring magnetic fields (spin-spin interactions).
3. *Matching of tumbling rate and Larmor frequency.* If the molecular tumbling rate is close to the Larmor frequency, there is efficient exchange between the lattice and the protium.

The *T1* time is the spin lattice relaxation, where the energy of protiums is dissipated to the surrounding molecular lattice. The *T1* time is therefore affected by the first factor in the list above. In a *T1w* image, the different relaxations in the longitudinal plane are compared, and the tissue with the largest component in the longitudinal plane will appear bright. In fatty tissue, there is efficient absorption of energy after an RF pulse, and fatty tissue quickly realigns its longitudinal magnetization. Fat therefore has a short *T1* time, and a large longitudinal component (Figure 3.2, relaxation in fat). In blood (water), the energy dissipation

between hydrogen nuclei is less efficient, meaning that blood needs longer time to relax, making the longitudinal component smaller than that of fat (Figure 3.2, relaxation in blood). In a *T1w* image, fat will therefore appear bright while blood will appear dark, as the longitudinal component of fat is larger than that of blood.

The *T2* relaxation time reflects the spin-spin interactions between magnetic fields of neighboring hydrogen nuclei, and is therefore particularly affected by the density of the protiums (factor 2 in the list above). A *T2w* image is based on differences in contributions to the transverse relaxation. Fat is closely packed, which leads to an efficient spin-spin relaxation, a short *T2* time, and a small contribution to the transverse component. However, the spin-spin relaxation in water is less efficient as water molecules are spaced apart and thus less likely to interact. This results in a longer *T2* time and a greater contribution to the transverse component. Thus, the magnetic relaxation contribution from hydrogen nuclei in water leads to a longer induced voltage in the receiver coil, which in turn leads to a hyperintense signal making blood appear bright in a *T2w* image, while fatty tissue remain dark. Finally, a third relaxation time, *T2**, takes field inhomogeneities into account. The *T2** relaxation time is therefore faster than the *T2* relaxation, as field inhomogeneities speed up the spin-spin relaxation.

With MRI it is possible to set diagnosis in a non-invasive manner, and the technique can be used to image deep brain tissue, muscles and fluid accumulations. An MR image can be very detailed by itself, and be sufficient to set a diagnosis. But in some cases, an external contrast agent may be administered to distinguish differences in vascularization or diffusion, which could indicate pathological distinct tissue from normal tissue. The topic of the next subsection is how these contrast agents can affect the relaxation of protons and to give an altered contrast in an MR image.

### 3.2 Contrast agents in MRI

Altering the relaxation of the NMV is the basis for enhanced or reduced contrast in MRI. Contrast agents are materials that are capable of altering the *T1* or *T2*/*T2** relaxation times. Although CAs affect both the *T1* and *T2* times, they are named according to the relaxation process they affect the most. [81] CAs that shorten the *T1* relaxation time are named *T1* CAs, while CAs that shorten the *T2* relaxation time are *T2* CAs. The efficacy of a CA is the relaxivity, $r_i$, which is a ratio of the relaxation rate, $R_i$ and the concentration of the contrast agent, $C_{CA}$,

$$r_i = \frac{R_i}{C_{CA}}$$

Where *i* is either *1* or *2* and refer to the *T1* or *T2* time respectively. The relaxivity of a contrast agent is a relative value to the relaxivity of water, $T_{i,\ water}$, and can be calculated experimentally from the observed relaxation time, $T_{i,\ observed}$, from:

$$r_i = \frac{\left[\frac{1}{T_{i,observed}} - \frac{1}{T_{i,water}}\right]}{C_{CA}}$$

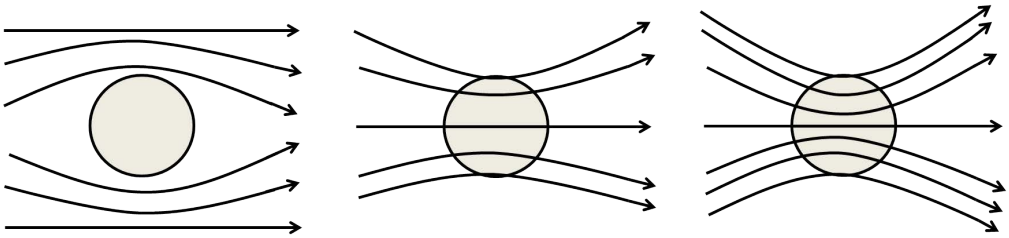


Figure 3.3: Magnetic flux density in dia, -para, and superparamagnetic materials

The relaxivity is defined as *"the increase in the relaxation rate of the solvent (water) induced by 1 mmol·L$^{-1}$ of the active ion of the contrast agent"*. [81]

In this thesis, paramagnetic and superparamagnetic CAs were prepared from manganese, gadolinium and iron. Although the paper on gadolinium NPs are listed as an additional paper, the origin of magnetic susceptibility is included here as it is often compared to the magnetic properties of manganese. This subsection describes the different magnetic properties of these materials and how it affects the contrast in MRI.

A magnetic field has direction and density, illustrated as magnetic flux lines in Figure 3.3. The number of flux lines per unit area is the *magnetic flux density* or *magnetic induction*. [82]A CA alters the magnetic flux density compared to the external magnetic flux. The extent to which a material is capable of altering the flux line density is called the *susceptibility*, which is the ratio of magnetic moments per volume material.[78, 80] Magnetic substances are then further categorized as *diamagnetic, paramagnetic, superparamagnetic* or *ferromagnetic* depending on their magnetic susceptibilities (Figure 3.3).

Diamagnetic atoms have paired electrons that interact negatively with the magnetic field, resulting in a lower magnetic flux density inside the material compared to the outside. Paramagnetic substances have a positive susceptibility, meaning that they orient and create magnetization in the same direction as the applied field, and thus slightly increase the magnetic density.

The rotation of electrical charges within a material is random and the energy of electrons is either spin-up or spin-down. If there are equal amounts of spin-up and spin-down electrons, they cancel each other out resulting in no net spin of charges. The configurations of electrons therefore determine the magnetic behavior of an atom. Most free atoms have a permanent magnetic dipole, however when in molecules or materials, the electronic configurations change. Typically, these configurations are closed shells that have a zero net spin, and the substance is diamagnetic. Exceptions to closed shells are the transition elements which have half-filled shells. Unclosed shells lead to a permanent magnetic dipole moment and paramagnetic susceptibility. Atoms with partly filled shells are the 3d (iron group), 4d (palladium group), 4f, (lanthanide group), 5d (platinum group) and 5f (actinide group). *T1* CAs are typically prepared from paramagnetic elements, such as gadolinium and manganese, as they effectively shorten the local *T1* time in the tissue. The emphasis will therefore be on the 4f and 3d group as they contain gadolinium, manganese and iron.

Paramagnetism is a property of the ion and not the material, meaning that it is $Gd^{3+}$ and $Mn^{2+}$ that are paramagnetic, and not their solid counterparts. Gadolinium is a lanthanide

element broadly used as a contrast agent due to its seven unpaired 4f electrons. These electrons have large magnetic dipole moments ($7\mu$) that lead to local fluctuations of the magnetic field that cause a reduction in the relaxation time of protiums. This increases the longitudinal component of the NMV which results in a distinct bright local signal. Chelates of gadolinium are used clinically as *T1* CAs (*e.g* Gadovist®, Magnevist®), as they provide a hyperintense region in a *T1w* image.[77,78]

Manganese ions have five unpaired 3d electrons ($5\mu$) that contribute to the relaxation of protiums. Albeit smaller magnetic moment than $Gd^{3+}$, the valence charge of $Mn^{2+}$ gives it interesting biological applications. For instance, $Mn^{2+}$ is a $Ca^{2+}$ analogue that can bind to enzymes (*e.g* calmodulin)[83] and enter through voltage-gated $Ca^{2+}$ ion channels in firing neurons. [84] This allows for *in vivo* neuronal tract tracing in a technique called *Manganese Enhanced MRI (MEMRI).* [85, 86]

*T2/T2** contrast can also be obtained from high concentrations of $Mn^{2+}$ ions [87,88] but high doses of $Mn^{2+}$ must be used with caution as it can accumulate in the brain and cause a toxic condition named *manganism*. [89] However, recent synthesis of manganese oxide-based NPs could lead to a resurgence of manganese as an MRI contrast agent. [90-93] For instance, manganese oxide NPs (MONPs) are *T2* active CAs, but they degrade in water within a reasonable time-frame (hours to days) and release *T1* active $Mn^{2+}$ ions. [91, 94-96]

Ferromagnetic materials have a strong positive susceptibility which gives a high magnetic density compared to the external magnetic field. The ferromagnetic materials are permanent magnets, which mean that they do not need an external magnetic field to be magnetic. [78] However, when a ferromagnetic substance, such as iron, is reduced in size below the dimensions of the magnetic domains, it becomes superparamagnetic. This property is confined to the iron oxide nanoparticles, which have positive magnetic susceptibility intermediate of ferromagnetism and paramagnetism. [97] Superparamagnetic materials can for instance be superparamagnetic iron oxide nanoparticles (SPIONs). As SPIONs are not permanent magnets, they do not aggregate in suspension due to magnetic interactions, which is very important for biological applications. The magnetic susceptibilities of SPIONs can therefore be switched on or off by an external magnetic field. This allows control over the magnetic properties of the material. The high magnetic susceptibilities of SPIONs affects the spin-spin relaxation time (*T2* and *T2**) and cause a more efficient relaxation in the transverse plane, resulting in a dark contrast in a *T2w* image. [98-100] SPIONs have paved the way for magnetic nanoparticles into the clinic (Lumirem/Gastromark®)[101] and are generally considered safe. [102, 103] However, the biocompatibility is a topic of debate, [18] and commercially available SPIONs have recently been retracted due to reports on toxicity.[104] Additionally, the hypointense signal from SPIONs can be confused with *e.g* magnetic susceptibilities, bleeding or calcification which can lead to inaccurate diagnosis.[78, 104, 105] However, recent reports on ultra-small iron oxide nanoparticles also demonstrates that they can be used as *T1* CAs, which produce a hyperintense signal mostly associated with paramagnetic materials. [106, 107]

The MR contrast imparted by NPs can be combined with other functionalities, for instance as either passive or active drug delivery vehicles. MRI CAs have also been shown to respond to several biomarkers (see Hingorani[108] and references therein). Some applications of multifunctional MR active NPs are discussed in the next subsection.

### 3.3 Nanoparticles as multifunctional contrast agents

Magnetic nanoparticles of iron oxide are already multifunctional; they are CAs in MRI and they can produce heat when exposed to an alternating magnetic field. This induced heating is called *hyperthermia*. If iron oxide NPs can be directed to tumors, hyperthermia can be used to kill malignant tissues. [109, 110] Nanoparticles for hyperthermia can either be injected directly into the tumor, or can be surface functionalized with targeting moieties that guide the NPs to the tumor.

In contrast to gold nanoparticles that were synthesized and stabilized in water with proteins, both iron and manganese oxide nanoparticles were decomposed in an organic solvent, giving NPs with a hydrophobic surface. As such, the metallic nanoparticles are not soluble in aqueous buffers and must be surface functionalized before they can be used in biological applications. Surface functionalization or stabilization depends on the properties of the stabilizing ligand. For instance, in paper V, we functionalized MONPs with L-DOPA which acts both as a stabilizing ligand and as a drug.

A common molecule for surface functionalization is dopamine. To increase the stability and biocompatibility of the NPs, a second molecule is attached on the N-terminus of dopamine, and this is most commonly polyethylene glycol (PEG). Dopamine-PEG molecules are first synthesized with carbodiimide chemistry before they are attached to the NP. Carbodiimide chemistry is a general procedure for creating a peptide bond between a primary amine (dopamine) and a carboxylic acid (PEG) *via* several intermediates (not shown):

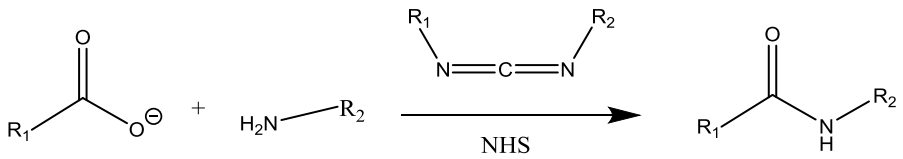


The negatively charged carboxylic group will undergo a nucleophilic attack to the partial positive carbodiimide ($R_1$-N=C=N-$R_2$). This in turn leads to a series of events finally resulting in peptide bond formation. *N*-hydroxysuccinimide (NHS) is added to stabilize one of the intermediates, and to increase the yield. [111, 112]

After synthesis of the dopamine-PEG molecules, the NPs are added to the reagent beaker, and the dopamine-PEG molecules attach to the NP. The hydroxyl groups of dopamine bridge with the surface oxide layer of the NP, while the second acid group of PEG will point towards the bulk and give steric and electrostatic stability to the suspension, as illustrated in Figure 3.4.[113, 114, 115] It is therefore ultimately the surface coverage of PEG-molecules that will decide the charge and hydrodynamic volume of the nanoparticle. Secondary moieties may be attached to the carboxylic group of PEG by performing a second round of carbodiimide chemistry. For an extensive review of surface functionalization of nanoparticles, see Sapsford *et al*. [97]

One of the main goals of nanomedicine is to deliver drugs to a specific site of action, for instance a malignant tumor. First and foremost, the biocompatibility of the NP system must be assessed as the NP can be toxic to the host. If an NP is being used for drug delivery purposes, one strategy is to deliver the drug intracellularly, which means that the nanoparticle must be able to traverse the cellular membrane. Therefore, interactions between cells and

nanoparticles are important to describe as they can give information on cellular uptake, clearance, and toxicity of nanoparticles. This is the topic of the next chapter.

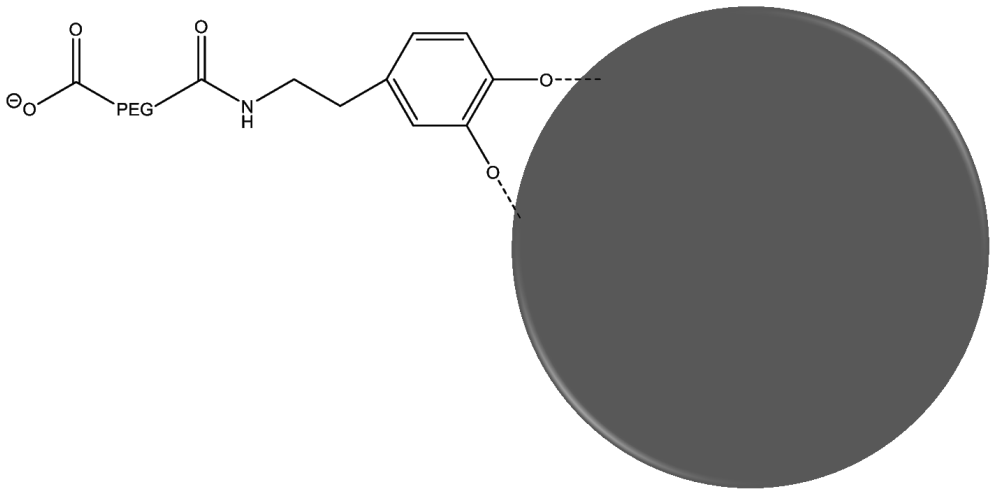


Figure 3.4: Surface functionalization of IONPs

# 4 Mechanisms of cellular uptake and cytotoxicity

Nanoparticles that are engineered to function in biological systems must be compatible with the microenvironment inside the host. The first step towards establishing the biocompatibility is to assess how cultured cells interact with nanoparticles. Are the nanoparticles taken up? Do they adhere to the cells or alter their viability in some way? Answers to these questions can be found with cellular viability assays.

In the context of this thesis, the biocompatibility of synthesized nanoparticles was tested against human and rodent cell lines with the aim of investigating their uptake and potential cytotoxicity. This chapter aims to give a general overview of the main entry routes to a mammalian cell, before the cellular effect on internalized NPs will be addressed.

## 4.1 Endocytosis

The first barrier between a nanoparticle and a cell is the extracellular matrix (ECM). This is a thick mesh of intertwined proteins and sugars that protrude from the cell. The cellular membrane is hidden below the ECM, and is a complex bilayer of phospholipids containing cholesterol and a plethora of proteins. The cellular membrane separates the extracellular fluid from the inner cytosolic environment. A vital osmotic pressure is obtained by permitting water molecules to move through aquaporins, [116] while salts like potassium and sodium are exchanged through ion channels. Molecules that do not have a specific channel or transporter over the cell membrane may be taken up through endocytosis. Generally, endocytosis occurs with a physical change in the cell membrane, resulting in entrapment of an extracellular molecule/component in an intracellular vesicle. Endocytosis is a highly dynamic process which involves the cytoskeleton and many intracellular proteins, some of which are believed yet to be discovered. A full description of the biochemistry of endocytosis is beyond the scope of this text, and the reader is referred to Doherty *et al* for an extensive review on the topic. [117] This subsection aims at describing the general concepts of endocytosis and point to characteristics of a nanoparticle that seem to be important for cellular entry. As nanoparticles have sizes comparable to biological molecules they can in principle traverse biological membranes through several of the routes described below. [118]

Endocytosis is a general term for cellular uptake and is further divided into *Phagocytosis, Pinocytosis,* and *Receptor-mediated endocytosis* (Figure 4.1). Phagocytosis, or cell eating, is the uptake of bacteria or protozoal pathogens and only occurs in a few specialized cells. Pinocytosis, or cell drinking, is the uptake of extracellular fluid, further divided into micro, -and macropinocytosis. The latter is recognized by filopodia that fold back onto and fuse with the membrane which result in large intracellular vacuoles containing extracellular fluid. Macropinocytosis is non-specific and receptor-independent, and is used to take up larger extracellular components, up to 5μm. [119] Micropinocytosis is uptake of smaller aliquots and is a general term for a range of internalization events. [120] Both phagocytosis and macropinocytosis involves the actin cytoskeleton.

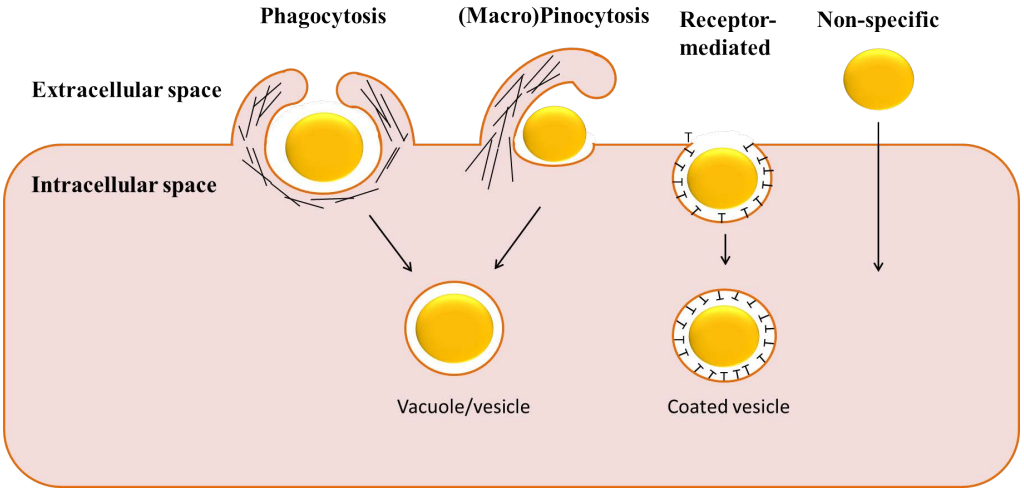


Figure 4.1: Major routes of endocytosis. The black lines in phagocytosis and pinocytosis represents actin filaments. [119] The orange line surrounding the cell represents the extracellular membrane.

Receptor-mediated endocytosis (RME) involves receptors situated on the extracellular membrane, [121] and is either caveolin- or clathrin-mediated, depending on the mechanism and vesicle size. Smaller species, as for instance viruses, are taken up *via* clathrin-mediated endocytosis, in which a small vesicle (100-120 nm) is formed and pinched off from the membrane with the aid of the protein clathrin. For even smaller species, caveolin-dependent endocytosis involves formation of a caveolae[XI] that is in the size range 60-80 nm. [119] Recently, a new class of cytoplasmic proteins are being recognized for their role in caveolin-mediated endocytosis, and these are the cavins. [122]

Assuming that an NP adheres to the cellular membrane, the second event that must take place is formation of a vesicle by wrapping of the membrane. Wrapping is a deformation of the local membrane structure that is restricted by the elastic properties of the membrane, the contact area between the NP and the concentration of receptors on the surface. For instance, if several large NPs adhere to the membrane, wrapping affects the global elasticity of the membrane, which may cause cellular rupture. Also, the time it takes for an NP to be endocytosed is related to its size; it takes longer time to wrap a large NP than a small. [123,124] In the scenario of receptor-mediated endocytosis, mobile surface receptors must move towards the adhered NP, lower the free energy of interaction and induce a wrapping event. [125, 126] It has been argued that the optimal size of NPs for uptake through receptor-mediated endocytosis is 25-30 nm. [127] Mu *et al* argues that when NPs are smaller than 20 nm, the adhesion energy to the membrane is too small to induce membrane wrapping. If receptor-mediated endocytosis is the route of entry, a large NP (<60 nm) would need a higher amount of available receptors than a small NP, and will thus deplete the membrane of receptors. In comparison, smaller NPs may not be able to recruit enough receptors, and may as such not be endocytosed. [128] However, if several small NPs adhere in clusters, the contact area may be large enough to induce receptor-mediated endocytosis. This may be one explanation for the fact that multiple NPs are imaged in a single vesicle[129], which we also observed in paper III (Figure 6.6h). With increased size, the time it takes to recruit receptors increases. As smaller

[XI] *Caveola* means "little cave" in latin

NPs do not need to recruit as many surface receptors as larger NPs, a more rapid uptake of smaller NPs may depend on the recruitment time of membrane receptors. With this in mind, it might seem apparent that small NPs (<10 nm) may be the optimal size. However, a literature review by Beddoes *et al* states that although smaller NPs appear to be more rapidly taken up by cells, they also appear to have higher cytotoxicity. [121]

Studies have shown that nanoparticles in the size range 20-50 nm have a good uptake in cells. [130, 131] This might correlate with the size-range of viruses (20-100 nm) that have evolved as to rapidly being taken up by cells. [132] A study by Roiter *et al* on adsorption of silica NPs on lipid bilayers showed that NPs larger than 22 nm reached full surface coverage of the lipid, while smaller NPs (1.2 -22 nm) created pores in the membrane. [133] Size does not only appear to govern the endocytosis of nanoparticles, but it seems as though exocytosis is size-dependent as well. For instance, the removal half-life of 14 nm AuNPs was much faster than removal half-life of 74 nm AuNPs.[134]

The aspect ratio, or shape, of the NP may also govern the cellular uptake mechanism. For instance, rod-like NPs with high aspect ratio were shown to be taken up more rapidly than cylindrical NPs in HeLa cells. [135] However, compared to spherical AuNPs, rod-shaped AuNPs were demonstrated to have a lower uptake. [134] In light of the discussion above, this might be explained as a result of the aspect ratio of rods. If a rod adheres to the cellular membrane with its transverse plane (side), this would result in a long membrane wrapping time compared to if the nanoparticle adhered to the cell membrane with its longitudinal plane (head). If RME was involved, a less efficient uptake could be described as a function of receptor recruitment time.

Interestingly, the size of the NPs may also decide their surface properties. NPs smaller than 2 nm may actually be hydrophobic, which gives them dramatically different interactions with the cellular membrane. The hydrophobic nature of these ultra-small NPs was explained based on the different orientation of water molecules surrounding the NP. Molecular dynamic simulations showed that NPs smaller than 2 nm interrupted hydrogen bonding between water molecules. [136] This might be an explanation for why small NPs tend to aggregate. A cluster of NPs would have a larger radius than single NPs and thus be less able to disrupt hydrogen bonds, be more hydrophilic which would cause an entropic gain to the water molecules. [137]

The properties of the surface molecules are very important for the biological properties of the NP. For instance, the charge of the surface molecule will effectively become the charge of the NP which in turn could add several nanometers to the hydrodynamic volume of the NP (Figure 3.4). [138] Additionally, the surface properties of the nanoparticle will determine the outcome of the first encounter between a nanoparticle and a biological medium. For instance, if the NP is negatively charged, adsorption of proteins will be less than for a positively charged NP. The surface charge of the NP may determine the adsorption of biological molecules. Ensheathing of NPs in a biological media is believed to occur in two steps, giving rise to two different sheathes; an inner hard layer, and an outer soft layer. The inner hard layer is rapidly formed and is comprised of sugars and amino acids. A second soft layer of vicinal proteins is slowly formed on top of the inner layer, and is ultimately the contact point between the NP and the cell. [121] Therefore, the hydrodynamic volume of a positively charged NP in a biological medium may be very different from that of a negatively charged NP. Many nanoparticles are surface functionalized/stabilized, and choosing a surface molecule that has the desired chemical properties is the first step towards preparing biocompatible NPs. Generally, the surface charge should be neutral or negatively charged as to avoid protein adsorption, and the magnitude of the charge should be large enough to avoid precipitation. To complicate the picture, the curvature of the NP can also have an effect on the surface coverage

of stabilizing molecules, which may be different on sharp edges compared to other morphologies.

The composition of the surface coverage of NPs may also affect the stiffness of the NP, which is another factor determining interactions with cells. A review by Mu *et al* describes that the stiffness of the NP define the route of endocytosis; stiff NPs enter through clathrin-mediated endocytosis, soft NPs are taken up through macropinocytosis, while NPs of intermediate stiffness can enter through several routes. [128] A review by Zhang *et al* points to several studies showing that the membrane wrapping time and endocytosis may be related to the stiffness of the NP relative to the stiffness of the cell membrane. NPs stiffer than the cellular membrane were endocytosed faster than softer NPs, because soft NPs tend to spread onto the membrane rather than being engulfed. [119]

All aspects of the nanoparticles appear to be important for their biological behavior: size, shape, surface charge, and softness of the nanoparticle are all factors that govern cellular uptake. Furthermore, NPs may have completely different affinities towards different cell types, which further complicate their biological characterization. Cells from different tissues may vary greatly in size, morphology, lipid membrane composition, membrane elasticity, concentration and presence of surface receptors, meaning that NP interactions most likely are tissue specific. Additionally, gravitational forces also play a role in *in vitro* studies as NPs may sediment onto the cells. This increases the likelihood of NP uptake and is an effect that is not translational to *in vivo* experiments. This is important to keep in mind when discussing *in vitro* results and before extrapolating ones conclusions to *in vivo* models.

However, if a nanoparticle is successfully taken up by a cell, the second challenge lies in inducing a desirable cellular response. If the aim is to induce cell death, then the nanoparticle must activate stress responses that push the cell into a spiral leading to apoptosis.

### 4.2 Apoptosis: Programmed cell death

A cell can die in two ways; either through *necrosis* or *apoptosis*. In necrosis, the cell bursts and spills all of its inner components to the surrounding environment. This can create an inflammatory response and tissue damage. However, controlled cell death, or apoptosis, is governed by intracellular caspaces that set off a cascade of other caspaces which destroy the intracellular compartments, before the cell shrinks and is engulfed by macrophages. In this way, the intracellular constituents of the cell are not spilled to surrounding tissue, but recycled.

Apoptosis is an all-or-nothing response, which means that once induced, it cannot be reversed. [139] Controlled cell death is a major part of sustaining a living organism, and cells with mutations leading to altered apoptosis are prone to develop cancer. [140]

Mitochondria play important roles in control of apoptosis. If the mitochondrial membrane is damaged by nanoparticles, this may induce apoptosis by release of proteins that activate the caspace cascade.[141,142] Oxidative phosphorylation is performed in the mitochondrial membrane, and involves formation of an oxygen radical, $\dot{O}^-$, which is highly reactive and potentially very harmful if it escapes the mitochondria. This reactive oxygen creates several other reactive oxygen species (ROS). However, the oxygen radical is rapidly reduced by the enzyme *superoxide dismutase* to hydrogen peroxide, which is further reduced to water by the enzyme *glutathione peroxidase*. [17]

A major concern regarding intracellular NPs is the generation of ROS and negative interactions with the cytoskeleton. [143, 144] SPIONs have been shown to induce oxidative stress

by generating reactive oxygen and nitrogen species. [103] Reduction of molecular oxygen inside the cell may occur due to reactions at the nanoparticle surface. [141] This means that nanoparticles can induce oxidative stress in the cell by increasing the concentration of ROS to levels higher than the turnover rate of superoxide dismutase and glutathione peroxidase, leading to increased cell death. [131]

It was mentioned in the subsection above that the surface charge of the NPs should be either neutral or negatively charged. One reason that positively charged NPs are considered toxic is that they have high electrostatic attraction to the negatively charged cellular surface. As such, positively charged NPs will adhere faster to the membrane and increase the possibility to severely damage the membrane. However, a study performed by Arvizo *et al* on AuNPs with different surface charges suggested that positively charged AuNPs perturbed the membrane potential of cells to a larger extent than neutral or negatively charged AuNPs. They specifically found that positively charged AuNPs caused a depolarization of the membrane potential which caused an increased influx of $Ca^{2+}$ ions. These ions are important regulators of cell growth, and may in the long term affect the viability of the cells. [145] Another effect ascribed to positively charged NPs was production of ROS. These NPs accumulated inside lysosomes, and from here induced production of ROS. However, the toxic effect was believed to be caused by release of lysosomal content rather than ROS production at the NP surface. In the same study, loss of membrane integrity and mitochondrial membrane potential was altered. Damage to the mitochondrial membrane and spilling of mitochondrial proteins can induce activation of apoptosis via activation of the proteins caspaces 3 and 9. [146]

This chapter has highlighted that it is not only the elemental components of the nanomaterial that is important for its biocompatibility, but secondary effects caused by the surface chemistry and morphology. Therefore, in designing bioimaging probes, the researcher must keep in mind how the different characteristics can impact the final biological response. It also becomes especially important to describe the physical and chemical properties of the nanomaterials *via* several experimental methods.

# 5 Experimental Techniques

This chapter gives a brief overview and description of the main experimental techniques used in this thesis. The focus will be direct applications for the work described herein rather than a general description. [XII]

## 5.1 UV-Visible spectroscopy

A colloidal suspension of 20-30 nm AuNPs is red because AuNPs absorb light in the red region of the electromagnetic spectrum. With a higher concentration of AuNPs the solution becomes darker, *i.e.* the absorbance increases, as less light is transmitted through the suspension. The absorbance, $A$, is defined as the logarithm of the incident beam, $P_0$, minus the logarithm of the transmitted beam, $P$:

$$A = log \frac{P_0}{P}$$

A molecule absorbs energy corresponding to its own characteristic frequency, and the emitted beam is attenuated based on concentration of molecules and the path length of which absorption occurs. [XIII] This relationship is called *Beers law* and describes that the absorbance is directly proportional to the concentration of species, $c$, and the path length, $b$:

$$A \propto cb$$
$$A = \varepsilon cb$$

With the proportionality constant, $\varepsilon$, being the molar absorptivity. [147]

The wavelength and intensity of AuNPs strongly depend on their physical size and shape, and a shift in the extinction band indicates a change in either of these properties. [33] An effect of the local refractive index can also be observed, for instance with absorption of proteins on the surface. [148, 149] UV-visible spectroscopy was used to describe the growth of Tf/BSA-stabilized AuNPs. In the case of BSA-stabilized AuNPs, the growth was monitored over time, by measuring the intensity in the LSPR extinction band at ~530 nm.

Proteins that contain the aromatic amino acids, phenylalanine, tyrosine and tryptophan, absorb light in the visible region, more specifically from 240-300 nm. [150] Thus, conformational changes in BSA and Tf upon growth of AuNCs and AuNPs can be monitored with UV-vis. However, a more accurate description of protein unfolding can be accomplished using fluorescence spectroscopy, as described in the following subsection.

[XII] AFM, (S)TEM, HRTEM and XRD was performed by Dr. Gurvinder Singh. XPS was performed by Sulalit Bandyophadyay. MR imaging and set-up was performed by Dr. Sjoerd Hak. Langmuir-trough studies were performed by Dr. Wilhelm Glomm and Dr. Sina M. Lystvet.

[XIII] The refractive index of the solvent and the material of the cuvette also affect absorption. However, as the same type of cuvettes and aqueous buffers were consistently used, no effect on the LSPR intensity or wavelength maxima was detected and is therefore not discussed.

## 5.2 Steady-state Fluorescence Spectroscopy

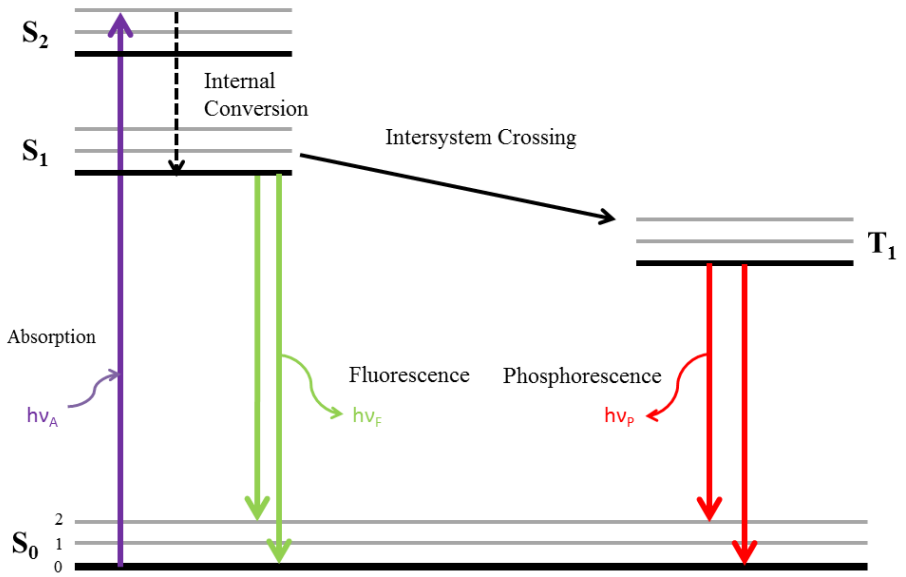


Figure 5.1: Jablonski diagram. Adapted from Lakowicz. [25]

When an incident photon matches the frequency of an electron in a molecule, atom, or nanostructure, the electron is excited from its ground state to a higher vibrational energy level. Relaxation of the excited electron causes energy dissipation in the form of heat and release of a photon. The emitted photon will always emit at longer wavelengths than the excitation photon, and this reduction in energy is called a *Stoke's shift*. The energy released as a photon is the luminescence, which is further subdivided into phosphorescence or fluorescence, depending on the processes in the excited state.

*Jablonski diagrams* are descriptions of the molecular processes that can occur in an excited state, and an example of such a diagram is shown in Figure 5.1. Transitions between states are always depicted as vertical lines, following the *Franck-Condon principle* of instantaneous absorption. The singlet ground electronic state, $S_0$, has several vibrational energy levels (0, 1, 2...), but is substantially lower in energy compared to the first ($S_1$) and second ($S_2$) electronic states. To reach an excited state, light with photon energy $hv$ is absorbed, where $v$ is the energy frequency and $h$ is Planck's constant[XIV]. Upon relaxation, molecules typically relax back to the $S_1$ state, through internal energy conversion, but without release of a photon. Internal conversion happens within $10^{-12}$ seconds or less, and is much faster than the time it takes for emission of fluorescence ($10^{-8}$ seconds). Excited electrons that have forbidden transitions back to the ground state can cross into a triplet state ($T1$), causing a

[XIV] $h = 6.62607004 \times 10^{-34}$ m$^2$ kg s$^{-1}$

further Stoke's shift, and giving rise to slowly emitting phosphorescence ($10^{-3}$ to $10^{0}$ seconds).

In the work described in this thesis, steady-state fluorescence spectroscopy was used to describe changes in protein conformation of BSA and Tf upon growth of AuNCs and AuNPs, as well as determining the size and growth of AuNCs situated on the protein backbone.

AuNCs are excited at 370 nm ($\lambda_{ex}$*=370nm)*, and depending on their size, emit at 450 nm and 650 nm. Smaller AuNCs ($Au_8$, $Au_{10}$,…) typically have an emission maxima at 450 nm, while it is 650nm for larger AuNCs ($Au_{25+}$). The intensity of each peak is related to the concentration of each specie, meaning that the population ratio of either large or small AuNCs can be determined with steady-state fluorescence spectroscopy.[23, 47] As was briefly mentioned in subsection 2.1, the aromatic amino acids are fluorophores in proteins and any changes in the emission profile can be explained due to changes in the microenvironment of the fluorophore. These are: changes in viscosity, exposure to solvent and/or rotational correlation time. Tryptophan is the dominating fluorophore in proteins and is selectively excited at 295 nm and emit near 340 nm.[151-153] Trp emission is a well-documented spectroscopic method for studying conformational changes such as partial unfolding in proteins.[25] Unfolding changes the local environment of Trp residues, and depending on the number and location of Trp, this might lead to changes in fluorescence line shape, with respect to both emission maximum and intensity. While changes in the fluorescence intensity alone can be difficult to interpret, shifts in the emission maximum towards longer wavelengths are generally linked to protein unfolding[24, 25, 60, 61, 63, 154] or exposure to an aqueous environment. [9, 25, 152]

When only AuNCs are present in the protein backbone, quenching of Trp might be caused by emission/excitation overlap between AuNCs and Trp in addition to increased exposure to water. [154] When AuNPs are present in concert with AuNCs, interpretation becomes even more complex, as additional interactions between colloids and fluorophores can involve resonance energy transfer (RET) and further quenching.[25]

With the multiple quenching events that take place in a BSA/Tf-AuNC-AuNP system, it is useful to apply an additional spectroscopic method to determine how the average lifetime of the fluorophore changes upon growth of gold nano species. One of these methods is *Time-correlated Single-Photon Counting.*

### 5.3 Time-correlated Single-Photon Counting

In steady-state fluorescence spectroscopy, the total amount of emitted photons is measured, which is useful for describing quenching and to characterize different populations of fluorophores. However, in a system involving several distinct fluorophores with overlapping emission spectra, it is not possible to distinguish the contribution of each fluorophore without time-correlated spectroscopy. For instance, BSA has two tryptophan residues, one situated in a hydrophobic pocket (Trp213) while the other is situated on the surface (Trp134).[18] The two Trp residues are excited with the same wavelength ($\lambda_{ex}$*=295 nm*) but the emission is dominated by Trp134. Thus, detecting the contribution form the buried Trp residue is difficult because it falls under the same emission spectra as the exposed Trp. Tf also has several Trp residues in its backbone, all of which contribute to the total emission spectra, but with different intensities. [155] However, with Time-correlated Single-photon counting (TCSPC), the contribution of each fluorophore can be determined, and as with steady-state fluorescence spectroscopy, a change in the Trp lifetime can give valuable insight into protein unfolding and quenching.

In TCSPC, a short pulse of a single wavelength, corresponding to the *hv* of a specific fluorophore, is sent from a light emitting diode (LED) to the sample. Following the pulse, the intensity and time-dependent decay of the fluorescence is measured, the intensity being proportional to the number of excited molecules. The decay relaxation over time, *Y(t),* is described with the following formula:

$$Y(t) = \sum_{i=1}^{N} \alpha_i e^{-k_i \tau_i}$$

Where *N* is the total number of fluorescent molecules, α, is the relative fraction or amplitude of each component at $t=0$, $k_i$ is the rate constant of each component. $\tau_i$ is the lifetime of a fluorophore, which is the average time from an electron is excited until it returns to the ground state.[156]

Upon Trp excitation ($\lambda_{ex}=278\ nm$), the decay of Tf -and BSA stabilized AuNCs-AuNPs was fit with a biphasic decay, as fitting at higher orders includes larger contributions from noise. A biphasic decay fitting yields one short ($\tau_1$) and one long ($\tau_2$) lifetime with their relative populations $\alpha_1$ and $\alpha_2$.[25] In addition, the other aromatic amino acids will contribute to the emission when excited at $\lambda_{ex}=278nm$, but these are neglected as Trp is the dominating fluorophore. [25, 148]

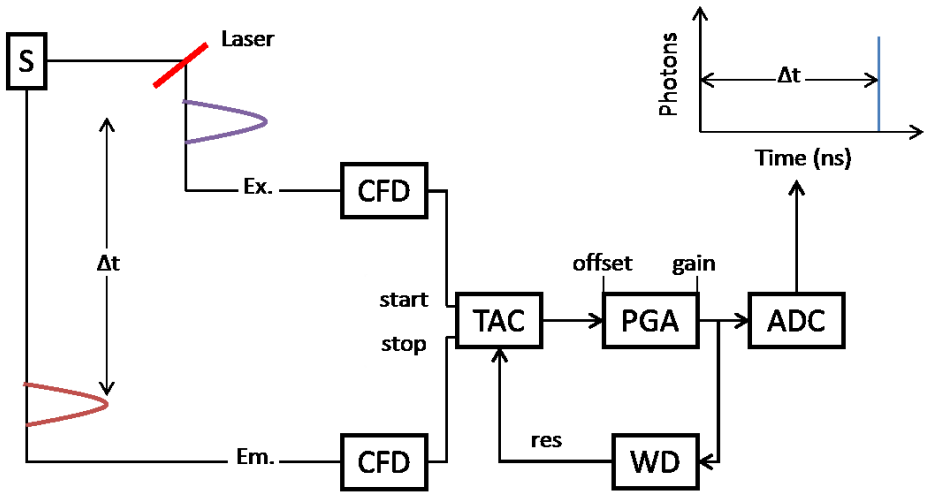


Figure 5.2: TCSPC. Adapted from Lakowicz.[25]

The electronic set-up of a typical TCSPC instrumentation is shown in
Figure 5.2. A sample is excited with a single pulse of light, and less than one photon is counted per laser pulse. The lifetime ($\Delta t=\tau$) between the excitation pulse and the observed photon is measured and stored. The signal, *S,* is passed through a *constant function discriminator (CFD)* that measures the arrival of the pulse. The signal is passed through a *time-to-amplitude converter (TAC),* where a voltage ramp is generated. The produced voltage is proportional to the length of the signal. A second CFD detects the emitted photon. [XV] The

[XV] In *reverse mode*, the signal from the emission is used to start the voltage ramp in the TAC, while the signal from the emitted photon is used to stop the voltage ramp

voltage produced in the TAC is amplified by a *programmable gain amplifier (PGA)* that converts the voltage to a numerical value via the *analog-to-digital converter (ADC)*. A *window discriminator (WD)* removes any signals that are not within a given range of voltages. From the WD, the voltage is recirculated back to the TAC, where it is stored as a single event.

## 5.4 Scanning transmission electron microscopy and High Resolution transmission electron microscopy

In addition to UV-visible spectroscopy and TCSPC, the size and presence of AuNPs in a sample can be confirmed with scanning transmission electron microscopy (STEM), and AuNCs can be imaged with even higher resolution TEM (HRTEM). As the metallic NPs have higher electron density than proteins, the protein will not be visible in a TEM image, and the morphology of the NPs can be determined. It is however worth to keep in mind that when using UV-vis spectroscopy the collective signals of all NPs is measured, while with TEM and HRTEM, only a small portion of the sample is imaged.

In STEM, an electron beam is emitted from an electron gun and focused through several optical configuration lenses before it reaches the sample. The final focusing lens is the objective lens which is responsible for the largest demagnification of the beam and is the most important lens for acquiring images. With the scan coils the probe is scanned over the sample which makes it possible to form a magnified image (Figure 5.3). [157]

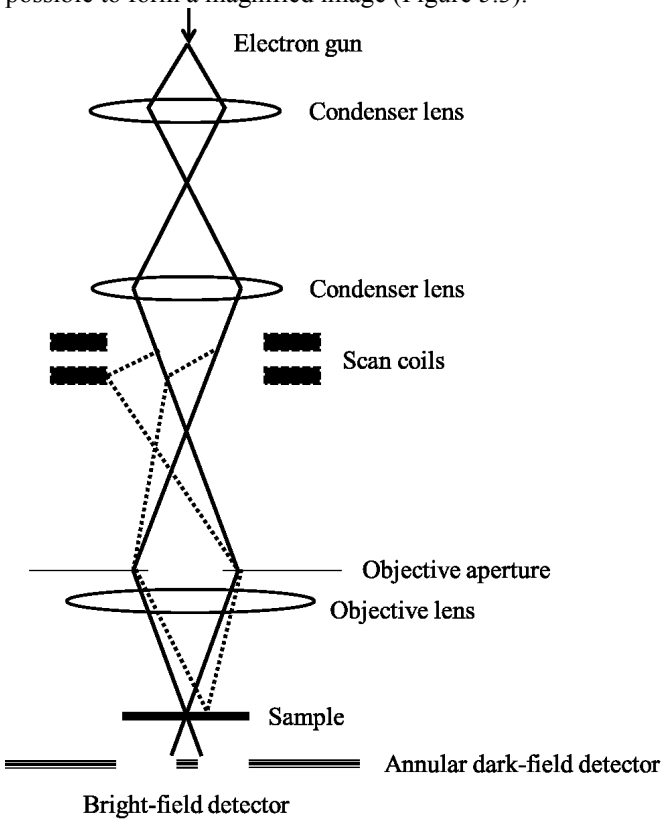


Figure 5.3: STEM aperture. Adapted from Pennycook. [157]

Even higher resolution of images can be acquired with HRTEM, as shown in Figure 5.4 a and b. The resolution of the STEM used here, is 0.4 nm, while the HRTEM had a resolution down to 0.1 nm. Several signals from a sample can be collected with STEM, but in the context of the papers described here, *bright field (BF)* and *annular dark field (ADF)* images were acquired. In a BF image, transmitted electrons that leave a sample at a relative low angle to the optic axis are detected, while in ADF, transmitted electrons that leave a sample at relatively high angles are detected (
Figure 5.4 c and d).

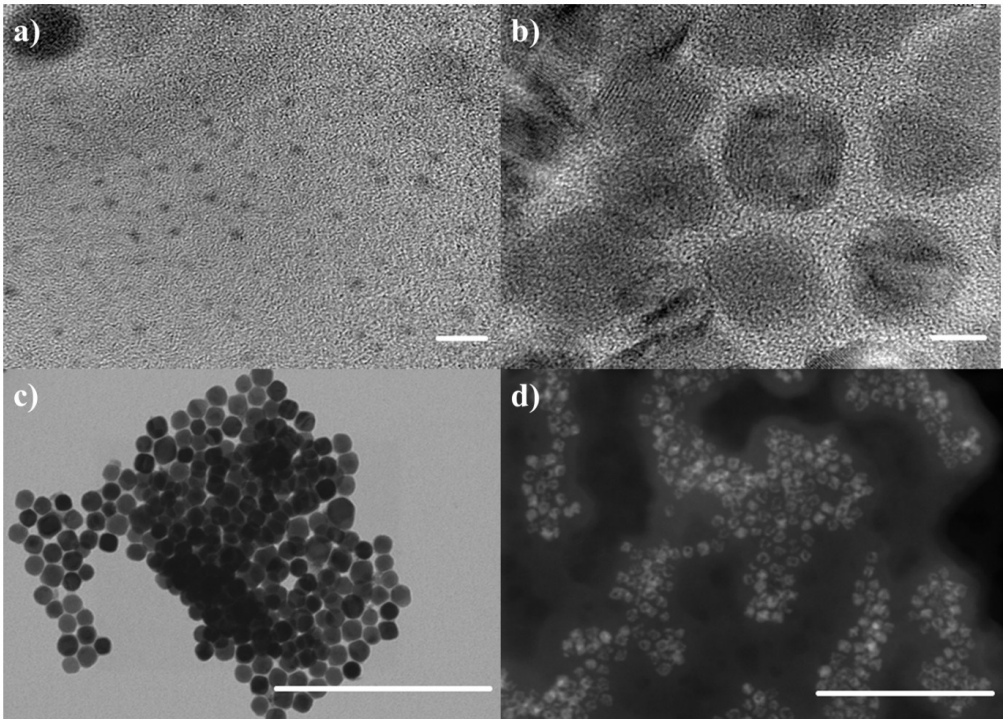


Figure 5.4: Example of a) HRTEM of AuNPs and AuNCs, scale bar = 5 nm, b) HRTEM of MONPs, scale bar = 5nm, c) STEM BF of FeO NPs, scale bar = 300 nm and d) STEM ADF of manganese oxide nanoparticles, scale bar = 200 nm.

## 5.5 Dynamic light scattering

While the dimensions and morphologies of NPs can be described with TEM, NPs in a solvent occupy volume larger than their diameter due to interactions with the solvent, or due to surface adsorbents such as proteins or other stabilizers. This volume is the *hydrodynamic volume* which can be measured using *dynamic light scattering (DLS)*. This parameter is important to determine, as the hydrodynamic volume of NPs can govern cellular uptake.

Generally, when an incident beam of light hits a suspension of NPs, the beam scatters in several directions. A detector measures the scattered light at a particular angle of

observation. The scattered light depends upon the molecular weight (size) of the sample, the angle of observation, and the concentration of the NPs. [158]

In the experiments described in this thesis, DLS was based on diffusion of NPs and by measuring the time-dependent intensities. NPs are not stationary in solution, but move in a random walk governed by Brownian motions. Therefore, the detected intensity of the scattered light will vary with the relative movement of the NPs. From these measurements, particularly small NPs that have a diameter much smaller than the wavelength of the incident beam can be detected ($d<<\lambda$). [159] The characteristic fluctuation times depend on the diffusion coefficient of the NPs, $D_0$, as described by the *Stoke's-Einstein* equation for spherical particles:[160]

$$D_0 = \frac{k_B T}{6\pi\eta R_H}$$

Where $k_B$ is Boltzmanns constant, $T$ is absolute temperature, $\eta$, is the viscosity of the solvent, and $R_H$ is the hydrodynamic radius of the sphere. Small NPs have a larger diffusion coefficient than bigger NPs, and will therefore have a more rapid fluctuating intensity.

The Stoke's-Einstein equation does not take into account interparticle interactions, that can lead to changes in diffusion. In systems of finite dilution, the measured diffusion coefficient is thus an apparent diffusion coefficient, $D_{app}$, which is related to the infinite dilution coefficient, $D_0$, by:

$$D_{app} = D_0[1 + k_D c]$$

Where $k_D$ is the DLS interaction parameter or the diffusion virial coefficient, and $c$ is the concentration of the NPs. By measuring the diffusion coefficients, the average size distribution of the NPs in a suspension is calculated.

## 5.6 Zeta potential

Nanoparticles are typically not stable in water by themselves, and are therefore surface functionalized for enhanced water stability. The molecules used for this purpose must be able to bind to the NP surface and have a hydrophilic moiety that causes the NP to be stable in water. The overall charge of the nanoparticle is determined by the charge of the stabilizing moiety, a value that can be determined with zeta potential measurements.

When a charged spherical nanoparticle is solubilized in an electrolyte solution, a cloud of coions and counterions immediately surrounds it. At the inner surface layer of the NP, the local concentration of counterions is significantly higher than the concentration of coions. The layer immediately surrounding the NP is called *the electrical double layer*. A charged NP in an electrolyte solution has an electrical potential that drops with the distance from its surface. The electrical potential $\psi(\mathbf{r})$ at a position **r** outside the particle is related to the charge density at the same point, $\rho_{el}(\mathbf{r})$, described by the *Poisson equation*:

$$\Delta\psi(r) = -\frac{\rho_{el}(r)}{\varepsilon_r \varepsilon_0}$$

Where $\Delta$ is the Laplacian, $\varepsilon_r$ is the relative permittivity of the electrolyte solution, and $\varepsilon_0$ is the permittivity of a vacuum. If the electrical potential is low:

$$\frac{ze\psi}{kT} << 1$$

The Poisson equation can be written as the *linearized Poisson-Boltzmann equation*, or the *Debye-Hückel equation*:

$$\Delta\psi = \kappa^2\psi$$

Where $\kappa$ is the *Debye-Hückel parameter* and the reciprocal is the *Debye length* which corresponds to the thickness of the electrical double layer, illustrated in Figure 5.5a. [161]

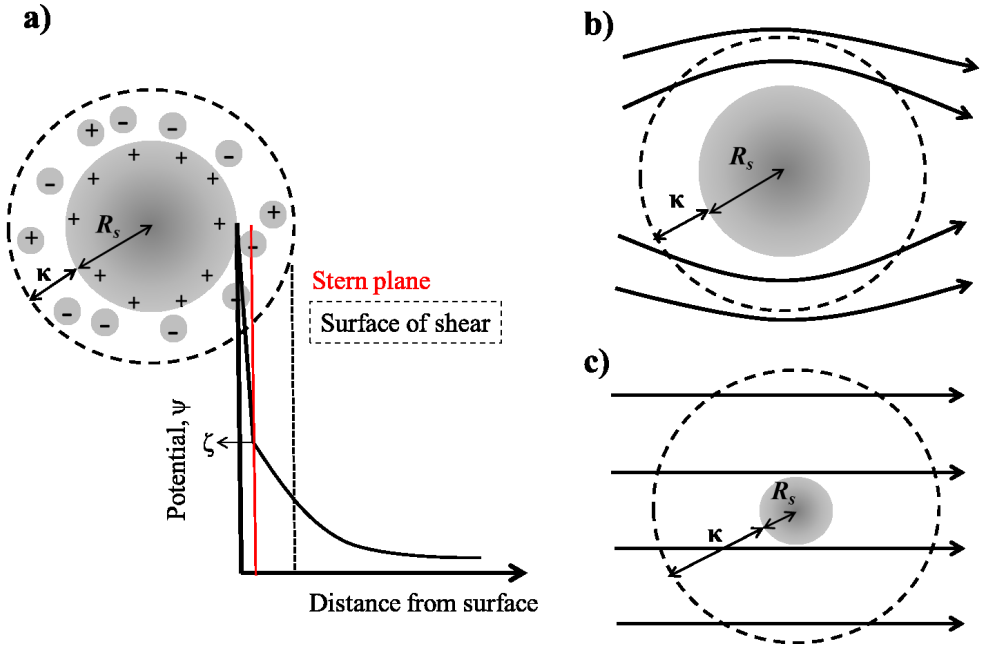


Figure 5.5: a) ζ-potential. A moving particle in a medium will affect the field lines depending on its particle radius, $R_s$. b) large particle will affect the field lines to a greater extent, compared to c) small. Adapted from Hiemenz.[160]

When an NP moves in a solution the layer of liquid immediately adjacent to the NP surface has the same velocity as the NP. The surface where there is relative motion between the NP and the liquid is called *the surface of shear*, and the electrical potential at the surface of shear is the *zeta potential*, illustrated in Figure 5.5. The numerical value and sign of the ζ-potential is used to describe colloidal stability, and values above |25| mV are considered sufficient for electrostatic repulsion between particles. [160] In the context of this thesis, ζ-potential measurements were used to evaluate the surface charge of iron and manganese oxide

nanoparticles after surface functionalization. The surface charge of an NP will dictate to which extent it interacts with a biological tissue. For instance, whether or not a nanoparticle is taken up by the cell or not, depends heavily on the surface charge of the particle. The extracellular matrix of human cells is negatively charged, and a positively charged NP may have unwanted electrostatic interactions with the membrane, [162, 163] hence a negatively or neutrally charged nanoparticle could be more favorable.

Depending on the ratio between $\kappa$ and the particle radius, $R_s$, different equations for the ζ-potential can be obtained. If $\kappa R_s > 100$, that is, when $\kappa$ is small compared to the particle radius, the *Helmholtz-Smoluchowski's equation* can be used to calculate the ζ-potential:

$$\zeta = \frac{\mu\eta}{\varepsilon_r \varepsilon_0}$$

The Helmholtz-Smoluchowski equation is used for large particles in polar media. In the other case, when $\kappa R_s < 0.1$, *Hückel's equation* is applied:

$$\zeta = \frac{3}{2}\frac{\mu\eta}{\varepsilon_r \varepsilon_0}$$

The Hückel equation describes small particles in non-aqueous media.
The Helmholtz-Smoluchowski and Hückel equations can be summarized to:

$$\zeta = C\frac{\mu\eta}{\varepsilon_r \varepsilon_0}$$

Where $C$ represents the two limiting cases of $\kappa R_s$:

1. Helmholtz-Smoluchowski: C = 1
2. Hückel: C = 3/2

The value of C shows the direct consequence of how the field lines surrounding a particle are affected by the particle radius (Figure 5.5 b and c). However, for all intermediate values of $\kappa R_s$, either the Helmholtz-Smoluchowski or Hückel equation describes the system adequately, or the more complicated *Henry's equation* must be used. However, in this thesis the Helmholtz-Smoluchowski equation was used. The argument being that using the same approximation consistently would render the data sets relatively comparable. [160]

## 5.7 X-ray Photoelectron Spectroscopy

It has already been established that the oscillation of valence/surface electrons in AUNPs cause LSPR that is detectable with UV-vis spectroscopy. Combined with TEM and HRTEM, the physical structure of a NP can be determined. However, the surface composition of the NP cannot be determined with microscopy; neither can UV-vis spectroscopy reveal any information about the inner electrons, *i.e* those situated closest to the atomic nucleus. Spectrometry must be employed to elucidate the surface properties of the NP, for instance to get information about the orientation of the stabilizer on the NP surface. The most common

technique for surface analysis is X-ray photoelectron spectroscopy (XPS) that provides information about the composition and chemical state 10 nm from the surface. [164] In the context here, XPS data provided information about molecules that were surface bound to a nanoparticle, such as L-DOPA bound to manganese oxide nanoparticles (MONPs), or AuNC surrounding AuNPs in a protein corona.

In XPS, the sample of interest is placed in a vacuum chamber where it is radiated with X-rays, UV light, or synchrotron radiation. Upon radiation, the emitted energy of the sample consists of three components. The first component is radiation with the same energy as the X-ray source (*hv*), and the second component is radiation which is characteristic to the material being studied (*hv'*). The third component consists of electrons and these photoelectrons are the basis for XPS. The photoelectrons are collected and focused by an electrostatic lens system and trafficked to an electron analyzer, and a spectrum is produced (Figure 5.6).

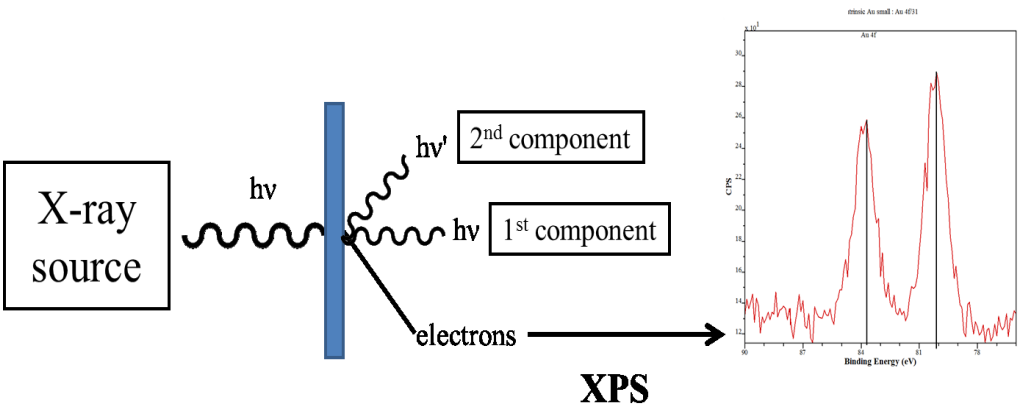


Figure 5.6: XPS. The intensity (related to the amount of excited electrons) is plotted as a function of the binding energy (electron volt). The spectra show the binding energy of gold atoms in a sample of BSA-stabilized AUNCs. [165]

Generally, a photoelectron is emitted by an incoming photon from the X-ray source. During the process of emission, the photon is annihilated and the energy is transferred to the electron. If the photon energy is sufficient, a photoelectron is emitted. The kinetic energy (KE) of the photon is the measured physical quantity that is related to the electron binding energy (EB) *via* the equation

$$KE = hv - BE - \varphi_{spec}$$

Where $\varphi_{spec}$ is the work function. Specifically, $\varphi_{spec}$ is the energy difference between the electrons bound to atoms/ions in the gas phase (vacuum level) and electrons bound to atoms/ions in the solid state (Fermi level). The work function represents the minimum required energy to remove an electron from a solid. Electrons that suffer from kinetic energy loss from traversing the sample are observed as background noise. [166, 167]

Valence electrons need less energy for excitation compared to core electrons. When an electron close to the core is emitted, it leaves a hole that is quickly filled by an outer-shell electron. The atom then ejects a second electron, named an *Auger electron*.

In order to get information on the surface characteristics of NPs, the spectra of an unmodified NP is compared to a NP with a surface molecule. For instance, an unmodified MONP is compared to a MONP with L-DOPA. If L-DOPA is chemically bonded to a manganese atom at the NP surface, the valence electrons need to redistribute to form the chemical bond. In turn, this affects the bond strength of the inner core electrons, with the effect of a chemical shift in the recorded spectrum. [165]

## 5.8 X-ray Powder Diffraction

As mentioned above, a sample that is excited with an X-ray source emit radiation and photoelectrons (Figure 5.6). The emitted photoelectrons are the basis for XPS, while the second component of the radiation, that is the specific material radiation, is the basis for X-ray diffraction (XRD).

In a typical XRD experiment, a sample is radiated with X-ray and the scattered radiation is collected through a moving detector. The different direction of the scattered radiation is directly related to the crystal structure of the material, and as such a material has its own characteristic XRD pattern. [168]

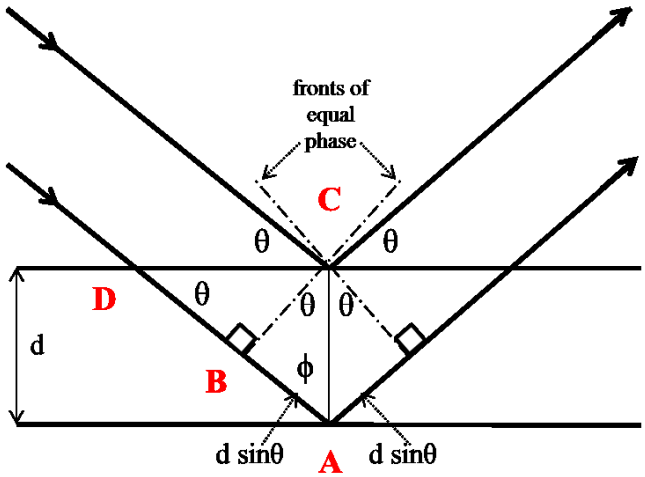


Figure 5.7: Interference geometry of a wave scattered from two planes, interspaced by d. [168]

The incident X-ray waves must have wavelengths comparable to the spacing between the atoms in the material. The interatomic spacing is called the *atomic periodicities*. Crystals that have isotropic atomic periodicities give sharp diffraction peaks, while crystals with impurities have less precise periodicities and show diffraction peaks that are broadened or distorted. In the work described here, XRD was used to confirm the presence of crystalline AuNPs synthesized by proteins, as well as describing the composition of different oxidation states of manganese in MONPs.

Figure 5.7 show the principles of XRD. An incident light with an angle θ hits the sample and the emitted radiation has a difference in path length corresponding to $2d\sin\theta$, where $d$ is the interplanar spacing When the path length difference from the top and bottom rays is equal to one wavelength, $\lambda$, constructive interference causes strong diffraction from the sample. This wavelength is defined with *Bragg's Law*:

$$\lambda = 2d\sin\theta$$

In an XRD spectrum, the Miller indices are used to specify from which planar spacing the diffraction is coming from. Each face of a crystal is presented in Miller indices *h, k,* and *l* which are defined as

$$h = \frac{a}{X},\ k = \frac{b}{Y},\ l = \frac{c}{Z}$$

Where *X, Y* and *Z* are coordinates in a three dimensional coordinate system (Figure 5.8). The notation for Miller lattices is that *(hkl)* represents a crystal face or lattice plane. [169]

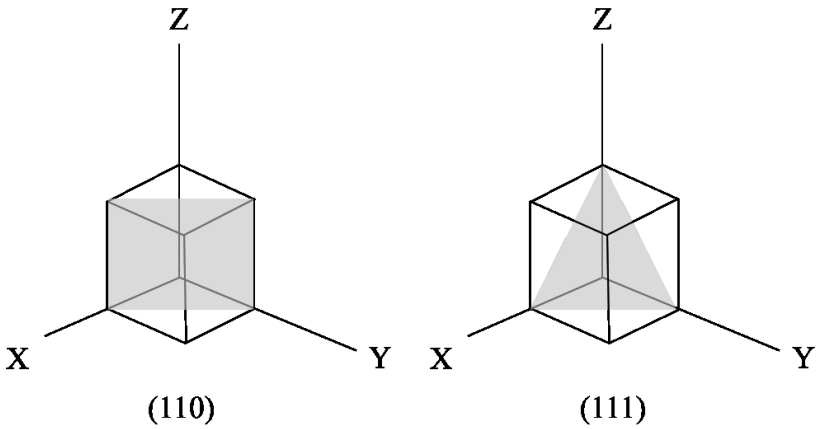


Figure 5.8: Miller indices. [169]

The specific peaks in an XRD pattern of a non-characterized sample are compared to standards to determine its crystallinity and any impurities.

## 5.9 Langmuir films and monolayer depositions

Upon determining the physical properties of the nanoparticles, the next step is to investigate how the nanoparticles behave in biological systems, particularly with model membranes. Membranes that mimic biological systems are simple models, but they allow repeated experimentations in controllable environments. [170] Equally important, they allow continuous monitoring of membrane alterations, which is not possible with a cell. [171]

Interactions between a monolayer and a surface active molecule can be performed with a Langmuir-Blodgett experiment, and the changes in the surface tension is continuously monitored and logged. There are several applications of the Langmuir-Blodgett technique, but the focus of this text will be on Langmuir film experiments and Langmuir-Schaefer depositions for microscopy.

In a typical experiment, water or an aqueous buffer is added in a through that has two compression barriers at the extreme edges. The barriers and the through are made of

hydrophobic materials (Teflon), which allow a water meniscus to form. The intrabarrier surface is separated from the extrabarrier space by a water meniscus. In the center of the through, a thin paper plate[XVI] is submerged into the liquid in such a way that a water meniscus forms midway on its sides. This paper plate reacts to changes in the surface pressure, and its movements at the surface is monitored by an electrobalance.

After adding the water/buffer to the through, the surface is rinsed for dust or foreign particles before the lipid is deposited on the surface. This causes some perturbations in the surface pressure, and the system is set to equilibrate and normalize before start. When depositing lipids or surface active agents (surfactants) on a water surface, the hydrophilic head group spontaneously orients towards the water, while the hydrophobic tails will point towards the air. The intrabarrier space determines the available surface area that the lipid molecules can spread onto, and therefore determine the density of lipids at the surface (area per molecule). When the surfactants completely fill the interface, they are said to produce a *monolayer*, or a *Langmuir monolayer*. [172]

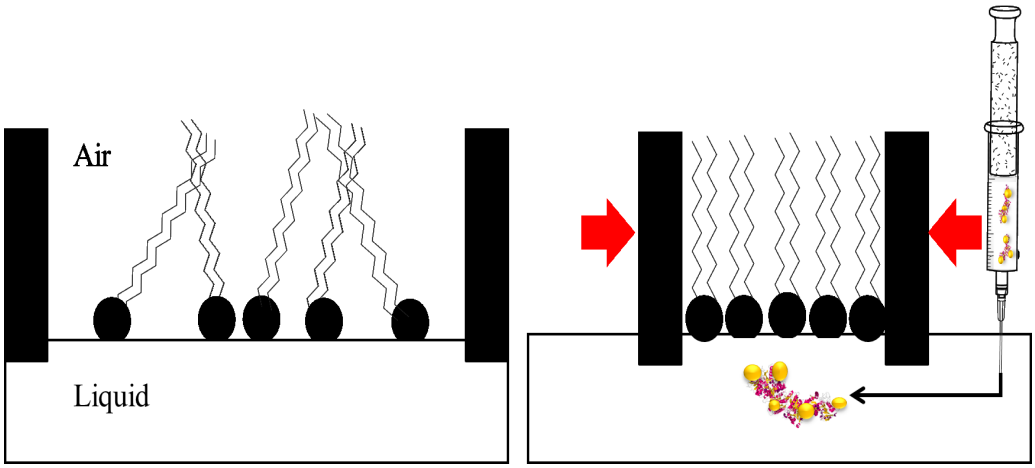


Figure 5.9: Langmuir monolayer. Compression of the film is done with barriers. After a monolayer is produced, a suspension of transferrin-stabilized gold nanoclusters is injected under the monolayer. [173]

From the aqueous side of the monolayer, the interface resembles that of a cellular membrane, and after forming the membrane the nanoparticles of interest are injected underneath the barriers in what is termed the *Injected method* (Figure 5.9). [170]

In paper I, Langmuir film interaction experiments were performed with a monolayer of phosphatidylserine (PBPS) and AuNCs stabilized with transferrin (Tf-AuINT). After forming a monolayer, the Tf-AuINT was injected under the barriers so as to not disturb the monolayer. With the paper plate, the change in the surface pressure was measured as a function of time, which revealed a remarkably high surface pressure compared to the lipid alone. This we interpreted as high interfacial interaction of the Tf-stabilized gold nanoconstruct that most likely penetrates the lipid film. To further investigate this, a part of the monolayer containing both Tf-AuINT and PBPS was deposited on a gold sputtered surface through a technique called *Langmuir-Schaefer deposition*, illustrated in Figure 5.10.

[XVI] A metallic *Wilhelmy plate* is also often used, but in paper I, a paper plate was used for all experiments.

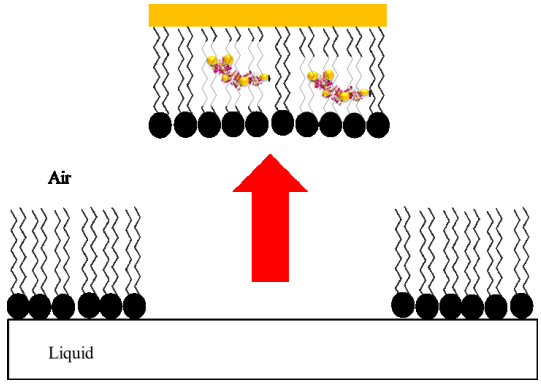


Figure 5.10: Langmuir-Schaefer depositions of lipid monolayers with transferrin-stabilized AuNCs

A gold sputtered plate was moved horizontally towards the surface, and kept there for 30 seconds with the aid of a vacuum pump. This allowed for the lipids and Tf-AuINT to adsorb to the plate. The adsorbed layer was then dried, and the surface was imaged with atomic force microscopy, as described in the next subsection.

## 5.10 Atomic Force Microscopy

With Atomic Force Microscopy (AFM) forces on the atomic scale can be detected and images of a surface can be acquired. The principle of AFM is based on movements of a flexible atomically sized tip which is moved over the sample surface with a piezoelectric scanner (Figure 5.11). This tip is fixed to a flexible spring that is called the cantilever. The tip is very sensitive, and is affected by force interactions with the surface to which the cantilever is deflected. A laser is directed to the tip of the cantilever, and photodiode detectors monitor the fluctuations of the tip by measuring the angle of the deflected beam. In AFM there are two modes of action, the *tapping mode* or the *contact mode*. In the tapping mode, the tip oscillates with a set frequency and is scanned over the surface. The electrostatic interactions between the surface and the tip will lead to alterations in the amplitude and frequency of the oscillations, which is related to the physical properties of the surface. The magnitude of the interactions are $10^{-11}$ to $10^{-6}$ N, and when the tip is held 10-100 nm from the surface, van der Waals and electrostatic forces can be sensed. In contact mode, the tip moves over the surface and the topography of the surface is described based on the deflections of the tip. [174-177]

One key advantage of AFM is that the images can be acquired in liquid, meaning that soft biological membranes can be imaged and characterized. Here, interactions between transferrin-stabilized AuNCs and a model biological membrane were investigated with AFM (paper I). A monolayer of lipids that had been exposed to Tf-AuNCs was deposited on a gold sputtered film with Langmuir deposition, as described in the previous subsection. Large perturbations to the lipid monolayer were observed in the sample where Tf-AuINT was present, which was not observable in the sample of pure lipid, and lipids that had interacted with the native protein. These changes were interpreted as incorporation of Tf-AuNCs into the lipid, which made it relevant to further describe these interactions with live cells.

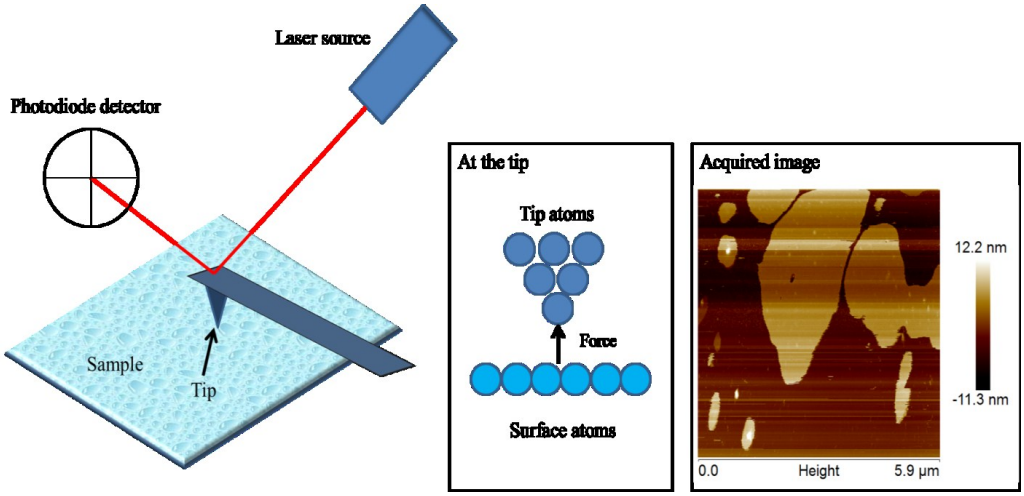

Figure 5.11: AFM principles. [175]

## 5.11 Cell cultures, labeling and viability assays

Although Langmuir and AFM are great methods for investigating interface interactions, they lack the complex membrane functions found in living cells. Also, any uptake of nanoparticles can be described by co-incubating a nanoparticle suspension with a particular cell culture, before ultramicrotome sectioning and TEM (See subsection 5.4).

The *in vitro* studies described in this thesis were mainly performed on human cancer cells and rodent olfactory ensheathing cells. The main work was performed with co-incubating nanoparticles with human glioblastoma-astrocytoma cell cultures and therefore the focus of this part will be on these cells.

Glioblastoma multiforme is the most common primary brain tumor in adults. [178, 179] It is highly aggressive [180] and exhibit low response to conventional chemotherapeutic drugs.[181] Cells acquired from a human donor show a more relevant biological response than commercially available cell lineages (*e.g* HeLa cells), that have been expanded for several generations. [182] Also, the rapid expansion and robustness of the glioblastoma-astrocytoma cell cultures makes them easy to work with.

Glioblastoma-astrocytoma cells (U-87 MG) were cultured in Eagle's Minimal Essential Medium (EMEM) with 1.25% gentamicin and 10% fetal bovine serum. The medium was supplemented with 2mM L-Glutamine, 1% non-essential amino acids (NEAA), and 1mM sodium pyruvate (NaP). After reaching a confluence of 60-70%, the cells were co-incubated with nanoparticles at different concentrations, and incubation times. In all cases, three parallels for each parameter were used, and unlabelled glioblastoma-astrocytoma cultures, at the same stage of confluence, were used as controls.

After labeling, a LIVE/DEAD® (Life Technologies) cell viability assay was performed. This method is a qualitative method, and the viability is assessed by comparing control cultures of cells. A LIVE/DEAD-cell viability assay evaluates the membrane integrity of cells, and consists of two different dyes: calcein AM (excitation/emission: 494/517nm) and ethidium homodimer-1 (excitation/emission: 517/617nm). In live cells, intracellular esterases react with calcein AM and yield a cytoplasmic green fluorescence. Ethidium homodimer-1

(EthD-1) diffuses through damaged cell membranes of dead cells, where it binds to nucleic acids and emits red fluorescence (Figure 5.12).

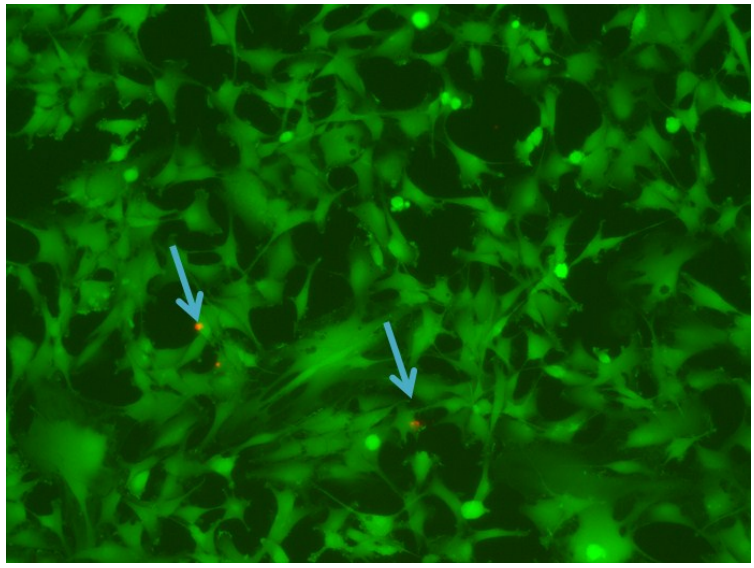

Figure 5.12: Glioblastoma-astrocytoma cells after LIVE/DEAD staining. Green cells are alive, while red cells are dead and indicated with arrows.

# 6 Results and Discussion

In this chapter, the main data and conclusions from papers I-V will be presented.

## 6.1 Paper I

**Self-assembly and characterization of transferrin-gold nanoconstructs and their interaction with bio-interfaces**

*Nanoscale,* **2015**, 3, (17) p. 8062-8070

The aim of Paper I was twofold. First we wanted to determine how adding a reducing agent affected the Tf structure and growth of gold nanoconstructs, and compare this to the intrinsic ability of Tf to reduce gold ions. [XVII] Previously, we have shown that a slight unfolding of the protein backbone have led to disruption of membranes, and the second aim was therefore to investigate if Tf-Au constructs had a higher membrane affinity compared to the native protein. [61, 63, 148]

Two synthesis methods were employed, named the *intrinsic* and *extrinsic*. With the intrinsic method, no external reducing agent was added, while in the extrinsic method, 200µL of $NaBH_4$ (1M) was added. Different concentrations of $Au^{3+}$ (in the form of tetrachloroauric acid, TCAA) were also used, with Tf as controls. An overview of the samples is given in table 6.1.

Table 6.1: Sample name and reagents

| Synthesis method | Sample name | 1M $NaBH_4$ (µL) | TCAA (mM) |
|---|---|---|---|
| Intrinsic | *Tf* | - | - |
| | *Tf-AuINT* | - | 5 |
| Extrinsic | *Tf-RED* | 200 | - |
| | *Tf-AuXL* | 200 | 1 |
| | *Tf-AuXH* | 200 | 5 |

An absorption band at 530 nm revealed that AuNPs were mainly synthesized when a high concentration of TCAA was used in combination with $NaBH_4$ (Tf-AuXH). However, broadened LSPR bands with lower intensities were also detected for Tf-AuINT and Tf-AuXL, indicating multimeric gold species. From these data, we concluded that $NaBH_4$ increases the population of AuNPs, and that the size/amount of AuNPs increases with the amount of TCAA added (Figure 6.1a).

AuNCs were detected with steady-state fluorescence spectroscopy ($\lambda_{ex}=370\ nm$) and the emission spectra showed an intense peak at 450 nm and 650 nm for Tf-AuINT. This indicates small ($Au_8$) and large ($Au_{25+}$) AuNCs, respectively (Figure 6.1b). An AuNP that is in close proximity to an AuNCs in the excited state has the capacity to scavenge emitted photons from the AuNC and quench the fluorescence. AuNPs were confirmed in Tf-AuXH, which caused a complete quenching of the fluorescence emission. However this was not the case for Tf-AuINT, which had a dominant Near- IR emission. Although smaller AuNPs were present in the intrinsic samples, it is ultimately the concentration of AuNPs that will determine the amount of AuNC quenching. This again points to the main difference in adding $NaBH_4$ or not; with a reducing agent, the concentration of AuNPs is higher, which increases the probability that an emitted photon from AuNC is quenched. Without a reducing agent, the synthesis was confined to produce mainly large AuNCs that were not quenched by AuNPs.

[XVII] Birgitte and Sondre are both first authors on this paper

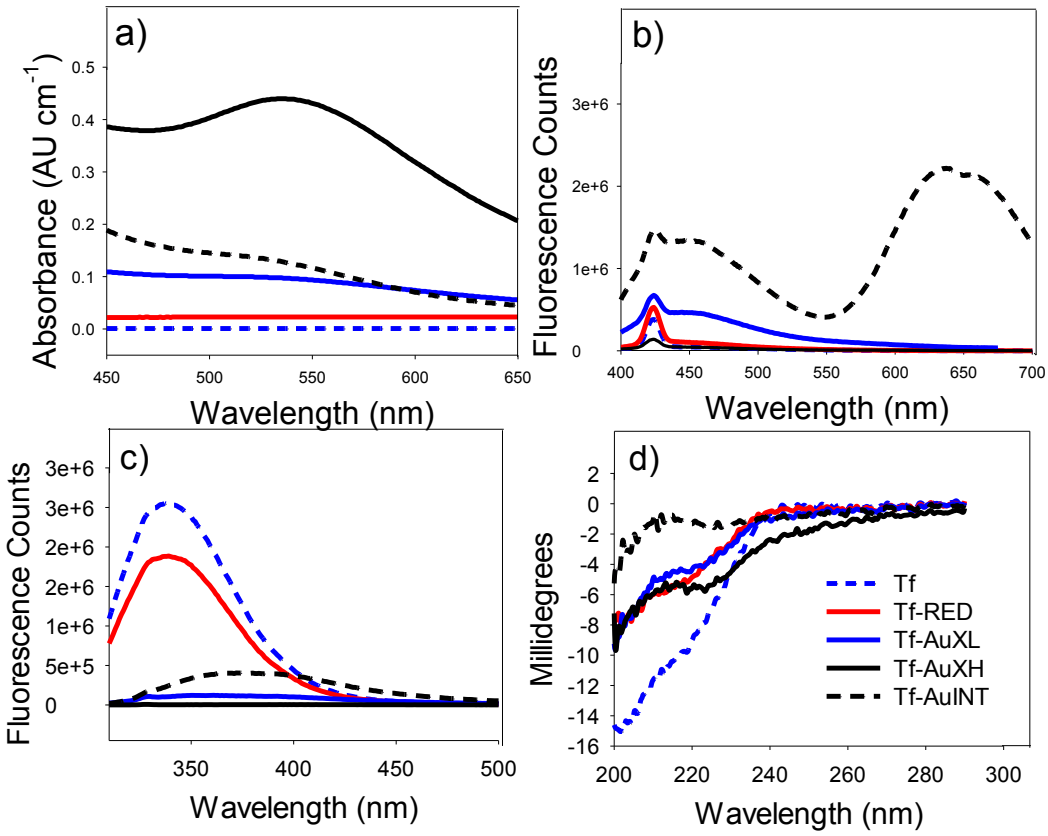


Figure 6.1: a) UV-Visble spectra showing LSPR for AuNPs synthesized with a high (Tf-AuXH) and low concentration of TCAA (Tf-AuXL) and AuNPs synthesized via the Intrinsic protocol (Tf-AuINT). All samples were compared to the pure protein (Tf) and Tf with added $NaBH_4$ (Tf-RED). b) Tf-AuNCs emission was measured with excitation $\lambda_{ex}$= 370nm. c) Trp emission of native Tf has the highest fluorescence intensity at 350nm when excited at $\lambda_{ex}$=295nm compared to Tf with $NaBH_4$ (Tf-RED), Tf-AuNCs prepared with no (Tf-AuINT), high (Tf-AuXH) and low (Tf-AuXL) concentration of TCAA. When a high concentration of TCAA is used, the Trp emission is almost completely quenched (Tf-AuXL). d) CD traces indicate structural changes in the protein backbone as the line shape changes when compared to the native protein (Tf), both with respect to $NaBH_4$ and TCAA.

HRTEM was used to complement the UV-visible and steady-state fluorescence spectroscopy measurements. AuNCs were observed in Tf-AuINT and Tf-AuXL samples, but not in Tf-AuXH, which was consistent with the steady-state data. AuNPs dominated the images of Tf-AuXH, which was expected due to the intensity of the LSPR band.

Changes in the protein structure upon AuNC and AuNP growth was assessed with steady-state fluorescence spectroscopy, circular dichroism (CD) and TCSPC. Based on the acquired data, the main conclusion is that the protein structure was affected by $NaBH_4$ and the amount of TCAA added. The combination of these two effects led to complete quenching of the Trp emission (Figure 6.1c, Tf-AuXH).

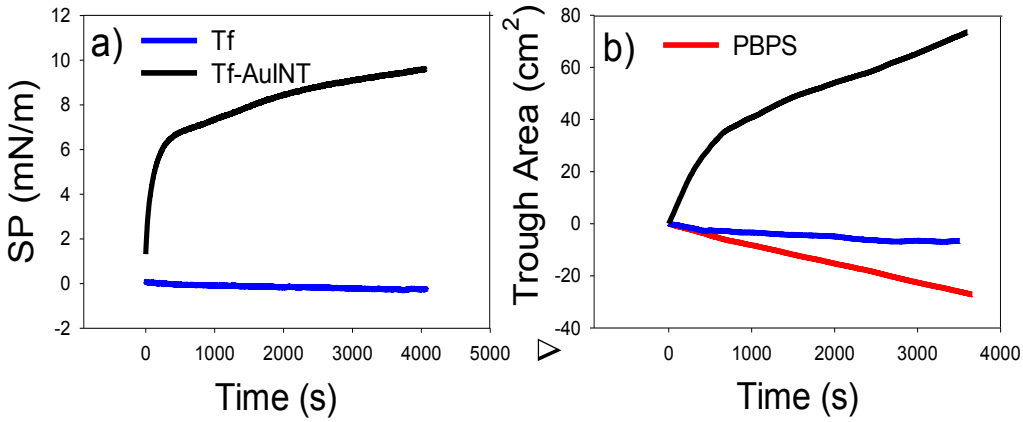


Figure 6.2: a) Surface pressure as a function of time show that compared to the native protein (Tf), the Tf-AuNCs prepared via the Intrinsic protocol (AuINT) is surface active. b) The delta surface area as a function of time indicates that Tf-AuINT has a higher surface activity compared to the pure lipid (PBPS) and the native protein (Tf).

The protein is the steric stabilizer of the system, and in particular when larger gold species are present (Tf-AuXH), the structural integrity of the protein is crucial to obtain a miscible suspension. The results from Trp lifetimes and emission indicated that the Tf structure was highly altered, which caused the extrinsic samples to crash out. Due to the instability of the suspension, these samples were not further studied with model membranes or biological membranes *in vitro* as these experiments involve buffered solutions which further increases the instability of NPs (due to reduction of the electrical double layer). However, the Tf-AuINT sample demonstrated sufficient solution stability and its interactions with a model biological membrane was investigated with Langmuir deposition and Atomic force microscopy (AFM).

The results show that Tf-AuINT had a large surface affinity compared to the native protein, which was explained as a direct result of protein unfolding (Figure 6.2). The perturbation of lipid monolayers were visualized with AFM by depositing a monolayer containing lipid and Tf-AuINT onto gold sputtered glass substrates (Langmuir-Schaefer method) and compared to lipid and Tf, and pure lipid. Compared to the other samples, Tf-AuINT disrupted the lipid membrane which was consistent with the acquired Langmuir data. The reason for the enhanced interfacial interactions of Tf-AuINT is most likely caused by increased exposure of hydrophobic residues in the protein following AuNCs formation, which is in agreement with fluorescence, CD, and earlier studies.[24, 60, 61, 63, 154]

The next step was to advance from a model membrane to living cellular membranes. We wanted to see if a difference in the membrane structure affected the affinity/interactions between Tf-AuINT, and for that reason we chose three different cell types; olfactory ensheathing cells (OECs), ovarian cancer cells (OCCs), and glioblastoma-astrocytoma cells (GA cells). The cytotoxicity was assessed with a LIVE/DEAD assay after co-incubating each cell type with three different concentrations of either Tf or Tf-AuINT for 4 hours. For all cell types, there were no increased cell death after incubation with Tf-AuINT or Tf, compared to the blank. Partial co-localization of the calcein – and EthD1-derived fluorescence was observed for the OECs, which suggests that Tf-AuINT is associated with the cell membrane,

either blocking the entry of the LIVE/DEAD dyes, or due to photophysical interactions between the Tf-AuINT and the dyes. If the latter were to be the case, similar observations should also have been made for the glioblastoma-astrocytoma as well as for the OCCs. However, this was not observed. The strong monolayer interactions observed for Tf-AuINT in Langmuir and AFM suggests that the co-localization was due to an enhanced Tf-AuINT affinity towards the OEC membrane that was not observed for the other cell types.

The main conclusion from this paper was that a strong reducing agent such as $NaBH_4$ can be used to grow AuNPs, but that $NaBH_4$ appear to cause a lot of damage to the Tf structure, which in turn leads to an unstable suspension. The most interesting constructs were synthesized with the intrinsic route. The capacity of Tf to intrinsically reduce TCAA resulted in AuNCs with high fluorescence intensity, and sufficient protein unfolding that gave radically different interfacial properties as compared to the native protein.

The reduction potential of $NaBH_4$ appeared to be too strong for the purpose of synthesizing AuNPs in a Tf scaffold. Perhaps a weaker reducing agent would impart less structural damage to the protein? Varying the concentration of added TCAA seemed promising for tuning growth of different populations of AuNCs and AuNPs, and insight to the growth mechanism could be gained by investigating the ratio of reactants. To answer these questions, we chose to use a flexible and robust protein, bovine serum albumin, a protein which has been widely reported for its ability to synthesize AuNCs and AuNPs.

## 6.2 Paper II

**Controlling the self-assembly and optical properties of gold nanoclusters and gold nanoparticles biomineralized with Bovine Serum Albumin**

*Manuscript under revision after peer-review in RSC Advances*

Synthesizing AuNCs and AuNPs seem to be dependent on the protein, reducing agent and amount of available gold precursor. [24, 47, 154] The incubation time for Tf-stabilized AuNPs/AuNCs were one week, and we have previously used the same incubation time for BSA- stabilized AuNPs/AuNCs. [154, 183] One week is a lot longer compared to the original synthesis of 12 hours[23], but have the benefit of producing larger species of gold. 12 hours incubation time is also reported by several others,[184-188] but overnight,[189] 15 hours,[136] 5 hours,[47, 187] and 2 hours[154] have also been used for BSA-AuNCs synthesis. The different incubation times yield different populations of AuNCs, revealing that the synthesis is highly time-dependent. With the range of different synthesis procedures reported, it is difficult to describe a growth mechanism without changing one synthesis parameter at a time.

The main aim of paper II was to evaluate which factors affect the growth of AuNCs and AuNPs and to describe the mechanism of growth in order to gain control over the synthesis and the optical properties of the system.

In the Tf-paper above, $NaBH_4$ appeared to alter the protein conformation to such an extent that the AuNP suspensions were destabilized. To avoid this, we chose to use ascorbic acid, which is a weaker reducing agent than $NaBH_4$ and compare the extrinsic synthesis with the intrinsic synthesis imparted solely by BSA. The intrinsic reduction potential of BSA had previously been shown to yield highly fluorescent AuNCs. [24] BSA may also give a better scaffold for AuNC and AuNP stabilization, as it can undergo major transitions without denaturation (see subsection 2.1). From the Tf-paper we had indications that reducing agents favored the growth of AuNPs, but that this process also depended on the concentration of TCAA. Therefore, in paper II, five different concentrations of TCAA were used and the growth of AuNCs and AuNPs *via* the intrinsic and extrinsic synthesis protocols was compared. The different samples are listed in table 6.2.

Table 6.2: Sample name and reagents

| BSA (mM) | TCAA (mM) | TCAA-Sample name | 2mM Ascorbic acid (µL) |
|---|---|---|---|
| 20 | 0<br>5<br>7.5<br>10<br>15<br>20 | Intrinsic | - |
| | | Extrinsic | 50 |

The results indicate that growth of AuNCs and AuNPs were affected by the amount of TCAA added, but that addition of ascorbic acid did not affect synthesis of AuNCs. However, synthesis of AuNPs seemed to be favored in the presence of ascorbic acid at high concentrations of TCAA. However, the standard deviation at 20 mM TCAA is very large compared to the other concentrations, which means lower reproducibility (Figure 6.3 a).

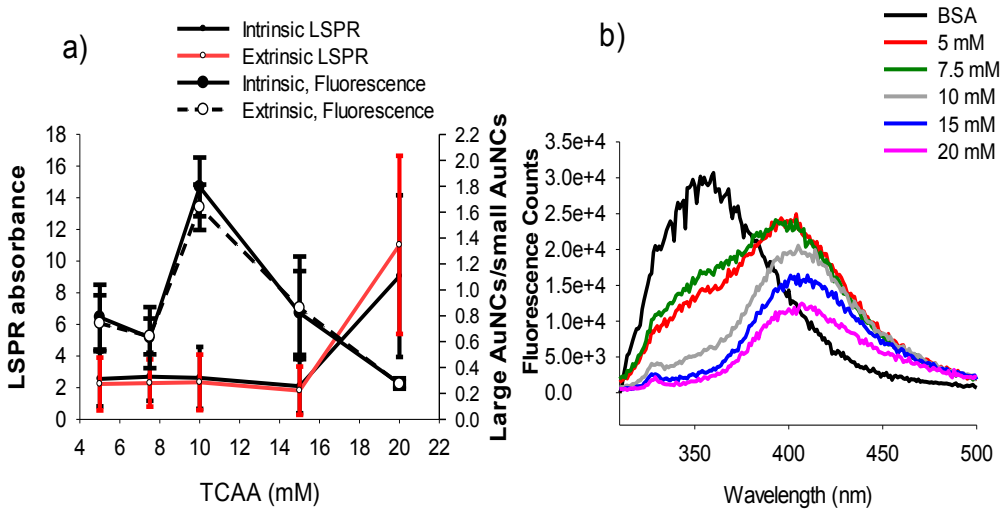


Figure 6.3: Integrals of a) LSPR absorption peak (500-600 nm) as a function of TCAA. Also shown is the integral of the emission peak of large AuNCs (560-730 nm) and small AuNCs (385-540 nm) were calculated and the population ratio was calculated by dividing the integral of the large with the integral of the small AuNCs. The ratio is shown as a function of TCAA. b) Changes in Trp emission spectra ($\lambda_{ex}$=*295 nm*) with incorporation of AuNCs and AuNPs.

Trp emission steadily decreased with increased population of AuNCs, and the lowest emission was detected in samples with AuNPs. This could mean that as the population of AuNPs or AuNCs increase, BSA responds by unfolding. Interestingly, the hidden Trp residues of BSA, Trp213, appear to be exposed with growth of AuNCs or AuNPs (Figure 6.3b). Even the large conformational changes of BSA did not compromise the solution stability of BSA-AuNPs. The BSA-AuNP and AuNC suspensions have a very long shelf life, and samples were stable for more than a year. Also, samples could be freeze-dried and suspended again without substantial loss in solution stability. This is an advancement compared to the solution stability of the Tf-stabilized AuNPs that quickly destabilized in buffered solutions.

The high NIR effect observed for AuNCs at 10mM TCAA might be a result of a metal-to-ligand/ ligand-to-metal charge-transfer (ML/LMCT) complex that is formed between the protein and the NIR AuNCs. This is believed to enhance the fluorescence intensities. However, in an ML/LMCT complex there is an exchange of electrons either from the metal to the protein or *vice versa*. If this was largely the case, either the protein or the AuNCs would be oxidized/reduced, which would destabilize the suspension with time. As the suspensions were very stable over long time periods (1 year), it is more likely that the high fluorescence intensity from NIR AuNCs is caused by capping of BSA. This would in turn cause shielding of the AuNC from water, which further would give a more intense fluorescence emission.

The main conclusion from the first part of the work was that no differences in size and population of AuNCs were found between the intrinsic and the extrinsic protocol. However, slightly larger AuNPs were observed when using the extrinsic protocol, which was also the case for the Tf-paper above. As with Tf, BSA appeared to be slightly affected by ascorbic acid, but not as drastically as that observed for Tf when using $NaBH_4$.

During the incubation time of one week, the BSA-stabilized gold nanoconstructs change colors depending on the protein:TCAA ratio and incubation time. Although we have previously hypothesized on the mechanism of AuNC growth,[24] we had never previously

measured the time-dependent changes to the protein and the time-dependent growth with spectroscopy. Due to the reproducibility of the data, we decided to follow the synthesis over one week. We chose the extrinsic synthesis method, as it had the tendency to produce larger AuNPs that would be easier to detect with UV-vis spectroscopy. The changes in Trp and AuNC emission were followed with steady-state fluorescence spectroscopy.

The results showed an increased LSPR intensity with time (Figure 6.4a), which means that growth of AuNP is a time-dependent process that depend upon the availability of gold ions. We interpreted the growth to be caused by shuffling and coalescence of AuNCs. Synthesis of AuNCs seems to be a very dynamic process that depend very much on the TCAA concentration and incubation time as well (Figure 6.4b and c). HRTEM images also revealed the coexistence of AuNCs and AuNPs, which we hypothesized from the time-resolved data (Figure 6.4d). The Trp emission is immediately affected by the onset of AuNC growth and the line spectra of the tryptophan emission remains the same during the whole week. But with time, the Trp emission appeared to increase, which could mean that BSA refolds to a more favorable position with less exposed hydrophobic parts. With time, there is an increase in the emission of AuNCs. Taking both these events into account, it seems likely that at thigh concentrations of TCAA, a reorganization of the protein backbone will bring AuNCs closer to each other, which would cause shuffling of AuNCs into AuNPs.

From these data, we were able to hypothesize on the following growth mechanism, illustrated in Figure 6.4e. When increasing the pH to above 10, BSA becomes **1)** negatively charged which induce electrostatic interactions with positively charged gold ions ($Au^{3+}$). Once in contact with amino acids (such as Tyr and His) $Au^{3+}$ is reduced to small AuNCs. **2)** Primary nucleation occurs when the local concentrations of gold ions are sufficiently high. Because reduction is performed by polar amino acids, it is likely that the primary nucleation occur at the protein surface, and not in the hydrophobic interior. The nucleation event causes an unfolding of the protein backbone. **3)** When increasing the TCAA concentrations, small AuNCs are shuffled into larger AuNCs due to conformational refolding of the protein. Growth of large AuNCs is also driven by an increased influx of $Au^{3+}$ from the bulk. **4)** The growth of AuNCs continue until they collide and self-assemble into a central AuNP that is surrounded by BSA-AuNCs.[24]

The protein-nanogold system offers an interesting and simple approach to synthesis of AuNCs and AuNPs, and the protein offer steric stabilization without the need for further surface stability. However, their applicability in bioimaging may be slightly impaired. When we performed *in vitro* assays with the Tf-AuNCs/AuNPs, we observed spectral interferences with the dyes. Additionally, we observed no cytotoxicity of glioblastoma-astrocytoma cells after incubation with BSA-AuNCs/AuNPs, which is an indication of biocompatibility. However, we wanted to synthesize NPs that could be taken up by cells, and from previous literature these were nanoparticles prepared with chemical synthesis. We chose to focus on nanoparticles prepared from gold, iron oxide, and manganese oxide nanoparticles as these have interesting optical and magnetic characteristics.

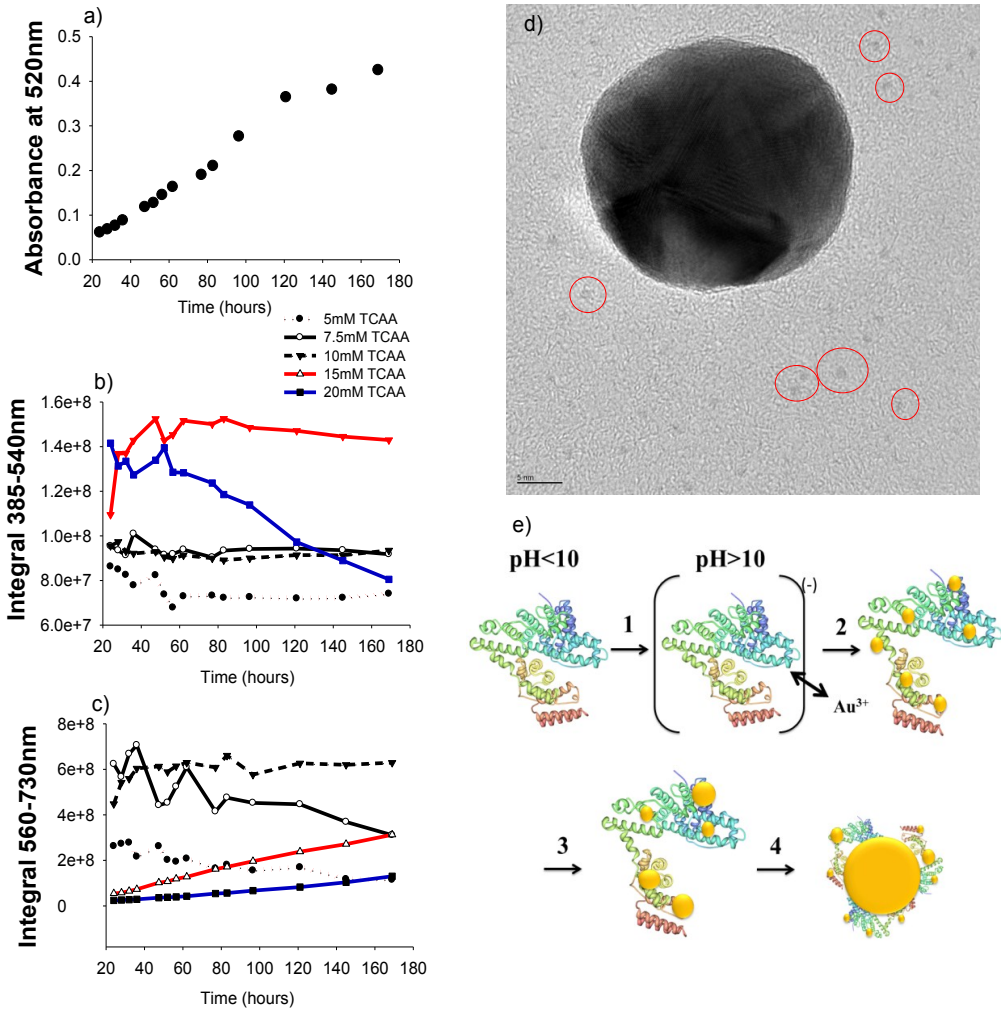


Figure 6.4: Graph a) shows the intensity at 520 nm (corresponding to the LSPR band of gold) as a function of time for the sample incubated with 20 mM TCAA. No LSPR-band was observed for any other samples. Graph b) shows the integral of the emission peak for the small AuNCs (385-540 nm) after subtracting the signal of native BSA. Graph c) show the integral of the emission peaks of large AuNCs (560-730 nm) after subtracting the signal of native BSA. Both graph b and c are shown as a function of time. d) HRTEM image of central AuNP surrounded by BSA-AuNCs. The AuNCs are encircles. Scale bar= 5 nm. e) Suggested mechanism for growth of AuNCs to AuNPs as a function of incubation time and concentration of TCAA.[16]

## 6.3 Paper III

**_Makura_-shaped gold nanostructures show high cytotoxicity in cancer cells**

*Manuscript in preparation*

The plasmon oscillations and subsequent absorption band of Au nanostructures (NS) is dependent on the size and aspect ratio of the NP, as well as the dielectric constant of the medium. Au NS that are non-spherical, can have plasmonic peaks longer than 700 nm, which is a significant bathochromic shift compared to the plasmonic peak of BSA-stabilized Au NPs at ~520 nm. In this region (near-IR), the autofluorescence from biological tissue is low, which gives a higher signal-to-noise ratio to Au NS absorption and making them easier to detect. [3] The aim of paper III was to synthesize Au NS with different sizes and shapes, characterize their morphology and optical properties, and then assess their cytotoxicity and uptake in glioblastoma-astrocytoma cells. In this part, the synthesis methods will not be discussed in full detail as the synthesis of the nanostructures was performed by Sulalit Bandyopadhyay. [XVIII] The focus will be on uptake and cytotoxicity of the different Au NS with glioblastoma-astrocytoma (GA) cells.

Five different shapes of Au NS were synthesized using a *silver assisted seed growth* mechanism assisted by cetyltrimethylammonium bromide (CTAB) which mediates the direction of growth. The resulting five different shapes and their absorption spectra are shown in Figure 6.5.

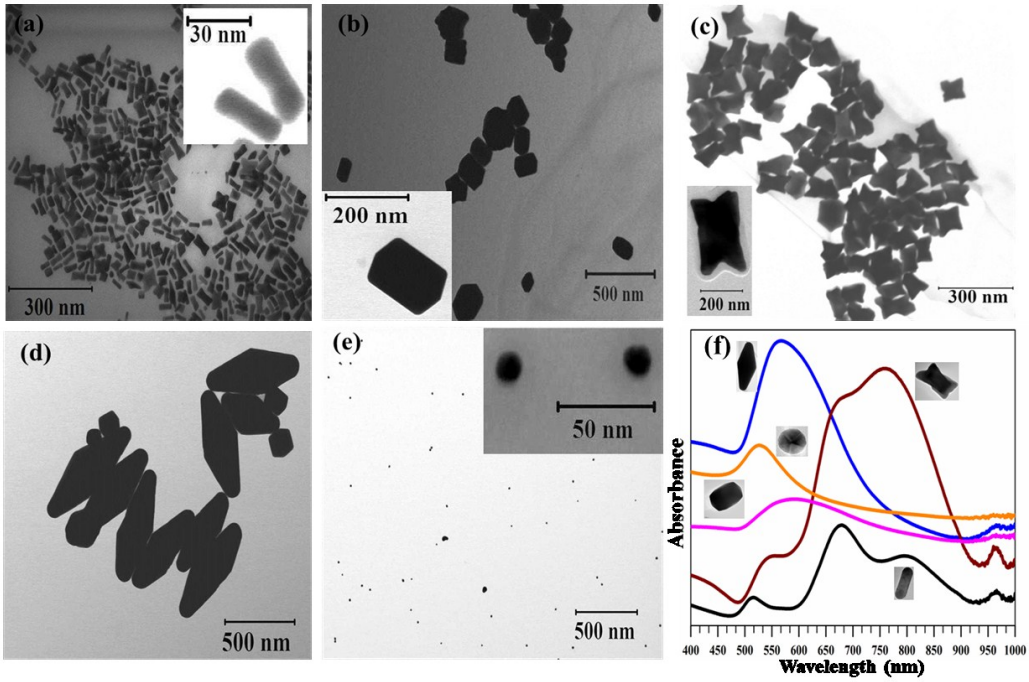


Figure 6.5: Different shapes of Au NS**.** a) Rods, b) Tetrahexahedra, c) Nanomakura, d) Bipyramids, e) spherical. The spectra in f) show the absorbance spectrum for each nanostructure.

[XVIII] Birgitte is second author on this manuscript, and was responsible for the *in vitro* work.

Table 6.3: Aspect ratio, hydrodynamic volume and zeta potential of gold nanoconstructs

| Shape | S(T)EM analysis | | | DLS Size (nm) | Zeta potential, MUA (mV) |
|---|---|---|---|---|---|
| | Long axis (nm) | Short axis (nm) | Aspect ratio (AR) | | |
| Nanorods | 45.1 ± 8.1 | 17.7 ± 6.3 | 2.8 ± 0.7 | 22.0 ± 0.3 | 24.1 ± 0.3 |
| Tetrahexahedra | 180.1 ± 25.4 | 128.8 ± 27.2 | 1.4 ± 0.3 | 81.4 ± 1.4 | -21.6 ± 0.6 |
| Nanomakura | 107.8 ± 15.3 | 71.0 ± 12 | 1.6 ± 0.3 | 72.1 ± 0.6 | -18.7 ± 0.2 |
| Bipyramids | 643.9 ± 84.7 | 266.1 ± 19.2 | 2.4 ± 0.3 | 156.4 ± 2.1 | -25.8 ± 2.1 |
| Spheres | 14.9 ± 4.4 | 14.9 ± 4.4 | 1.0 ± 0.0 | 16.6 ± 1.2 | -36.8 ± 0.4 |

Figure 6.5f shows the UV-vis spectra of all the gold nanoconstructs prepared in this paper. Au NS display tunable LSPR characteristics over the UV-Vis –visible- near IR range, with plasmon bands that split up into multiplets for anisotropic structures. The nanorods (Figure 6.5a) show at least three distinct bands at 516 nm, 679 nm and 796 nm, the most intense band observed at 679 nm. The emergence of a third band can be associated with the polydispersity of the nanorods that is caused by an etching effect of oleic acid. This leads to the formation of nanorods with rough edges, and subsequently an alteration of the plasmon. Both transverse (557 nm) and longitudinal resonance peaks (760 nm) are observed for nanomakura (Figure 6.5c), which has a more jagged surface compared to the nanorods. The larger structures (Figure 6.5b: tetrahexahedra and Figure 6.5d: bipyramids), single and broad LSPR peaks are observed at 568 nm and 593 nm respectively. CTAB is a positively charged surfactant that can have a strong electrostatic attraction to the negatively charged extracellular matrix. Its positive charge may induce proteins to adsorb on the surface, and as such alter the process of endocytosis. [162] Because of the unwanted effects of CTAB, it CTAB was removed from the surface by a two-step exchange procedure, primarily with PEG-SH and secondly with a displacing alkanethiol named 11-mercaptoundecanoic acid (MUA). Table 6.3 show the surface charge (zeta potential) of the AuNCs after surface exchange.

All nanostructures were negatively charged, except the nanorods. [190] This might be an effect of the sharp edges on the rods which may have made it difficult to exchange CTAB. DLS measurements are based on a spherical particle assumption, which means that DLS data may be inaccurate for non-spherical NS. This is also reflected in the size of non-spherical Au NS as S(T)EM data deviates from DLS measurements. NS have a higher rotational probability along the short axis, making the DLS data different than the S(T)EM.

Whether or not NS are taken up in cells depends on the physicochemical properties, aspect ratio (AR), and surface characteristics of the NS, as well as the cell type. [191-193] The surface charge and surface molecules (*e.g* Transferrin)[134, 194] may be more determining than size, for specific or unspecific endocytosis.[162] Moreover, the morphology of the NS will in turn determine the surface coverage of stabilizing or targeting molecules, and as such Au NS of various shapes are believed to interact differently with cells. [118] To get a better understanding on how morphology and charge affect cellular uptake, stable MUA-coated Au NS were co-incubated with GA cells for 24 hours, and the effect of shape and concentration on the cytotoxicity were assessed with a LIVE/DEAD assay supplemented with a nuclear stain (Figure 6.6a).

We hypothesized that the rod-shaped Au NS would cause more damage to the cells, due to their high aspect ratio and apparent positive charge. However, the highest cell death was found for the NS shaped as nanomakura at the highest concentration of NS/cell media (Figure 6.6a). All types of Au NS were found to associate with the cell membrane, but Au NS shaped as nanomakura and nanorods appeared to be taken up by the cells as they were observed close to the nucleus. Au NS taken up via receptor-mediated endocytosis may eventually end up in the Golgi apparatus, [118, 195] and this may explain the apparent trafficking of nanomakura NS towards the nucleus (Figure 6.6 g). However, uptake of Au NS cannot be confirmed with light microscopy, as it is not possible to confirm if NPs are taken up or if they are simply associated with the extracellular matrix. However, the concentration-dependent cytotoxicity of GA cells with incubation of nanomakura Au NS indicated some kind of cellular interaction/uptake.[196] Due to this, uptake of nanomakura Au NS was followed with TEM for 2, 6, 12 and 24 hours after co-incubation with GA cells. [XIX]

TEM-results confirmed that nanomakura Au NS were taken up by the cells. 2 hours after co-incubation nanomakura with glioblastoma-astrocytoma cells, the nanomakura appear to be invaginated by the cellular membrane in a mechanism which resembles receptor-mediated endocytosis (Figure 6.6b). At later stages, what looks like macropinocytosis is observed (Figure 6.6h). The latter is believed to occur when large objects enter a cell, and macropinocytosis may have been induced by aggregation of NS. At 24 hours, the uptake of nanomakura Au NS appeared to continue, which may have been caused by the high extracellular concentration of the NS (Figure 6.6k, l). At 24 hours, the cells seem to detach from the surface, which is an indication of cellular death (Figure 6.6 m).

This paper demonstrates that Au NS of different shapes can be taken up by human cancer cells, and their optical properties nominate them for applications in bioimaging.

[XIX] Ultramicrotome sectioning and TEM (80 kV) was performed by Nan E. Tostrup Skogaker at the Cellular and Molecular Imaging Core Facility (CMIC), Norwegian University of Science and Technology (NTNU).

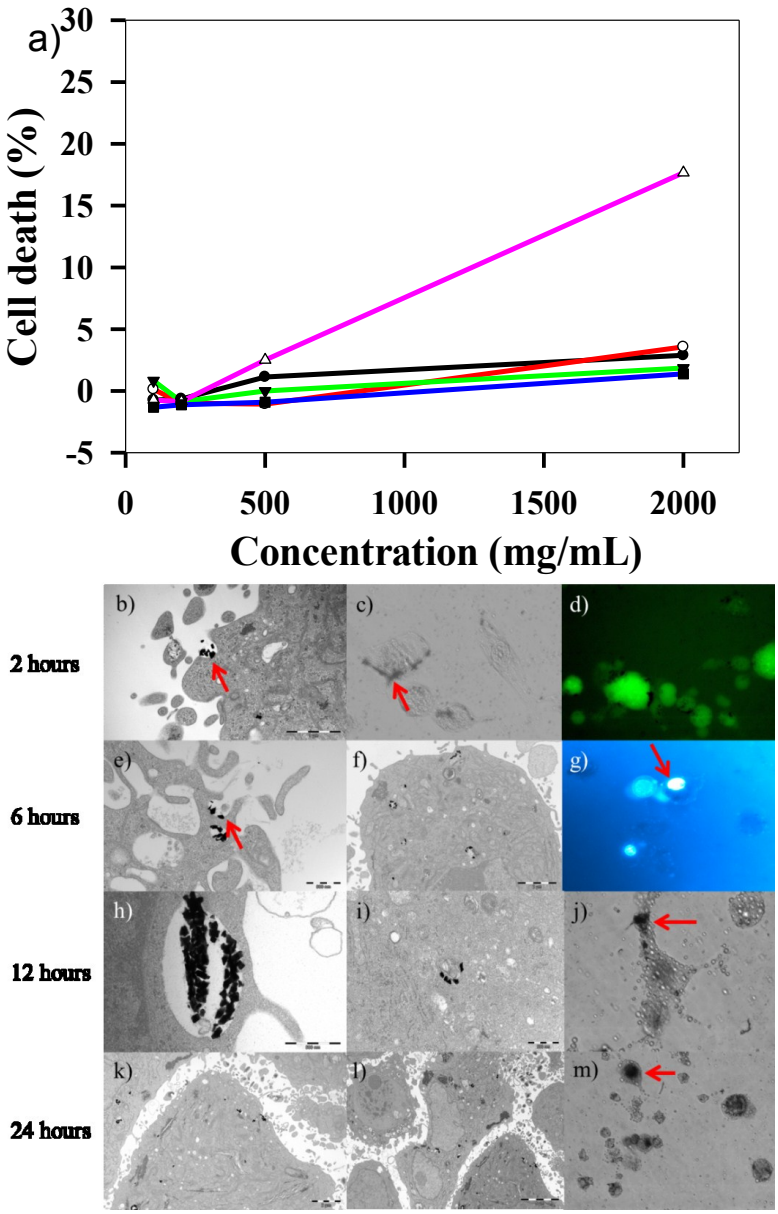


Figure 6.6**:** a) Percentage cell death of GA cells as a function of concentration of Au NS. The incubation time was 24 hours. Images b)-m) are acquired after incubation of nanomakura-shaped gold nanostructures in glioblastoma-astrocytoma cells taken at several time points up to 24 hours. b) TEM show an invagination of the cellular membrane (error bar=1 µm), and c) halogen and d) fluorescence images show association of nanomakura Au NS at the cellular membrane. e) Uptake of nanomakura Au NS were observed after 6 hours (error bar=500 nm), f) with uptake in intracellular vesicles (error bar=2µm). g) staining of the nucleus suggest that nanomakura Au NS were excluded from the nucleus. h) TEM images taken after 12 hours suggests uptake via macropinocytosis (error bar=500 nm), with i) intravesicular location of nanomakura Au NS (error bar=500 nm). j) Intracellular compartmentalization was also visible from the microscopy. Uptake of nanomakura Au NS continued at 24 hours as seen in TEM images k) (error bar=2 µm) and l) (error bar=5 µm). m) Detachment of GA cells from the surface was observed, which most likely is an indication of cell death.

## 6.4 Paper IV

**Pentatwinned iron oxide nanoparticles as glioblastoma-astrocytoma cell actuators**[XX]

*Manuscript in preparation*

It has been established that AuNPs of different shapes and sizes have optical properties in the visible region of the electromagnetic spectrum, as was shown in paper III. Another material that is emerging as a promising candidate for bioimaging applications is iron. NPs of iron oxide (IONPs) can be used as CAs in MRI due to their strong magnetic susceptibilities that can give a hypointense/negative signal in an MR image. Due to the high resolution of MRI, IONPs can also be visualized inside cells, which may for instance become important for studies involving regeneration of the central nervous system. [99]

The aim of this paper was threefold. The first aim was to synthesize and characterize novel IONPs. The second aim was to investigate shape-dependent uptake of IONPs in glioblastoma-astrocytoma cells, and the third aim was to see if IONPs could actuate these cells when under the influence of a static magnetic field. Thus, the third aim involves describing novel IONPs for hyperthermia applications.

As the shape and size of gold nanoparticles show different optical responses, the magnetic properties of IONPs may also seem to be size, - and shape-dependent. In recent years, synthesis of IONPs can be tuned in such a way to give structures that are non-spherical, for instance cubic, rod-shaped, or pyramidal. Four types of IONPs with different shapes and sizes were synthesized: spherical, cubic, octahedral and pentatwinned. All shapes synthesized here are depicted in Figure 6.7, except the spherical IONPs. A novel shape was synthesized by Dr. Gurvinder Singh, and the shape has been termed *pentatwinned*. A pentatwinned structure has five facets (Figure 6.7 a) that appear to have assembled from two separate structures (encircled in Figure 6.7 b).

[XX] Birgitte and Gurvinder contributed equally to this work.

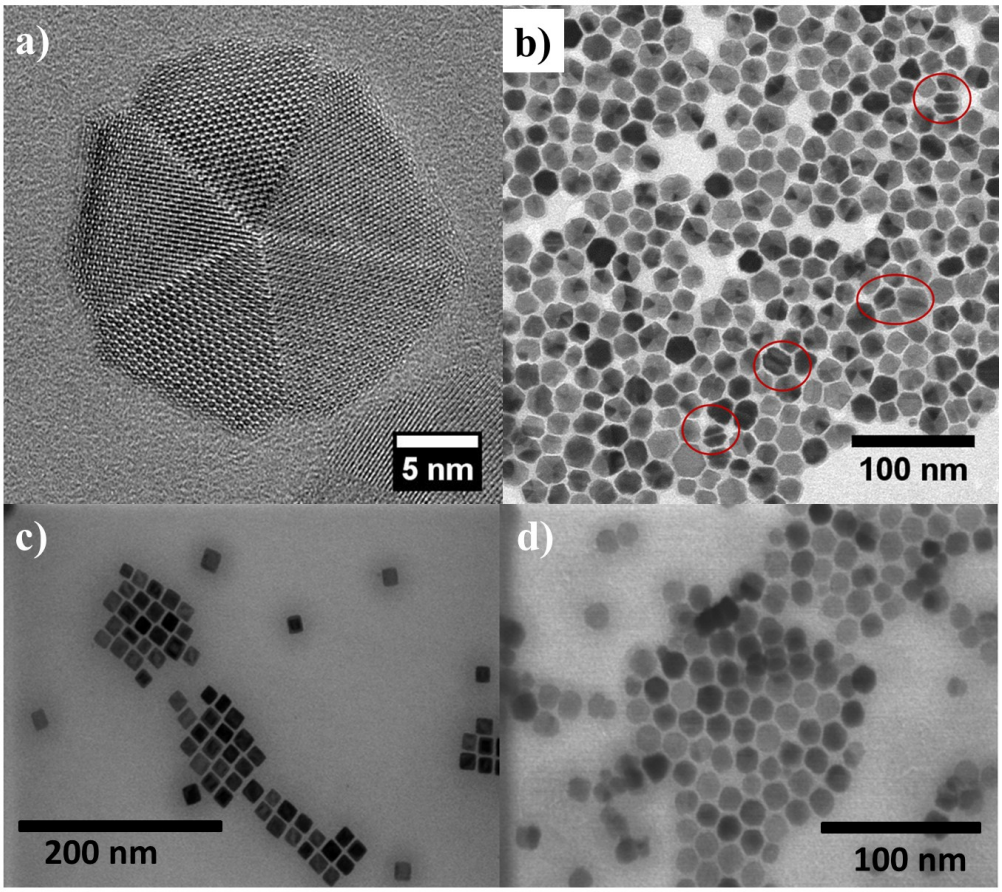


Figure 6.7: Image a) shows HRTEM image of pentatwinned structure. TEM image b) show that pentatwinned IONPS seem to assemble from two smaller structures. Images c) show TEM image of cubic IONPs, while d) show TEM image of octhaedra shaped IONPs. The spherical IONPs are not shown.

The focus on the discussion will be on the *in vitro* data, as they were performed by Birgitte Hjelmeland McDonagh.

The interactions of IONPs were investigated *in vitro* on glioblastoma-astrocytoma cells. The aim was to determine if cellular interactions and uptake were shape-, and concentration dependent. Two different concentrations were used (100 and 500 µg/mL, *v/v*: NP suspension/cell media), as we had indications from paper III that the uptake of NPs appear to be concentration dependent. A LIVE/DEAD assay supplemented with a nuclear stain was added to the cell cultures 24 hours after co-incubation with IONPs (Figure 6.8). However, the dyes were not used to determine the cytotoxicity, but used to visualize the cell nucleus and cellular membranes to give sufficient contrast between the cells and the nanoparticles.

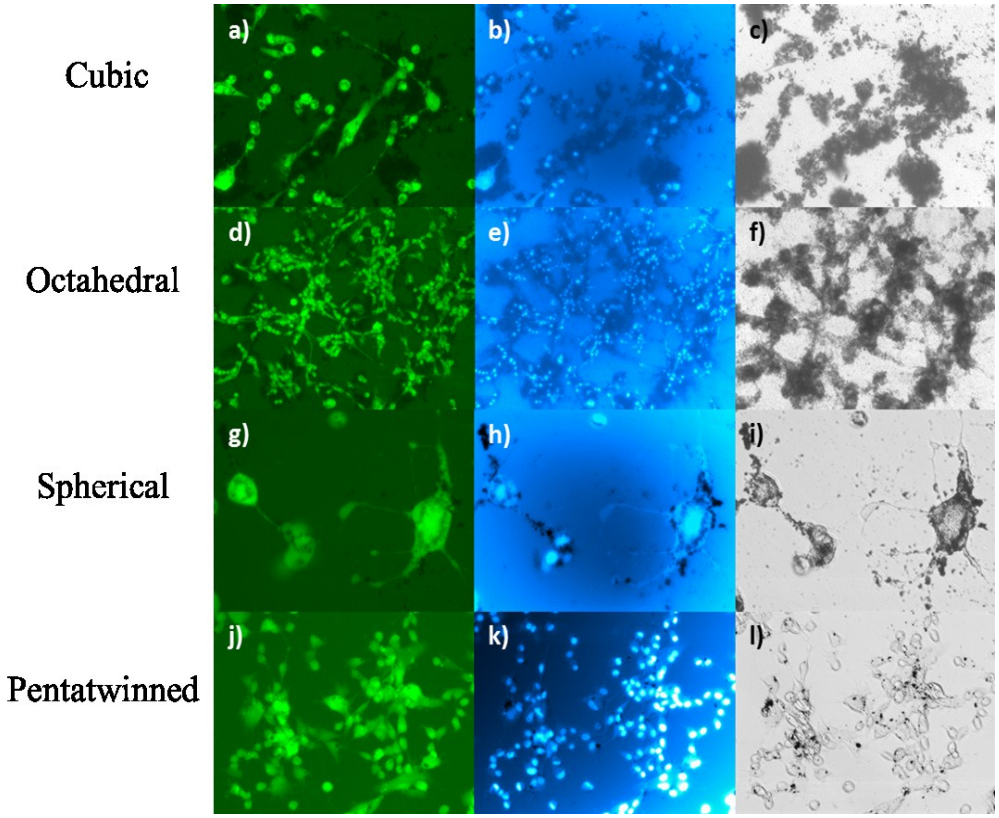


Figure 6.8: Uptake of IONPs of different shapes 24 hours after co-incubation with glioblastoma-astrocytoma cells. Images in the first column to the left show cells stained with calcein. Images in the mid column show the same cells stained with nuclear stain, and the column to the right show the cells imaged with halogen light. Images a)-c) show cubic IONPs (500 µg/mL), d)-f) octahedral IONPs (500 µg/mL), g)-i) spherical IONPs (100 µg/mL), and j)-l) pentatwinned IONPs (500 µg/mL).

Uptake of NPs is hypothesized to be size-dependent, and only a small difference in size may determine if the NP is taken up or not. [130] From the *in vitro* data, the spherical IONPs appeared to center around the perinuclear region of the cells (Figure 6.8 g-i), while this is movement was less clear for the pentatwinned IONPs (Figure 6.8 j-l). Translocation of NPs has previously been shown to accumulate in the perinuclear region, which is associated with NPs internalized in endosomal and or lysosomal vesicles. [135] In addition to size, surface functionalization has been shown to be very important for the uptake of NPs in cells. [145, 197] One widely used method for surface functionalization is attachment of poly(ethylene)glycol (PEG). PEG is hydrophilic and is generally accepted to withstand protein adsorption and is broadly used for surface stabilization of iron oxide nanoparticles.[198,199]

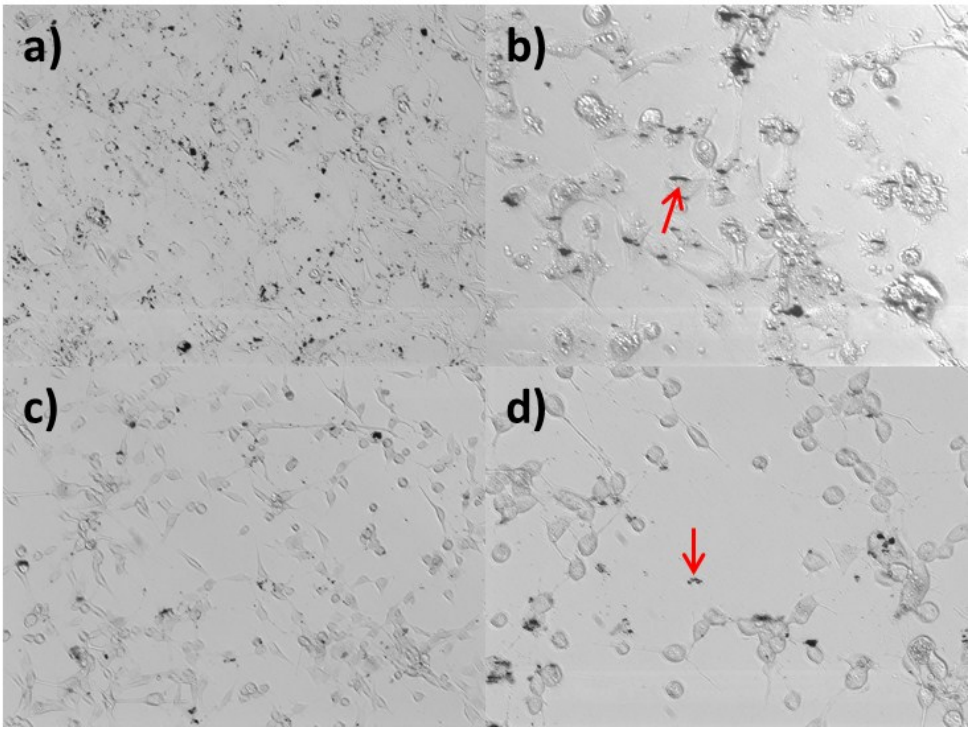

Figure 6.9 Alignment of IONPs in magnetic field. Cells incubated with pentatwinned IONPs a) before and b) after placement in magnetic field. Arrows indicate the NPs. Cells with spherical IONPs c) before and d) after placement in magnetic field also show tendency towards field alignment.

However, when the shape of the NPs is different than spherical, surface functionalization may not be homogeneous and the orientation of PEG molecules may be different on surfaces with different curvature. Particularly, the orientation of PEG-molecules on IONPs has been shown to be important for protein adsorption. [144]

IONPs of cubical and octahedral shape appeared to cluster outside of the cells (Figure 6.8 a-f), which probably is an effect of unsuccessful stability in the cell medium. However, less clustering was observed with spherical (Figure 6.8 g-i) and pentatwinned (Figure 6.8 j-l) IONPs and images gave indications of uptake in glioblastoma-astrocytoma cells. Due to the sharp edges of the cubic and octahedral IONPs, the surface coverage and stability from PEG-molecules may not have been sufficient, which would have caused destabilization in cell media. For instance, the facets of cubic IONPs would allow for a different orientation of PEG-molecules compared to spherical IONPs, and the shape effect might here be more important than the size.

As the cubic and octahedral IONPs did not appear to be taken up by the glioblastoma-astrocytoma cells, they are less likely to give motility to cells under a magnetic field. Therefore, glioblastoma-astrocytoma cells were again incubated with spherical and pentatwinned NPs for 24 hours, before imaging under a constant magnetic field. [XXI]

[XXI] Two magnets were placed on each side of the incubation flask and placed under a fluorescence microscope. Images were acquired as a function of time.

Hyperthermia is a therapeutic procedure based on heating specific tissue up to 41-43° C with an alternating magnetic field with the aim of destroying the tissue. Particularly, malignant cancer cells that tend to be resistant towards radiation therapy seem to be more susceptible to hyperthermia compared to normal tissue.[200] However, one reason that hyperthermia is not an established protocol is because achieving sufficient local heating of cancer cells without affecting surrounding healthy tissue is problematic. One way of solving this problem is do directly inject IONPs into the tumor and then apply an alternating magnetic field. [201]

Comparing the time-dependent movement of cells under a static magnetic field showed that cells incubated with pentatwinned IONPs showed a higher tendency for motility compared to cells incubated with spherical IONPs and cells without IONPs. Also, alignment of pentatwinned IONPs appeared to be stronger than spherical IONPs, which may be caused by their different magnetic properties. Additionally, the magnetic responses suggest that the pentatwinned structures are capable of producing more heat than the spherical IONPs, which would be beneficial for the intended application.

## 6.5 Paper V

**L-DOPA coated manganese oxide nanoparticles as dual MRI contrast agents and drug delivery vehicles**

*Accepted in SMALL*

Although iron nanoparticles seem to be readily taken up by cells, iron oxide NPs are superparamagnetic and have a strong impact on the magnetic field. This leads to a hypointense signal, which could be confused with other artefacts, such as bleeding and calcification.[78, 105] Surface functionalization of iron oxide NPs is well established, but drug release is slightly harder to accomplish as the drug is usually covalently bound to the surface. Also, the issue of clearance of the NPs still remains to be solved. In paper V we have tried to address these issues by synthesizing manganese oxide nanoparticles (MONPs) that dissolve in an aqueous environment, releasing *T1* active $Mn^{2+}$ ions. The MONPs are *T2* CAs, meaning that we have a system able to provide dual contrast and complementary MR images. Concomitantly, the degradation of the NPs offers the possibility for passive drug release, as the surface gradually disappears, the surface-bound drug will be released.

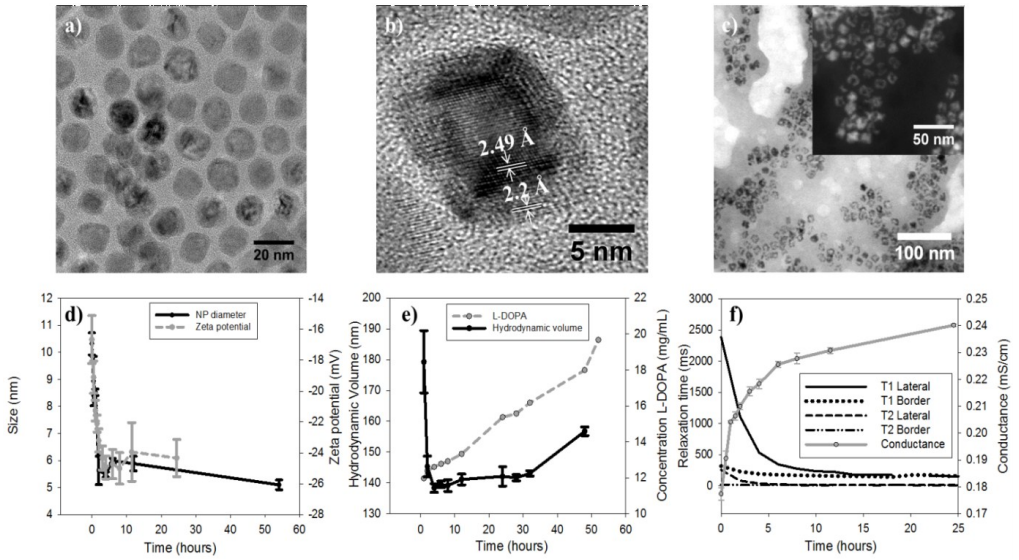


Figure 6.10: MONPs degrade in water and release L-DOPA. a) TEM of MONPs in organic phase b) HRTEM image of MONPs before surface modification c) TEM of L-DOPA coated MONPs, 1 hour in water (pH=6.8). Inset shows dark field image of hollow MONPs after 1 hour in water d) Size and ζ-potential of MONPs as a function of time e) Hydrodynamic volume and concentration of L-DOPA as a function of time f) *T1* and *T2* relaxation time in pig eyes upon injection of MONPs, as a function of time. "Lateral" refers to the opposite side of the injection site, while "Center" refers to the mid part of the pig eye. Conductance as a function of time is also shown.

Characterization of MONPs was performed with TEM, HRTEM, magnetic measurements, XRD and XPS. Release of L-DOPA was performed with UV-visible spectroscopy and XPS, while the degradation of MONPs was studied with ζ-potential measurements, conductance, DLS, TEM, HRTEM and finally MRI. Figure 6.10 show the main results from the characterization of MONPs and the drug release. Our main finding from the characterization

of MONPs was that they appear to have a core-shell structure, with an $Mn_2O_3$ core, and a shell comprised of MnO ( Figure 6.10 a and b). Measurements on their magnetic properties showed ferromagnetic contributions from $Mn_2O_3$ and antiferromagnetic contributions that were ascribed to a small quantity of MnO in the shell. Upon surface functionalization, dark-field and bright-field TEM images ( Figure 6.10c), combined with DLS and conductance measurements, strongly suggested that MONPs dissolve in water and release $Mn^{2+}$ ions as well as L-DOPA.

One obvious way of determining release of $Mn^{2+}$ was to visualize the degradation with MRI, where the *T1*/*T2** effect would be visible. Due to long scan times, a model matrix such as agarose gels could be used, but since the ultimate *in vivo* study was to be carried out in rodent eyes, dead pig eyes were used as a matrix instead. Pig eyes are similar to human eyes, their size allows for a good signal-to-noise ratio, and they offer a more biologically relevant matrix compared to agarose gels, which are more widely used.[202] For this study, MONPs coated with L-DOPA were freshly prepared, injected into pig eyes, and scanned with MRI over a period of 35 hours. The acquired *T1* and *T2** weighted images are shown in Figure 6.11 a-f, and demonstrate the gradual release of *T1* active $Mn^{2+}$ ions as well as a decrease in the *T2* contrast. From these data, we concluded that the MONPs can work as time-dependent *T1*/*T2** CAs and we ultimately tested their contrast switch *in vivo* in rats.

The rodent visual system is an established model for investigating damage and repair in the central nervous system (CNS), [99, 203] as it is easily accessible and immune privileged.[204, 205] Visualizing the optic nerve (ON) tract is accomplished by administering contrast agents into the vitreous body of the eye. The hypothesis was that with time, released $Mn^{2+}$ would diffuse across the retinal ganglion cells and ultimately be transported through the ON and onwards in an anterograde manner. [88, 203, 88, 203, 206] The presence of $Mn^{2+}$ would in such case be visible due to the inherent *T1* contrast. Our main findings were that the contrast in the rat retina was significantly enhanced compared to the contralateral control eye immediately after injecting a suspension of MONPs (Figure 6.12g).

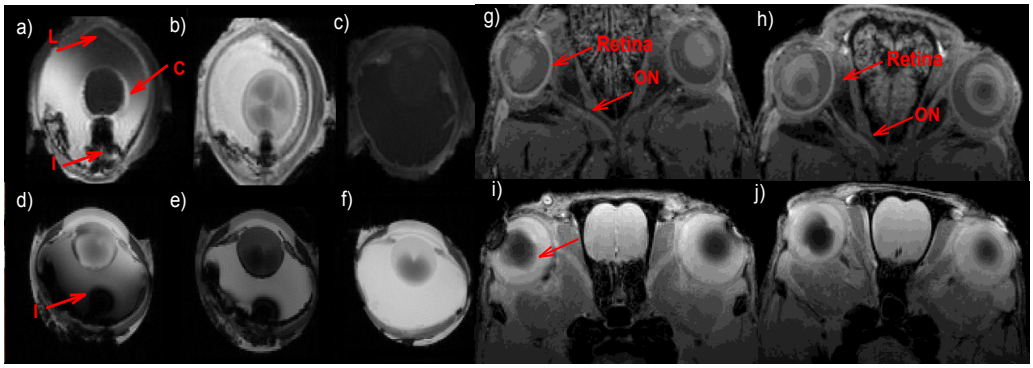


Figure 6.12: *Ex vivo* and *in vivo* degradation of MONPs. Images a) and b) show the T1w images of a pig eye injected with MONPs, acquired immediately after injection and after 34 hours, respectively. "L" refers to the lateral side of the injection site "I", while "C" refers to the central part of the pig eye. Images d) and e) show the complementary T2*w images immediately after injection and 34 hours post injection, respectively. Image c) is the T1w and image f) is the T2*w image of the control eye, immediately after injection and 34 hours after injection, respectively. g) T1w and i) T2*w image of rat ON and retina, 1 hour post injection. h) T1w and j) T2*w image of rat ON and retina, 24 hours post injection.

With time, the contrast in the ON increased as well, supporting the hypothesis of anterograde $Mn^{2+}$ transport (Figure 6.12h). MONPs appeared to stay in the vitreous body, but appeared to move closer to the retina with time, which was observed as negative contrast in the *T2**w images. However, high local concentrations of $Mn^{2+}$ are also prone to give *T2*/*T2** contrast, and it is likely that these contribute to the negative contrast as well.

The main conclusions from paper V is therefore that MONPs can function as dual contrast agents in MRI, and that they also release L-DOPA upon degradation. However, one challenge that we did not manage to solve was to determine the exact concentration of MONPs in a suspension. The complex degradation of MONPs appears to take place in contact with air and in contact with water. Thus, estimating the exact relaxivities in a suspension of MONPs as a function of MONP concentration was not possible or reproducible.

# 7 Concluding remarks and future work

This thesis aimed at synthesizing a range of multifunctional nanoparticles for bioimaging applications, mainly focusing on plasmonic and superpara- and paramagnetic nanomaterials.

The first part of this thesis concerned biomineralization of gold from the proteins human transferrin and bovine serum albumin. Gold nanomaterials synthesized in transferrin showed fluorescent gold structures with near infrared emission that make them highly applicable for bioimaging. Also, the transferrin-gold nanoconstructs showed a remarkable increase in surface affinity compared to the native protein, which we ascribe to unfolding of hydrophobic residues that are more prone to perturb monolayers. The *in vitro* data also suggests increased membrane affinities, but that these might be cell type specific. From the work in paper I, we had indications that changing $NaBH_4$ to ascorbic acid could potentially be favorable for the protein stability, and that differences in gold precursor concentration could be important to tune the size of the gold nanoclusters and nanoparticles. These hypotheses were tested and largely confirmed in paper II, but we were unable to describe the same membrane perturbations for BSA-stabilized gold as we described for the Tf-stabilized gold. This might be explained based on differences in the biological properties of the proteins. Tf can bind to Tf receptors and should therefore have a higher affinity towards cancer cells compared to BSA. Although the protein-stabilized plasmonic and fluorescent structures have very strong absorbance and emission properties, spectral overlap with the cell assay dyes made it difficult to argue the applicability of these constructs as bioimaging probes. Rather, the optical properties could be utilized in for instance sensing applications, which are based on quenching or enhancement of emission intensities or absorbance. Several studies on sensing with BSA-stabilized gold have been described, [70, 72, 184] and we are currently planning to study if these constructs can be used as sensors as well.

For both protein-systems we were unable to observe endocytosis of protein-stabilized gold nanostructures. As we were interested in describing cellular interactions with nanomaterials, we shifted our attention to chemically synthesized AuNPs and superpara- and paramagnetic NPs. These will most likely be easier to observe *in vitro* as they have a higher density than the cells. The aim of paper III and IV was to synthesize nanomaterials of different sizes and shapes, investigate how these properties affect interactions and uptake in glioblastoma-astrocytoma cells, and describe how their optical and superpara- and paramagnetic properties can be used for bioimaging.

In paper III, five nanostructures of gold were synthesized that showed several plasmonic peaks according to their aspect ratio. A novel structure named *nanomakura* was synthesized which had a plasmonic peak from 650-850 nm. This is a substantial bathochromic shift compared to BSA-stabilized AuNPs that had their maximum absorbance around 520-530 nm. In addition to the shift in LSPR peak, the nanomakura also showed high cellular cytotoxicity in glioblastoma-astrocytoma cells that was subtantially different than any of the other structures in this paper. The interactions were further described with TEM imaging, and confirmed that the nanomakura were taken up by the glioblastoma-astrocytoma cells. These promising results nominate the nanomakura for further work *in vivo* as they can be used for instance in hyperthermia[207, 208] and drug delivery, [209] while being simultaneously imaged.

The interesting shape-effects observed from the gold nanoparticles led us to investigate whether the glioblastoma-astrocytoma cells had similar responses to iron oxide

nanoparticles. In paper IV, four types of IONPs with different shapes were synthesized and their uptake and actuation *in vitro* was described. The initial results suggest that the pentatwinned IONPs had a high uptake in the cells, and were able to actuate the cells to a greater extent than spherical IONPs, when placed under a static magnetic field.

IONPs are T2 CAs, that some argue are less beneficial for bioimaging. Existing literature on manganese oxide nanoparticles suggested that they could degrade *in vivo* and release $Mn^{2+}$ ions. We surface functionalized the NPs with L-DOPA with the hypothesis that degrading nanoparticles would give a release of the surface bound drug. We were able to demonstrate degradation of MONPs *ex vivo* and *in vivo* and that this caused a simultaneous hyper-, and hypointense signal in MRI while at the same time releasing a therapeutic drug. Although the physiological effect of L-DOPA was not investigated, future studies with L-DOPA functionalized MONPs should involve a Parkinson's disease model system.

# References


1. Heiligtag, F. J.; Niederberger, M. *Mater. Today* **2013,** 16, (7–8), 262-271.
2. Baker, M. *Nat Meth* **2010,** 7, (12), 957-962.
3. Hahn, M.; Singh, A.; Sharma, P.; Brown, S.; Moudgil, B. *Anal. Bioanal. Chem.* **2011,** 399, (1), 3-27.
4. Le Trequesser, Q.; Seznec, H.; Delville, M.-H., Functionalized nanomaterials: their use as contrast agents in bioimaging: mono- and multimodal approaches. In *Nanotechnology Reviews*, 2013; Vol. 2, p 125.
5. Biju, V. *Chem. Soc. Rev.* **2014,** 43, (3), 744-764.
6. Yao, J.; Yang, M.; Duan, Y. *Chem. Rev.* **2014,** 114, (12), 6130-6178.
7. Stirling, P. C.; Lundin, V. F.; Leroux, M. R. *EMBO reports* **2003,** 4, (6), 565-570.
8. Hartl, F.-U.; Hlodan, R.; Langer, T. *Trends Biochem. Sci.* **1994,** 19, (1), 20-25.
9. De Paoli Lacerda, S. H.; Park, J. J.; Meuse, C.; Pristinski, D.; Becker, M. L.; Karim, A.; Douglas, J. F. *ACS Nano* **2010,** 4, (1), 365-379.
10. Chiti, F.; Dobson, C. M., Protein misfolding, functional amyloid, and human disease. 2006; Vol. 75, pp 333-366.
11. Polymeropoulos, M. H.; Lavedan, C.; Leroy, E.; Ide, S. E.; Dehejia, A.; Dutra, A.; Pike, B.; Root, H.; Rubenstein, J.; Boyer, R.; Stenroos, E. S.; Chandrasekharappa, S.; Athanassiadou, A.; Papapetropoulos, T.; Johnson, W. G.; Lazzarini, A. M.; Duvoisin, R. C.; Di Iorio, G.; Golbe, L. I.; Nussbaum, R. L. *Science* **1997,** 276, (5321), 2045-2047.
12. Walsh, D. M.; Klyubin, I.; Fadeeva, J. V.; Cullen, W. K.; Anwyl, R.; Wolfe, M. S.; Rowan, M. J.; Selkoe, D. J. *Nature* **2002,** 416, (6880), 535-539.
13. Muchowski, P. J. *Neuron* **2002,** 35, (1), 9-12.
14. Dorn, M.; e Silva, M. B.; Buriol, L. S.; Lamb, L. C. *Comput. Biol. Chem.* **2014,** 53, Part B, 251-276.
15. Bujacz, A.; Zielinski, K.; Sekula, B. *Proteins* **2014,** 82, (9), 2199-208.
16. Moreland, J. L.; Gramada, A.; Buzko, O. V.; Zhang, Q.; Bourne, P. E. *BMC Bioinformatics* **2005,** 6.
17. Nelson, D. L.; Cox, M. M., *Lehninger Principles of Biochemistry*. 5 ed.; W.H Freeman and Company: USA, 2008.
18. Cao, X. L.; Li, H. W.; Yue, Y.; Wu, Y. *Vib. Spectrosc* **2013,** 65, 186-192.
19. Dockal, M.; Carter, D. C.; Rüker, F. *J. Biol. Chem.* **2000,** 275, (5), 3042-3050.
20. Sen, P.; Ahmad, B.; Khan, R. *Eur. Biophys. J.* **2008,** 37, (8), 1303-1308.
21. Christensen, H.; Pain, R. H. *Eur. Biophys. J.* **1991,** 19, (5), 221-229.
22. Weiner, S.; Dove, P. M. *Reviews in Mineralogy and Geochemistry* **2003,** 54, (1), 1-29.
23. Xie, J.; Zheng, Y.; Ying, J. Y. *J. Am. Chem. Soc.* **2009,** 131, (3), 888-889.
24. Volden, S.; Lystvet, S. M.; Halskau, O.; Glomm, W. R. *Rsc Advances* **2012,** 2, (31), 11704-11711.
25. Lakowicz, J. R., *Principles of Fluorescence Spectroscopy*. 3 ed.; Springer: USA, 2006.
26. Daniels, T. R.; Delgado, T.; Rodriguez, J. A.; Helguera, G.; Penichet, M. L. *Clin. Immunol.* **2006,** 121, (2), 144-158.
27. Gomme, P. T.; McCann, K. B.; Bertolini, J. *Drug Discov. Today* **2005,** 10, (4), 267-273.
28. Curry, S.; Mandelkow, H.; Brick, P.; Franks, N. *Nat. Struct. Mol. Biol.* **1998,** 5, (9), 827-835.
29. He, X. M.; Carter, D. C. *Nature* **1992,** 358, (6383), 209-215.

30. El Kadi, N.; Taulier, N.; Le Huérou, J. Y.; Gindre, M.; Urbach, W.; Nwigwe, I.; Kahn, P. C.; Waks, M. *Biophys. J.* **2006,** 91, (9), 3397-3404.
31. Bloomfield, V. *Biochemistry* **1966,** 5, (2), 684-689.
32. Faraday, M. *Philos. Trans. R. Soc. London* **1857,** 147, 145-181.
33. Wang, C.; Astruc, D. *Chem. Soc. Rev.* **2014,** 43, (20), 7188-7216.
34. Zheng, J.; Nicovich, P. R.; Dickson, R. M., Highly fluorescent noble-metal quantum dots. 2007; Vol. 58, pp 409-431.
35. Gautier, C.; Bürgi, T. *Chemphyschem* **2009,** 10, (3), 483-492.
36. Mayer, K. M.; Hafner, J. H. *Chem. Rev.* **2011,** 111, (6), 3828-3857.
37. Jain, P. K.; ElSayed, I. H.; El-Sayed, M. A. *Nano Today* **2007,** 2, (1), 18-29.
38. Jain, P. K.; Huang, X.; El-Sayed, I. H.; El-Sayed, M. A. *Acc. Chem. Res.* **2008,** 41, (12), 1578-1586.
39. Qian, H.; Zhu, M.; Wu, Z.; Jin, R. *Acc. Chem. Res.* **2012,** 45, (9), 1470-1479.
40. Yuan, C. T.; Chou, W. C.; Tang, J.; Lin, C. A.; Chang, W. H.; Shen, J. L.; Chuu, D. S. *Opt. Express* **2009,** 17, (18), 16111-16118.
41. Eustis, S.; El-Sayed, M. A. *Chem. Soc. Rev.* **2006,** 35, (3), 209-217.
42. Aikens, C. M. *J. Phys. Chem. Lett.* **2011,** 2, (2), 99-104.
43. de Heer, W. A. *Rev. Mod. Phys.* **1993,** 65, (3), 611-676.
44. Janssens, E.; Neukermans, S.; Lievens, P. *Curr. Opin. Solid State Mater. Sci.* **2004,** 8, (3–4), 185-193.
45. Reber, A. C.; Khanna, S. N.; Castleman Jr, A. W., Chapter 9 - Superatoms: From Motifs to Materials. In *Science and Technology of Atomic, Molecular, Condensed Matter & Biological Systems*, Purusottam, J.; Castleman, A. W., Eds. Elsevier: 2010; Vol. Volume 1, pp 365-381.
46. Wu, Z.; Jin, R. *Nano Lett.* **2010,** 10, (7), 2568-2573.
47. Le Guével, X.; Hötzer, B.; Jung, G.; Hollemeyer, K.; Trouillet, V.; Schneider, M. *J. Phys. Chem. C* **2011,** 115, (22), 10955-10963.
48. Szunerits, S.; Boukherroub, R. *Chem. Commun.* **2012,** 48, (72), 8999-9010.
49. Brust, M.; Walker, M.; Bethell, D.; Schiffrin, D. J.; Whyman, R. *J. Chem. Soc., Chem. Commun.* **1994**, (7), 801-802.
50. Sau, T. K.; Murphy, C. J. *J. Am. Chem. Soc.* **2004,** 126, (28), 8648-8649.
51. Kimling, J.; Maier, M.; Okenve, B.; Kotaidis, V.; Ballot, H.; Plech, A. *The Journal of Physical Chemistry B* **2006,** 110, (32), 15700-15707.
52. Llevot, A.; Astruc, D. *Chem. Soc. Rev.* **2012,** 41, (1), 242-257.
53. Guo, S.; Wang, E. *Anal. Chim. Acta* **2007,** 598, (2), 181-192.
54. Aili, D.; Enander, K.; Rydberg, J.; Lundström, I.; Baltzer, L.; Liedberg, B. *J. Am. Chem. Soc.* **2006,** 128, (7), 2194-2195.
55. Aili, D.; Gryko, P.; Sepulveda, B.; Dick, J. A. G.; Kirby, N.; Heenan, R.; Baltzer, L.; Liedberg, B.; Ryan, M. P.; Stevens, M. M. *Nano Lett.* **2011,** 11, (12), 5564-5573.
56. Chen, P.; Selegard, R.; Aili, D.; Liedberg, B. *Nanoscale* **2013,** 5, (19), 8973-8976.
57. Liu, X.; Wang, Y.; Chen, P.; Wang, Y.; Zhang, J.; Aili, D.; Liedberg, B. *Anal. Chem.* **2014,** 86, (5), 2345-2352.
58. Daniel, M.-C.; Astruc, D. *Chem. Rev.* **2004,** 104, (1), 293-346.
59. Brewer, S. H.; Glomm, W. R.; Johnson, M. C.; Knag, M. K.; Franzen, S. *Langmuir* **2005,** 21, (20), 9303-9307.
60. Lystvet, S. M.; Volden, S.; Yasuda, M.; Halskau, O.; Glomm, W. R. *Nanoscale* **2011,** 3, (4), 1788-1797.
61. Lystvet, S. M.; Volden, S.; Halskau, O.; Glomm, W. R. *Soft Matter* **2011,** 7, (24), 11501-11509.

62. Tsai, D.-H.; DelRio, F. W.; Keene, A. M.; Tyner, K. M.; MacCuspie, R. I.; Cho, T. J.; Zachariah, M. R.; Hackley, V. A. *Langmuir* **2011,** 27, (6), 2464-2477.
63. Lystvet, S. M.; Volden, S.; Singh, G.; Rundgren, I. M.; Wen, H.; Halskau, O.; Glomm, W. R. *The Journal of Physical Chemistry C* **2013,** 117, (5), 2230-2238.
64. Zahir, F.; Rizwi, S. J.; Haq, S. K.; Khan, R. H. *Environ. Toxicol. Pharmacol.* **2005,** 20, (2), 351-360.
65. Yan, Z.; Yuen, M.-F.; Hu, L.; Sun, P.; Lee, C.-S. *RSC Advances* **2014,** 4, (89), 48373-48388.
66. Chevrier, D. M.; Chatt, A.; Zhang, P. *Journal of Nanophotonics* **2012,** 6, (1), 064504-1-064504-16.
67. Lin, Y.-H.; Tseng, W.-L. *Anal. Chem.* **2010,** 82, (22), 9194-9200.
68. Chen, Z.; Qian, S.; Chen, J.; Cai, J.; Wu, S.; Cai, Z. *Talanta* **2012,** 94, 240-245.
69. Hu, D.; Sheng, Z.; Gong, P.; Zhang, P.; Cai, L. *Analyst* **2010,** 135, (6), 1411-1416.
70. Tao, Y.; Lin, Y.; Ren, J.; Qu, X. *Biosensors Bioelectron.* **2013,** 42, 41-46.
71. Michalet, X.; Pinaud, F. F.; Bentolila, L. A.; Tsay, J. M.; Doose, S.; Li, J. J.; Sundaresan, G.; Wu, A. M.; Gambhir, S. S.; Weiss, S. *Science* **2005,** 307, (5709), 538-544.
72. Cui, M. L.; Liu, J. M.; Wang, X. X.; Lin, L. P.; Jiao, L.; Zhang, L. H.; Zheng, Z. Y.; Lin, S. Q. *Analyst* **2012,** 137, (22), 5346-5351.
73. Xi, D.; Dong, S.; Meng, X.; Lu, Q.; Meng, L.; Ye, J. *RSC Advances* **2012,** 2, (33), 12515-12524.
74. Zhang, X. *Cell Biochem. Biophys.* **2015**.
75. Chenjie, X.; Tung, G. A.; Shouheng, S. *Chem. Mater.* **2008,** 20, (13), 4167-4169.
76. Zhang, A.; Tu, Y.; Qin, S.; Li, Y.; Zhou, J.; Chen, N.; Lu, Q.; Zhang, B. *J. Colloid Interface Sci.* **2012,** 372, (1), 239-244.
77. Xu, W.; Kattel, K.; Park, J. Y.; Chang, Y.; Kim, T. J.; Lee, G. H. *PCCP* **2012,** 14, (37), 12687-12700.
78. Westbrook, C., Kaut Roth, C., Talbot, J., *MRI in Practice*. 4 ed.; Blackwell Publishing Ltd: USA, 2011.
79. Silverstein, R. M., Webster, F.X., Kiemle, D.J., *Spectrometric identification of organic contributions*. 7 ed.; John Wiley & Sons, Inc.: Hoboken, NJ, 2005.
80. Bleaney, B. I., *Electricity and magnetism / B. I. Bleaney and B. Bleaney*. Oxford University Press: London, 1976.
81. Estelrich, J.; Sánchez-Martín, M. J.; Busquets, M. A. *International Journal of Nanomedicine* **2015,** 10, 1727-1741.
82. Fulay, P., *Electronic, Magnetic, and Optical Materials*. CRC Press: Boca Raton, Florida, USA, 2010.
83. Massaad, C. A.; Pautler, R. G. *Methods in Molecular Biology (Clifton, N.j.)* **2011,** 711, 145-174.
84. Silva, A. C.; Bock, N. A. *Schizophr. Bull.* **2008,** 34, (4), 595-604.
85. Aoki, I.; Wu, Y.-J. L.; Silva, A. C.; Lynch, R. M.; Koretsky, A. P. *NeuroImage* **2004,** 22, (3), 1046-1059.
86. Olsen, Ø.; Kristoffersen, A.; Thuen, M.; Sandvig, A.; Brekken, C.; Haraldseth, O.; Goa, P. E. *J. Magn. Reson. Imaging* **2010,** 32, (3), 551-560.
87. Thuen, M.; Berry, M.; Pedersen, T. B.; Goa, P. E.; Summerfield, M.; Haraldseth, O.; Sandvig, A.; Brekken, C. *J. Magn. Reson. Imaging* **2008,** 28, (4), 855-865.
88. Mørch, Ý. A.; Sandvig, I.; Olsen, Ø.; Donati, I.; Thuen, M.; Skjåk-Bræk, G.; Haraldseth, O.; Brekken, C. *Contrast Media Mol. Imaging* **2012,** 7, (2), 265-275.
89. Fitsanakis, V. A.; Zhang, N.; Avison, M. J.; Gore, J. C.; Aschner, J. L.; Aschner, M. *Neurotoxicology* **2006,** 27, (5), 798-806.

90. Zhen, Z.; Xie, J. *Theranostics* **2012,** 2, (1), 45-54.
91. Chen, Y.; Yin, Q.; Ji, X.; Zhang, S.; Chen, H.; Zheng, Y.; Sun, Y.; Qu, H.; Wang, Z.; Li, Y.; Wang, X.; Zhang, K.; Zhang, L.; Shi, J. *Biomaterials* **2012,** 33, (29), 7126-7137.
92. Kueny-Stotz, M.; Garofalo, A.; Felder-Flesch, D. *Eur. J. Inorg. Chem.* **2012**, (12), 1987-2005.
93. Choi, E. S.; Park, J. Y.; Baek, M. J.; Xu, W.; Kattel, K.; Kim, J. H.; Lee, J. J.; Chang, Y.; Kim, T. J.; Bae, J. E.; Chae, K. S.; Suh, K. J.; Lee, G. H. *Eur. J. Inorg. Chem.* **2010**, (28), 4555-4560.
94. Lim, E. K.; Kim, T.; Paik, S.; Haam, S.; Huh, Y. M.; Lee, K. *Chem. Rev.* **2015,** 115, (1), 327-394.
95. Xing, R.; Zhang, F.; Xie, J.; Aronova, M.; Zhang, G.; Guo, N.; Huang, X.; Sun, X.; Liu, G.; Bryant, L. H.; Bhirde, A.; Liang, A.; Hou, Y.; Leapman, R. D.; Sun, S.; Chen, X. *Nanoscale* **2011,** 3, (12), 4943-4945.
96. Kim, T.; Momin, E.; Choi, J.; Yuan, K.; Zaidi, H.; Kim, J.; Park, M.; Lee, N.; McMahon, M. T.; Quinones-Hinojosa, A.; Bulte, J. W. M.; Hyeon, T.; Gilad, A. A. *J. Am. Chem. Soc.* **2011,** 133, (9), 2955-2961.
97. Sapsford, K. E.; Algar, W. R.; Berti, L.; Gemmill, K. B.; Casey, B. J.; Oh, E.; Stewart, M. H.; Medintz, I. L. *Chem. Rev.* **2013,** 113, (3), 1904-2074.
98. Li, L.; Jiang, W.; Luo, K.; Song, H.; Lan, F.; Wu, Y.; Gu, Z. *Theranostics* **2013,** 3, (8), 595-615.
99. Sandvig, I.; Thuen, M.; Hoang, L.; Olsen, Ø.; Sardella, T. C. P.; Brekken, C.; Tvedt, K. E.; Barnett, S. C.; Haraldseth, O.; Berry, M.; Sandvig, A. *NMR Biomed.* **2012,** 25, (4), 620-631.
100. Huang, G.; Li, H.; Chen, J.; Zhao, Z.; Yang, L.; Chi, X.; Chen, Z.; Wang, X.; Gao, J. *Nanoscale* **2014,** 6, (17), 10404-10412.
101. Sun, C.; Lee, J. S. H.; Zhang, M. *Adv. Drug Del. Rev.* **2008,** 60, (11), 1252-1265.
102. Raschzok, N.; Muecke, D. A.; Adonopoulou, M. K.; Billecke, N.; Werner, W.; Kammer, N. N.; Zielinski, A.; Behringer, P. A.; Ringel, F.; Huang, M. D.; Neuhaus, P.; Teichgräber, U.; Sauer, I. M. *Mol. Imag. Biol.* **2011,** 13, (4), 613-622.
103. Mahmoudi, M.; Hofmann, H.; Rothen-Rutishauser, B.; Petri-Fink, A. *Chem. Rev.* **2012,** 112, (4), 2323-2338.
104. Weissleder, R.; Nahrendorf, M.; Pittet, M. J. *Nature Materials* **2014,** 13, (2), 125-138.
105. Kim, B. H.; Lee, N.; Kim, H.; An, K.; Park, Y. I.; Choi, Y.; Shin, K.; Lee, Y.; Kwon, S. G.; Na, H. B.; Park, J. G.; Ahn, T. Y.; Kim, Y. W.; Moon, W. K.; Choi, S. H.; Hyeon, T. *J. Am. Chem. Soc.* **2011,** 133, (32), 12624-12631.
106. Luo, Y.; Yang, J.; Yan, Y.; Li, J.; Shen, M.; Zhang, G.; Mignani, S.; Shi, X. *Nanoscale* **2015**.
107. Tromsdorf, U. I.; Bruns, O. T.; Salmen, S. C.; Beisiegel, U.; Weller, H. *Nano Lett.* **2009,** 9, (12), 4434-4440.
108. Hingorani, D. V.; Bernstein, A. S.; Pagel, M. D. *Contrast Media Mol. Imaging* **2015,** 10, (4), 245-265.
109. Xu, C.; Sun, S. *Adv. Drug Del. Rev.* **2013,** 65, (5), 732-743.
110. Ito, A.; Shinkai, M.; Honda, H.; Kobayashi, T. *J. Biosci. Bioeng.* **2005,** 100, (1), 1-11.
111. Nakajima, N.; Ikada, Y. *Bioconj. Chem.* **1995,** 6, (1), 123-130.
112. Montalbetti, C. A. G. N.; Falque, V. *Tetrahedron* **2005,** 61, (46), 10827-10852.
113. Patel, D.; Kell, A.; Simard, B.; Xiang, B.; Lin, H. Y.; Tian, G. *Biomaterials* **2011,** 32, (4), 1167-1176.
114. Losic, D.; Yu, Y.; Aw, M. S.; Simovic, S.; Thierry, B.; Addai-Mensah, J. *Chem. Commun.* **2010,** 46, (34), 6323-6325.

115. Williams, A.; Ibrahim, I. T. *Chem. Rev.* **1981,** 81, (6), 589-636.
116. Day, R. E.; Kitchen, P.; Owen, D. S.; Bland, C.; Marshall, L.; Conner, A. C.; Bill, R. M.; Conner, M. T. *Biochimica et Biophysica Acta (BBA) - General Subjects* **2014,** 1840, (5), 1492-1506.
117. Doherty, G. J.; McMahon, H. T. *Annu. Rev. Biochem.* **2009,** 78, (1), 857-902.
118. Canton, I.; Battaglia, G. *Chem. Soc. Rev.* **2012,** 41, (7), 2718-2739.
119. Zhang, S.; Gao, H.; Bao, G. *ACS Nano* **2015**.
120. Riezman, H.; Munn, A.; Geli, M. I.; Hicke, L. *Experientia* **1996,** 52, (12), 1033-1041.
121. Beddoes, C. M.; Case, C. P.; Briscoe, W. H. *Adv. Colloid Interface Sci.* **2015,** 218, 48-68.
122. Parton, R. G.; del Pozo, M. A. *Nat. Rev. Mol. Cell Biol.* **2013,** 14, (2), 98-112.
123. Tzlil, S.; Deserno, M.; Gelbart, W. M.; Ben-Shaul, A. *Biophys. J.* 86, (4), 2037-2048.
124. Deserno, M.; Gelbart, W. M. *The Journal of Physical Chemistry B* **2002,** 106, (21), 5543-5552.
125. Gao, H.; Shi, W.; Freund, L. B. *Proc. Natl. Acad. Sci. U. S. A.* **2005,** 102, (27), 9469-9474.
126. Bao, G.; Bao, X. R. *Proc. Natl. Acad. Sci. U. S. A.* **2005,** 102, (29), 9997-9998.
127. Zhang, S.; Li, J.; Lykotrafitis, G.; Bao, G.; Suresh, S. *Adv. Mater.* **2009,** 21, (4), 419-424.
128. Mu, Q.; Jiang, G.; Chen, L.; Zhou, H.; Fourches, D.; Tropsha, A.; Yan, B. *Chem. Rev.* **2014,** 114, (15), 7740-7781.
129. Shang, L.; Nienhaus, K.; Nienhaus, G. *Journal of Nanobiotechnology* **2014,** 12, (1), 5.
130. Chithrani, B. D.; Ghazani, A. A.; Chan, W. C. W. *Nano Lett.* **2006,** 6, (4), 662-668.
131. Jiang, W.; KimBetty, Y. S.; Rutka, J. T.; ChanWarren, C. W. *Nat Nano* **2008,** 3, (3), 145-150.
132. Osaki, F.; Kanamori, T.; Sando, S.; Sera, T.; Aoyama, Y. *J. Am. Chem. Soc.* **2004,** 126, (21), 6520-6521.
133. Roiter, Y.; Ornatska, M.; Rammohan, A. R.; Balakrishnan, J.; Heine, D. R.; Minko, S. *Nano Lett.* **2008,** 8, (3), 941-944.
134. Chithrani, B. D.; Chan, W. C. W. *Nano Lett.* **2007,** 7, (6), 1542-1550.
135. Gratton, S. E. A.; Ropp, P. A.; Pohlhaus, P. D.; Luft, J. C.; Madden, V. J.; Napier, M. E.; DeSimone, J. M. *Proceedings of the National Academy of Sciences* **2008,** 105, (33), 11613-11618.
136. Chen, P. C.; Chiang, C. K.; Chang, H. T. *J. Nanopart. Res.* **2013,** 15, (1).
137. Chiu, C.-c.; Moore, P. B.; Shinoda, W.; Nielsen, S. O. *The Journal of Chemical Physics* **2009,** 131, (24), 244706.
138. Oh, N.; Park, J.-H. *International Journal of Nanomedicine* **2014,** 9, (Suppl 1), 51-63.
139. Alberts B, J. A., Lewis J, et al. Molecular Biology of the Cell. 4th edition. New York: Garland Science; 2002. Programmed Cell Death (Apoptosis) Available from: http://www.ncbi.nlm.nih.gov/books/NBK26873/.
140. Lowe, S. W.; Lin, A. W. *Carcinogenesis* **2000,** 21, (3), 485-495.
141. Nel, A.; Xia, T.; Mädler, L.; Li, N. *Science* **2006,** 311, (5761), 622-627.
142. Wang, C.; Youle, R. J. *Annu. Rev. Genet.* **2009,** 43, 95-118.
143. Colombo, M.; Carregal-Romero, S.; Casula, M. F.; Gutierrez, L.; Morales, M. P.; Bohm, I. B.; Heverhagen, J. T.; Prosperi, D.; Parak, W. J. *Chem. Soc. Rev.* **2012,** 41, (11), 4306-4334.
144. Sant, S.; Poulin, S.; Hildgen, P. *Journal of Biomedical Materials Research Part A* **2008,** 87A, (4), 885-895.

145. Arvizo, R. R.; Miranda, O. R.; Thompson, M. A.; Pabelick, C. M.; Bhattacharya, R.; Robertson, J. D.; Rotello, V. M.; Prakash, Y. S.; Mukherjee, P. *Nano Lett.* **2010,** 10, (7), 2543-2548.
146. Wang, F.; Bexiga, M. G.; Anguissola, S.; Boya, P.; Simpson, J. C.; Salvati, A.; Dawson, K. A. *Nanoscale* **2013,** 5, (22), 10868-10876.
147. Skoog, D. A., West, D.M., Holler, F.J., Crouch, S.R., *Fundamentals of Analytical Chemistry*. 8 ed.; Brooks/Cole, Cengage Learning: Canada, 2004.
148. Lystvet, S. M.; Volden, S.; Yasuda, M.; Halskau Jr, O.; Glomm, W. R. *Nanoscale* **2011,** 3, (4), 1788-1797.
149. Li, X.; Jiang, L.; Zhan, Q.; Qian, J.; He, S. *Colloids Surf. Physicochem. Eng. Aspects* **2009,** 332, (2–3), 172-179.
150. Bailey, J. E.; Beaven, G. H.; Chignell, D. A.; Gratzer, W. B. *Eur. J. Biochem.* **1968,** 7, (1), 5-14.
151. Gelamo, E. L.; Silva, C. H. T. P.; Imasato, H.; Tabak, M. *Biochimica et Biophysica Acta - Protein Structure and Molecular Enzymology* **2002,** 1594, (1), 84-99.
152. Sułkowska, A. *J. Mol. Struct.* **2002,** 614, (1-3), 227-232.
153. Möller, M.; Denicola, A. *Biochem. Mol. Biol. Educ.* **2002,** 30, (3), 175-178.
154. Lystvet, S. M.; Volden, S.; Singh, G.; Yasuda, M.; Halskau, O.; Glomm, W. R. *RSC Advances* **2013,** 3, (2), 482-495.
155. James, N. G.; Byrne, S. L.; Steere, A. N.; Smith, V. C.; MacGillivray, R. T. A.; Mason, A. B. *Biochemistry* **2009,** 48, (13), 2858-2867.
156. Xie, H.; Tkachenko, A. G.; Glomm, W. R.; Ryan, J. A.; Brennaman, M. K.; Papanikolas, J. M.; Franzen, S.; Feldheim, D. L. *Anal. Chem.* **2003,** 75, (21), 5797-5805.
157. Pennycook, S. J., Nellist, P.D *Scanning Transmission Electron Microscopy: Imaging and Analysis*. Springer: New York, 2011.
158. Painter, P. C., Coleman, M.M., *Fundamentals of polymer Science*. 2 ed.; CRC press: Boca Raton, 1997.
159. Hassan, P. A.; Rana, S.; Verma, G. *Langmuir* **2015,** 31, (1), 3-12.
160. Hiemenz, P. C., Rajagopalan, R., *Principles of colloid and surface chemistry*. 3 ed.; CRC Press: Boca Raton, Florida, USA, 1997.
161. Ohshima, H., *Electrical phenomena at Interfaces and Biointerfaces*. Wiley: Hoboken, New Jersey, 2012.
162. Chithrani, D. B. *Mol. Membr. Biol.* **2010,** 27, (7), 299-311.
163. Mistry, A.; Stolnik, S.; Illum, L. *Mol. Pharm.* **2015**.
164. Turner, N. H.; Schreifels, J. A. *Anal. Chem.* **1992,** 64, (12), 302R-320R.
165. Siegbahn, K. *J. Electron. Spectrosc. Relat. Phenom.* **1990,** 51, 11-36.
166. Hollander, J. M.; Jolly, W. L. *Acc. Chem. Res.* **1970,** 3, (6), 193-200.
167. van der Heide, P., *X-Ray Photoelectron Spectroscopy : An Introduction to Principles and Practices*. John Wiley & Sons: Hoboken, NJ, USA, 2011.
168. Fultz, B., Howe, J., *Transmission Electron Microscpy and Diffractometry of Materials*. Springer Verlag: Berlin Heidelberg, 2013.
169. Mullin, J. W., *Crystallization*. 4 ed.; Elsevier Butterworth-Heinemann: Burlington, MA, 2001.
170. Glomm, W. R.; Volden, S.; Halskau Jr, Ø.; Ese, M. H. G. *Anal. Chem.* **2009,** 81, (8), 3042-3050.
171. Giner-Casares, J. J.; Brezesinski, G.; Möhwald, H. *Current Opinion in Colloid & Interface Science* **2014,** 19, (3), 176-182.
172. Langmuir, I. *J. Am. Chem. Soc.* **1917,** 39, (9), 1848-1906.

173. Wally, J.; Halbrooks, P. J.; Vonrhein, C.; Rould, M. A.; Everse, S. J.; Mason, A. B.; Buchanan, S. K. *J. Biol. Chem.* **2006,** 281, (34), 24934-44.
174. Li, K.; Du, S.; Van Ginkel, S.; Chen, Y., Atomic Force Microscopy Study of the Interaction of DNA and Nanoparticles. In *Nanomaterial*, Capco, D. G.; Chen, Y., Eds. Springer Netherlands: 2014; Vol. 811, pp 93-109.
175. Whited, A. M.; Park, P. S. H. *Biochim. Biophys. Acta* **2014,** 1838, (1, Part A), 56-68.
176. Meyer, E. *Prog. Surf. Sci.* **1992,** 41, (1), 3-49.
177. Binnig, G.; Quate, C. F.; Gerber, C. *Phys. Rev. Lett.* **1986,** 56, (9), 930-933.
178. Würth, R.; Barbieri, F.; Florio, T. *BioMed Research International* **2014,** 2014.
179. Yuan, X.; Curtin, J.; Xiong, Y.; Liu, G.; Waschsmann-Hogiu, S.; Farkas, D. L.; Black, K. L.; Yu, J. S. *Oncogene* **2004,** 23, (58), 9392-9400.
180. Suvà, M. L.; Riggi, N.; Janiszewska, M.; Radovanovic, I.; Provero, P.; Stehle, J. C.; Baumer, K.; Le Bitoux, M. A.; Marino, D.; Cironi, L.; Marquez, V. E.; Clément, V.; Stamenkovic, I. *Cancer Res.* **2009,** 69, (24), 9211-9218.
181. Pallini, R.; Ricci-Vitiani, L.; Banna, G. L.; Signore, M.; Lombardi, D.; Todaro, M.; Stassi, G.; Martini, M.; Maira, G.; Larocca, L. M.; De Maria, R. *Clin. Cancer. Res.* **2008,** 14, (24), 8205-8212.
182. Lucey, B. P.; Nelson-Rees, W. A.; Hutchins, G. M. *Arch. Pathol. Lab. Med.* **2009,** 133, (9), 1463-1467.
183. Volden, S.; Lystvet, S. M.; Halskau, Ø.; Glomm, W. R. *RSC Advances* **2012,** 2, (31), 11704-11711.
184. Hu, L.; Han, S.; Parveen, S.; Yuan, Y.; Zhang, L.; Xu, G. *Biosensors Bioelectron.* **2012,** 32, (1), 297-299.
185. Wang, M.; Mei, Q.; Zhang, K.; Zhang, Z. *Analyst* **2012,** 137, (7), 1618-1623.
186. Wang, Y.; Chen, J.; Irudayaraj, J. *ACS Nano* **2011,** 5, (12), 9718-9725.
187. Das, T.; Ghosh, P.; Shanavas, M. S.; Maity, A.; Mondal, S.; Purkayastha, P. *Nanoscale* **2012,** 4, (19), 6018-6024.
188. Zhang, M.; Dang, Y. Q.; Liu, T. Y.; Li, H. W.; Wu, Y.; Li, Q.; Wang, K.; Zou, B. *J. Phys. Chem. C* **2013,** 117, (1), 639-647.
189. Raut, S.; Chib, R.; Rich, R.; Shumilov, D.; Gryczynski, Z.; Gryczynski, I. *Nanoscale* **2013,** 5, (8), 3441-3446.
190. Shaw, C. F. *Chem Rev* **1999,** 99, (9), 2589-2600.
191. Dykman, L. A.; Khlebtsov, N. G. *Chem. Rev.* **2014,** 114, (2), 1258-1288.
192. Chu, Z.; Zhang, S.; Zhang, B.; Zhang, C.; Fang, C. Y.; Rehor, I.; Cigler, P.; Chang, H. C.; Lin, G.; Liu, R.; Li, Q. *Sci. Rep.* **2014,** 4.
193. Cartiera, M. S.; Johnson, K. M.; Rajendran, V.; Caplan, M. J.; Saltzman, W. M. *Biomaterials* **2009,** 30, (14), 2790-2798.
194. McDonagh, B. H.; Volden, S.; Lystvet, S. M.; Singh, G.; Ese, M.-H.; Ryan, J. A.; Lindgren, M.; Sandvig, A.; Sandvig, I.; Glomm, W. R. *Nanoscale* **2015**.
195. Mosesson, Y.; Mills, G. B.; Yarden, Y. *Nature Reviews Cancer* **2008,** 8, (11), 835-850.
196. Yen, H.-J.; Hsu, S.-h.; Tsai, C.-L. *Small* **2009,** 5, (13), 1553-1561.
197. Gupta, A. K.; Gupta, M. *Biomaterials* **2005,** 26, (13), 1565-1573.
198. Laurent, S.; Forge, D.; Port, M.; Roch, A.; Robic, C.; Vander Elst, L.; Muller, R. N. *Chem. Rev.* **2010,** 110, (4), 2574-2574.
199. Verma, A.; Stellacci, F. *Small* **2010,** 6, (1), 12-21.
200. Sneed, P. K.; Stauffer, P. R.; McDermott, M. W.; Diederich, C. J.; Lamborn, K. R.; Prados, M. D.; Chang, S.; Weaver, K. A.; Spry, L.; Malec, M. K.; Lamb, S. A.; Voss, B.;

Davis, R. L.; Wara, W. M.; Larson, D. A.; Phillips, T. L.; Gutin, P. H. *International Journal of Radiation Oncology*Biology*Physics* **1998,** 40, (2), 287-295.
201. Silva, A. C.; Oliveira, T. R.; Mamani, J. B.; Malheiros, S. M. F.; Malavolta, L.; Pavon, L. F.; Sibov, T. T.; Amaro, E.; Tannús, A.; Vidoto, E. L. G.; Martins, M. J.; Santos, R. S.; Gamarra, L. F. *International Journal of Nanomedicine* **2011,** 6, 591-603.
202. Guduric-Fuchs, J.; Ringland, L. J.; Gu, P.; Dellett, M.; Archer, D. B.; Cogliati, T. *Mol. Vis.* **2009,** 15, 1915-1928.
203. Sandvig, A.; Sandvig, I.; Berry, M.; Olsen, Ø.; Pedersen, T. B.; Brekken, C.; Thuen, M. *J. Magn. Reson. Imaging* **2011,** 34, (3), 670-675.
204. Zhou, R.; Caspi, R. R. *F1000 Biol. Rep.* **2010,** 2, (1).
205. Cramer, A. O.; MacLaren, R. E. *Curr. Gene Ther.* **2013,** 13, (2), 139-151.
206. Thuen, M.; Singstad, T. E.; Pedersen, T. B.; Haraldseth, O.; Berry, M.; Sandvig, A.; Brekken, C. *J. Magn. Reson. Imaging* **2005,** 22, (4), 492-500.
207. Kabb, C. P.; Carmean, R. N.; Sumerlin, B. S. *Chemical Science* **2015,** 6, (10), 5662-5669.
208. O'Neal, D. P.; Hirsch, L. R.; Halas, N. J.; Payne, J. D.; West, J. L. *Cancer Lett.* **2004,** 209, (2), 171-176.
209. Visaria, R. K.; Griffin, R. J.; Williams, B. W.; Ebbini, E. S.; Paciotti, G. F.; Song, C. W.; Bischof, J. C. *Mol. Cancer Ther.* **2006,** 5, (4), 1014-1020.

# APPENDED PAPERS

# Contributions

**Paper I**

Dr. Sondre Volden and I contributed equally to this paper. Most of the characterization of the Tf-AuNCs was done prior to my involvement. Characterization included: CD, TCSPC, Steady-state fluorescence spectroscopy, AFM, Langmuir, STEM, and UV. My main responsibility was to perform the cell experiments, and prepare fresh Tf-AuNCs for these studies, as well as finalize the manuscript for submission.

**Paper II**

I did all experimental work in this paper, except HR TEM, TEM, and XRD which was performed by Dr. Gurvinder Singh. XPS was performed by Sulalit Bandyopadhyay, while ICP-MS was performed at the Dept. of Chemistry. Dr. Eugene Kim performed the CT experiments. All samples characterized by others were synthesized by me. I was responsible for writing the manuscript.

**Paper III**

Sulalit Bandyopadhyay synthesized the different Au NS, and surface coated the Au NS prior to cell work. I was responsible for performing the cell work, as well as preparing cell pellets for ultramicrotome sectioning and TEM. TEM was performed by Nan E. Tostrup Skogaker at the Cellular and Molecular Imaging Core Facility. I was responsible for writing the second part of the paper which included *in vitro* work.

**Paper IV**

Dr. Gurvinder Singh and I are equal contributors to this paper. Gurvinder was responsible for synthesis of the different shaped IONPs. I prepared the IONPs for cell interaction studies, by coating the IONPs with PEG. I was responsible for the *in vitro* work, as well as discussing the results.

**Paper V**

Dr. Gurvinder Singh and I collaborated in synthesizing the initial batch of the MONPs. I found out experimentally that MONPS can be surface-coated with L-DOPA. I prepared all samples for characterization, *in vivo* and *ex vivo* work. I also synthesized and surface functionalized the IONPs, which was not included in the manuscript, but placed in supporting information. Time-resolved degradation characterization was mainly done by me, but in cooperation with Sulalit Bandyopadhyay. XPS was performed by Sulalit Bandyopadhyay. Magnetic characterization was performed by Dr. Davide Peddis. XRD, TEM, and HR TEM was performed by Dr. Singh. Dr. I. Sandvig planned and performed the intravitreal injections on all animals. Dr. Hak was responsible for MRI scanning, which included planning the study, optimizing the scanning sequence, and handling the animals. Dr. Hak also suggested the pig eyes as *ex vivo* models. I aided Dr. Hak and Dr. I. Sandvig with the practicalities. Augestad and I worked together in preparing the animals for scanning, MR scanning, and euthanasia. I was responsible for processing the MRI data as well as writing the manuscript.

# Paper I

**Self-assembly and characterization of transferrin–gold nanoconstructs and their interaction with bio-interfaces**

Nanoscale

PAPER

View Article Online
View Journal

Cite this: DOI: 10.1039/c5nr01284h

# Self-assembly and characterization of transferrin–gold nanoconstructs and their interaction with bio-interfaces

Birgitte H. McDonagh,*†[a] Sondre Volden,†[a] Sina M. Lystvet,[a] Gurvinder Singh,[b] Marit-Helen G. Ese,[c] Joseph A. Ryan,[d] Mikael Lindgren,[e] Axel Sandvig,[f,g] Ioanna Sandvig[g,h] and Wilhelm R. Glomm*[a,i]

Received 25th February 2015,
Accepted 29th March 2015

DOI: 10.1039/c5nr01284h

www.rsc.org/nanoscale

Transferrin (Tf) conjugated to gold nanoparticles and clusters combine the protein's site-specific receptor targeting capabilities with the optical properties imparted by the nano-sized gold. We have described two different synthesis protocols, one yielding fluorescent Tf-stabilized gold nanoclusters (AuNCs) and one yielding Tf-stabilized gold nanoparticles that exhibit localized surface plasmon resonance. We demonstrate that the synthetic route employed has a large influence both on the gold nanostructure formed, and also on the structural integrity of the protein. A slight protein unfolding allows stronger interaction with lipids, and was found to significantly perturb lipid monolayers. Interactions between the protein–gold nanostructures and three different cell types were also assessed, indicating that the enhanced membrane affinity may be attributed to intercellular membrane differences.

## Introduction

The optical properties of nanosized gold are size-dependent. The small gold nanoclusters (AuNCs) range from a few to tens of atoms and exhibit size-dependent molecular fluorescence. At 3 nm and above, the nanosized gold becomes plasmonic nanoparticles that absorb light in the visible region of the electromagnetic spectrum.[1,2] AuNCs and AuNPs can be synthesized *via* a biomineralized synthesis using proteins, resulting in AuNCs and AuNPs being stabilized in a protein template. This class of hybrid nanomaterials has potential applications in bioimaging,[3–8] targeted drug delivery[4,5,8] and sensing.[9–12]

Synthesis of protein–AuNC constructs is typically achieved *via* incubation of a protein solution with tetrachloroauric acid (TCAA) either in the presence of a reducing agent such as ascorbic acid[5,6,13,14] or sodium borohydride ($NaBH_4$),[15,16] or by utilizing the intrinsic redox potential of amino acid residues in the polypeptide chain such as tyrosine and histidine.[3,4,8–12,15,17] Irrespective of the synthesis procedure, growth of protein–AuNCs has been revealed to be protein-mediated as well as highly protein-dependent.[16,17]

While much emphasis has been placed on the properties and applications of the embedded metal nanoclusters, little has been reported on the effect of AuNC incorporation into the structure and properties of the protein scaffold. Recently, we have reported that functionalizing proteins with AuNCs results in tunable, protein-dependent changes in structure and function of the polypeptide scaffold.[16,17] Moreover, we have demonstrated that combining proteins and gold on the nanoscale might result in emergent properties (*i.e.*, properties not characteristic of either protein or gold) such as enhanced membrane-affecting properties[15,18,19] and even anticancer activity.[15]

Transferrin (Tf) is a multi-tasking iron-binding protein which has been much researched for active drug delivery due to its efficient site-specific targeting of receptors that are over-expressed on cancer cell surfaces.[20–22] See *e.g.* McCann[20] and references therein for a review of the clinical applications of Tf. The ability of Tf to successfully target its specific receptor

[a]*Ugelstad Laboratory, Department of Chemical Engineering, Norwegian University of Science and Technology (NTNU), 7491 Trondheim, Norway. E-mail: birgitte.h.mcdonagh@ntnu.no; Fax: +47-73 59 40 80; Tel: +47-73 55 03 25*
[b]*Department of Materials Science and Engineering, Norwegian University of Science and Technology (NTNU), N-7491 Trondheim, Norway*
[c]*SINTEF Energy Research, P.O. Box 4761 Sluppen, N-7465 Trondheim, Norway*
[d]*Department of Chemistry, Iona College, New Rochelle, New York, USA*
[e]*Department of Physics, Norwegian University of Science and Technology (NTNU), N-7491 Trondheim, Norway*
[f]*Division of Pharmacology and Clinical Neurosciences, Department of Neurosurgery, Umeå University, 901 87 Umeå, Sweden*
[g]*Department of Neuroscience, Faculty of Medicine, Norwegian University of Science and Technology (NTNU), N-7491, Trondheim, Norway*
[h]*John Van Geest Centre for Brain Repair, Department of Clinical Neurosciences, University of Cambridge, CB2 OPY Cambridge, UK*
[i]*Sector for Biotechnology and Nanomedicine, SINTEF Materials and Chemistry, Trondheim, Norway*
†These authors contributed equally to this work.

has been observed while it is conjugated to drug carrier systems such as quantum dots,[23] liposomes[24] and gold nanoparticles.[25] Recently, Schneider and coworkers reported that Tf-stabilized AuNCs display similar targeting and cellular uptake characteristics as the native protein. Here, we have used iron-free transferrin as a scaffold for AuNC synthesis *via* two synthetic routes; one relying solely on the reduction potential of the protein, and one wherein an extrinsic reducing agent ($NaBH_4$) was added (these protocols are hereafter referred to as intrinsic and extrinsic, respectively). For the Tf–AuNC constructs presented here, we have characterized the photophysical properties, the effect on the Tf structure, how the incorporation of AuNCs results in enhanced membrane-affecting properties compared to the native protein, and the concomitant effect on cell membrane interaction.

## Materials and methods

### Preparation of Tf–AuNCs

**Intrinsic protocol.** Apo-transferrin (Sigma) was dissolved in MQ-water to obtain a total concentration of 10 mg $mL^{-1}$. Tf–AuNCs were prepared by adding 1 : 1 (v/v) of tetrachloroauric acid (5 mM, TCAA, Sigma) before adjusting the pH to above 10 (250 μL, 1 M NaOH). As a reference, Tf (10 mg $mL^{-1}$) was mixed 1 : 1 (v/v) with MQ-water and the pH adjusted as described. The samples were left to react for one week at 37 °C. In order to remove excess TCAA, the samples were dialysed against deionized (MilliQ) water for two hours, before water exchange and dialysis overnight. The samples prepared for cell viability studies were dialysed as described, but against phosphate buffer (pH = 7.4). The samples prepared using the intrinsic protocol are named *Tf–AuINT*. The phosphate buffer was prepared by mixing dipotassium hydrogen phosphate ($K_2HPO_4$, 50 mM, Merck) and potassium dihydrogen phosphate ($KH_2PO_4$, 50 mM, Merck) to a final pH of 7.4.[15]

**Extrinsic protocol.** Samples were prepared and dialysed as described for the intrinsic protocol, but in addition, an extrinsic reducing agent ($NaBH_4$, 200 μL, 1 M) was added immediately after TCAA. The same Tf stock solution as described for the intrinsic protocol was used. The reference was prepared as for the intrinsic protocol, except that 200 μL $NaBH_4$ (1 M) was added. This sample was named *Tf-RED*. Two different concentrations of TCAA were used in order to form AuNCs and AuNPs. For Tf–AuNCs, a low concentration of TCAA (1 mM) was added 1 : 1 (v/v) to the Tf-stock solution before adding 200 μL $NaBH_4$. These samples were named *Tf–AuXL*. For extrinsic synthesis of Tf–AuNPs, the same concentration of TCAA as Tf–AuINT was used (5 mM), with the addition of 200 μL $NaBH_4$ (1 M). These samples were named *Tf–AuXH*.

**Scanning transmisison electron microscopy (STEM).** A Hitachi S-5500 electron microscope operating at 30 kV accelerating voltage was used to record TEM images. Prior to TEM imaging, samples were prepared by placing a few microliters of Tf–AuNC solution on a TEM grid, before drying and imaging.

High resolution transmission electron microscopy (HR-TEM) images were acquired on a JEOL JEM-2100 (200 kV). The samples were prepared by depositing a few μl drops of nanoparticle or nanocluster solution on a copper grid coated with an amorphous carbon layer, and allowed to dry prior to imaging.

**UV-visible spectroscopy.** UV-visible spectroscopy was performed on a Shimadzu UV-2401PC spectrophotometer using UV probe 2.10 software. The Tf-concentration was 10 μM.

**Steady-state fluorescence spectroscopy.** Steady-state fluorescence was measured on a Fluorolog-3 HORIBA Jobin Yvon apparatus, using excitation wavelengths $\lambda_{ex}$ = 295 and 370 nm. The Tf concentration was 3.6 μM, and all samples were measured in triplicate.

**Time correlated single photon counting (TCSPC).** For TCSPC, an IBH TCSPC spectrometer was employed. The prompt was recorded by setting the emission monochromator at the same wavelength as the light source ($\lambda_{em}$ = 280 nm). For the lifetime measurement of the samples, the emission monochromator was set to $\lambda_{em}$ = 360 nm, with a bandpass of 8 nm for both prompt and samples.

**Circular dichroism (CD).** Circular dichroism (CD) was measured on an Olis DSM 1000CD apparatus, equipped with a lamp power supply LPS-220B from Photon Technology International. The user interface was an Olis online instrument system, and the software was OLIS GlobalWorks. For CD measurements, the scan range was set from 290 to 200 nm, with 720 increments. The Tf concentration was 2.3 μM, and the cuvette path length was 10 mm. The grid was 2400 lines per mm, and the slit width was 6.32 mm. Each sample was scanned three times, using the phosphate buffer as blank.

**Langmuir film experiments.** A KSV Langmuir Minitrough double barrier system (KSV LTD, Finland) was used and the experiments were controlled through the manufacturer's own software. The Langmuir was equipped with a Teflon trough (250 mL) and Delrin barriers. The surface pressure probe was made of paper (pre-soaked in buffer media). Prior to all of the experiments, any surface impurities were removed with a Pasteur pipette connected to a vacuum pump. The AuNC samples prepared using the extrinsic protocol were not stable in aqueous solutions and were determined to be unfit for Langmuir film experiments. However, samples of Tf and Tf–AuINT (1 mL, 12.5 μM) had greater stability in solution and were found suitable for Langmuir film experiments. The interfacial activity of the air/buffer surface for each Tf–gold construct was studied by filling the trough (250 mL) with phosphate buffer, closing the barriers to 90 mm, and zeroing the balance. The sample was then injected underneath the lipid surface, from outside of the barriers using a syringe with a ~90° needle.[26] The barriers were kept in a constant position, and the surface pressure was recorded over time. For lipid interaction studies, PBPS (60 μL, 0.25 mg $mL^{-1}$ dissolved in $CHCl_3$) was compressed with a barrier speed 5 mm $min^{-1}$ until it reached a surface pressure of 10 mN $m^{-1}$. The system was set to have a constant surface pressure of 10 mN $m^{-1}$ before Tf or Tf–AuINT was injected as described above. The required surface area was then measured as a function of time.

 

**Langmuir–Schaefer deposition.** Gold-covered glass plates were prepared for film deposition by immersion in Piranha solution ($H_2SO_4$–$H_2O_2$, 3 : 1)[27] for 20 minutes before flushing with deionized (MilliQ) water and drying with pressured air. The Tf and Tf–AuINT samples (1 mL, 12.5 μM) were injected as described above, under a lipid film of PBPS. The protein–lipid mixture was left to equilibrate for one hour before the Langmuir–Schaefer deposition was made. The gold-sputtered glass plate was introduced horizontally towards the lipid/air surface, using a vacuum pump to hold the plate. The gold-covered plate was kept at the surface for 30 seconds before it was lifted up again. The adsorbed layer was then dried in air, and imaged with AFM.

**Atomic force microscopy (AFM).** ScanAsyst mode AFM images were acquired by multimode atomic force microscopy (Nanoscope V controller) and digital instruments at room temperature. AFM tips with a spring constant ~0.4 N $m^{-1}$ were purchased from Bruker AFM probes. Samples were prepared as described by the Langmuir–Schaefer deposition method.

**Cell viability studies.** Low passage rat olfactory ensheathing cells (OECs, $P$ = 6), human glioblastoma–astrocytoma cells (U-87 MG, $P$ > 8) and ovarian cancer cells (OCCs, TOV112D) were expanded in six well plates (Costar® 3335, Corning CellBIND® surface, Corning Inc., NY, USA) at 37 °C, with 7% and 5% $CO_2$, respectively, until 70% confluence.

**OEC culture.** OECs purified from neonatal Fischer rats at P7, were seeded on poly-L-lysine-treated multi-well plates (Costar® 3335, Corning CellBIND® surface, Corning Inc., NY, USA) at a density of 1 × $10^4$ cells $cm^{-2}$. The cultures were fed with Dulbecco's modified Eagle's medium (DMEM) GlutaMAX® (Sigma) with 1.25% gentamicin (Sigma) and 5% fetal bovine serum (Autogen Bioclear, Wiltshire, UK) supplemented with 41.6% SATO, 2.7% fibroblast growth factor (FGF, Peprotech), 0.27% heregulin (hrgβ1, R&D Systems Europe Ltd, Abingdon, UK) and 0.05% forskolin (Sigma).

**Glioblastoma–astrocytoma culture.** Human glioblastoma–astrocytoma cells (U-87 MG, ECACC, Salisbury, UK) were cultured in Eagle's minimal essential medium (EMEM) with 1.25% gentamicin (Sigma) and 10% fetal bovine serum (Autogen Bioclear, Wiltshire, UK). The cultures were supplemented with 2 mM L-glutamine, 1% non-essential amino acids (NEAA, Sigma), and 1 mM sodium pyruvate (NaP, Sigma).

**OCC culture.** Human ovarian cancer cells (OCCs, CRL-11731, ATCC, USA) were cultured in a 1 : 1 (v/v) solution of Medium 199 (Invitrogen) and Medium 105 (Invitrogen) with 15% fetal bovine serum (Autogen Bioclear, Wiltshire, UK).

**Cell labeling with Tf–AuNCs and Tf.** Cells at 70% confluency were labeled with Tf and Tf–AuINT at concentrations of nanoparticles/media volume of 1 μg $mL^{-1}$, 100 μg $mL^{-1}$ and 1 mg $mL^{-1}$, and incubated at 37 °C for 4 hours. Unlabeled OEC, OCC and glioblastoma–astrocytoma cultures, at the same stage of confluence, were used as controls.

**LIVE/DEAD® assay.** A LIVE/DEAD-cell viability assay (Invitrogen, Life Technologies) evaluates the membrane integrity of cells, and consists of two different dyes: calcein AM (excitation/emission: 494/517 nm) and ethidium homodimer-1 (excitation/emission: 517/617 nm). In live cells, intracellular esterases react with calcein AM and yield a cytoplasmic green fluorescence. Ethidium homodimer-1 (EthD-1) diffuses over damaged cell membranes of dead cells, where it binds to nucleic acids and emits red fluorescence. After labeling with Tf–AuINT and Tf, LIVE/DEAD-cell viability was performed on OECs, glioblastoma–astrocytoma cells and OCCs as described by the manufacturer, with one exception. Instead of adding both dyes in one solution, two separate solutions of EthD-1 (12 μL EthD-1) in PBS (Sigma, 4.5 mL), and calcein (2.7 μL) in PBS (Sigma, 4.5 mL) were prepared for visualization of dead and live cells, respectively. The reason for this was based on the observations of spectral interactions between the fluorescent dyes and the Tf–AuNCs. Three parallels of each cell culture were assayed with either calcein or EthD-1 solutions in 1 : 1 (v/v), and left to react for 30 min at 37 °C before imaging. Imaging of the LIVE/DEAD-cell viability assay was performed on an Axiovert 200M fluorescence microscope (Zeiss, Germany), at 40× or 10× magnification, using AxioVision Rel. 4.3 software. Images were later processed with ImageJ 1.46.

## Results and discussion

The results are grouped into the following categories: photophysical properties of the Tf–AuNC constructs, the effect of incorporation of AuNCs on the Tf structure, interaction with lipid monolayers, and cellular interaction studies.

### Photophysical properties of the Tf–AuNC constructs

Synthesis of protein-stabilized gold can yield several gold species that coexist in or around the protein backbone. In samples where only AuNCs are present, the AuNCs can be detected with fluorescence spectroscopy. When the availability of gold precursors is high or when an extrinsic reducing agent is added, growth of larger AuNPs can occur wherein AuNC-stabilized proteins self-assemble around gold nanoparticles exhibiting localized surface plasmon resonance (LSPR).[16] When AuNPs and AuNCs are in close proximity, the AuNPs can quench the fluorescence emitted from AuNCs.[28]

Thus, in a sample with predominantly AuNPs, fluorescence emission of AuNCs is quenched, while the UV-visible absorbance of plasmonic AuNPs increase.

UV-visible spectra of the different Tf–AuNCs studied here, as well as the reference systems (Tf only and Tf treated with $NaBH_4$), are shown in Fig. 1a. While the spectral line shape was found to vary both with respect to the synthetic route and concentration of TCAA, all the Tf-stabilized nano gold systems displayed a broad absorption band from ~450 to 600 nm, compared to the protein alone. This is an indication of multimeric gold species.[15–17] While the LSPR feature is prominent in the Tf–AuXH system, the band observed for Tf–AuINT has lower absorbance and occurs at shorter wavelengths, indicating smaller AuNPs. The larger AuNPs synthesized *via* the extrinsic route is thus most likely a result of the added extrinsic reducing agent ($NaBH_4$).

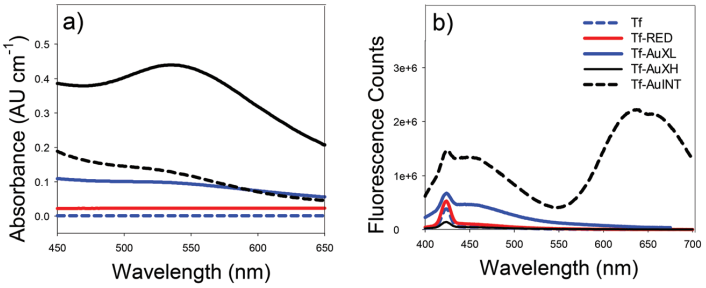


**Fig. 1** (a) UV-Visible spectra showing LSPR for AuNPs synthesized with a high (Tf–AuXH) and low concentration of TCAA (Tf–AuXL) and AuNPs synthesized *via* the intrinsic protocol (Tf–AuINT). All samples were compared to the pure protein (Tf) and Tf with added $NaBH_4$ (Tf-RED). (b) Tf–AuNC emission was measured with excitation $\lambda_{ex}$ = 370 nm.

The fluorescence profile of protein-templated AuNCs upon excitation at ~370 nm is typically assigned to contributions from gold nanoclusters containing 8 atoms ($Au_8$, $\lambda_{em}$ ~ 450 nm) and gold nanoclusters with 25 atoms ($Au_{25}$, $\lambda_{em}$ ~ 650 nm).[3,5,7,9,11,13] In order not to overstate the accuracy of our obtained results, we have opted to classify the AuNCs as either "small" (~$Au_8$, $\lambda_{em}$ ~ 450 nm) or "large" ($Au_{25+}$, $\lambda_{em}$ ≥ 600 nm).[15–17] Steady-state emission spectra of the Tf–AuNCs upon excitation at 370 nm are shown in Fig. 1b. Emission spectra from Tf and Tf treated with $NaBH_4$ (Tf-RED) are shown as references. From the emission spectra shown in Fig. 1b, the fluorescence line shape of the Tf–AuNCs varies both with respect to the synthetic route and the concentration of TCAA added. The Tf–AuNCs obtained using the extrinsic synthesis route (Tf–AuXL and Tf–AuXH) and the lowest concentration of TCAA (Tf–AuXL) resulted in modest fluorescence emission at ~450 nm, indicating the presence of small AuNCs ($Au_8$), whereas no fluorescence at this wavelength could be detected for the higher TCAA concentration (Tf–AuXH). From the spectra acquired for Tf–AuXL, the concentration of gold precursors (TCAA) will have an effect on the size of the AuNCs. We attribute the absence of emission at 450 nm for Tf–AuXH to efficient quenching from AuNPs that are in close proximity to the AuNCs (see Fig. 1a for the UV-visible spectrum of the potential energy acceptor). Synthesis of Tf–AuNCs *via* the intrinsic synthesis route resulted in Tf–AuNCs with vastly improved fluorescence intensity, as seen from the Tf–AuINT spectrum in Fig. 1b. In addition to the contribution from small AuNC emission at ~450 nm, the fluorescence of the Tf–AuINT is dominated by emission above 600 nm. The exact determination of the number of gold atoms associated with each emitting protein-embedded AuNCs population is very complex, and the emission attributed to the larger AuNCs often comprises at least two contributions. This can be observed from the bimodal peak at 650 nm in Fig. 1b (Table 1).

Because of the complex interactions between fluorescent AuNCs and colloidal gold, HRTEM can be used as complementary to UV-visible and steady-state fluorescence spectroscopy. Indeed, for the intrinsic protocol (Tf–AuINT, Fig. 2a, b) both AuNPs and AuNCs were found. A larger population of AuNPs was found for Tf–AuXH, while no AuNPs were found for Tf–AuXL. The only difference between Tf–AuINT and Tf–AuXH is the addition of $NaBH_4$ in the latter. From UV-visible, steady-

**Table 1** Overview of excitation and emission wavelengths used in steady-state fluorescence spectroscopy and TCSPC

| Excitation ($\lambda_{ex}$) | Emission ($\lambda_{em}$) | Species |
|---|---|---|
| $\lambda_{ex}$ = 370 nm | $\lambda_{em}$ = 450 nm | AuNCs($Au_8$) |
| $\lambda_{ex}$ = 370 nm | $\lambda_{em}$ = 650 nm | AuNCs($Au_{25+}$) |
| $\lambda_{ex}$ = 295 nm | $\lambda_{em}$ = 350 nm | Tryptophan in Tf |
| $\lambda_{ex}$ = 278 nm | $\lambda_{em}$ = 350 nm | Tryptophan and tyrosine in Tf |

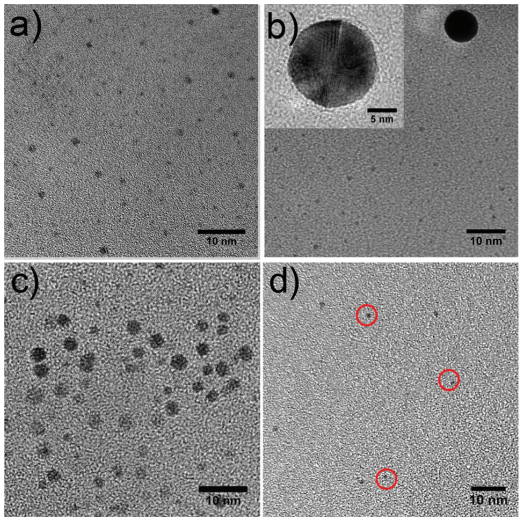


**Fig. 2** (a) HR-TEM image of AuNCs prepared *via* the Intrinsic protocol (Tf-AuINT). (b) Co-existance of AuNPs and AuNCs synthesized *via* the intrinsic protocol (Tf-AuINT). The inset show a Tf-stabilized AuNP synthesized from the Tf only. Image (c) show HRTEM images of AuNCs and AuNPs synthesized *via* the extrinsic protocol, with high (Tf-AuXH) and (d) low (Tf-AuXL) amount of TCAA added. The red circles indicate AuNCs.

 

state fluorescence spectra and HRTEM images, the addition of $NaBH_4$ clearly increases the amount of AuNPs in the sample. Although AuNPs are also present in the intrinsic samples, it is ultimately the concentration of AuNPs that will determine the amount of AuNC quenching. Tf–AuINT has a dominant near-infrared (NIR) fluorescence together with weak LSPR (Fig. 1a), indicating that the concentration of AuNPs is less compared to Tf–AuXH.

In order to further investigate the photophysical properties of the Tf-stabilized AuNCs, time-correlated fluorescence data were collected at $\lambda_{em}$ = 650 nm using time-resolved single photon counting (TCSPC) spectroscopy with an excitation wavelength of $\lambda_{ex}$ = 373 nm. The steady-state emission (Fig. 1b) of Tf–AuXL is very low at 450 nm and is completely absent for Tf–AuXH. Because of this, no lifetimes could be obtained for these samples. However, time-resolved fluorescence data for Tf–AuINT ($\lambda_{em}$ = 650 nm) were collected, and fitted with a biphasic decay.

The fractional contribution of each decay time to the steady-state intensity, $f$, can be determined from the decay times, $\tau$, and $\alpha$ which is the relative population of the components at $t$ = 0, and is shown in eqn (1).[28]

$$f_i = \frac{\alpha_i \tau_i}{\sum_j \alpha_j \tau_j} \quad (1)$$

All the Tf systems studied here were best fit by biphasic decay, yielding one short ($\tau_1$) and one long ($\tau_2$) lifetime and their relative populations $\alpha_1$ and $\alpha_2$.[28] Lifetimes of 0.49 ns and 1.78 ns, with corresponding populations 33.7% and 66.3% were determined for Tf–AuINT. Peak broadening and bimodal fluorescence at ~650 nm with steady-state fluorescence emission (Fig. 1b) combined with two observable lifetimes at 650 nm, could reveal the presence of at least two different-sized AuNCs.

### The effect of AuNC formation on the transferrin structure

Tryptophan (Trp) emission is a well-documented spectroscopic method for studying conformational changes such as partial unfolding in proteins.[28] Unfolding changes the local environment of Trp residues, and depending on the number and location of the Trp residues, this might lead to changes in the fluorescence line shape, with respect to both emission maximum and intensity. While changes in fluorescence intensity alone can be difficult to interpret, shifts in the emission maximum towards longer wavelengths are generally linked to protein unfolding.[15–19,28] Trp emission spectra ($\lambda_{ex}$ = 295 nm) of the systems studied here are shown in Fig. 3a. For the Tf–AuNCs synthesized by the extrinsic route, it is apparent that $NaBH_4$ affects the local environment of Trp residues, leading to a reduction of Trp emission intensity compared to that of the native protein. While the exact effect of $NaBH_4$ on Tf conformation cannot be elucidated from the Trp fluorescence alone, the spectra in Fig. 3a reveal that the synthesis of Tf–AuNCs *via* the extrinsic protocol employed here leads to changes in Trp emission not attributable to the reducing agent alone, but is strongly dependent on TCAA concentration. Specifically, a low concentration of TCAA resulted in a red-shift as well as a severe attenuation of Trp fluorescence (Tf–AuXL). Increasing the TCAA concentration while at the same time adding $NaBH_4$ resulted in complete quenching of Trp emission (Tf–AuXH). Within this sample, large AuNPs were formed, which implies that the larger the gold species, the greater the change in protein conformation.

Using a biomineralization-inspired synthesis protocol (no $NaBH_4$, Tf–AuINT) a red-shift and broadening of the fluorescence line shape and an overall attenuation of the signal was observed. Although not as severe as was found for Tf–AuXL, the partial unfolding of the polypeptide chain is attributed to incorporation of large AuNCs.

The effect of AuNC formation on the Trp environment was also studied using TCSPC with $\lambda_{ex}$ = 278 nm, the results are summarized in Table 2. As for Tf–AuINT, the time-resolved fluorescence data were best fit with biphasic decay (eqn (1)). In addition, the average lifetime, $\bar{\tau}$, was calculated as shown in eqn (2):[28]

$$\bar{\tau} = \frac{\alpha_1 {\tau_1}^2 + \alpha_2 {\tau_2}^2}{\alpha_1 \tau_1 + \alpha_2 \tau_2} = f_1 \tau_1 + f_2 \tau_2 \quad (2)$$

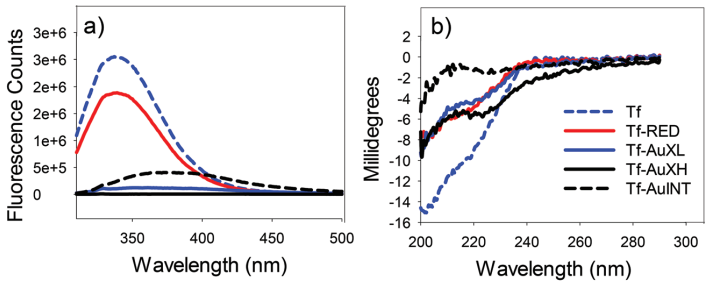


Fig. 3 (a) Trp emission of native Tf has the highest fluorescence intensity at 350 nm when excited at $\lambda_{ex}$ = 295 nm compared to Tf with $NaBH_4$ (Tf-RED), Tf–AuNCs prepared with no (Tf–AuINT), high (Tf–AuXH) and low (Tf–AuXL) concentration of TCAA. When a high concentration of TCAA is used, the Trp emission is almost completely quenched (Tf–AuXL). (b) CD traces indicate structural changes in the protein backbone as the line shape changes when compared to the native protein (Tf), both with respect to $NaBH_4$ and TCAA.

**Table 2** TCSPC data for Tf, Tf-RED and Tf–AuNC emission ($\lambda_{ex}$ = 278 nm, $\lambda_{em}$ = 360 nm) and CD data. Tf refers to pure transferrin, while Tf-RED is Tf with added $NaBH_4$. Tf–AuXL was prepared by adding a low concentration of TCAA (extrinsic protocol), while Tf–AuINT was synthesized *via* the intrinsic protocol. $\tau_1$ and $\tau_2$ is the short and long lifetime, respectively, while $\alpha_1$ and $\alpha_2$ is the corresponding population. $\bar{\tau}$ is the average lifetime calculated from the relative populations and their respective lifetimes. The CD measurement is a ratio of the mean residual ellipticity at 200 and 222 nm

| TCSPC ($\lambda_{ex}$ = 278 nm, $\lambda_{em}$ = 360 nm) | | | | | | CD |
|---|---|---|---|---|---|---|
| | $\tau_1$ (ns) | $\tau_2$ (ns) | $\alpha_1$ (%) | $\alpha_2$ (%) | $\bar{\tau}$ (ns) | $I_{200}/I_{222}$ |
| Tf | 1.45 | 3.52 | 55 | 45 | 2.8 | 1.7 |
| Tf-Red | 1.47 | 3.62 | 56 | 44 | 2.9 | 1.8 |
| Tf–AuXL | 0.64 | 3.11 | 54 | 46 | 2.6 | 2.7 |
| Tf–AuINT | 1.06 | 4.03 | 36 | 64 | 3.6 | 4.0 |

It should be noted that by using an excitation wavelength of 278 nm, the collected signal also contains minor contributions from other aromatic amino acid residues such as tyrosine in addition to Trp fluorescence.[28] From the results shown in Table 2, neither the lifetimes nor the associated populations are significantly affected by the addition of $NaBH_4$. No lifetimes could be obtained for the Tf–AuXH sample, which is in agreement with the complete quenching observed from steady-state fluorescence (Fig. 3a). For the Tf–AuXL system, there is a minor decrease in the average lifetime compared to the native protein. This is attributed to a decrease in Trp lifetimes, in particular $\tau_1$, whereas the associated populations remain relatively unchanged. We attribute this to quenching from increased solvent exposure due to partial unfolding, energy transfer (FRET) to the embedded AuNCs, or a combination of these effects.[15,16] The biggest change in the average lifetime was calculated for Tf–AuINT. This indicates larger changes in the local environment of Trp compared to native Tf.

Specifically, both population and lifetime of $\tau_2$ increases relative to Tf only, whereas the opposite is seen for $\tau_1$. The complex structure of the Tf–AuINT system with AuNCs of different sizes in each protein, with multiple proteins assembled around a central AuNP core (9.42 ± 0.16 nm), makes the interpretation of the TCSPC results with respect to the effect on the protein structure qualitative at best.

In order to better elucidate the effect of AuNC incorporation on the protein structure, circular dichroism (CD) measurements were performed on the systems studied here. The CD spectra shown in Fig. 3b reveal that the Tf secondary structure is significantly affected by incorporation of AuNCs and by the reducing agent used in the extrinsic protocol. These findings are consistent with what we have reported earlier.[15,16] In order to ascertain that the observed changes in CD profiles did not emanate from signal attenuation, scattering contribution or reduction in protein concentration due to aggregation and subsequent precipitation, changes in the CD line shape were estimated *via* the ratio of mean residual ellipticity at 200 nm and 222 nm ($I_{200}/I_{222}$, Table 2). A reduction of protein concentration or signal attenuation due to scattering from gold species is expected to result in a signal reduction without affecting the line shape. However, since the line shape varies between the species studied here as shown in Table 2, it is likely that the changes in the CD profile compared to Tf only are due to structural changes in the protein, which is also in agreement with steady-state and time-resolved Trp fluorescence results.

### Interaction with lipid monolayers

We have previously demonstrated that modification of proteins with gold nanoparticles and clusters can significantly alter lipid interaction compared to the native protein.[15,18,19]

The change in surface pressure upon injecting Tf and Tf–AuINT under an air/water interface (phosphate buffer, pH 7.4) is shown in Fig. 4a. The AuNC samples prepared using the extrinsic protocol were not found to be sufficiently stable for the Langmuir experiments. Consequently, only Tf and Tf–AuINT results are shown here. Injecting Tf only into the PBPS lipid layer did not yield any measurable changes in the surface pressure even after an hour, indicating that the native protein has negligible surface activity under these conditions. On the other hand, the injection of Tf–AuINT resulted in a rapid and significant surface pressure increase, revealing that modifi-

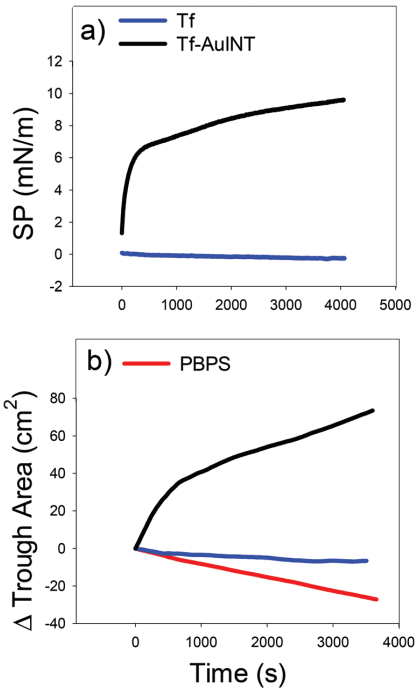


**Fig. 4** (a) Surface pressure as a function of time shows that compared to the native protein (Tf), the Tf–AuNCs prepared *via* the intrinsic protocol (AuINT) is surface active. (b) The delta surface area as a function of time indicates that Tf–AuINT has a higher surface activity compared to the pure lipid (PBPS) and the native protein (Tf).

 

cations with AuNCs result in increased surface activity of the protein. This is likely due to the increased exposure of hydrophobic residues in the protein following AuNC formation, which is in agreement with fluorescence and CD results presented above, as well as earlier studies.[15–19]

The average changes in the trough area upon injection of Tf and Tf–AuINT under a precompressed phospholipid film are shown in Fig. 4b. The lipid used here, porcine phosphatidylserine (PBPS), is negatively charged and is partly dissolved (~20%) during the experimental time frame used here (60 minutes at 10 mN $m^{-1}$). Thus, the traces shown in Fig. 4b are corrected for phospholipid drift by normalizing with respect to time-dependent surface area behavior of PBPS only. While using the injection method to investigate protein–lipid interactions in a Langmuir trough, the reproducibility is strongly dependent on the injection rate as well as the injection depth, *i.e.* the distance between the tip of the needle and the lipid monolayer.[29] In particular, the experiment must be discarded if the needle penetrates the lipid film, or if air bubbles are injected into the subphase and are disturbing the monolayer. Despite the systematic uncertainties introduced by the injection method, the injection of Tf under a lipid film results in a slight loss of surface area, indicating loss of film material compared to PBPS only. Conversely, the injection of Tf–AuINT results in a significant surface area increase, indicating a larger amount of film material at the air–water surface compared to PBPS only. We attribute the increased surface area upon injection of Tf–AuINT to intercalation into the lipid monolayer due to the increased surface activity of the protein–AuNCs construct, as has been reported for similar constructs based on alpha-lactalbumin interacting with PBPS.[15]

As Tf only did not reveal any measurable surface activity, the apparent loss of film material when injecting Tf under the PBPS monolayer is likely due to bulk interactions between Tf and dissolved lipids. Binding of PBPS molecules to Tf shifts the equilibrium between monolayer-bound and dissolved lipids, leading to further loss of film material.

Atomic force microscopy was further employed to visualize morphological changes in the lipid film upon introduction of Tf and Tf–AuINT. Fig. 5a shows a monolayer of pure anionic PBPS lipid uniformly deposited onto the gold surface *via* the Langmuir–Schaefer method in contrast to the bare gold sputtered surface as shown in Fig. 5b, confirming the monolayer deposition of lipid molecules. The lipid film is made from the assembly of small regions with an average height and width ~1.7 nm and ~16 nm respectively, as displayed in Fig. 5c and d. Inserting Tf and Tf–AuINT underneath the lipid film held at 10 mN $m^{-1}$ causes a perturbation in the film where the lipid regions severely collapse (Fig. 5e, f). AFM results reveal a large extent of disruption in the case of Tf–AuINT, with no discernible packing of lipid regions and only the collapsed film with gold nanoclusters having a wide size distribution. Therefore, Tf–AuINT has a high propensity to intercalate into the negatively charged lipid film as compared to Tf only. This is also in agreement with a recent study of alpha-lactalbumin protected gold nanoclusters.[15]

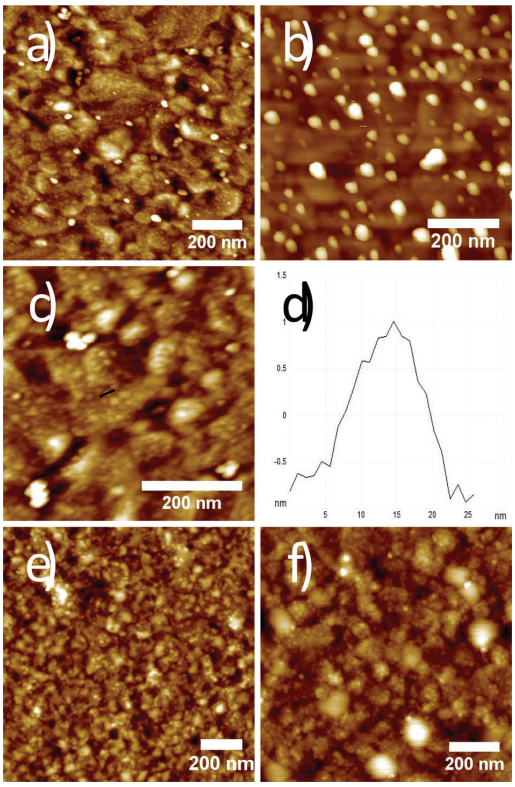


Fig. 5 AFM topographical images of lipid films deposited by the Langmuir–Schaefer method at 10 mN $m^{-1}$ onto gold sputtered glass substrates. (a) Pure PBPS lipid film showing uniform deposition. (b) Gold sputtered surface prior to lipid deposition. (c) High resolution view of lipid film and (d) section analysis of lipid regions. (e) Disruption in the PBPS lipid film caused by insertion of Tf protein and (f) Tf protein modified gold nanocluster.

## Cell viability studies

Three different cell types were chosen to assess the interaction with Tf–AuINT. Two human cancerous cell lines, ovarian cancer cells (OCCs) and brain cancer cells (glioblastoma–astrocytoma cells), and non-cancerous cells (olfactory ensheating cells, OECs) were incubated with three different concentrations of Tf and Tf–AuINT and the viability was assessed with a LIVE/DEAD assay. For all cell types, there was no increased cell death after incubation with Tf–AuINT or Tf, compared to the blank. One of the dyes in the LIVE/DEAD assay, ethidium homodimer, chelates with DNA and emits red light when excited at 430 nm. The dye can only move through compromised cell membranes, and will therefore stain dead cells red. A typical dead cell is shown in Fig. 6e. Live cells express calcein AM ($\lambda_{ex}$ = 495, $\lambda_{em}$ = 515), as they have esterases that cleave calcein AM to a green fluorescent molecule. Live cells therefore typically have an even intracellular distribution of

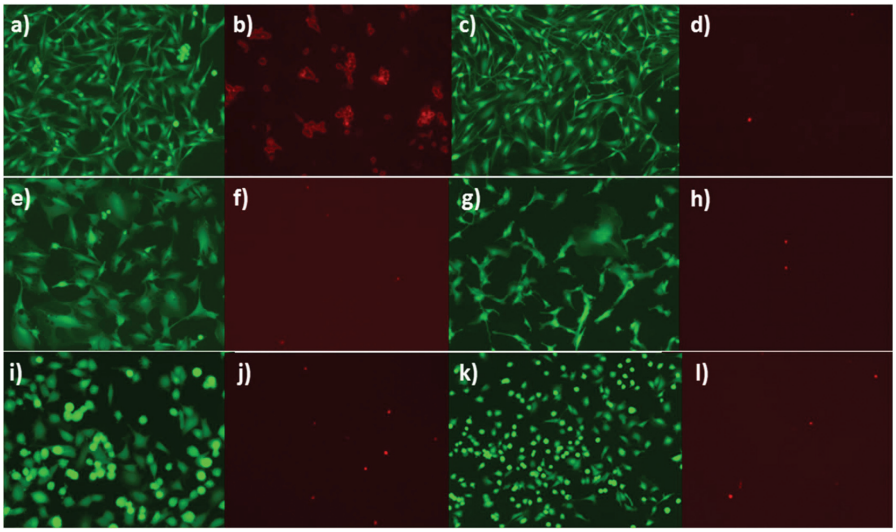


**Fig. 6** Colocalization of dyes at the membranes of OECs. All cells were incubated for four hours with different concentrations of Tf (1 μg $mL^{-1}$, 100 μg $mL^{-1}$ and 1 mg $mL^{-1}$) and Tf–AuINT (1 μg $mL^{-1}$, 100 μg $mL^{-1}$ and 1 mg $mL^{-1}$) before staining with the LIVE/DEAD assay. (a) Live and (b) dead OECs with 1 μg per mL Tf–AuINT, control (c) live and (d) dead OECs. Glioblastoma cells are imaged from (e)–(h), with (e) and (f) displaying cells after incubation of 1 mg per mL Tf–AuINT, and (g) and (h) show the control. Images (i)–(l) show (i) live and (j) dead OCCs after incubation of 1 mg per mL Tf–AuINT, and the control (k) live and (l) dead cells.

green fluorescent dye, as can be seen in Fig. 6f. However, for the OEC cell culture, incubation with Tf–AuINT results in partial colocalization of the calcein and EthD1-derived fluorescence. This might indicate that Tf–AuINT is associated with the cell membrane, blocking the entry of ethidium homodimer and calcein, or that there is some photophysical interaction between the Tf–AuINT and the dyes. If the latter were to be the case though, similar observations should have also been made for the glioblastoma–astrocytoma cells as well as for the OCCs. In the absence of such evidence, and given that Tf–AuINT showed a strong tendency towards the monolayer surface (Fig. 4), we attribute the colocalisation of the dyes to an enhanced Tf–AuINT affinity with the OEC membrane (Fig. 6b). However, unlike OECs, glioblastoma–astrocytoma cells and OCCs did not exhibit colocalisation of calcein with EthD-1 after incubation with Tf–AuINT (Fig. 6e, f and i–j). Assuming that colocalisation of the dyes may indeed be attributed to enhanced Tf–AuINT affinity towards the cell membrane, the different interactions of the Tf–AuINT with the different cell types may be attributed to intercellular membrane differences between glioblastoma and astrocytoma,[30,31] as well as OCC-cells and OECs.

## Conclusions

We have synthesized Tf-stabilized gold nanostructures using two synthesis routes – with and without the aid of an extrinsic reducing agent ($NaBH_4$). From our results, we can conclude that the amount of AuNPs synthesized strongly depends on whether or not $NaBH_4$ is added, and that the concentration of TCAA is important (Tf–AuXL). Not just the size of the AuNCs and AuNPs seems to be affected by the TCAA concentration and reducing agent, but also the solution stability of Tf–Au constructs appear to be affected. There is a delicate balance between the reducing agent aiding nanostructure formation and causing irreversible unfolding of the polypeptide chain. However, it seems as though a slight unfolding of the protein backbone is favourable for membrane interactions, as Langmuir experiments and AFM clearly show that Tf–AuINT has a greater tendency to interact with biological films, compared to Tf alone. These findings are in agreement with previously published results.[15,18,19] *In vitro* membrane interaction studies on three different cell types indicate that Tf–AuINT might have a different affinity towards different cell types.

## Abbreviations

| | |
|---|---|
| Tf | Transferrin |
| TCAA | Tetrachloroauric acid |
| Tf–AuINT | Transferrin stabilized gold prepared *via* the intrinsic protocol |
| Tf–AuXL | Transferrin stabilized gold prepared with low concentration of TCAA, *via* the extrinsic protocol |
| Tf–AuXH | Transferrin stabilized gold prepared with high concentration of TCAA, *via* the extrinsic protocol |
| Tf-RED | Transferrin incubated with $NaBH_4$ |

 

| | |
|---|---|
| AuNCs | Gold nanoclusters |
| AuNPs | Gold nanoparticles |
| Trp | Tryptophan |

## Acknowledgements

The authors acknowledge the Department of Chemical Engineering, NTNU, for financial support. Acknowledgements are also given to Moreland *et al*.[32] and Xu *et al*[33] for providing the necessary software (Protein Workshop 4.2.0) for preparation of 3D imaging of Tf. Axel Sandvig and Ioanna Sandvig acknowledge financial support by the Central Norway Regional Health Authority-NTNU Liaison Committee. Gurvinder Singh thanks NTNU Nanolab for providing instrumentation facilities and NORTEM seed project for providing Transmission Electron Microscopy facility. The Research Council of Norway is acknowledged for the support to the Norwegian Micro- and Nano-Fabrication Facility, NorFab (197411/V30).

## Notes and references

1 W. A. Deheer, *Rev. Mod. Phys.*, 1993, **65**, 611.
2 J. Zheng, P. R. Nicovich and R. M. Dickson, in *Annual Review of Physical Chemistry*, Annual Reviews, Palo Alto, 2007, vol. 58, p 409.
3 J. P. Xie, Y. G. Zheng and J. Y. Ying, *J. Am. Chem. Soc.*, 2009, **131**, 888.
4 H. Y. Chen, B. W. Li, X. Y. Ren, S. N. Li, Y. X. Ma, S. S. Cui and Y. Q. Gu, *Biomaterials*, 2012, **33**, 8461.
5 X. Le Guevel, N. Daum and M. Schneider, *Nanotechnology*, 2011, **22**, 7.
6 A. Retnakumari, J. Jayasimhan, P. Chandran, D. Menon, S. Nair, U. Mony and M. Koyakutty, *Nanotechnology*, 2011, **22**, 11.
7 Y. C. Shiang, C. C. Huang, W. Y. Chen, P. C. Chen and H. T. Chang, *J. Mater. Chem.*, 2012, **22**, 12972.
8 C. J. Sun, H. Yang, Y. Yuan, X. Tian, L. M. Wang, Y. Guo, L. Xu, J. L. Lei, N. Gao, G. J. Anderson, X. J. Liang, C. Y. Chen, Y. L. Zhao and G. J. Nie, *J. Am. Chem. Soc.*, 2011, **133**, 8617.
9 T. H. Chen and W. L. Tseng, *Small*, 2012, **8**, 1912.
10 L. Z. Hu, S. Han, S. Parveen, Y. L. Yuan, L. Zhang and G. B. Xu, *Biosens. Bioelectron.*, 2012, **32**, 297.
11 X. X. Wang, Q. Wu, Z. Shan and Q. M. Huang, *Biosens. Bioelectron.*, 2011, **26**, 3614.
12 F. Wen, Y. H. Dong, L. Feng, S. Wang, S. C. Zhang and X. R. Zhang, *Anal. Chem.*, 2011, **83**, 1193.
13 X. Le Guével, B. Hötzer, G. Jung, K. Hollemeyer, V. Trouillet and M. Schneider, *J. Phys. Chem. C*, 2011, **115**, 10955.
14 A. Retnakumari, S. Setua, D. Menon, P. Ravindran, H. Muhammed, T. Pradeep, S. Nair and M. Koyakutty, *Nanotechnology*, 2010, 21.
15 S. M. Lystvet, S. Volden, G. Singh, I. M. Rundgren, H. Wen, O. Halskau and W. R. Glomm, *J. Phys. Chem. C*, 2013, **117**, 2230.
16 S. M. Lystvet, S. Volden, G. Singh, M. Yasuda, O. Halskau and W. R. Glomm, *RSC Adv.*, 2013, **3**, 482.
17 S. Volden, S. M. Lystvet, O. Halskau and W. R. Glomm, *RSC Adv.*, 2012, **2**, 11704.
18 S. M. Lystvet, S. Volden, O. Halskau and W. R. Glomm, *Soft Matter*, 2011, **7**, 11501.
19 S. M. Lystvet, S. Volden, M. Yasuda, O. Halskau and W. R. Glomm, *Nanoscale*, 2011, **3**, 1788.
20 P. T. Gomme and K. B. McCann, *Drug Discovery Today*, 2005, **10**, 267.
21 Z. M. Qian, H. Y. Li, H. Z. Sun and K. Ho, *Pharmacol. Rev.*, 2002, **54**, 561.
22 A. Yersin, T. Osada and A. Ikai, *Biophys. J.*, 2008, **94**, 230.
23 W. C. W. Chan and S. M. Nie, *Science*, 1998, **281**, 2016.
24 S. Anabousi, U. Bakowsky, M. Schneider, H. Huwer, C. M. Lehr and C. Ehrhardt, *Eur. J. Pharm. Sci.*, 2006, **29**, 367.
25 P. H. Yang, X. S. Sun, J. F. Chiu, H. Z. Sun and Q. Y. He, *Bioconjugate Chem.*, 2005, **16**, 494.
26 W. R. Glomm, S. Volden, Ø. Halskau Jr. and M. H. G. Ese, *Anal. Chem.*, 2009, **81**, 3042.
27 W. R. Glomm, Ø. Halskau Jr., A. M. D. Hanneseth and S. Volden, *J. Phys. Chem. B*, 2007, **111**, 14329.
28 J. R. Lakowicz, *Principles of Fluorescence Spectroscopy*, Springer, New York, 2006.
29 W. R. Glomm, S. Volden, O. Halskau and M. H. G. Ese, *Anal. Chem.*, 2009, **81**, 3042.
30 H. He, C. A. Conrad, C. L. Nilsson, Y. Ji, T. M. Schaub, A. G. Marshall and M. R. Emmett, *Anal. Chem.*, 2007, **79**, 8423.
31 A. J. Yates, D. K. Thompson, C. P. Boesel, C. Albrightson and R. W. Hart, *J. Lipid Res.*, 1979, **20**, 428.
32 J. L. Moreland, A. Gramada, O. V. Buzko, Q. Zhang and P. E. Bourne, *BMC Bioinf.*, 2005, 6.
33 D. Xu and Y. Zhang, *PLoS One*, 2009, 4.

# Paper II

**Controlling the self-assembly and optical properties of gold nanoclusters and gold nanoparticles biomineralized with Bovine Serum Albumin**

Received 00th January 20xx,
Accepted 00th January 20xx

DOI: 10.1039/x0xx00000x

www.rsc.org/

# Controlling the self-assembly and optical properties of gold nanoclusters and gold nanoparticles biomineralized with Bovine Serum Albumin

Birgitte H. McDonagh,[a] Gurvinder Singh,[b] Sulalit Bandyopadhyay,[a] Sina M. Lystvet,[a] Joseph A. Ryan,[c] Sondre Volden,[a] Eugene Kim,[d] Ioanna Sandvig,[e,f] Axel Sandvig,[f,g] Wilhelm R. Glomm[a, h]

While the size-dependent optical properties of BSA-stabilized gold nanoclusters are well known, the time-dependent growth mechanism remains to be described. Herein, we systematically compare two synthesis methods with and without ascorbic acid, and show that tuning of BSA-stabilized gold nanoclusters (AuNCs) of different sizes can be performed without the aid of an extrinsic reducing agent and with good reproducibility. We also show that adding ascorbic acid yields larger BSA-stabilized gold nanoparticles (AuNPs), and that AuNPs can only form above a threshold gold precursor concentration. Using computed tomography, we describe how these biomineralized AuNPs show size-dependent X-ray attenuation. Growth of BSA-stabilized AuNCs and AuNPs, over a range of gold precursor concentrations, was followed with steady-state fluorescence and UV-vis spectroscopy for one week, constituting the first study of its kind. Based on our results, we propose a mechanism for BSA-stabilization of AuNCs and AuNPs that can further aid in selective growth of discrete AuNCs and AuNPs.

## Introduction

Applications of protein-stabilized gold nanoparticles (AuNPs) and particularly gold nanoclusters (AuNCs) have increased dramatically since the introduction of the latter in 2009. [1] The main feature of nanometer sized gold is their remarkable size-dependent optical properties. [2, 3] The molecular sized AuNCs fluoresce, while AuNPs (>2nm) exhibit localized surface plasmon resonance (LSPR), resulting in absorbance of visible light. [4-7] Stable, biocompatible fluorescent probes with large Stoke's shifts that emit fluorescence in the Near IR (NIR) range are particularly interesting, as emission is outside the emission region typical of biological tissue.

The amount of atoms in AuNCs follows a shell model named the *Jellium model* with the corresponding magic numbers 2, 8, 10, 20, 26, 34, 40. An analogy to the Jellium model is the electronic structure of atoms, in which each shell is stable with an optimal amount of electrons. As the stability of an atom is governed by closed valence shells, so is the stability of magic numbered nanoclusters. [8-10]

The size-dependent fluorescence of AuNCs can be measured using steady-state fluorescence spectroscopy. However, the actual origin of fluorescence is not clear, as it can arise from the metal core, or from interactions between the metal core and surface ligands. [4] Particularly, electron-rich atoms appear to affect the fluorescence intensity in a positive manner. Wu *et al* suggests that this can occur in two ways; either as a charge transfer or direct donation of delocalized ligand electrons. [11] Proteins offer a plethora of energy donating atoms, such as S, N and O, and can therefore collectively enhance the fluorescence intensity via surface interactions if they are used as capping agents.

The blood plasma protein *bovine serum albumin* (BSA) was the first protein shown to synthesize and stabilize AuNCs. [1] BSA is the major transporter of drugs and metals in the body, and as such has a high affinity for metals.[12, 13] BSA is also documented to have an affinity for planar and curved gold surfaces. [14-16]

Biomineralization of gold with BSA can give a range of different-sized AuNCs, which in turn show size-dependent fluorescence. The reduction potential of BSA is also strong enough to synthesize AuNPs, and the surface stability imparted by BSA makes these AuNPs more stable in biological buffers compared to citrate-covered AuNPs (Figure 1 b-d).

AuNCs and AuNPs are increasingly being used for a range of different applications in bioimaging, [17] such as optical labels in drug delivery, [18, 19] diagnostics, [20] and as sensors of heavy metal ions, [21, 22] to mention a few. In particular, applications of colloidal AuNPs with diameters less than 100 nm are emerging as promising contrast agents for Computed Tomography (CT)[23].

[a] Ugelstad Laboratory, Department of Chemical Engineering, Norwegian University of Science and Technology (NTNU), 7491 Trondheim, Norway
[b] Department of Materials Science and Engineering, Norwegian University of Science and Technology (NTNU), N-7491 Trondheim, Norway
[c] Department of Chemistry, Iona College, New Rochelle, New York, USA
[d] Department of Circulation and Medical Imaging, Norwegian University of Science and Technology (NTNU), N-7491 Trondheim, Norway
[e] John Van Geest Centre for Brain Repair, Department of Clinical Neurosciences, University of Cambridge, CB2 OPY Cambridge, UK
[f] Department of Neuroscience, Faculty of Medicine, Norwegian University of Science and Technology (NTNU), N-7491, Trondheim, Norway
[g] Division of Pharmacology and Clinical Neurosciences, Department of Neurosurgery, Umeå University, 901 87 Umeå, Sweden
[h] Sector for Biotechnology and Nanomedicine, SINTEF Materials and Chemistry, Trondheim, Norway

* Corresponding author: Tel: +47-73 55 03 25, fax: +47-73 59 40 80, e-mail: birgitte.h.mcdonagh@ntnu.no,

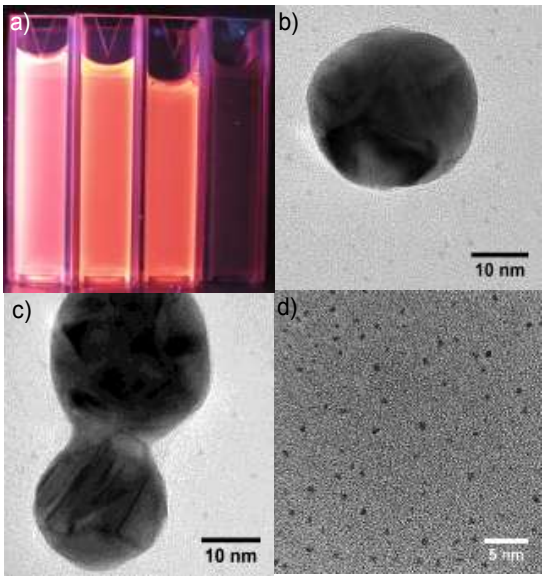


Figure 1: BSA acts as a scaffold for growth of AuNCs and AuNPs. a) Image of BSA-AuNCs and BSA-AuNPs excited with UV-lamp ($\lambda_{ex}$=365 nm). The size of the AuNCs increase from left to right. The dark sample to the right contains AuNPs which do not fluoresce. b,c) High resolution TEM (HR-TEM) images reveal polycrystalline AuNPs with different domains that are surrounded by Vis AuNCs. d) HR-TEM image of AuNCs.

However, the key to all of these applications remains controlling the size of the AuNCs and AuNPs.

Gold nanoparticles can be prepared *via* several methods. For instance, adding an extrinsic reducing agent such as $NaBH_4$ can be used for preparing gold nano rods, and different aspect ratios can be obtained by changing the concentration of $NaBH_4$. [24] However, recent reports indicate $NaBH_4$ as an extrinsic reducing agent of protein stabilized AuNCs and AuNPs may perturb the solution stability of the protein-AuNC complex due to alterations of the protein structure. This again may be caused by interactions with the $NaBH_4$ and the protein, or that larger gold species are synthesized in the presence of $NaBH_4$, causing the protein to unfold in a greater extent. [25, 26]

The synthesis of AuNCs and AuNPs with BSA has previously been studied with respect to pH,[27] dependences on gold precursor concentrations, [25] and temperature. [1, 22] Ascorbic acid is sometimes added as an extrinsic reducing agent in order to reduce the BSA concentration required,[27] but the effect of ascorbic acid is not completely understood. In fact, studies have shown that ascorbic acid can associate with BSA [28-30] and even quench AuNCs' fluorescence [31] if not removed via *e.g* dialysis. Different incubation times have also been reported, but more thorough studies revealing how the incubation time affects size-tuning of BSA-AuNCs or AuNPs are needed. Protein-directed growth of AuNCs is protein dependent, and addition of an extrinsic reducing agent may be redundant to obtain fluorescent AuNCs. [32]

The mechanism of AuNC growth is still not fully understood despite many reports on the synthesis of BSA-stabilized AuNCs and AuNPs. Since different synthesis protocols and conditions are typically being used between studies, it is problematic to deduce an overall mechanism, which in turn makes it difficult to describe and control the size of BSA-stabilized gold. In order to get a better understanding of the mechanism, there is a need for studies that systematically change one synthesis parameter at a time.

This paper has two aims. First we want to ascribe which parameters are important for self-assembly of gold nanostructures in BSA. This we investigate by varying the concentration of gold precursor, and the presence of an extrinsic reducing agent. The effect of an extrinsic reducing agent (ascorbic acid) is determined by comparing two synthesis methods named the *extrinsic* and *intrinsic* method. The former refers to reduction of gold ions with the aid of ascorbic acid as an extrinsic reducing agent, while the latter method solely depends on the intrinsic reduction potential of BSA. The second aim is to describe a growth mechanism for AuNCs and AuNPs in the BSA scaffold, by using time as the dependent variable.

This paper demonstrates that we can influence the size and thus the optical properties of BSA-AuNCs and AuNPs by varying the above mentioned synthesis parameters. We also describe how synthesis of either BSA-stabilized AuNCs and/or AuNPs can be achieved, and show that size-tunability of AuNCs can be achieved without the presence of ascorbic acid. Finally, we suggest a description of the growth mechanism from AuNCs to AuNPs that can be used to not only get a better understanding of the underlying mechanisms, but also for size-tunability of fluorescent AuNCs or AuNPs with LSPR.

## Experimental

Bovine Serum Albumin (67kDa), hydrogen tetrachloroaureate (III)·3 $H_2O$ (TCAA) and L-ascorbic acid were purchased from Sigma. Stock solutions of BSA (20mg/mL) were freshly prepared in MilliQ-water for each experiment. TCAA (1.18g, 3mmol) was dissolved in MilliQ-water (34.7mL) to make a stock solution (100mM). The TCAA stock solution was then diluted with MilliQ-water to 5, 7.5, 10, 15 and 20mM. BSA from the same batch was used for all samples described. Prior to the reaction, protein TCAA solutions were heated to 37°C. Here, two methods were used for synthesis in the absence and presence of an extrinsic reducing agent, hereafter labelled as the **intrinsic method** and the **extrinsic method**, respectively**. The intrinsic method**: TCAA (2.5mL; 5, 7.5, 10, 15 and 20mM) was added to BSA (2.5mL) at 37°C and stirred (300 rpm) for five minutes. 0.1M NaOH (100-300uL) was added until the solution had a pH of 11. Tyrosine is the amino acid in BSA which is thought to reduce TCAA to NCs and NPs [1]. The phenol group of tyrosine has a $pK_a$ of 10.1,[33] meaning that the synthesis of protein-gold must be performed at high pH-values for maximum reducing capacity. The pH has previously been shown to have an effect on growth of larger NCs, particularly at high pH-values a more prominent growth of large gold NCs has been reported. [27] The reaction was kept in an incubator (37°C) for 1 week followed by dialysis (MWCO: 14kDa) in MilliQ-water. The dialysis was performed with an exchange of the dialyzing solution after two hours, before leaving it overnight to remove excess TCAA. **The extrinsic method:** Ascorbic acid (0.35mg/mL, 50uL) was added immediately after TCAA before pH adjustment. Samples were diluted in MilliQ-water to 1mg BSA/mL before spectroscopic measurements, assuming that the protein concentration did not change with dialysis.

**Steady-state fluorescence spectroscopy** was performed using a Fluorolog-3 HORIBA Jobin Yvon spectrofluorometer with the excitation wavelengths $\lambda_{ex}$*=295nm* and $\lambda_{ex}$*=370nm*. The slit widths were kept at 3 nm and 5 nm, respectively.

**Time-correlated single-photon counting** was performed on the same apparatus as steady-state fluorescence spectroscopy. The protein concentration was 1mg/mL. For measuring tryptophan lifetimes and populations, a 280 nm NanoLED was used as the light source and the emission wavelength was set to $\lambda_{em}$*=360nm*. The bandpass was kept at 14.5nm.

**UV-visible spectroscopy** was performed on a Shimadzu UV-2401PC spectrophotometer in the range 200-800nm. The data were analyzed using UVProbe2.1 software.

**X-ray photoelectron spectroscopy (XPS)** analyses were performed using a Kratos Axis Ultra DLD spectrometer (Kratos Analytical, UK), equipped with a monochromatized aluminum X-ray source (Al, hu = 1486.6 eV) operating at 10 mA and 15 kV (150 W). A hybrid lens (electrostatic and magnetic) mode was employed along with an analysis area of approximately 300 µm X 700 µm. Survey spectra were collected over the range of 0-1100 eV binding energy with an analyzer pass energy of 160 eV, and high resolution spectra of Au 4f were obtained with an analyzer pass energy of 20 eV. XPS data were processed with Casa XPS software (Casa Software Ltd., UK).

**High-resolution inductive coupled plasma-mass spectrometry (ICP-MS)** measurements were performed on an ELEMENT 2 from Thermo Electronics with $ArCH_4$ plasma and tested against three blanks. Samples were autoclaved under high pressure with an UltraClave (Milestone) in 50% $HNO_3$ (v/v) at 80°C.

**High resolution transmission electron microscopy (HR-TEM)** images were acquired on a JEOL JEM-2100 (200 kV). The samples were prepared by depositing a few drops of nanoparticles or nanoclusters suspension on a copper grid coated with amorphous carbon layer, and allowed to dry prior to imaging

**X-ray powder diffraction (XRD)** patterns of lyophilized BSA-AuNPs and BSA- AuNCs were obtained from a Bruker DaVinci2 diffractometer using Cu Kα (λ= 1.54056 °A) in the 2θ range with 10–75 degree.

**Computed tomography (CT)** imaging was performed with a Skyscan 1176 micro-CT scanner (Bruker micro-CT, Kontich, BE). Samples of BSA-AuNPs were dialysed against phosphate buffered saline (pH=7.4) before measurements. A phantom consisting of three 0.3 ml centrifuge tubes filled with saline and two BSA-AuNP solutions with concentrations of 15 mg/ml and 30 mg/ml was scanned using the following parameters: 0.5 mm Al filter, 50 kVp, 500 µA, 63 ms exposure, 5 averages, 0.7° rotation step, 180° rotation, 35 µm voxel size. Another, similar phantom containing three samples of BSA-AuNPs (20mg/mL) with different average sizes (6nm, 26nm and 36nm) were scanned with the same imaging parameters. The central 20 slices were reconstructed using the Feldkamp cone-beam reconstruction algorithm to measure the attenuation coefficients (AC) of each suspension. Regions of interest (ROI) were
defined around the inner circumference of each tube in each image slice. The means and standard deviations (s.d) of the ACs within the ROIs were computed.

## Results and Discussion

Immediately after adjusting the pH to 11 for the BSA-TCAA mixture, the solutions changed colour from yellow to orange, brown or red, depending on the amount of TCAA added. After one week incubation time, the most prominent colour change was observed for samples incubated with the highest concentration of TCAA, going from red to dark purple. This change in colour is attributed to AuNPs (>2nm) large enough to exhibit LSPR. [4]

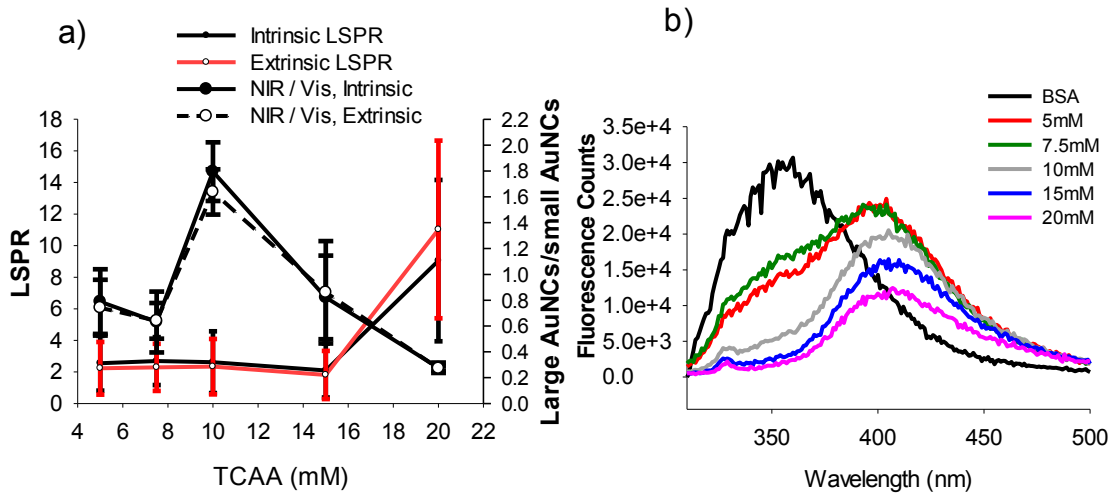


Figure 2: Integrals of a) LSPR absorption peak (500-600 nm) as a function of TCAA synthesized *via* intrinsic and extrinsic method. The integrals of the fluorescence emission ($\lambda_{ex}$*=370 nm*) of NIR AuNCs (560-730 nm) and Vis AuNCs (385-540 nm) was calculated. The integral of the NIR AuNCs was divided by the integral of Vis AuNCs to show the relative growth of the two sizes of AuNCs. This was done for both the intrinsic and the extrinsic protocol. b) Changes in Trp emission spectra ($\lambda_{ex}$*=295 nm*) as a function of gold precursor (TCAA).

LSPR appears when the frequency of the incident light matches the oscillation frequency of the surface electrons, relative to the positively charged metallic lattice, leading to an enhancement in the amplitude. [4-7] AuNPs with a dark purple color show an intense UV-visible light extinction band centered at 520nm (Figure S1). Under the conditions reported here, we found that there is a threshold for appearance of AuNPs that lies in between 15 and 20 mM TCAA (Figure 2a). Larger AuNPs were formed when ascorbic acid was added, implying that ascorbic acid contribute to the reduction of TCAA. This is in agreement with earlier studies (see e.g. Le Guèvel[27]) and is also expected, as the presence of an extrinsic reducing agent lowers the energy barrier towards nucleation and growth of nano crystals. The presence of AuNPs was confirmed with HR-TEM (Figure 1b and c), and crystallinity was observed with X-ray powder diffraction (Figure S4), and is also in accordance with values determined in previous studies. [34, 35]

**Size of BSA-gold is dependent on gold precursor concentration**

In contrast to AuNPs, AuNCs have discrete electronic structures such as HOMO-LUMO band gap openings with transitions smaller than the Fermi wavelength.[4] This results in molecule-like properties such as size-dependent fluorescence (Figure 1a). [36, 37] AuNCs vary in size from 0.2nm to 2nm, which for gold corresponds to a few atoms up to several hundreds of atoms. [2, 38] The amount of gold atoms in AuNCs likely follows the Jellium model, which describes clusters as being of a magic number of atoms (=2, 8, 13, 25, 38, 55…). Populations of AuNCs can be described by fluorescence spectroscopy. AuNCs are excited at 370 nm ($\lambda_{ex}$*=370nm)* and emit at 450 nm and 600-700 nm, depending on their size (Figure S2). Here, the peak at 450 nm is attributed to populations of smaller AuNCs ($Au_8$, $Au_{13}$ *etc*) which are hereon referred to as Vis AuNCs as they emit in the visible region of the electromagnetic spectrum. The fluorescence between 600 and 700nm is attributed to populations of larger AuNCs ($Au_{25}$), hereon referred to as NIR AuNCs. [1, 27]

The large NIR fluorescence intensity observed for AuNCs at 10mM TCAA might be a result of a metal-to-ligand/ligand-to-metal charge-transfer (ML/LMCT) complex that is formed between the protein and the NIR AuNCs. This is hypothesized to enhance the fluorescence intensities. However, in an ML/LMCT complex there is an exchange of electrons either from the metal to the protein or *vice versa*. If this was largely the case, either the protein or the AuNCs would be oxidized/reduced, which would destabilize the suspension with time. Thus, as the suspensions were very stable over long time periods (>1 year), it is more likely that the high fluorescence intensity from NIR AuNCs is caused by capping of BSA. This would in turn cause shielding of the AuNC from water, which further would give a more intense fluorescence emission.

The AuNCs prepared with the intrinsic method show the same intensity and reproducibility as samples synthesized with ascorbic acid. Given that the concentration of ascorbic acid used was in accordance with previous literature. [27, 39] This finding suggests that the concentration of ascorbic acid used here does not significantly aid BSA in reducing $Au^{3+}$ to AuNCs. At low concentrations, there are predominantly Vis clusters present, but as the concentration of TCAA increases, so does the population of NIR AuNCs (Figure 2b). However, as AuNPs emerge, detecting the presence of AuNCs with fluorescence spectroscopy becomes highly complex as the interactions between colloids and fluorophores can involve resonance energy transfer and quenching. [7] The Vis AuNCs on the other hand, seem to be unaffected by the presence of AuNPs as their fluorescence intensities continue to increase with TCAA concentration. The most probable reason for this is that the emission from Vis AuNCs is out of range of AuNP quenching or that Vis AuNCs are too far away from AuNPs. Appearance of AuNPs occurs only at high concentrations of TCAA (20mM, Figure 2a). At 20mM TCAA, there is a substantial decrease in the emission of NIR AuNCs (Figure 2b), as well as a bathochromic shift of the emission peak at 650 nm (Figure S2). This could be caused by NIR AuNCs being quenched by AuNPs, coalescence of NIR AuNCs into AuNPs, or a combination of both.

With X-ray photoelectron spectroscopy, the binding energy of surface photoelectrons can be measured. Higher binding energies indicate that the surface electrons are more associated with the metal, and less prone to movement between metallic surfaces. [27, 40, 41] A lower binding energy means that the surface electrons have less affinity to the metallic core. Here, BSA-AuNCs show gold peaks at 80.1 and 83.8eV, while BSA-AuNPs show a shift to higher binding energies (84.9eV and 81.2eV, respectively. Figure S5). The peaks for BSA-AuNPs are also broadened, and show higher intensities compared to the BSA-AuNCs. Because XPS can only detect elemental compositions of surfaces down to 10nm[42-44], a shift to higher binding energies with higher concentrations of TCAA, means that Vis AuNCs are present on the surface of the protein. It also implies that NIR AuNCs are not on the surface and (i) has either coalesced into NPs or (ii) are buried in BSA. The XPS spectra, combined with HR TEM images (Figure 1b and c) strongly suggests that AuNCs coexist with AuNPs, and imply that the AuNPs are covered with BSA-AuNCs as passivating ligands.

**Tryptophan emission is altered due to size of BSA-stabilized AuNCs and AuNPs.**

BSA is a very flexible protein and can undergo major conformational changes without denaturation.[45-47] The flexibility is important for the amount of gold that can be loaded onto the protein backbone. Changes in the conformation of BSA can be described by steady-state fluorescence spectroscopy by exciting the amino acid tryptophan (Trp). The indole ring in Trp is the dominant fluorophore in proteins, absorbing light near 295 nm and emitting near 340 nm.[48, 49] Indole is very sensitive to solvent polarity and can reveal the location of tryptophan residues in proteins. Typically, emissions from exposed Trp residues are red-shifted, while buried Trp residues will have a blue-shifted emission. [7, 50] Stoke's shifts and quenching of tryptophan emission is usually explained by an exposure to the aqueous environment. [7, 49, 51] BSA has two tryptophan residues; one situated in a hydrophobic pocket (Trp213) while the other is situated on the surface (Trp134).[47] Because Trp213 is hidden inside native BSA, the tryptophan emission ($\lambda_{ex}$ *=295 nm*) is thought to be dominated by Trp134. Therefore, any changes in the emission are ascribed to structural changes in the protein. [25, 49, 52] Steady-state fluorescence spectroscopy was used to measure Trp emission in BSA containing different sizes and populations of nano-sized gold. Trp134 in native BSA has an emission maximum at approximately 350 nm in water. This maximum was steadily quenched and shifted towards longer wavelengths as the size of the nano-sized gold increased (Figure 2b). No differences between the intrinsic and extrinsic methods were observed with TCAA concentrations above 5mM. However, the emission of BSA incubated with ascorbic acid had the largest standard deviations (Figure S3), which could imply that not all of

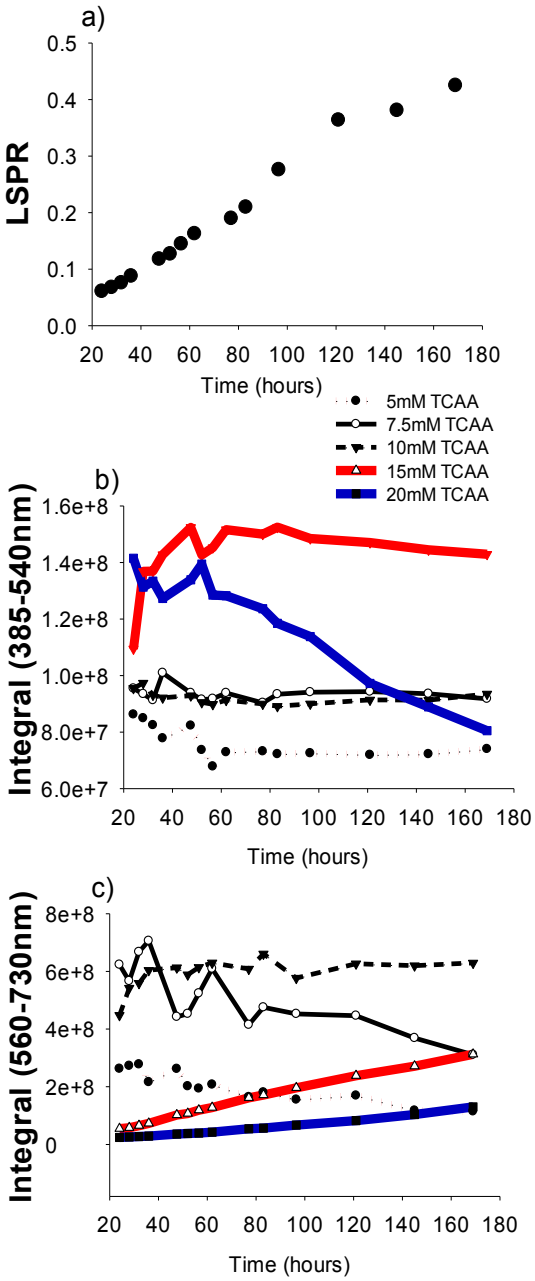


Figure 4: Graph a) shows the LSPR intensity at 520nm as a function of time for the sample incubated with 20mM TCAA. No LSPR-band was observed for any other samples. Graph b) shows the integral of the emission peak for the Vis AuNCs (385-540 nm) after subtracting the signal of native BSA. Graph c) show the integral of the emission peaks of NIR AuNCs (560-730 nm) after subtracting the signal of native BSA. Both graph b and c are shown as a function of time. The lines for 15 and 20 mM TCAA have been highlighted as they show the most consistent changes.

the ascorbic acid was removed *via* dialysis because it was bound to the protein.

The Trp emission (Figure 2b) curve has an inflection point approximately at 360 nm, which is best observed with the 5mM curve (red). As AuNCs are excited at 370 nm, it is likely that the decrease in Trp emission is not only caused by exposure to the surface, but also by quenching of adjacent AuNCs. After 360nm, the Trp emission intensity slowly increases to 450 nm, before it decreases again.

The whole emission profile of BSA is drastically altered from TCAA concentrations of 10mM and above, meaning that the protein has undergone large conformational changes. At 10mM TCAA there is a dramatic change in the Trp emission from 300 to 400 nm. At this particular concentration of TCAA, the highest ratio of NIR AuNCs was determined (Figure 2a). This means that with a bigger population of NIR AuNCs, the probability that a quencher is adjacent to a Trp residue increases. However, Trp quenching cannot only be explained by AuNC quenching alone. With increased population of nano-sized gold, BSA unfolds and exposes Trp134 to water, which will be a large contributor to quenching.[25] Unfolding also leads to exposure of the buried tryptophan residue (Trp213), which emission emerge at ~320nm for samples containing 10-20mM TCAA.

From time-correlated single photon spectroscopy (TCSPC) a large difference in the Trp lifetimes of native BSA and BSA with AuNPs (20mM TCAA) was detected (Table S2). This indicates that the fluorophore on average spends less time in the excited state, which is probably caused by an increased exposure to water or energy transfer to BSA-gold, or a combination of the two. [25]

Combining the TCSPC data with steady-state fluorescence data, we ascribe quenching of Trp emission as concomitant effect of increased size of BSA-AuNCs/AuNPs. Interestingly, even though the Trp emission reveals large structural changes in BSA, the BSA-AuNP solution did not show any signs of aggregation after 12 months of storage. This means that the conformational changes induced by nano-sized gold are not large enough to severely denature BSA, and compromise its solution stability. The long shelf-life of BSA-AuNP suspensions enhances their utility *e.g* in sensing and imaging applications.[53-55]

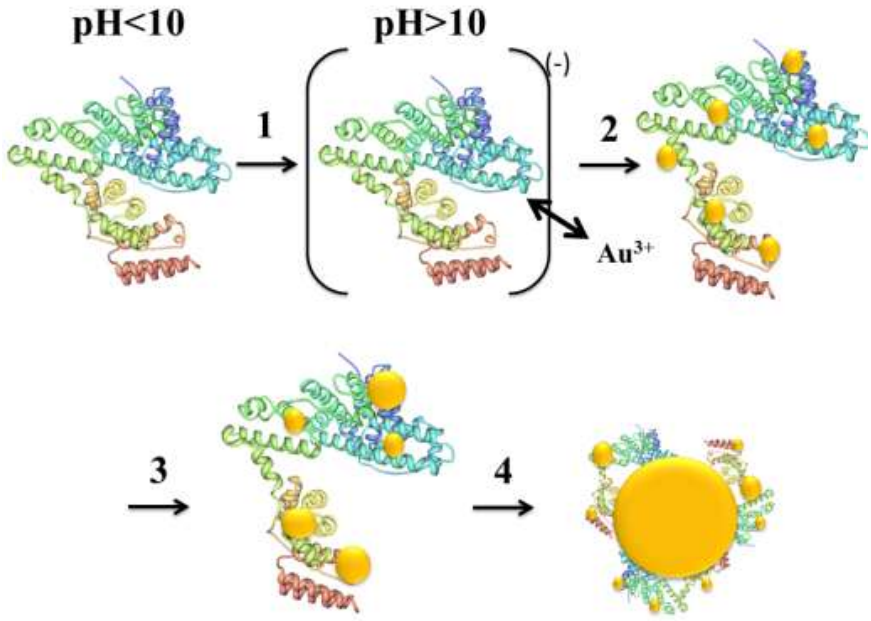


Figure 5: Proposed mechanism for growth of AuNPs stabilized by BSA. 1) Increasing the pH to above 10 causes BSA to be negatively charged which induces electrostatic interactions with the gold ions. 2) Vis AuNCs that emit in the visible region of the EM spectrum start to form, 3) and depending on time and concentration of TCAA, larger NIR AuNCs and 4) AuNPs are formed via a shuffling of NIR AuNCs. It should be noted that the structure of the denatured protein is used only as illustration, and not as an accurate description of the conformation

**Proposed mechanism for biomineralization of AuNCs and AuNPs**

We have established that changing the ratio of BSA/TCAA yields different populations of nanometer-sized gold, and that ascorbic acid is not needed for synthesis of AuNCs, but that it is beneficial for biomineralization of AuNPs.

The incubation time for the samples prepared above was one week, [25, 32] which is much longer compared to the original synthesis of 12 hours.[1] 12 hours incubation time is also reported by several others,[39, 56-59] but overnight,[60] 15 hours,[22] 5 hours,[27, 39] and 2 hours[25] have also been used for BSA-AuNCs synthesis. The different incubation times yield different populations of AuNCs, revealing that the synthesis is highly time-dependent.

We wanted to elucidate the time-dependent changes in the protein and what appears to be a dynamic interchange between Vis and NIR AuNCs that could give further insight to the nucleation and growth processes. In order to address this issue, biomineralization of AuNCs and AuNPs with BSA was followed for one week.

In Figure 5 we have illustrated what we suggest as the self-assembly mechanism of BSA-stabilized AuNCs and AuNPs. Initially, the pH is raised to above 10 so that BSA becomes negatively charged (step 1, Figure 5). [61] Positively charged gold ions are then electrostatically attracted to BSA, particularly in areas rich in tyrosine and histidine which are the major reducing amino acids. Once the local concentration of gold ions is high enough, nucleation occurs (step 2), and further growth of AuNCs is caused by an increased influx of gold ions, or due to coalescence, or both (step 3). If the concentration of TCAA is high enough, AuNPs are synthesized most likely due to coalescence of several proteins surrounding an AuNP core (step 4). The work described herein appears to follow the general mechanism described by Volden *et.al.* [32]

The initial electrostatic interactions of $Au^{3+}$ ions will favor nucleation at sites high in concentration of negatively charged amino acids. This in turn suggests that nucleation is likely to take place in these regions as well. Indeed, the reduction in Trp emission observed in Figure 2b (5 and 7.5mM TCAA) could be an effect of exactly that. Nucleation that takes place close to a dominating fluorophore would in turn cause quenching, as AuNCs can interact with the emitted photons from Trp213. This also leans towards the fact that nucleation does not take place in the central hydrophobic regions of the protein, as Trp134 emission is not quenched with increased concentration of gold ions (Figure 2b, 10-20 mM TCAA, Trp peak at 320 nm).

Biomineralization of AuNPs is highly time-dependent, with AuNPs of 20 nm occurring after one week of incubation with BSA, but only at high concentrations of TCAA (20 mM, Figure 4a). Synthesis of AuNCs, however, is not equally linear and straight-forward. Up until 60 hours of incubation time, there are large fluctuations in the populations of Vis AuNCs (Figure 4b). Beyond 60 hours, the population sizes decrease but at different rates. The largest changes are seen with the highest concentration of TCAA, which seem to inversely follow the growth of AuNPs (Figure 4a), suggesting increased quenching of AuNCs with appearance of AuNPs. For samples containing 15 and 20 mM TCAA, decrease in populations of Vis AuNCs is followed by growth of NIR AuNCs, which

is not equally observed for the other samples (Figure 4c). This suggests that Vis AuNCs coalesce into NIR AuNCs, and that this is most prominent when high concentrations of TCAA are added. For samples containing 5-10 mM TCAA, there are particularly large fluctuations in the emissions for NIR AuNCs up until approximately 100 hours. During the time course of the experiment, peak shoulders were consistently observed for the NIR AuNCs, but not for the Vis AuNCs. Emission peaks of AuNCs that broaden and have shoulders indicate that different discrete AuNC populations of magic Jellium numbers are present in the protein backbone.[25, 62] This means that there are at least two populations of NIR AuNCs present, and that the population sizes are changing based on the available amount of $Au^{3+}$. The spectral line shape of 7.5mM TCAA is particularly interesting (Figure S9). In the beginning of the reaction, the peak at 650 nm has a shoulder that lies to the left, but after 62 hours of reaction time, the shoulder has shifted to the right, meaning that AuNCs of higher magic Jellium numbers are formed. At 62 hours, there are minor changes in the population of Vis AuNCs, which could mean that growth of larger AuNCs is caused by an influx of $Au^{3+}$ to the protein surface from the bulk, rather than coalescence of Vis AuNCs as the latter would have revealed a decrease in the population of Vis AuNCs.

It is very important to point out that emission of AuNCs tend to be higher at short incubation times, with the exception of NIR AuNCs for samples containing 15 and 20 mM TCAA. This suggests that synthesis of AuNCs with high quantum yields should be performed with incubation times below 40 hours.

Volden *et al* also points to the flexibility of the protein as a key feature for synthesis of AuNCs. The Trp emission was also followed with time, and revealed how BSA rapidly undergoes conformational changes during the biomineralization process. The Trp emission line shape did not change after 24 hours incubation time (Figure S10) but had the same shape as that observed after one week (Figure 2b). With the sample prepared at 20 mM TCAA, the changes during the week were less prominent, which indicates that the protein has less chances of conformational changes due to the NIR AuNCs and AuNPs present in its backbone. However, changes to the emission of the other samples were observed and is worth highlighting. The samples containing 5-15 mM TCAA actually showed an increase in the Trp emission at the end of the week compared to 24 hours. Increased emission of Trp represents a refolding of the BSA with time. As size and amount of AuNCs grow, BSA is forced to stretch and expose hydrophobic pockets to the aqueous environment. At some point, the unfavorable interactions between hydrophobic residues and water will force the protein to change conformation. Refolding of BSA may in turn bring Vis AuNCs closer to each other, which would increase the probability of coalescence into NIR AuNCs. The concomitant decrease in the Vis AuNCs (Figure 4b) could therefore be an effect of refolding of BSA that is greater with time. It is likely that NIR AuNCs also remain in the protein backbone as they can be visualized with HR TEM (Figure 1 b-c) and measured with steady-state fluorescence spectroscopy.

The easy size tuning, low toxicity, excellent stability, and optical properties of BSA-stabilized AuNCs and AuNPs render these constructs highly useful in several applications. For instance, we have initial data suggesting that BSA-AuNPs show size-dependent X-ray attenuation, which can be used in computed tomography (Figure S7).

## Conclusions

We have systematically compared the role of BSA in reducing $Au^{3+}$ to AuNCs of different sizes using two different synthesis protocols – with and without the addition of ascorbic acid as an extrinsic reducing agent. Our results demonstrate that the presence of ascorbic acid plays a minor role in the formation of BSA-AuNCs, but that ascorbic acid yields larger BSA-AuNPs. We have also shown that the size of BSA-AuNCs and BSA-AuNPs is in turn dependent on the TCAA concentration and the incubation time. BSA is a robust and flexible protein that can carry a substantial amount of AuNCs in its backbone, and can even stabilize AuNPs without denaturing, showing great solution stability even after one year. We suggest that gold nanoparticles grow at the expense of NIR nanoclusters, and that this is enabled by the flexibility of BSA. We have also shown that at lower TCAA concentrations, Vis and NIR AuNCs co-exist in the protein backbone, and that this ratio is tunable. The mechanism described here can be easily applied for size-selection of BSA stabilized AuNCs and AuNPs, tuning the growth towards different applications.

## Acknowledgements

The authors acknowledge the Department of Chemical Engineering, NTNU, for financial support. Sulalit Bandyopadhyay acknowledges the Faculty of Natural Sciences and Technology, NTNU for financial support. Gurvinder Singh thanks NTNU Nanolab for providing instrumentation facilities. The Research Council of Norway is acknowledged for the support to the Norwegian Micro- and Nano-Fabrication Facility, NorFab (197411/V30). Axel Sandvig and Ioanna Sandvig acknowledge financial support by the Central Norway Regional Health Authority NTNU Liaison Committee. Finally, acknowledgements are given to Moreland *et al*[63] for providing necessary software for preparation of 3D imaging of BSA.

## References

1. Xie, J.; Zheng, Y.; Ying, J. Y. *J. Am. Chem. Soc.* **2009,** 131, (3), 888-889.
2. Le Guevel, X. *IEEE Journal on Selected Topics in Quantum Electronics* **2014,** 20, (3).
3. Qu, X.; Li, Y.; Li, L.; Wang, Y.; Liang, J.; Liang, J. *Journal of Nanomaterials* **2015,** 2015, 23.
4. Qian, H.; Zhu, M.; Wu, Z.; Jin, R. *Acc. Chem. Res.* **2012,** 45, (9), 1470-1479.
5. Jain, P. K.; Huang, X.; El-Sayed, I. H.; El-Sayed, M. A. *Acc. Chem. Res.* **2008,** 41, (12), 1578-1586.
6. Jain, P. K.; ElSayed, I. H.; El-Sayed, M. A. *Nano Today* **2007,** 2, (1), 18-29.
7. Lakowicz, J. R., *Principles of Fluorescence Spectroscopy*. 3 ed.; Springer: USA, 2006.
8. de Heer, W. A. *Rev. Mod. Phys.* **1993,** 65, (3), 611-676.
9. Janssens, E.; Neukermans, S.; Lievens, P. *Curr. Opin. Solid State Mater. Sci.* **2004,** 8, (3–4), 185-193.
10. Reber, A. C.; Khanna, S. N.; Castleman Jr, A. W., Chapter 9 - Superatoms: From Motifs to Materials. In *Science and Technology of Atomic, Molecular, Condensed Matter & Biological Systems*, Purusottam, J.; Castleman, A. W., Eds. Elsevier: 2010; Vol. Volume 1, pp 365-381.
11. Wu, Z.; Jin, R. *Nano Lett.* **2010,** 10, (7), 2568-2573.

12. Bal, W.; Christodoulou, J.; Sadler, P. J.; Tucker, A. *J. Inorg. Biochem.* **1998,** 70, (1), 33-39.
13. Sadler, P. J.; Viles, J. H. *Inorg. Chem.* **1996,** 35, (15), 4490-4496.
14. Ni Dhubhghaill, O. M.; Sadler, P. J.; Tucker, A. *J. Am. Chem. Soc.* **1992,** 114, (3), 1118-1120.
15. Glomm, W. R.; Halskau Jr, Ø.; Hanneseth, A. M. D.; Volden, S. *Journal of Physical Chemistry B* **2007,** 111, (51), 14329-14345.
16. Brewer, S. H.; Glomm, W. R.; Johnson, M. C.; Knag, M. K.; Franzen, S. *Langmuir* **2005,** 21, (20), 9303-9307.
17. Sun, C.; Yang, H.; Yuan, Y.; Tian, X.; Wang, L.; Guo, Y.; Xu, L.; Lei, J.; Gao, N.; Anderson, G. J.; Liang, X. J.; Chen, C.; Zhao, Y.; Nie, G. *J. Am. Chem. Soc.* **2011,** 133, (22), 8617-8624.
18. Lu, W.; Zhang, Y.; Tan, Y. Z.; Hu, K. L.; Jiang, X. G.; Fu, S. K. *J. Controlled Release* **2005,** 107, (3), 428-448.
19. Khandelia, R.; Jaiswal, A.; Ghosh, S. S.; Chattopadhyay, A. *Small* **2013,** 9, (20), 3494-3505.
20. Retnakumari, A.; Jayasimhan, J.; Chandran, P.; Menon, D.; Nair, S.; Mony, U.; Koyakutty, M. *Nanotechnology* **2011,** 22, (28).
21. Xie, J.; Zheng, Y.; Ying, J. Y. *Chem. Commun.* **2010,** 46, (6), 961-963.
22. Chen, P. C.; Chiang, C. K.; Chang, H. T. *J. Nanopart. Res.* **2013,** 15, (1).
23. Cole, L. E.; Ross, R. D.; Tilley, J. M.; Vargo-Gogola, T.; Roeder, R. K. *Nanomedicine* **2015,** 10, (2), 321-341.
24. Zhang, L.; Xia, K.; Lu, Z.; Li, G.; Chen, J.; Deng, Y.; Li, S.; Zhou, F.; He, N. *Chem. Mater.* **2014,** 26, (5), 1794-1798.
25. Lystvet, S. M.; Volden, S.; Singh, G.; Yasuda, M.; Halskau, O.; Glomm, W. R. *RSC Advances* **2013,** 3, (2), 482-495.
26. McDonagh, B. H.; Volden, S.; Lystvet, S. M.; Singh, G.; Ese, M.-H.; Ryan, J. A.; Lindgren, M.; Sandvig, A.; Sandvig, I.; Glomm, W. R. *Nanoscale* **2015**.
27. Le Guével, X.; Hötzer, B.; Jung, G.; Hollemeyer, K.; Trouillet, V.; Schneider, M. *J. Phys. Chem. C* **2011,** 115, (22), 10955-10963.
28. Nafisi, S.; Bagheri Sadeghi, G.; Panahyab, A. *J. Photochem. Photobiol. B: Biol.* **2011,** 105, (3), 198-202.
29. Sun, L.; Zhang, J.; Liu, K. *Anal. Lett.* **2007,** 40, (16), 3050-3059.
30. Tukamoto, T.; Ozeki, S.; Hattori, F.; Ishida, T. *Chem. Pharm. Bull.* **1974,** 22, (2), 385-389.
31. Wang, X.; Wu, P.; Hou, X.; Lv, Y. *The Analyst* **2013,** 138, (1), 229-233.
32. Volden, S.; Lystvet, S. M.; Halskau, Ø.; Glomm, W. R. *RSC Advances* **2012,** 2, (31), 11704-11711.
33. Nelson, D. L.; Cox, M. M., *Lehninger Principles of Biochemistry*. 5 ed.; W.H Freeman and Company: USA, 2008.
34. Geetha, R.; Ashokkumar, T.; Tamilselvan, S.; Govindaraju, K.; Sadiq, M.; Singaravelu, G. *Cancer Nanotechnol.* **2013,** 4, (4-5), 91-98.
35. Jiao, J.; Zhang, H.; Yu, L.; Wang, X.; Wang, R. *Colloids Surf. Physicochem. Eng. Aspects* **2012,** 408, 1-7.
36. Lin, C. A. J.; Yang, T. Y.; Lee, C. H.; Huang, S. H.; Sperling, R. A.; Zanella, M.; Li, J. K.; Shen, J. L.; Wang, H. H.; Yeh, H. I.; Parak, W. J.; Chang, W. H. *ACS Nano* **2009,** 3, (2), 395-401.
37. Yuan, C. T.; Chou, W. C.; Tang, J.; Lin, C. A.; Chang, W. H.; Shen, J. L.; Chuu, D. S. *Opt. Express* **2009,** 17, (18), 16111-16118.
38. Aikens, C. M. *J. Phys. Chem. Lett.* **2011,** 2, (2), 99-104.
39. Das, T.; Ghosh, P.; Shanavas, M. S.; Maity, A.; Mondal, S.; Purkayastha, P. *Nanoscale* **2012,** 4, (19), 6018-6024.
40. Peters, S.; Peredkov, S.; Neeb, M.; Eberhardt, W.; Al-Hada, M. *Surf. Sci.* **2013,** 608, 129-134.
41. Tanaka, A.; Takeda, Y.; Imamura, M.; Sato, S. *Physical Review B* **2003,** 68, (19), 195415.
42. McArthur, S. L. *Surf. Interface Anal.* **2006,** 38, (11), 1380-1385.
43. Sezen, H.; Suzer, S. *Thin Solid Films* **2013,** 534, 1-11.
44. Hajati, S.; Tougaard, S. *Anal. Bioanal. Chem.* **2010,** 396, (8), 2741-2755.
45. El Kadi, N.; Taulier, N.; Le Huérou, J. Y.; Gindre, M.; Urbach, W.; Nwigwe, I.; Kahn, P. C.; Waks, M. *Biophys. J.* **2006,** 91, (9), 3397-3404.
46. Bloomfield, V. *Biochemistry* **1966,** 5, (2), 684-689.
47. Cao, X. L.; Li, H. W.; Yue, Y.; Wu, Y. *Vib. Spectrosc* **2013,** 65, 186-192.
48. Gelamo, E. L.; Silva, C. H. T. P.; Imasato, H.; Tabak, M. *Biochimica et Biophysica Acta - Protein Structure and Molecular Enzymology* **2002,** 1594, (1), 84-99.
49. Sułkowska, A. *J. Mol. Struct.* **2002,** 614, (1-3), 227-232.
50. Xu, J.; Chen, J.; Toptygin, D.; Tcherkasskaya, O.; Callis, P.; King, J.; Brand, L.; Knutson, J. R. *J. Am. Chem. Soc.* **2009,** 131, (46), 16751-16757.
51. De Paoli Lacerda, S. H.; Park, J. J.; Meuse, C.; Pristinski, D.; Becker, M. L.; Karim, A.; Douglas, J. F. *ACS Nano* **2010,** 4, (1), 365-379.
52. Hierrezuelo, J. M.; Nieto-Ortega, B.; Carnero Ruiz, C. *J. Lumin.* **2014,** 147, 15-22.
53. Vasimalai, N.; John, S. A. *Analytical Methods* **2013,** 5, (20), 5515-5521.
54. Wei, S. C.; Hsu, P. H.; Lee, Y. F.; Lin, Y. W.; Huang, C. C. *ACS Applied Materials and Interfaces* **2012,** 4, (5), 2652-2658.
55. Liu, Z.; Luo, L.; Dong, Y.; Weng, G.; Li, J. *J. Colloid Interface Sci.* **2011,** 363, (1), 182-186.
56. Hu, L.; Han, S.; Parveen, S.; Yuan, Y.; Zhang, L.; Xu, G. *Biosensors Bioelectron.* **2012,** 32, (1), 297-299.
57. Wang, M.; Mei, Q.; Zhang, K.; Zhang, Z. *Analyst* **2012,** 137, (7), 1618-1623.
58. Wang, Y.; Chen, J.; Irudayaraj, J. *ACS Nano* **2011,** 5, (12), 9718-9725.
59. Zhang, M.; Dang, Y. Q.; Liu, T. Y.; Li, H. W.; Wu, Y.; Li, Q.; Wang, K.; Zou, B. *J. Phys. Chem. C* **2013,** 117, (1), 639-647.
60. Raut, S.; Chib, R.; Rich, R.; Shumilov, D.; Gryczynski, Z.; Gryczynski, I. *Nanoscale* **2013,** 5, (8), 3441-3446.
61. Peng, Z. G.; Hidajat, K.; Uddin, M. S. *J. Colloid Interface Sci.* **2004,** 271, (2), 277-283.
62. Zheng, J.; Nicovich, P. R.; Dickson, R. M., Highly fluorescent noble-metal quantum dots. 2007; Vol. 58, pp 409-431.
63. Moreland, J. L.; Gramada, A.; Buzko, O. V.; Zhang, Q.; Bourne, P. E. *BMC Bioinformatics* **2005,** 6.

 

# Supporting information

## Controlling the self-assembly and optical properties of gold nanoclusters and gold nanoparticles biomineralized with Bovine Serum Albumin

Birgitte H. McDonagh,[a] Gurvinder Singh,[b] Sulalit Bandyopadhyay,[a] Sina M. Lystvet,[a] Joseph A. Ryan,[c] Sondre Volden,[a] Eugene Kim,[d] Ioanna Sandvig,[e,f] Axel Sandvig,[f,g] Wilhelm R. Glomm[a, h]

[a.] *Ugelstad Laboratory, Department of Chemical Engineering, Norwegian University of Science and Technology (NTNU), 7491 Trondheim, Norway*
[b.] *Department of Materials Science and Engineering, Norwegian University of Science and Technology (NTNU), N-7491 Trondheim, Norway*
[c.] *Department of Chemistry, Iona College, New Rochelle, New York, USA*
[d.] *Department of Circulation and Medical Imaging, Norwegian University of Science and Technology (NTNU), N-7491 Trondheim, Norway*
[e.] *John Van Geest Centre for Brain Repair, Department of Clinical Neurosciences, University of Cambridge, CB2 OPY Cambridge, UK*
[f.] *Department of Neuroscience, Faculty of Medicine, Norwegian University of Science and Technology (NTNU), N-7491, Trondheim, Norway*
[g.] *Division of Pharmacology and Clinical Neurosciences, Department of Neurosurgery, Umeå University, 901 87 Umeå, Sweden*
[h.] *Sector for Biotechnology and Nanomedicine, SINTEF Materials and Chemistry, Trondheim, Norway*

*Correspondence to: birgitte.h.mcdonagh@ntnu.no

**LSPR absorption of BSA-stabilized AuNPs and steady-state fluorescence emission of AuNCs**

Figure S1 show the appearance of gold conduction band as observed with UV-Visible for both intrinsic and extrinsic synthesis. The spectrum shows the absorbance of gold nanoparticles at ~520nm for the extrinsic synthesis route.

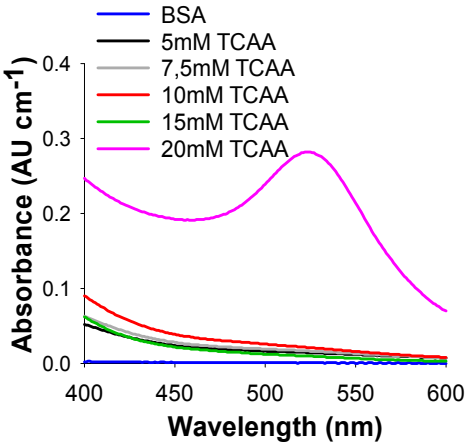


Figure S1: LSPR of BSA-stabilized AuNPS

Figure S2 show the Steady-state fluorescence spectra of fluorescent gold nanoclusters ($\lambda_{ex}$ *=370 nm*) prepared via the extrinsic method. Figure S3 show the integral of the Trp emission ($\lambda_{ex}$ *=295 nm)* as a function of TCAA.

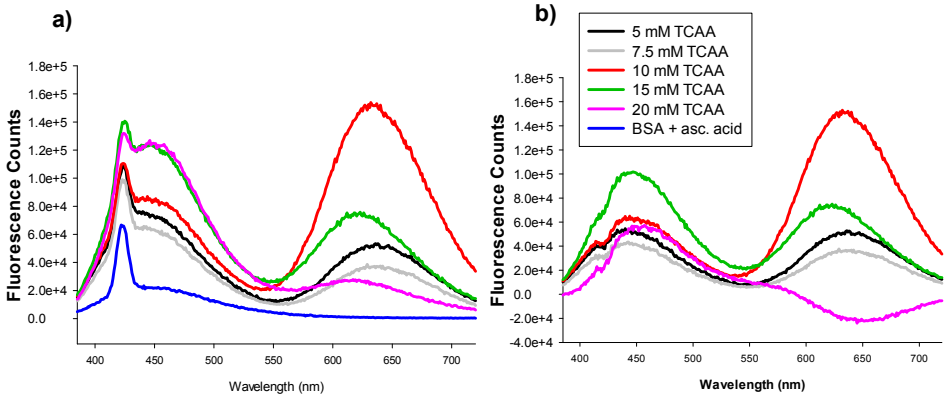


Figure S2. Spectra in a) show the emission of AuNCs with the contributing emission from BSA. Spectra b), the emission from BSA has been subtracted from all spectra, to show the contribution of only AuNCs.

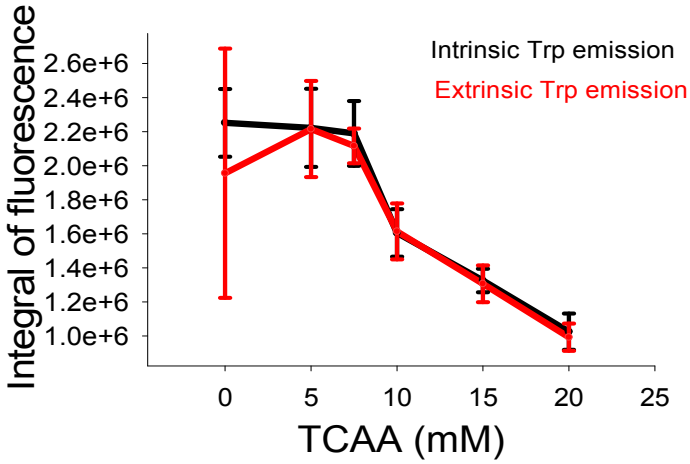


Figure S3: Integral of Trp emission (310-450 nm) as a function of TCAA. The red lines show the extrinsic Trp emission, while the black line show the intrinsic integral of Trp emission.

X-ray powder diffraction of BSA and BSA AuNPs

Figure S4 show the XRD-patterns for pure BSA (red line) and for BSA-AuNPs (black), and reveal crystalline structures of the BSA stabilized AuNPs.

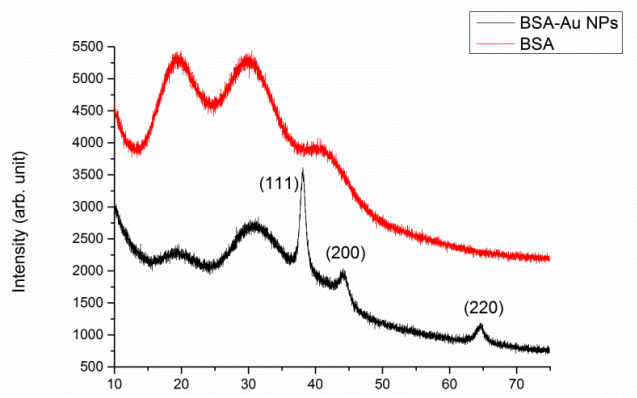


Figure S4: XRD patterns of BSA and BSA stabilized AuNPs

**High-resolution inductive coupled plasma-mass spectrometry (ICP-MS)**

Inductive- coupled plasma mass spectroscopy (ICP-MS) is a powerful technique for determining the elemental composition in a sample. The yield of gold determined by ICP-MS measurements is higher for the samples where nanoparticles are present, with a yield of 0.5%. The average yield for the intrinsic method is slightly higher than the extrinsic.

Table S1 show the amount of gold associated with samples with low amount of gold (7.5mM TCAA) and high amount of gold (20mM TCAA).

**Table S1: Amount of gold associated with BSA determined by ICP-MS**

| Added TCAA (mM) | Gold intrinsic (ug/L) | Gold extrinsic (ug/L) | Average yield intrinsic (%) | Average yield extrinsic (%) |
|---|---|---|---|---|
| 7.5 | 2.7<br>5.0<br>4.0 | 3.3<br>5.0<br>4.2 | 0.26±0.080 | 0.28±0.055 |
| 20 | 21.3<br>15.2<br>25.7 | 21.3<br>18.0<br>15.2 | 0.53±0.13 | 0.46±0.075 |

**X-ray photoelectron spectroscopy (XPS)**

Figure S5 show the X-ray photoelectron (XPS) spectra of two samples of BSA-gold.

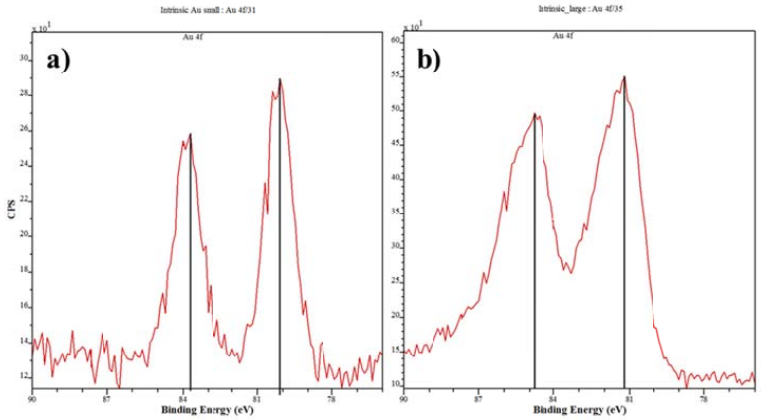


Figure S5: XPS spectra of **a)** BSA AuNCs and **b)** BSA AuNPs synthesized via the Intrinsic protocol. The AuNCs were synthesized with 5mM TCAA, while the AuNPs were synthesized with 20mM TCAA.

**Time Correlated Single Photon Counting (TCSPC)**

Time-correlated single-photon counting (TCSPC) measures the intensity decay of fluorophores on a nanosecond timescale.[7] Fluorescence lifetime measurements can give information about variation in the local environment of a fluorophore [8,9] and conformational changes in proteins. [10,11] TCSPC was performed with a 280 nm LED ($\lambda_{ex}$=*280nm*), and measuring the emission at 360 nm ($\lambda_{em}$=*360nm*). The fractional contribution of each decay time to the steady-state intensity, $f_i$ is determined from the decay times, $T_i$ and $B_i$ which is the relative population of the components at $t = 0$, as shown in equation S1. [7]

$$f_i = \frac{B_i T_i}{\sum_j B_j T_j} \qquad \text{(S1)}$$

All samples were best fit by biphasic decay, yielding one short ($T_1$) and one long ($T_2$) lifetime and their relative populations $B_1$ and $B_2$.

**Table S2: Lifetimes and Populations**

| Synthesis | TCAA (mM) | T1 (ns) | B1 (%) | T2 (ns) | B2 (%) |
|---|---|---|---|---|---|
| Intrinsic | 0 | 1.5±0.021 | 33.2±0.18 | 4.9±0.027 | 8.1±0.0049 |
| | 5 | 1.1±0.021 | 37.5±0.22 | 4.4±0.030 | 8.3±0.0048 |
| | 7,5 | 0.91±0.015 | 41.6±0.23 | 4.3±0.033 | 7.0±0.0043 |
| | 10 | 0.47±0.020 | 69.6±0.40 | 3.5±0.047 | 5.7±0.0041 |
| | 15 | 0.38±0.018 | 91.8±0.48 | 3.6±0.088 | 3.1±0.0029 |
| | 20 | 0.24±0.0083 | 160.4±0.85 | 3.7±0.095 | 1.8±0.0022 |
| Extrinsic | 0 | 2.04±0.031 | 22.7±0.13 | 5.9±0.028 | 8.68±0.0046 |
| | 5 | 1.63±0.027 | 26.5±0.14 | 4.7±0.033 | 6.9±0.0038 |
| | 7,5 | 1.45±0.027 | 27.6±0.15 | 5.4±0.033 | 7.03±0.038 |
| | 10 | 1.09±0.021 | 35.0±0.17 | 5.1±0.047 | 4.5±0.030 |
| | 15 | 0.81±0.017 | 40.9±0.20 | 5.5±0.052 | 3.6±0.023 |
| | 20 | 0.43±0.013 | 68.9±0.37 | 5.0±0.058 | 3.7±0.023 |

From 7.5mM-10mM TCAA, there is a large decrease in T1 and T2 for both the intrinsic and extrinsic synthesis. At 10mM TCAA, steady-state fluorescence data show an increased growth of large AuNCs, indicating that large AuNCs induce more prominent conformational changes compared to small AuNCs. From 7.5-10mM, the T1 for the intrinsic synthesis is reduced by a factor of 2.7, while the extrinsic T1 is reduced by a factor of 2. Since the protein is the sole reducing agent in the intrinsic synthesis, shorter lifetimes could indicate that there are larger changes in the polypeptide chain when ascorbic acid is not present.

The lifetime populations for the intrinsic and extrinsic samples show that as the size of gold increases, there is an increased short lifetime population (B1), and a concerted decreased long lifetime population (B2). The short and long populations show the relative percentage of fluorophores for the short and long lifetimes, respectively. At concentrations below 7.5mM TCAA chi-squared values ($\chi^2 \sim 1$) indicated a good fit, while above 7.5mM TCAA chi-squared values ($\chi^2 > 2$) were less ideal. Increasing the exponential fit for samples with concentrations above 7.5mM, would give a better fit, but with more contribution from noise. [7] The data above 7.5mM TCAA can therefore not be used quantitatively, but qualitatively to indicate what happens to the protein when the concentration of TCAA is increased.

The prominent increase in B1 at 10mM could be an effect of the large conformational changes in BSA that takes place when large AuNCs appear. At 10mM TCAA, steady-state data of Trp emission reveal large changes in protein conformation, which would greatly affect TCSPC data as well. Because the lifetimes were measured with a 280 nm LED, it could be that as BSA changes conformation, tyrosine residues are exposed and contribute to the emission, thus increasing the overall lifetime populations. [7,12] Overall, the results reveal the same trend of lifetimes and populations for BSA with or without ascorbic

acid. With increased size of BSA-gold, the short (T1) and long (T2) lifetimes decreased, while the short lifetime populations (B1) increased and the long lifetime populations (B2) decreased. There is a large difference in the short and long lifetimes of native BSA and BSA with AuNPs (20mM TCAA) indicating that the fluorophore on average spends less time in the excited state, which is probably caused by an increased exposure to water or energy transfer to BSA-gold, or a combination of the two. [13] Increased quenching of Trp emission with size of BSA-gold was also observed with steady-state fluorescence, showing that the protein gradually changes conformation as a result of the gold size.

**Toxicity assay on glioblastoma-astrocytoma cells**

Misfolded proteins are usually devoid of normal biological activity and can aggregate or interact with cells in an unwanted manner. [14,15] For example, in Alzheimer's disease, neurodegeneration is caused by amyloid plaques formed by misfolded β-amyloid protein aggregation.[16,17] As shown earlier, the tryptophan emission intensity was found to be inversely proportional to the size of gold, meaning that the folding of BSA is more affected with larger species of gold. If BSA-AuNCs or BSA-AuNPs either do or do not aggregate or interact with cell membranes, they could be used in different applications. Biocompatible constructs of BSA-stabilized gold can be used as drug delivery vehicles, while BSA-stabilized gold that aggregate and interact with cell membranes can be used as a drug in itself.

To this end, we tested the interaction of our BSA stabilized AuNCs and AuNPs with glioblastoma-astrocytoma cells *in vitro* and thus assessed their suitability as potential drug delivery vehicles in the therapy of glioblastoma multiforme. Glioblastoma multiforme is the most common primary brain tumor in adults. [18,19] It is very aggressive [20] and exhibit low response to conventional chemotherapeutic drugs.[21] Despite advances in therapy, [19] the estimated median survival of affected patients is one year.[20] To our knowledge, this is the first reported study on BSA-stabilized gold interaction performed on brain cancer cells. Previously, we have shown that the protein is important for the stability and size-tunability of the gold nanoconstructs. [13] Recently, we showed that synthesis of Transferrin-stabilized AuNCs had large surface affinities towards monolayers, and tended to localize on cell membranes *in vitro*. [22]

Human glioblastoma astrocytoma cells (U-87 MG, Sigma Aldrich) were cultured in Eagle's Minimal Essential Medium (EMEM) with 1.25% gentamicin (Sigma) and 10% fetal bovine serum (Autogen Bioclear, Wiltshire, UK). The cultures were supplemented with 2mM L-Glutamine, 1% non-essential amino acids (NEAA) (Sigma), and 1mM sodium pyruvate (NaP) (Sigma). Cells were labelled with BSA, BSA-AuNCs and BSA-AuNPs at concentrations of BSA/media volume of 1mg/mL, and incubated at 37°C for 24 hours. Unlabelled glioblastoma-astrocytoma cultures, at the same stage of confluence, were used as controls. After labeling, a LIVE/DEAD® cell viability assay (Invitrogen, Life Technologies) was performed on glioblastoma-strocytoma cultures. LIVE/DEAD® solution was prepared in 4.5mL PBS with 2.7µL calcein (InVitrogen), and 12µL ethidium homodimer (Invitrogen), was added to each well at 1:1 (v/v) and left to react for 30 minutes at 37°C. A LIVE/DEAD assay is a method for quickly assessing if there is a substantial cell death in one cell population compared to another. By taking images of the same magnification in the same area for all samples (*i.e* in the centre of the cell plate), it is possible to get information of the overall cell death. In Figure S6, dead cells were counted and the average amount of dead cells per image was calculated.

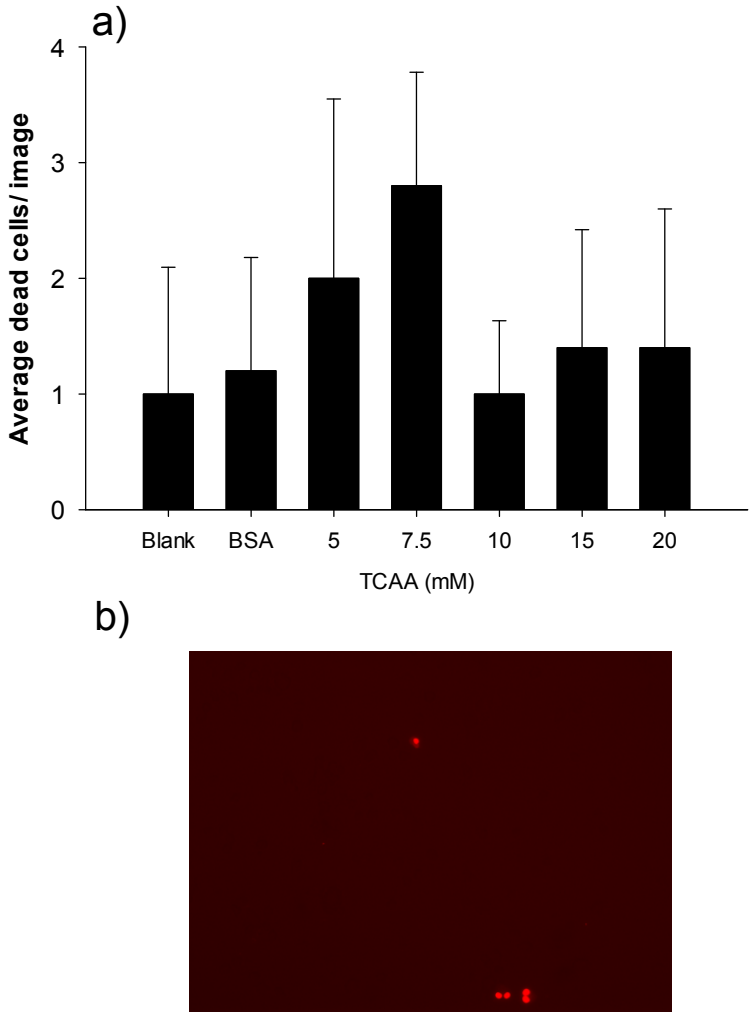


Figure S6: Dead glioblastoma-astrocytoma cells after incubation with BSA-AuNCs and BSA-AuNPs. a) Dead glioblastoma-astrocytoma cells counted with different concentrations of TCAA. The number of images counted per sample were 5. b) Glioblastoma astrocytoma cells grow very fast, and can therefore have multinucleate cells. In the example given, cell nuclei that lay very close to each other is counted as one cell.

No increased cell death was observed for any BSA-stabilized gold when compared to blank samples. This suggests that the BSA-stabilized gold described here do not aggregate or negatively impact cell membranes, which opens up for drug delivery applications. Compared to previous work on different proteins, these results indicate that the membrane affinity is also dependent on the protein. [13,22]

**Computed Tomography**

X-ray computerized tomography is a diagnostic imaging technique based on different tissue absorptions. For improved diagnostics, organic contrast agents (CAs) containing iodine is commonly used for enhanced attenuation. However, these CAs have very short circulation times. Because of their surface plasmon resonance, and inherently high attenuation coefficients (at 100keV gold has an attenuation coefficient of 5.16, while iodine has 1.94) AuNPs below 100nm have attracted a lot of attention as potential CT CAs. [48, 49] Here, three batches of large BSA-stabilized AuNPs were synthesized and their X-ray attenuation coefficients were measured (Figure S7). The size of the BSA-AuNPs determined the CT attenuation, with the smallest AuNPs giving the best attenuation. This is most likely caused by an increase in the surface area with decreasing size[50]. The mechanism of BSA-AuNP growth presented here can be used to determine the optimal size for CT imaging. The attenuation coefficient increase linearly with BSA-AuNP concentration which is comparable to what has been reported in previous studies with PEG-coated AuNPs for in vivo CT imaging. [51, 52]

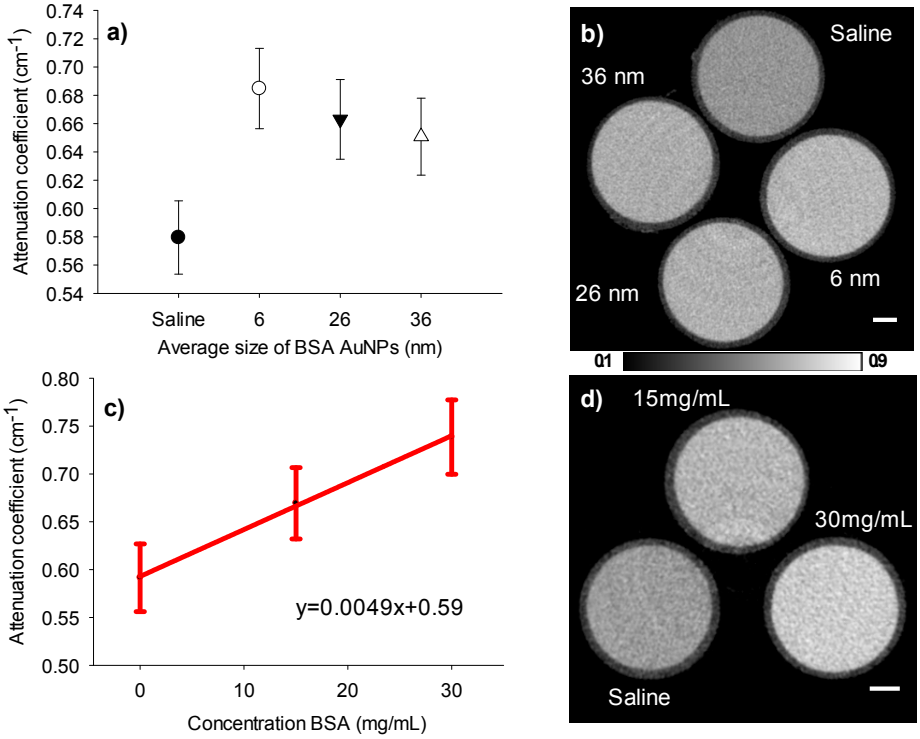


Figure S7: X-ray attenuation of BSA-AUNPs. a) With increasing size, the attenuation coefficient decrease. Saline is shown as a control. b) A slice of the reconstructed attenuation coefficient map of the CT phantom consisting of saline and three BSA-AuNP solutions (20 mg/ml) with different average sizes (6nm, 26nm, and 36nm). The scale bar is equal to 1 mm. c) Plot of the mean attenuation coefficient vs. BSA-AuNP concentration for the sample with the highest attenuation coefficient in a), *i.e* the sample containing average sized AuNPs of 6nm. Error bars indicate standard deviations. Solid line represents the linear regression line. d) Reconstructed image slice of the phantom from suspensions plotted in c).

For Computed tomography, sizes of the AuNPs were determined with ImageJ, and size fitting was determined with OriginPro 9.0 software. For the largest sample, a Gaussian fit was used, while for the two smallest samples a LogNormal fit was used. Figure S8 show some of the images acquired with STEM, and the calculated average and standard deviations.

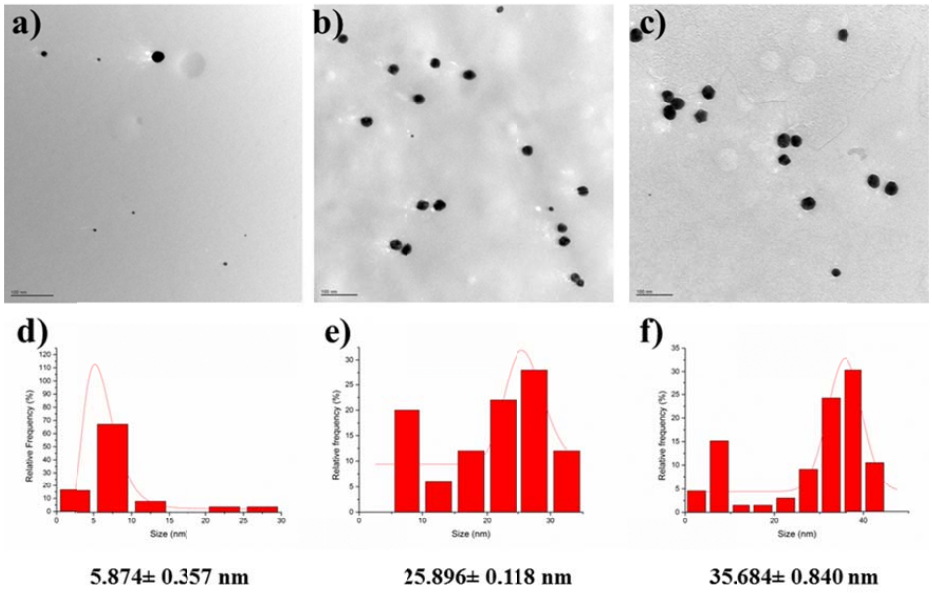


Figure S8: Size-determination of BSA AuNPs for Computed tomography. Images a)-c) show STEM-images of BSA-AuNPs. The error bar is 100 nm for all images. Graphs d)-f) show the fitted averages and standard deviations for the image a)-c), respectively.

**Time-resolved steady-state fluorescence spectra of Trp ($\lambda_{ex}$=*295nm*) and AuNC emission ($\lambda_{ex}$=*370nm*)**

Figure S9 displays steady-state fluorescence emission spectra ($\lambda_{ex}$=*370nm*) for six samples incubated with different amounts of TCAA and ascorbic acid (*i.e* the extrinsic method). Figure S10 show the tryptophan emission ($\lambda_{ex}$=*295nm*) from the same samples. Spectra were recorded over the time span of one week. The blue lines in each specter show the emission after 24 hours incubation time, while the red lines show the emission after 1 week (169 hours). The emission from Trp residues in BSA did not change much over the time course of 169 hours.

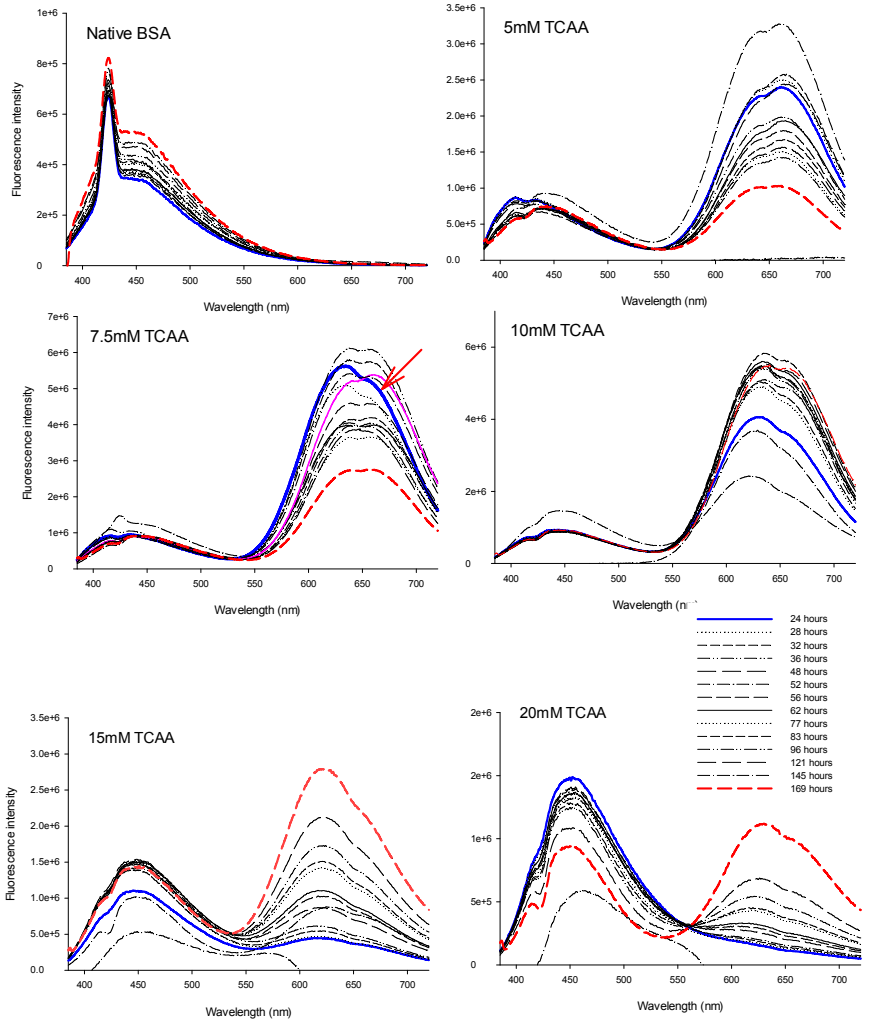


Figure S9: Time-dependent growth of gold nanoclusters followed by steady-state fluorescence, $\lambda_{ex}$=370nm**.** The six graphs show spectra of six different samples incubated with the extrinsic method taken over a time-period of one week. The BSA

spectra were subtracted for all samples to show only the contribution of the AuNC emission. The arrow indicates a shift in the shoulder from left to right after 62 hours.

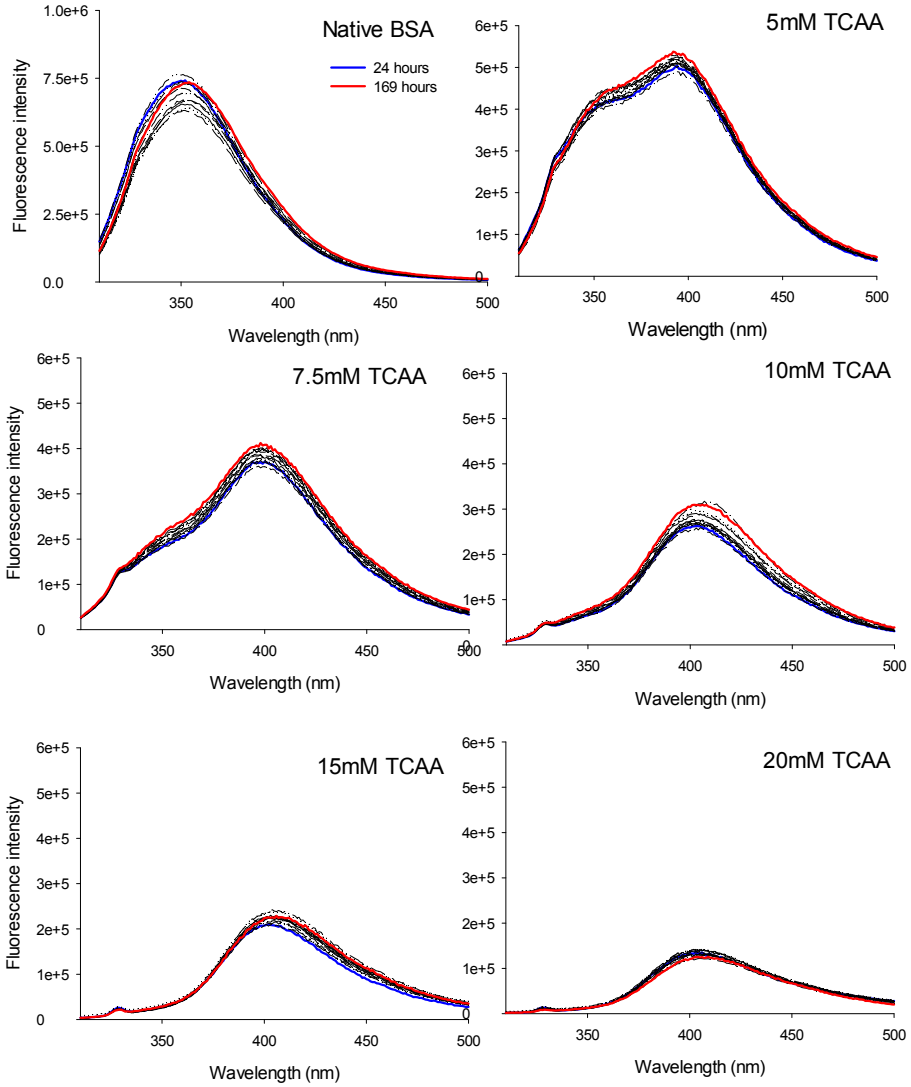


**Figure S10: Changes in tryptophan emission with time and different gold precursor concentrations.** Red line is after 24 hours, blue line is after one week. The purple line in graph *Native BSA* is the emission of tryptophan after 52 hours.

The integral of the Trp emission as a function of time is given in figure S11.

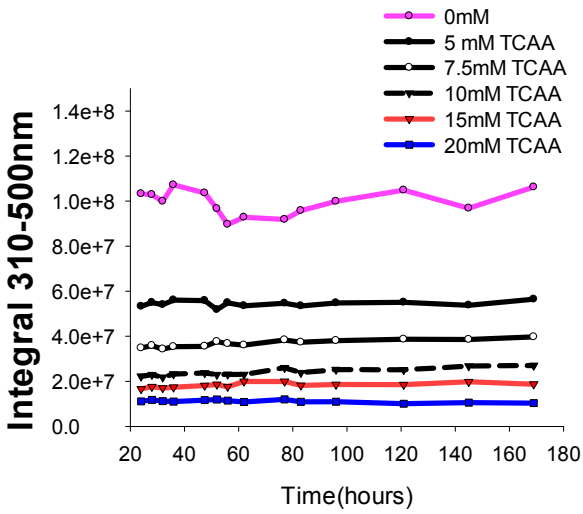


**Figure S11:** Trp emission integral as a function of time and concentration of TCAA.

**References:**


(1) Peters, S.; Peredkov, S.; Neeb, M.; Eberhardt, W.; Al-Hada, M. *Surf. Sci.* **2013**, *608*, 129.
(2) Le Guével, X.; Hötzer, B.; Jung, G.; Hollemeyer, K.; Trouillet, V.; Schneider, M. *J. Phys. Chem. C* **2011**, *115*, 10955.
(3) Tanaka, A.; Takeda, Y.; Imamura, M.; Sato, S. *Physical Review B* **2003**, *68*, 195415.
(4) McArthur, S. L. *Surf. Interface Anal.* **2006**, *38*, 1380.
(5) Sezen, H.; Suzer, S. *Thin Solid Films* **2013**, *534*, 1.
(6) Hajati, S.; Tougaard, S. *Anal. Bioanal. Chem.* **2010**, *396*, 2741.
(7) Lakowicz, J. R. *Principles of Fluorescence Spectroscopy*; 3 ed.; Springer: USA, 2006.
(8) Yuan, C. T.; Chou, W. C.; Tang, J.; Lin, C. A.; Chang, W. H.; Shen, J. L.; Chuu, D. S. *Opt. Express* **2009**, *17*, 16111.
(9) Castelli, F.; White, H. D.; Forster, L. S. *Biochemistry* **1988**, *27*, 3366.
(10) Julien, O.; Wang, G.; Jonckheer, A.; Engelborghs, Y.; Sykes, B. D. *Proteins: Structure, Function and Bioinformatics* **2012**, *80*, 239.
(11) Hochstrasser, R. M.; Negus, D. K. *Proc. Natl. Acad. Sci. U. S. A.* **1984**, *81*, 4399.
(12) Lystvet, S. M.; Volden, S.; Yasuda, M.; Halskau Jr, O.; Glomm, W. R. *Nanoscale* **2011**, *3*, 1788.
(13) Lystvet, S. M.; Volden, S.; Singh, G.; Yasuda, M.; Halskau, O.; Glomm, W. R. *RSC Advances* **2013**, *3*, 482.
(14) De Paoli Lacerda, S. H.; Park, J. J.; Meuse, C.; Pristinski, D.; Becker, M. L.; Karim, A.; Douglas, J. F. *ACS Nano* **2010**, *4*, 365.
(15) Chiti, F.; Dobson, C. M. 2006; Vol. 75, p 333.
(16) Polymeropoulos, M. H.; Lavedan, C.; Leroy, E.; Ide, S. E.; Dehejia, A.; Dutra, A.; Pike, B.; Root, H.; Rubenstein, J.; Boyer, R.; Stenroos, E. S.; Chandrasekharappa, S.; Athanassiadou, A.; Papapetropoulos, T.; Johnson, W. G.; Lazzarini, A. M.; Duvoisin, R. C.; Di Iorio, G.; Golbe, L. I.; Nussbaum, R. L. *Science* **1997**, *276*, 2045.
(17) Walsh, D. M.; Klyubin, I.; Fadeeva, J. V.; Cullen, W. K.; Anwyl, R.; Wolfe, M. S.; Rowan, M. J.; Selkoe, D. J. *Nature* **2002**, *416*, 535.
(18) Würth, R.; Barbieri, F.; Florio, T. *BioMed Research International* **2014**, *2014*.

(19) Yuan, X.; Curtin, J.; Xiong, Y.; Liu, G.; Waschsmann-Hogiu, S.; Farkas, D. L.; Black, K. L.; Yu, J. S. *Oncogene* **2004**, *23*, 9392.
(20) Suvà, M. L.; Riggi, N.; Janiszewska, M.; Radovanovic, I.; Provero, P.; Stehle, J. C.; Baumer, K.; Le Bitoux, M. A.; Marino, D.; Cironi, L.; Marquez, V. E.; Clément, V.; Stamenkovic, I. *Cancer Res.* **2009**, *69*, 9211.
(21) Pallini, R.; Ricci-Vitiani, L.; Banna, G. L.; Signore, M.; Lombardi, D.; Todaro, M.; Stassi, G.; Martini, M.; Maira, G.; Larocca, L. M.; De Maria, R. *Clin. Cancer. Res.* **2008**, *14*, 8205.
(22) McDonagh, B. H.; Volden, S.; Lystvet, S. M.; Singh, G.; Ese, M.-H.; Ryan, J. A.; Lindgren, M.; Sandvig, A.; Sandvig, I.; Glomm, W. R. *Nanoscale* **2015**.

# Paper III

**_Makura_-shaped gold nanostructures show high cytotoxicity in cancer cells**

# *Makura*-shaped gold nanostructures show high cytotoxicity in cancer cells

*Sulalit Bandyopadhyay*[*,1], *Birgitte H. McDonagh*[1], *Gurvinder Singh*[2], *Axel Sandvig*[3,4], *Ioanna Sandvig*[4,5], *Wilhelm Robert Glomm*[1,6]

[1] Ugelstad Laboratory, Department of Chemical Engineering,

[2] Department of Materials Science and Engineering,

[3] Division of Pharmacology and Clinical Neurosciences, Department of Neurosurgery, Umeå University, 901 87 Umeå, Sweden

[4] Department of Neuroscience, Norwegian University of Science and Technology (NTNU), Trondheim, Norway.

[5] Department of Clinical Neurosciences, University of Cambridge, England, UK

[6] Sector for Biotechnology and Nanomedicine, SINTEF Materials and Chemistry, N-7465 Trondheim, Norway.

[*]*Corresponding author's email address:* sulalit.bandyopadhyay@ntnu.no

Is not included due to copyright

# Paper IV

**Pentatwinned iron oxide nanoparticles as glioblastoma-astrocytoma cell actuators**

Is not included due to copyright

# Paper V

**L-DOPA coated manganese oxide nanoparticles as dual MRI contrast agents and drug delivery vehicles**

WILEY-VCH

DOI:10.1002/smll.201502545
**Article type: Communication**

# L-DOPA coated manganese oxide nanoparticles as dual MRI contrast agents and drug delivery vehicles

*Birgitte Hjelmeland McDonagh*, Gurvinder Singh, Sjoerd Hak, Sulalit Bandyopadhyay, Ingrid Lovise Augestad, Davide Peddis, Ioanna Sandvig, Axel Sandvig, and Wilhelm Robert Glomm*

Birgitte Hjelmeland McDonagh, Sulalit Bandyopadhyay, Dr. Wilhelm Robert Glomm
Uglestad Laboratory, Department of Chemical Engineering, Norwegian University of Science and Technology, 7491, Norway
E-mail: birgitte.h.mcdonagh@ntnu.no
Dr. Gurvinder Singh,
Department of Materials Science and Engineering, Norwegian University of Science and Technology, 7491, Norway
Dr. Sjoerd Hak,
Department of Circulation and Medical Imaging, Norwegian University of Science and Technology, 7491, Norway
Ingrid Lovise Augestad, Dr. Ioanna Sandvig, Dr. MD. Axel Sandvig
Department of Neuroscience, Norwegian University of Science and Technology, 7491, Norway
Dr. Davide Peddis,
Institute of Structure and Matter, National Research Council, Monterotondo Scalo, Italy
Dr. Ioanna Sandvig
John Van Geest Centre for Brain Repair, Department of Clinical Neurosciences, University of Cambridge, CB2 OPY Cambridge, UK
Dr. MD. Axel Sandvig
Division of Pharmacology and Clinical Neurosciences, Department of Neurosurgery, Umeå University, 901 87, Sweden
Dr. Wilhelm Robert Glomm
Sector for Biotechnology and Nanomedicine, SINTEF Materials and Chemistry, 7465, Norway

Keywords: Manganese, Contrast Agents, MRI, L-DOPA

Imaging soft tissue of the human body with magnetic resonance imaging (MRI) is sometimes crucial for determining an accurate diagnosis. Acquired images can reveal obstructed blood flow, abnormal tissue structure and vascularization. To improve the accuracy of diagnosis, the contrast can be altered by administering magnetically active contrast agents (CAs), typically comprised of chelated ions such as gadolinium ($Gd^{3+}$) and manganese ($Mn^{2+}$). CAs can either enhance or decrease the contrast in the tissue depending on their magnetic susceptibilities, and CAs are referred to as either *positive* or *negative*, respectively. With the upsurge in synthesis and characterization of magnetically active nanoparticles (NPs), new nanoparticle-based systems with potential applications towards theranostics are emerging. NPs have longer blood circulation times as compared to chelates, [1] and the large surface-to-volume ratio of NPs results in a greater contact area between magnetically active centers and the tissue. Moreover,

the large surface area of NPs can be modified with biologically compatible molecules and drugs, which allows for simultaneous diagnostics and therapy.

Superparamagnetic iron oxide NPs (SPION) are widely used as they produce a dark/negative contrast in a T2/T2*-weighted image. SPIONs are used commercially (Lumirem®/Gastromark®), [2-4] and can be targeted to cancer tumors and as such provide therapy and diagnostics. [5-8] However, the hypointense signal can be confused with *e.g* magnetic susceptibilities, bleeding or calcification which can lead to inaccurate diagnosis.[9-11] In light of this, positive *T1* CAs are generally preferred because they give a hyperintense signal that is easier to distinguish from surrounding tissue and is less likely to be confused with artefacts. *T1* CAs are typically prepared from paramagnetic elements, such as $Gd^{3+}$ and $Mn^{2+}$, as they effectively shorten the local spin-lattice relaxation time (*T1* time). While chelates of gadolinium are used in the clinics (*e.g* Gadovist, Magnevist),[1,9] they suffer from challenges such as short circulation times, and severe side effects in patients with poor kidney function. [12, 13] Novel *T1* CAs must address these issues and simultaneously give equal or better contrast. Gadolinium NPs or polymeric nanoparticles conjugated with $Gd^{3+}$ show good signal-to-noise ratio and have been shown to target and visualize tumors. [14-17] However, there are several interesting benefits with using manganese-based CAs for MRI applications and drug delivery.

$Mn^{2+}$ ions are $Ca^{2+}$ analogues and can enter neurons through voltage-gated $Ca^{2+}$ ion channels, [18] which enables *in vivo* neuronal tract tracing in Manganese Enhanced MRI (MEMRI). [19, 20] Administrating high concentrations of $Mn^{2+}$ ions can affect the *T2*/*T2** times as well, [21,22] however, high doses of $Mn^{2+}$ can accumulate in the brain and cause a toxic condition named *manganism*. [23] Because of the toxicity, manganese-chelates are still regarded as alternative CAs in MRI. However, recent synthesis of manganese oxide-based NPs could lead to a resurgence of manganese as an MRI contrast agent, [24-27] and a recent report by Zhang et al demonstrate the efficacy of $Mn^{2+}$ ions as imaging probes for visualizing delivery of cancer therapeutic drugs. [28] Also, manganese oxide NPs (MONPs) are *T2/T2** active CAs, but they also degrade in water within a reasonable time-frame (hours to days). [25, 29-31] This is interesting for MR applications because MONPs that degrade, release $Mn^{2+}$ ions, which are very efficient *T1* CAs. [32-35] MONPs therefore offer a potentially very useful time-dependent *T2*/*T2** to *T1* contrast switch that allows both complementary MR images and improved diagnostics. [32]

Generally, metal oxide NPs are surface functionalized to be stable in water, by attaching either a stabilizing ligand, or a functional molecule which not only imparts colloidal stability but also an additional diagnostic/therapeutic function to the NP. The neurotransmitter dopamine is frequently used as a surface anchor connecting the surface oxide layer of the metal oxide NP with an outer polymer shell. [36-38] The hallmark of Parkinson's disease (PD) is gradual degeneration of dopaminergic neurons in the *Substantia Nigra pars compacta* (SNpc), leading to deficient dopamine content and severe cognitive and motor deficits. Dopamine is an important neurotransmitter for the function of the human retina and optic nerve (ON) [39, 40] and visual impairments in PD are common. [41] The symptoms can be caused by deficient dopamine content, [41] or from fiber layer thinning of the optic nerve. [42,43] Although dopamine is biologically relevant, the properties of its precursor, *L*-3,4-dihydroxyphenylalanine (L-DOPA), are far more interesting. L-DOPA is carried across the BBB *via* the LAT1 transporter, and is decarboxylated to dopamine in capillary endothelial cells. [44, 45] L-DOPA is orally administered and currently the drug of choice for patients suffering from Parkinson's disease (PD).

In the current work we aimed to develop L-DOPA stabilized MONPs which release $Mn^{2+}$ ions and L-DOPA simultaneously, a combined release which has not been reported previously. While L-DOPA can act as a scaffold for attachment to other functional molecules,[46] L-DOPA used both as a stabilizer and active drug is a novel concept.

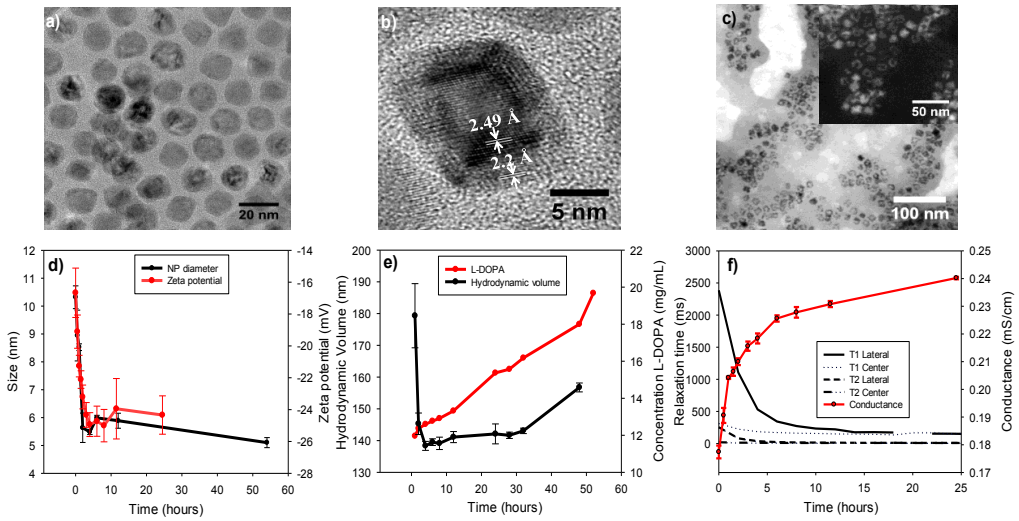


**Figure 1: MONPs degrade in water and release L-DOPA. a)** TEM of MONPs in organic phase **b)** HRTEM image of MONPs before surface modification **c)** TEM of L-DOPA coated MONPs, 1 hour in water (pH=6.8). Inset shows dark field image of hollow MONPs after 1 hour in water **d)** Diameter of MONPs and ζ-potential of MONPs as a function of time **e)** Hydrodynamic volume and concentration of L-DOPA as a function of time **f)** *T1* and *T2* relaxation time in pig eyes upon injection of MONPs, as a function of time. "Lateral" refers to the opposite side of the injection site, while "Center" refers to the mid part of the pig eye. Conductance as a function of time is also shown.

The objectives of this study were as follows: First, we wanted to characterize how fast and in what way the MONPs degrade in water. Second, we wanted to determine the magnetic properties of MONPs, and whether release of $Mn^{2+}$ from MONPs is efficient enough to gain complementary images *in vivo*. Finally, we wanted to determine whether L-DOPA is released from the NPs, which may be of value for potential applications in Parkinson's disease (PD).

In a typical synthetic procedure, MONPs (15±5 nm) were synthesized *via* thermal decomposition of Mn-oleate in a high boiling point organic solvent (**Figure 1a**). [47, 48] High resolution transmission electron microscopy (HRTEM) suggests a core-shell morphology of $Mn_2O_3$-MnO NPs (Figure 1b). The lattice fringe spacing of the core (~2.49 Å) corresponds to the separation between the (211) lattice planes of tetragonal $Mn_3O_4$. The lattice spacing of the shell (~2.2 Å) corresponds well to (200) interplanar spacing of MnO. The MnO shell has an average thickness of ~2.1 nm. The X-ray diffraction (XRD) pattern also suggests the presence of mixture of phases in MONPs (Figure S2).[49] The investigation of magnetic properties confirms the morpho-structural characterization, suggesting the presence of $Mn_3O_4$-MnO phases. Bulk $Mn_3O_4$ is a ferrimagnetic spinel-type compound (Curie temperature, $T_{C,Mn2O3}$=43 K), while MnO is an antiferromagnetic compound (Néel temperature, $T_{N,\ MnO}$=100 K). [49] Temperature dependence of magnetization measuring in Field Cooling (FC) condition shows a transition around 40 K (close to $T_C$ of $Mn_3O_4$) suggesting that the magnetic behavior of the sample is dominated by the ferrimagnetic $Mn_3O_4$ (Figure S3). This is supported by the field dependence of magnetization, showing a quasi-static behavior at 5 K and paramagnetic behavior at 80 K (above $T_C$). It is important to underline that the hysteresis loop at 5 K shows a clear non-saturating character at high field, suggesting the presence of an antiferromagnetic

contribution that can be ascribed to the presence of a small quantity of MnO in the shell. [49-51] In addition, X-ray photoelectron spectroscopy (XPS) showed mixed oxidation states of MONPs (Figure S4-6), that further support the HRTEM, XRD and magnetic measurements described above.

A simple one-step protocol was used to functionalize the MONPs with L-DOPA and transfer the NPs from organic to water phase.[52] After functionalization, MONPs were collected with centrifugation and dispersed in MilliQ water (5mg/mL). Earlier studies have shown that when anchoring dopamine on metallic NPs, the two hydroxyl groups in the aromatic ring bind to the oxide layer of the NP surface, and the amine group is oriented towards the bulk.[36-38] At the pH used here (pH=6.8), the carboxylic acid moiety of L-DOPA is deprotonated, and functionalized MONPs were found to be negatively charged (Figure 1d). As L-DOPA only differs from dopamine by a carboxylic group, the surface organization of L-DOPA is most likely identical to that of dopamine, *i.e.*; with its carboxylic group pointing outwards. From XPS measurements, MONPs surface functionalized with L-DOPA showed the presence of nitrogen, which was absent prior to functionalization (Figure S.5). Also, high resolution C1 spectra showed contribution of C-O, C-N, C-C and O-C=O, which combined with the N-peak suggests that the L-DOPA molecules are anchored to MONPs *via* its two hydroxyl groups. Thus, bulk-oriented carboxylic acid groups can act as anchor points for addition of secondary molecules onto NPs by covalent bonding with amine groups, *e.g. via* carbodiimide chemistry.

After one hour in water, the average MONP diameter is halved (Figure 1d). TEM images reveal that MONPs are no longer dense particles, but smaller structures with a quadratic edge and a hollow interior (Figure 1c). This indicates that MONPs degrade via oxidation and dissolve in water, releasing $Mn^{2+}$. [33] Oxidation of NPs that leads to hollow or porous structures is caused by the Kirkendall effect, which describes that atomic diffusion is caused by an exchange of vacancies, and not by an interchange of atoms. [53] Here, the outward diffusion of $Mn^{2+}$ ions is exchanged with an inward flux of vacancies. With time, the manganese oxide shell breaks and the fragments continue to degrade until they are completely dissolved (Figure S1).

The hydrodynamic diameter (Figure 1e) is significantly larger than the diameter estimated from TEM images (Figure 1d), which is expected. This is an effect of the high charge density of the MONPs measured by the ζ- potential (Figure 2a), which contributes to a higher hydration. The increase in ζ-potential with time (Figure 2a) could also be an effect of changes in adlayer concentration, reorientation, or change in the surface affinity of L-DOPA.

Functional molecules are usually attached to NPs with a covalent bond, and a successful drug delivery vehicle must not only carry the drug, but also release it. Breaking the covalent bond *in vivo* can be a challenge, and may impair drug delivery efficiency. Since MONPs disintegrate in water, L-DOPA will eventually be released form the MONPs. The bulk concentration of L-DOPA steadily increases with decreasing NP diameter (Figure 1e). Our results show that the MONPs disintegrate in water within 50 hours, releasing L-DOPA into the surrounding medium.

In order to assess their use as CAs in biological systems, the time-dependent contrast switch of MONPs was described in pig eyes, *ex vivo*. Pig eyes are similar to human eyes, the specimen size allows for a good signal-to-noise ratio, and they offer a more biologically relevant matrix compared to agarose gels, which are more widely used.[54] MONPs coated with L-DOPA were freshly prepared, injected into pig eyes, and scanned with MRI over a period of 34 hours.

Release of $Mn^{2+}$ is clearly visible in the *T1w* image, as it takes the form of a bright hyperintense cloud surrounding the hypointense injection site (Figure 2a). In the *T2*w* image, the $Mn^{2+}$ ions and MONPs give rise to negative contrast as well, proving the dual properties of manganese as active *T1* and *T2** CAs (Figure 2d). [32] With time, the negative contrast

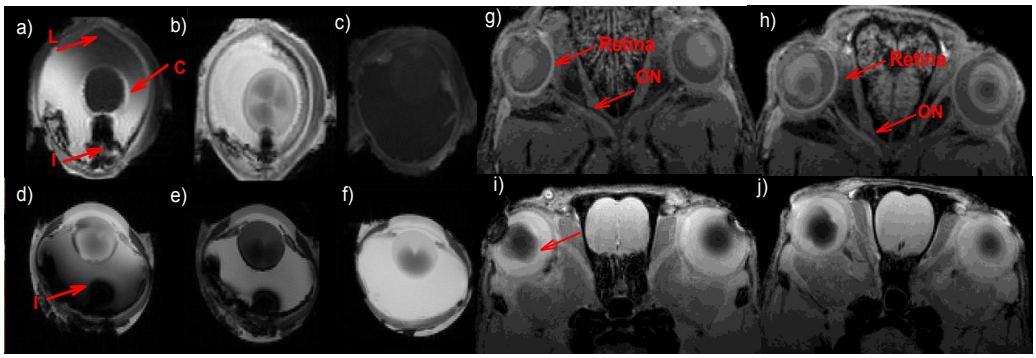


**Figure 2: *Ex vivo* and *in vivo* degradation of MONPs.** Images **a)** and **b)** show the *T1w* images of a pig eye injected with MONPs, acquired immediately after injection and after 34 hours, respectively. "L" refers to the lateral side of the injection site "I", while "C" refers to the central part of the pig eye. Images **d)** and **e)** show the complementary *T2*w* images immediately after injection and 34 hours after injection, respectively. Image **c)** is the *T1w* and image **f)** is the *T2*w* image of the control eye, immediately after injection and 34 hours after injection, respectively. **g)** *T1w* and **i)** *T2*w* image of rat ON and retina, 1 hour post injection. **h)** *T1w* and **j)** *T2*w* image of rat ON and retina, 24 hours post injection.

decreases in both the *T1w* (Figure 2b) and *T2*w* (Figure 2e) images, while the positive contrast in the *T1w* image completely fills the whole intravitreal space (Figure 2b). The *T1* and *T2* relaxation times in the pig eyes rapidly decrease after injection of MONPs. In particular, the *T1* relaxation time at the center of the eye decreases with a simultaneous increase in the conductance (Figure 1f). A change in the conductance indicates a change in the ionic strength of the suspension. [55] The change in conductance and the concomitant effect on relaxation times and *ex vivo* contrast, suggests that MONPs disintegrate into $Mn^{2+}$.

The rodent visual system is an established model for investigating damage and repair in the central nervous system (CNS), [3, 56, 57] as it is easily accessible and immune privileged.[58, 59] Enhanced visualization of the ON tract can be achieved by administering contrast agents into the vitreous body. Additionally, the retina may act as a barrier to the MONPs while at the same time allowing the $Mn^{2+}$ ions to traverse through and visualize the optical nerve. This will spatially separate the *T1* contrast obtained from $Mn^{2+}$ ions from the *T2** contrast of the MONPs that will be trapped in the vitreous body.

The contrast in the rat retina is significantly enhanced compared to the contralateral control eye immediately upon injection of MONPs (Figure 2g). The *T2** contrast (Figure 2i, j) is not clearly separated from the rodent lens, but after 24 hours, the contrast moves towards the retina. This movement is also seen in the complementary *T1w* images (Figure 2 h). With time, the contrast in the ON increases as well (Figure 2h). MONPs are likely too large to be taken up by the retinal ganglion cells, but $Mn^{2+}$ ions can.[22, 56] We have previously used $MnCl_2$ to study optic nerve regeneration in several animal models. [22, 56, 60] However, using MONPs opens up for complementary and long term imaging without injecting additional doses of CAs.

**In conclusion**, we have developed MONPs functionalized with L-DOPA that gradually degrade in biological media, releasing $Mn^{2+}$ ions and L-DOPA. A combination which has not been described previously. As CAs in MRI, MONPs give negative contrast, but as they disintegrate in water, a concomitant release of $Mn^{2+}$ ions gives a positive contrast. The system described here, thus offers a time-dependent switch in the MR contrast from dark to

bright, which allows for complementary imaging and enhanced diagnosis. While further studies are needed to determine the effect of L-DOPA coated MONPs in a PD model, we have herein described a system that can release L-DOPA and that has potential as a drug delivery vehicle.

**Experimental Section**

*Chemicals.* L-DOPA (3,4-dihydroxy-L-phenylalanine), anhydrous n-hexane (95%), chloroform, dimethyl sulfoxide (DMSO) and hexadecane was purchased from Sigma. Mn(II) chloride tetrahydrate. (99.0%) was purchased from Fluka. Sodium oleate (97.0%) was purchased from TCI. Oleic acid (90%) was purchased from Alfa Aesar.

*Synthesis of MONPs from Mn-Oleate.* First, Mn-Oleate was prepared by reacting $MnCl_2$. with sodium oleate as reported in the literature. [[1]] Briefly, $MnCl_2.4H_2O$ (9.96 mmol, 3.95g) and sodium oleate (60.76 mmol, 18.5 g) were added into the mixture of water (40mL), ethanol (30mL) and anhydrous n-hexane (70mL). The mixture was left to react for 4 hours at 70°C. Mn-Oleate was washed twice with water and collected with a separation funnel. MONPs were synthesized by thermal decomposition of a Mn-oleate complex. [2] Briefly, 1.32 g Mn-Oleate was dissolved in the mixture of 600µL oleic acid and 20 mL hexadecane. The solution was slowly heated up to 300°C with 3.0°C/min under vigorous stirring and argon atomsphere. The solution was left to react for 40 minutes before cooling to room temperature. MONPs were precipitated with 20mL hexane and 80 mL acetone followed by centrifugation. After discarding the supernatant, the precipitated solid was washed twice with hexane and acetone. Finally, MONPs were dispersed in toluene.

*Surface coating of MONPs with L-DOPA.* A modified procedure based on Xie *et al* [3] was used to coat MONPs with L-DOPA. Briefly, 5mg of dried MONPs were dissolved in chloroform and mixed with 20mg L-DOPA and 2mL DMSO and stirred to form a homogeneous solution. The suspension was heated to 70°C and left to react for one hour under inert atmosphere. MONPs surface coated with L-DOPA were collected by centrifugation (4500rpm, 10 min). After removal of the chloroform and DMSO, the product was re-dispersed in acetone and centrifuged again to remove unbound L-DOPA. This step was reiterated until the product adhered to the centrifuge tube. The product was left to dry overnight before characterization.

*UV-visible spectroscopy* was performed on a Shimadzu UV-2401PC spectrophotometer in the range 200-800nm using UVProbe2.1 as software.

*Scanning (Transmission) electron microscopy (STEM)* images were acquired in bright-field S(T)EM mode using a Hitachi S-5500 electron microscope operating at 30 kV accelerating voltage. TEM grids were prepared by placing a drop (20 µL) of the MONP solution on a Formvar carbon coated copper grid (Electron Microscopy Sciences) and allowing the solvent to evaporate at room temperature, prior to imaging. The average sizes of NPs were determined with log normal fitting using *OriginPro 9.0 64bit* software.

*High resolution transmission electron microscopy (HR-TEM)* images were acquired on a JEOL JEM-2100 (200 kV). The samples were prepared by depositing a few µl drop of nanoparticle solution on a copper grid coated with amorphous carbon layer, and allowed to dry prior to imaging.

*X-ray powder diffraction (XRD)* patterns of dried MONPs were obtained from a Bruker DaVinci2 diffractometer using Cu Kα (λ= 1.54056 ˚A) in the 2θrange with 10–75 degree.

*X-ray photoelectron spectroscopy (XPS)* analyses were performed using a Kratos Axis Ultra DLD spectrometer (Kratos Analytical, UK), equipped with a monochromatized aluminum X-ray source (Al, hυ = 1486.6 eV) operating at 10 mA and 12 kV (150 W). A hybrid lens (electrostatic and magnetic) mode was employed along with an analysis area of approximately 300 µm X 700 µm. Survey spectra were collected over the range of 0-1100 eV binding energy with analyzer pass energy of 160 eV, and high resolution spectra of C 1s, O 1s, N 1s, and Mn

2p were obtained with an analyzer pass energy of 20 eV. XPS data were processed with Casa XPS software (Casa Software Ltd., UK).

*ζ-potential, mobility and conductance measurements* were performed with a Malvern Zetasizer Nano-ZS instrument at 20°C and results analyzed using DTS software.

*Magnetic measurements.* The dc magnetization measurements were performed by a Quantum Design SQUID magnetometer ($H_{max}$ = 5 T). To avoid any movement of the nanoparticles during the measurements, the sample, in form of powder, was immobilized in epoxy resin. Magnetization versus temperature measurements were performed using the zero-field-cooled (ZFC) and field-cooled (FC). ZFC− FC magnetization measurements were carried out by cooling the sample from room temperature to 5 K in zero magnetic field; then a static magnetic field was applied. $M_{ZFC}$ was measured during warming up from 5 to 300 K, whereas $M_{FC}$ was recorded during the subsequent cooling.

*In vivo* and *Ex vivo* Magnetic Resonance Imaging was performed on a 7T Bruker Scanner (Biospec 70/20 AS, Bruker Biospin MRI, Ettlingen, Germany). All animal procedures were in accordance with the Norwegian Ethics Committee for the use of laboratory animals. For *in vivo* imaging, a 86 mm volume resonator for RF transmission, and a receive only actively decoupled rat head quadrature surface coil was used. Rats were put to sleep with 2% isoflurane (Sigma) in 30% $O_2$ and 70% $N_2$ before intraperitoneal injection of Haldol (Janssen, 0.4mg/100g rat) for complete anesthesia. 12 Sprague Dawley rats (n=12) received a unilateral, intravitreal injection of 5µL of either MONP-L-DOPA (865nmol, n=2, 433nmol, n=1, or 18.2nmol, n=3) or $Fe_2O_3$-PEG nanoparticles (179nmol n=1 or 17.9nmol n=5) as control. The contralateral eye was used as control. Because MONPs-L-DOPA immediately starts to degrade once dissolved in water, the nanoparticles were dissolved by sonication right before injection. Rats were placed in an animal bed with water heating (37° C), and the respiration rate was continuously monitored using a pressure-sensitive probe (SA Instruments, New York, NY, USA). In order to reduce artifacts from eye movements, eye gel (Viscotears®, Novartis) was applied before sealing the eyelids using medical tape (3M). **T1** *FLASH and MGE specifics.* Using paravision 5.1 (Bruker, Bruker Biospin MRI, Ettlingen, Germany), rats were imaged with a T2*-weighted multi gradient echo (MGE, echo time (TE) of 6 ms repetition time (TR) of 1000 ms, flip angle (FA) of 30°, field of view (FOV) of 28x25 mm, matrix (MTX) of 224x200, 20 slices of 0.667 mm, and 5 averages, lasting 16 min and 40 s) and a T1 weighted 3D-FLASH (TE of 3.53 ms, TR of 12 ms, FA of 30°, FOV of 35x27x22 mm, MTX of 224x173x141, zero fill acceleration of 1.34, 12 averages, lasting 33 min and 38 s).Rats injected with MONPs-L-DOPA were imaged 1, 24 and 48 hours post injection, while rats injected with $Fe_2O_3$-PEG nanoparticles were imaged 24 and 48 hours post injection.

*Ex vivo studies in pig eyes.* 500µL of either $Fe_2O_3$-PEG (10g/L, 89.5µmol) or 500µL MONPs-L-DOPA (9.5g/L, 86.5µmol) were injected in the intravitreous body of pig eyes (Noroc, Duroc or Norwegian Farm pig, obtained from *Nortura*). A third eye was used as a control. The three eyes were placed in a 2ml centrifuge tube, with the reference eye in the middle. T1-FLASH and MGE images and T2 and T1 maps were continuously collected at room temperature over a time span of 50 hours, using a 72 mm transmit receive volume resonator. T1- weighted images were collected using a3D FLASH sequence (TE of 3.65 ms, TR of 12 ms, FA of 30°, FOV of 72x32x30 mm, MTX of 240x107x100, zero fill acceleration of 1.34, 12 averages, lasting 14 min and 46 s) and T2*-weighted images were obtained with a MGE sequence (TE of 6 ms), TR of 2600 ms, FA of 30°, FOV of 32x30 mm, MTX of 107x100, 65 slices of 1 mm, and 3 averages, lasting 13 min). Note that these sequences are very similar to the sequences used in vivo. T1-maps were obtained with a spin echo sequence (TE of 8.45 ms, TR of 225, 230, 250, 300, 500, 1000, 2000, 5000, 12000 ms, FOV of 72x32 mm, MTX of 144x64, 15 slices of 1 mm, 1 average, lasting 22 min and 56 s) and T2-maps were obtained with a multi slice multi echo sequence (TE of 11.2 ms, echo spacing of 11.2 ms and 50 echos, TR of 12000 ms, FOV of 72x32 mm, MTX of 144x64, 15 slices of 1 mm, 1 average, lasting

12 min and 48 s). All MR images were processed using in-house developed software in MatLab R2012a and Image J 1.

**Supporting Information**
Supporting Information is available from the Wiley Online Library.

**Acknowledgements:** The Department of Chemical Engineering, NTNU, is acknowledged for financial support. The Research Council of Norway is acknowledged for the support to the Norwegian Micro- and Nano-Fabrication Facility, NorFab (197411/V30). Ioanna and Axel Sandvig would like to thank the Liaison Committee between the Central Norway Regional Health Authority (RHA) and the Norwegian University of Science and Technology (NTNU). Support from the Norwegian Financial Mechanism 2009–2014 and the Czech Ministry of Education, Youth and Sports under Project Contract no. MSMT-28477/2014; project 7F14057 is acknowledged.

1. Xu, W.; Kattel, K.; Park, J. Y.; Chang, Y.; Kim, T. J.; Lee, G. H. *PCCP* **2012,** 14, (37), 12687-12700.
2. Li, L.; Jiang, W.; Luo, K.; Song, H.; Lan, F.; Wu, Y.; Gu, Z. *Theranostics* **2013,** 3, (8), 595-615.
3. Sandvig, I.; Thuen, M.; Hoang, L.; Olsen, Ø.; Sardella, T. C. P.; Brekken, C.; Tvedt, K. E.; Barnett, S. C.; Haraldseth, O.; Berry, M.; Sandvig, A. *NMR Biomed.* **2012,** 25, (4), 620-631.
4. Huang, G.; Li, H.; Chen, J.; Zhao, Z.; Yang, L.; Chi, X.; Chen, Z.; Wang, X.; Gao, J. *Nanoscale* **2014,** 6, (17), 10404-10412.
5. Artemov, D.; Mori, N.; Okollie, B.; Bhujwalla, Z. M. *Magn. Reson. Med.* **2003,** 49, (3), 403-408.
6. Jalalian, S. H.; Taghdisi, S. M.; Shahidi Hamedani, N.; Kalat, S. A. M.; Lavaee, P.; ZandKarimi, M.; Ghows, N.; Jaafari, M. R.; Naghibi, S.; Danesh, N. M.; Ramezani, M.; Abnous, K. *Eur. J. Pharm. Sci.* **2013,** 50, (2), 191-197.
7. Yu, M. K.; Jeong, Y. Y.; Park, J.; Park, S.; Kim, J. W.; Min, J. J.; Kim, K.; Jon, S. *Angew. Chem. Int. Ed.* **2008,** 47, (29), 5362-5365.
8. Kievit, F. M.; Zhang, M. *Acc. Chem. Res.* **2011,** 44, (10), 853-862.
9. Westbrook, C., Kaut Roth, C., Talbot, J., *MRI in Practice*. 4 ed.; Blackwell Publishing Ltd: USA, 2011.
10. Kim, B. H.; Lee, N.; Kim, H.; An, K.; Park, Y. I.; Choi, Y.; Shin, K.; Lee, Y.; Kwon, S. G.; Na, H. B.; Park, J. G.; Ahn, T. Y.; Kim, Y. W.; Moon, W. K.; Choi, S. H.; Hyeon, T. *J. Am. Chem. Soc.* **2011,** 133, (32), 12624-12631.
11. Weissleder, R.; Nahrendorf, M.; Pittet, M. J. *Nature Materials* **2014,** 13, (2), 125-138.
12. Kuo, P. H.; Kanal, E.; Abu-Alfa, A. K.; Cowper, S. E. *Radiology* **2007,** 242, (3), 647-649.
13. Penfield, J. G.; Reilly, R. F. *Nat Clin Pract Neph* **2007,** 3, (12), 654-668.
14. Vuu, K.; Xie, J.; McDonald, M. A.; Bernardo, M.; Hunter, F.; Zhang, Y.; Li, K.; Bednarski, M.; Guccione, S. *Bioconj. Chem.* **2005,** 16, (4), 995-999.
15. Cao, C.-Y.; Shen, Y.-Y.; Wang, J.-D.; Li, L.; Liang, G.-L. *Sci. Rep.* **2013,** 3, 1024.
16. Liu, Y.; Chen, Z.; Liu, C.; Yu, D.; Lu, Z.; Zhang, N. *Biomaterials* **2011,** 32, (22), 5167-5176.
17. Park, J. Y.; Baek, M. J.; Choi, E. S.; Woo, S.; Kim, J. H.; Kim, T. J.; Jung, J. C.; Chae, K. S.; Chang, Y.; Lee, G. H. *ACS Nano* **2009,** 3, (11), 3663-3669.
18. Silva, A. C.; Bock, N. A. *Schizophr. Bull.* **2008,** 34, (4), 595-604.

19. Aoki, I.; Wu, Y.-J. L.; Silva, A. C.; Lynch, R. M.; Koretsky, A. P. *NeuroImage* **2004,** 22, (3), 1046-1059.
20. Olsen, Ø.; Kristoffersen, A.; Thuen, M.; Sandvig, A.; Brekken, C.; Haraldseth, O.; Goa, P. E. *J. Magn. Reson. Imaging* **2010,** 32, (3), 551-560.
21. Thuen, M.; Berry, M.; Pedersen, T. B.; Goa, P. E.; Summerfield, M.; Haraldseth, O.; Sandvig, A.; Brekken, C. *J. Magn. Reson. Imaging* **2008,** 28, (4), 855-865.
22. Mørch, Ý. A.; Sandvig, I.; Olsen, Ø.; Donati, I.; Thuen, M.; Skjåk-Bræk, G.; Haraldseth, O.; Brekken, C. *Contrast Media Mol. Imaging* **2012,** 7, (2), 265-275.
23. Fitsanakis, V. A.; Zhang, N.; Avison, M. J.; Gore, J. C.; Aschner, J. L.; Aschner, M. *Neurotoxicology* **2006,** 27, (5), 798-806.
24. Zhen, Z.; Xie, J. *Theranostics* **2012,** 2, (1), 45-54.
25. Chen, Y.; Yin, Q.; Ji, X.; Zhang, S.; Chen, H.; Zheng, Y.; Sun, Y.; Qu, H.; Wang, Z.; Li, Y.; Wang, X.; Zhang, K.; Zhang, L.; Shi, J. *Biomaterials* **2012,** 33, (29), 7126-7137.
26. Kueny-Stotz, M.; Garofalo, A.; Felder-Flesch, D. *Eur. J. Inorg. Chem.* **2012**, (12), 1987-2005.
27. Choi, E. S.; Park, J. Y.; Baek, M. J.; Xu, W.; Kattel, K.; Kim, J. H.; Lee, J. J.; Chang, Y.; Kim, T. J.; Bae, J. E.; Chae, K. S.; Suh, K. J.; Lee, G. H. *Eur. J. Inorg. Chem.* **2010**, (28), 4555-4560.
28. Zhang, L.; Zhang, Z.; Mason, R. P.; Sarkaria, J. N.; Zhao, D. *Sci. Rep.* **2015,** 5, 9874.
29. Lim, E. K.; Kim, T.; Paik, S.; Haam, S.; Huh, Y. M.; Lee, K. *Chem. Rev.* **2015,** 115, (1), 327-394.
30. Xing, R.; Zhang, F.; Xie, J.; Aronova, M.; Zhang, G.; Guo, N.; Huang, X.; Sun, X.; Liu, G.; Bryant, L. H.; Bhirde, A.; Liang, A.; Hou, Y.; Leapman, R. D.; Sun, S.; Chen, X. *Nanoscale* **2011,** 3, (12), 4943-4945.
31. Kim, T.; Momin, E.; Choi, J.; Yuan, K.; Zaidi, H.; Kim, J.; Park, M.; Lee, N.; McMahon, M. T.; Quinones-Hinojosa, A.; Bulte, J. W. M.; Hyeon, T.; Gilad, A. A. *J. Am. Chem. Soc.* **2011,** 133, (9), 2955-2961.
32. Shapiro, E. M.; Koretsky, A. P. *Magn. Reson. Med.* **2008,** 60, (2), 265-269.
33. Shin, J.; Anisur, R. M.; Ko, M. K.; Im, G. H.; Lee, J. H.; Lee, I. S. *Angewandte Chemie - International Edition* **2009,** 48, (2), 321-324.
34. Berkowitz, A. E.; Rodriguez, G. F.; Hong, J. I.; An, K.; Hyeon, T.; Agarwal, N.; Smith, D. J.; Fullerton, E. E. *Physical Review B - Condensed Matter and Materials Physics* **2008,** 77, (2).
35. Salazar-Alvarez, G.; Sort, J.; Suriñach, S.; Baró, M. D.; Nogués, J. *J. Am. Chem. Soc.* **2007,** 129, (29), 9102-9108.
36. Patel, D.; Kell, A.; Simard, B.; Xiang, B.; Lin, H. Y.; Tian, G. *Biomaterials* **2011,** 32, (4), 1167-1176.
37. Xu, C.; Xu, K.; Gu, H.; Zheng, R.; Liu, H.; Zhang, X.; Guo, Z.; Xu, B. *J. Am. Chem. Soc.* **2004,** 126, (32), 9938-9939.
38. Huang, J.; Xie, J.; Chen, K.; Bu, L.; Lee, S.; Cheng, Z.; Li, X.; Chen, X. *Chem. Commun.* **2010,** 46, (36), 6684-6686.
39. Reis, R. A. M.; Ventura, A. L. M.; Kubrusly, R. C. C.; de Mello, M. C. F.; de Mello, F. G. *Brain Res. Rev.* **2007,** 54, (1), 181-188.
40. Kubrusly, R. C. C.; Guimarães, M. Z. P.; Vieira, A. P. B.; Hokoç, J. N.; Casarini, D. E.; De Mello, M. C. F.; De Mello, F. G. *J. Neurochem.* **2003,** 86, (1), 45-54.
41. Harnois, C.; Di Paolo, T. *Invest. Ophthalmol. Vis. Sci.* **1990,** 31, (11), 2473-2475.
42. Inzelberg, R.; Ramirez, J. A.; Nisipeanu, P.; Ophir, A. *Vision Res.* **2004,** 44, (24), 2793-2797.
43. Archibald, N. K.; Clarke, M. P.; Mosimann, U. P.; Burn, D. J. *Brain* **2009,** 132, (5), 1128-1145.
44. Pardridge, W. M. *NeuroRx* **2005,** 2, (1), 3-14.

45. Laterra J, K. R., Betz LA, et al., *Blood-Brain Barrier. In: Siegel GJ, Agranoff BW, Albers RW, et al., editors. Basic Neurochemistry: Molecular, Cellular and Medical Aspects*. 6 ed.; Lippincott-Raven, Available from: http://www.ncbi.nlm.nih.gov/books/NBK28180/: Philadelphia, 1999.
46. Bae, K. H.; Lee, K.; Kim, C.; Park, T. G. *Biomaterials* **2011,** 32, (1), 176-184.
47. Schladt, T. D.; Graf, T.; Tremel, W. *Chem. Mater.* **2009,** 21, (14), 3183-3190.
48. Chen, W.; Lu, F.; Chen, C. C. V.; Mo, K. C.; Hung, Y.; Guo, Z. X.; Lin, C. H.; Lin, M. H.; Lin, Y. H.; Chang, C.; Mou, C. Y. *NMR Biomed.* **2013,** 26, (9), 1176-1185.
49. Si, P. Z.; Li, D.; Choi, C. J.; Li, Y. B.; Geng, D. Y.; Zhang, Z. D. *Solid State Commun.* **2007,** 142, (12), 723-726.
50. Si, P. Z.; Li, D.; Lee, J. W.; Choi, C. J.; Zhang, Z. D.; Geng, D. Y.; Brück, E. *Appl. Phys. Lett.* **2005,** 87, (13), 1-3.
51. Belviso, C.; Agostinelli, E.; Belviso, S.; Cavalcante, F.; Pascucci, S.; Peddis, D.; Varvaro, G.; Fiore, S. *Microporous Mesoporous Mater.* **2015,** 202, (C), 208-216.
52. Xie, J.; Chen, K.; Huang, J.; Lee, S.; Wang, J.; Gao, J.; Li, X.; Chen, X. *Biomaterials* **2010,** 31, (11), 3016-3022.
53. Yin, Y.; Rioux, R. M.; Erdonmez, C. K.; Hughes, S.; Somorjal, G. A.; Alivisatos, A. P. *Science* **2004,** 304, (5671), 711-714.
54. Guduric-Fuchs, J.; Ringland, L. J.; Gu, P.; Dellett, M.; Archer, D. B.; Cogliati, T. *Mol. Vis.* **2009,** 15, 1915-1928.
55. Atkins, P. W.; De Paula, J., *Atkins' physical chemistry*. Oxford University Press: Oxford, 2014; p XXV, 1008 s. : ill.
56. Sandvig, A.; Sandvig, I.; Berry, M.; Olsen, Ø.; Pedersen, T. B.; Brekken, C.; Thuen, M. *J. Magn. Reson. Imaging* **2011,** 34, (3), 670-675.
57. Sandvig, I.; Sandvig, A., Using Manganese-Enhanced MRI to Assess Optic Nerve Regeneration. In *Axon Growth and Regeneration*, Murray, A. J., Ed. Springer New York: 2014; Vol. 1162, pp 233-249.
58. Zhou, R.; Caspi, R. R. *F1000 Biol. Rep.* **2010,** 2, (1).
59. Cramer, A. O.; MacLaren, R. E. *Curr. Gene Ther.* **2013,** 13, (2), 139-151.
60. Thuen, M.; Singstad, T. E.; Pedersen, T. B.; Haraldseth, O.; Berry, M.; Sandvig, A.; Brekken, C. *J. Magn. Reson. Imaging* **2005,** 22, (4), 492-500.

# Supporting Information

**L-DOPA coated manganese oxide nanoparticles as dual MRI contrast agents and drug delivery vehicles**

*Birgitte Hjelmeland McDonagh*, Gurvinder Singh, Sjoerd Hak, Sulalit Bandyopadhyay, Ingrid Lovise Augestad*, *Davide Peddis*, *Ioanna Sandvig*, *Axel Sandvig, and Wilhelm Robert Glomm*

**Degradation of MONPs**

The aqueous degradation of MONPs coated with L-DOPA was followed with STEM. Representative images are shown in Fig. S.1.

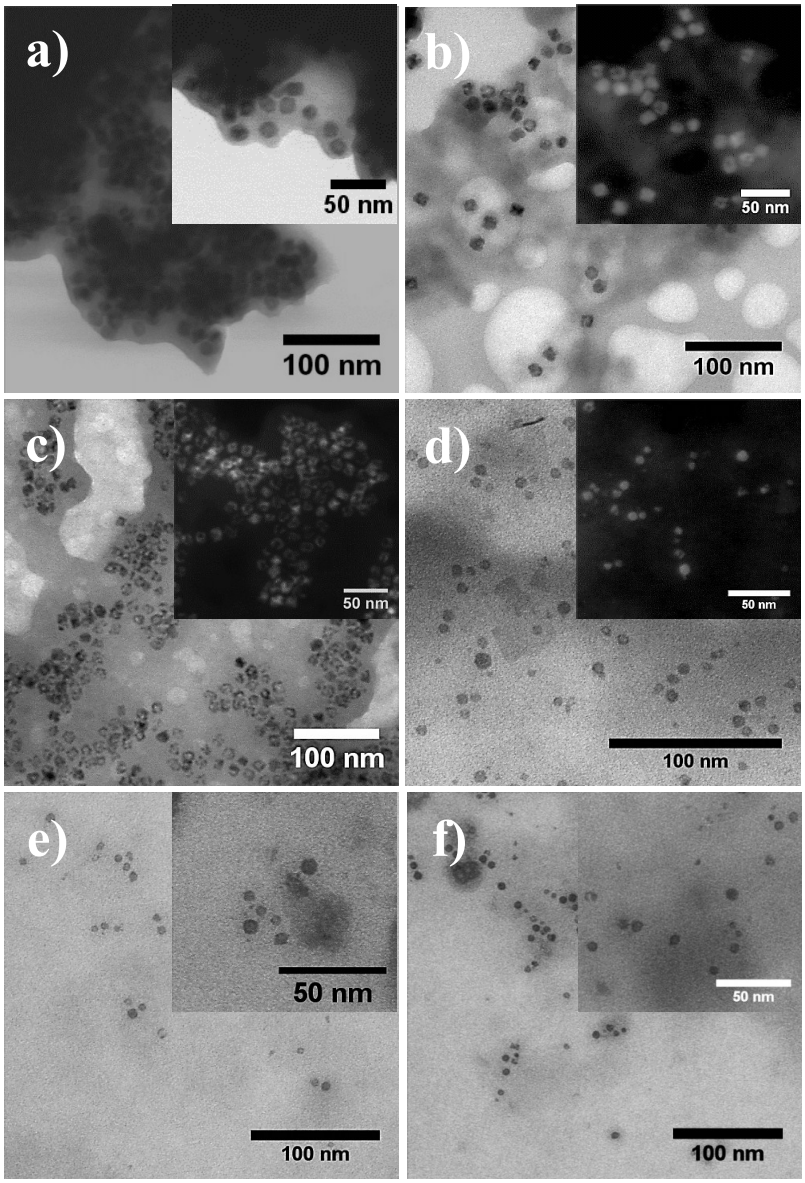


**Fig. S1: Bright field STEM images of MONPs** after a) 0 hour, b) 0.5 hour (dark field (DF) STEM image in inset shows the formation of hollow NPs, c) 1 hour (DF-STEM image in inset shows the formation hollow or c-shape type NPs), d) 4 hours (DF-STEM image in inset shows degradation of small MONPs), e) 12 hours, and f) 54 hours.

**X-ray diffraction, X-ray photoelectron spectroscopy and magnetic properties of MONPs**

X-ray diffraction patterns of MONPs suggests the presence of two species of manganese oxide; $Mn_3O_4$ and a small quantity of MnO (Fig S.2)

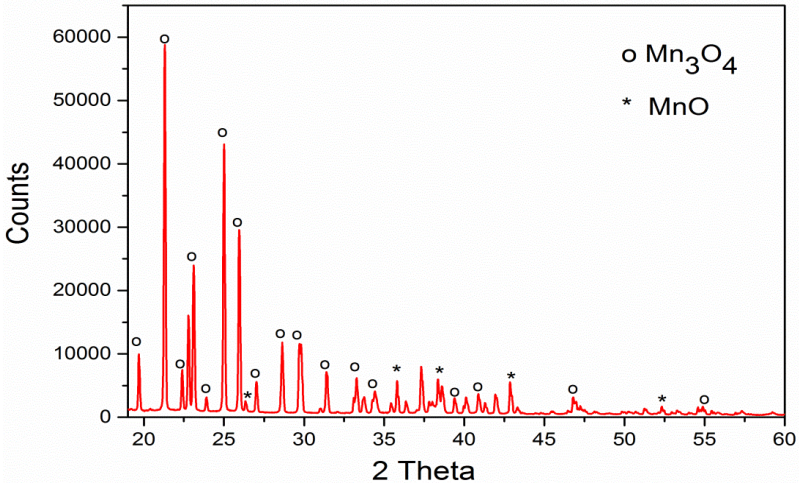


**Fig. S2: XRD data for MONPs**

Bulk $Mn_3O_4$ is a spinel- type compound with ferromagnetic structure (Tc = 43 K). The spinel structure is based on a closed-packed oxygen lattice, in which tetrahedral ($T_d$) and octahedral ($O_h$) intesryicial sites are occupied by the cations (i.e.$Mn^{2+}$, $Mn^{3+}$). In this structure ferrimagnetic ordering occurs because the $J_{TO}$ negative exchange interaction between magnetic cations occupying $T_d$ and $O_h$ sites dominates the negative intra-sublattice exchange interactions $J_{TT}$ and $J_{OO}$, causing each of the two magnetic sublattice sites $T_d$ and $O_h$ to be aligned[1]. The net magnetization is then proportional to the difference between the $T_d$ and $O_h$ sublattice magnetization. On the other hand, MnO shows completely different magnetic properties with and antiferromagnetic magnetic structure (Néel temperature 100 K)[4] and zero magnetic moments in bulk system. Small magnetic moments can be observed in nanoparticles due the presence of uncompensated surface spins.[2] Temperature dependence of magnetization has been investigated by means of zero field cooling (ZFC), and field cooling (FC) curves. $M_{ZFC}$ shows a maximum at 33 K ($T_{max}$) that can be ascribed to the superparamagnetic blocking temperature ($T_b$) of the MONPs (Fig. S.3). For a non-interacting NP system, $T_{max}$ can be considered as directly proportional to the average blocking temperature ($<T_b>$), with a proportionality constant of $\beta = 1 - 2$, depending on the particle size distribution. [4, 5] Below 16 K, the $M_{FC}$ curve shows a decreased temperature dependence, suggesting the presence of some dipolar interactions between NPs. [6] This is supported by the field dependence of magnetization recorded at 5 and 80 K: At 80 K, a paramagnetic behavior is observed, as expected for temperatures above $T_c$. At 5K, magnetic hysteresis is observed, confirming the presence of magnetic NPs (quasi-static magnetic behavior). It is interesting to observe that despite a reversible behavior of magnetization above 3 tesla a non-saturating charterer is observed at high field. This suggests the presence of an antiferromagnetic contribution that can be ascribe to the presence of a small quantity of MnO. [6, 7]

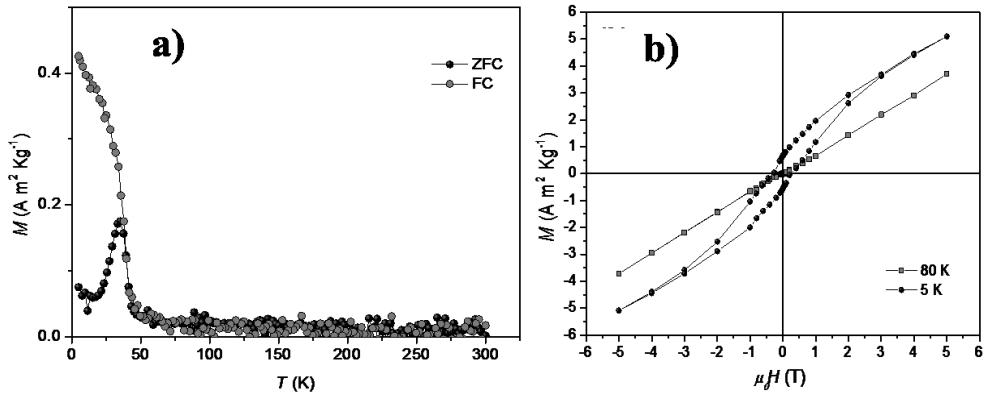


**Fig. S3:** a) ZFC (full symbols) and FC (empty symbols) recorded under and applied field of 0.05T. b) M vs H curves recorded at 5 (full symbols) and 80 K (empty symbols).

In order to get supporting evidences about chemical state and surface chemistry of MONPs prior and after surface modification, X-ray photoelectron spectroscopy (XPS) analysis was carried out. In high resolution spectra of Mn2p of MONPs, the doublet ($2p_{3/2}$, $2p_{1/2}$) has been observed at the separation of 11.77 eV due to spin-orbit splitting (Fig. S4b). An $Mn2p_{3/2}$ peak can be deconvoluted into three components. The components at ~641.2 and ~642 eV can be assigned to characteristics of $Mn^{2+}$ and $Mn^{3+}$. [8] A third component, which appears at ~645 eV, is difficult to assign due to lack of reported literature. However, since this peak is close to $Mn^{4+}$ cations, it may be related to a different coordination behavior of $Mn^{4+}$. These results confirm the mixed oxide behavior of MONPs, which are in agreement with our HRTEM, XRD and magnetic measurement results.

Prior to surface functionalization, MONPs are capped with oleic acid which can be confirmed from a high resolution XPS spectra of C1s indicating peaks at ~285 and ~289 eV corresponding to C-C/C=C and O-C=O, respectively (Fig. S4c). [9] After functionalization of MONPs with L-DOPA, a wide scan XPS spectra shows the presence of an "N" peak which was absent before the functionalization (Fig. S5a, and Fig. S4a). We did not observe any significant difference of high resolution spectra of Mn2p after the surface functionalization which was collected immediately after the dispersion of MONPs in water phase (Fig. S5b). A high resolution C1s spectra reveals the presence of five components which can be assigned to C-C (~285 eV), C-N (~286 eV), C-O (~286.5 eV), O-C=O (~289 eV), and $\pi \rightarrow \pi^*$ (~291.4 eV) respectively, suggesting the successful coating of L-DOPA on MONPs. [9] Moreover, the main component (~400 eV) in N1s spectra also indicates the presence of primary amine (-$NH_2$) on the MONPs surface. [9] From these results, it can be inferred that L-DOPA molecules anchor to MONPs via hydroxyl groups.

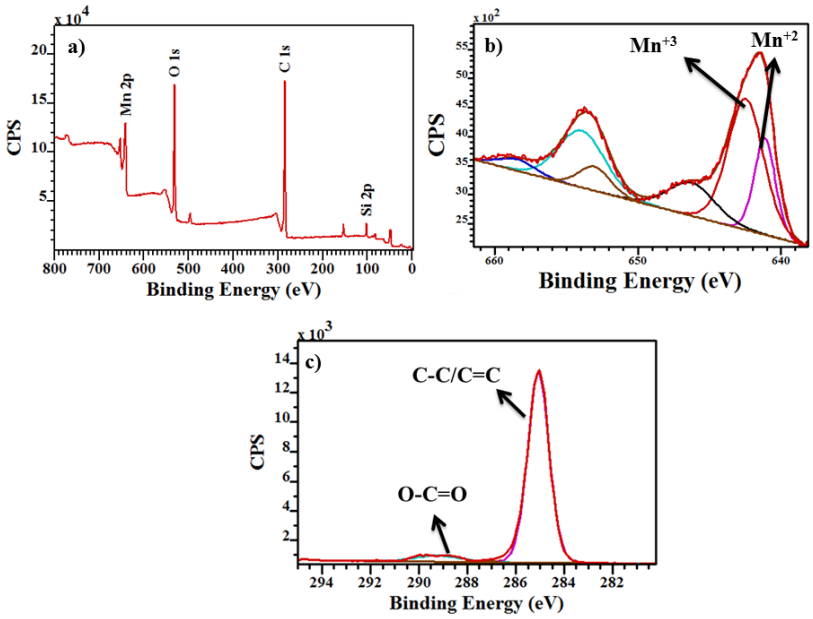


**Fig. S4:** a) A wide scan XPS spectra of oleic acid coated MONPs; b) high resolution XPS spectra of Mn2p and c) high resolution XPS spectra of C1s.

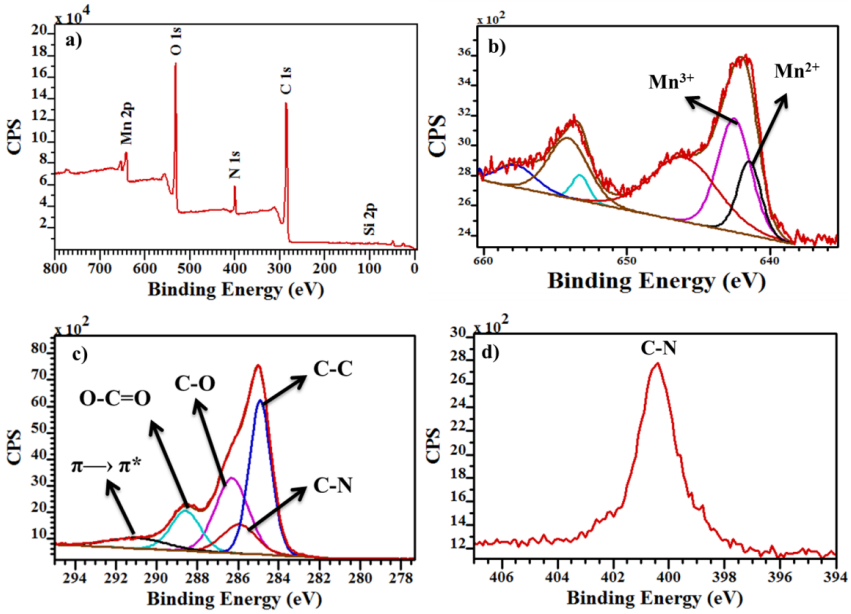


**Fig. S5**: a) A wide scan XPS spectra of L-DOPA coated MONPs; b) high resolution XPS spectra of Mn2p; c) high resolution XPS spectra of C1s and d) high resolution XPS spectra N1s.

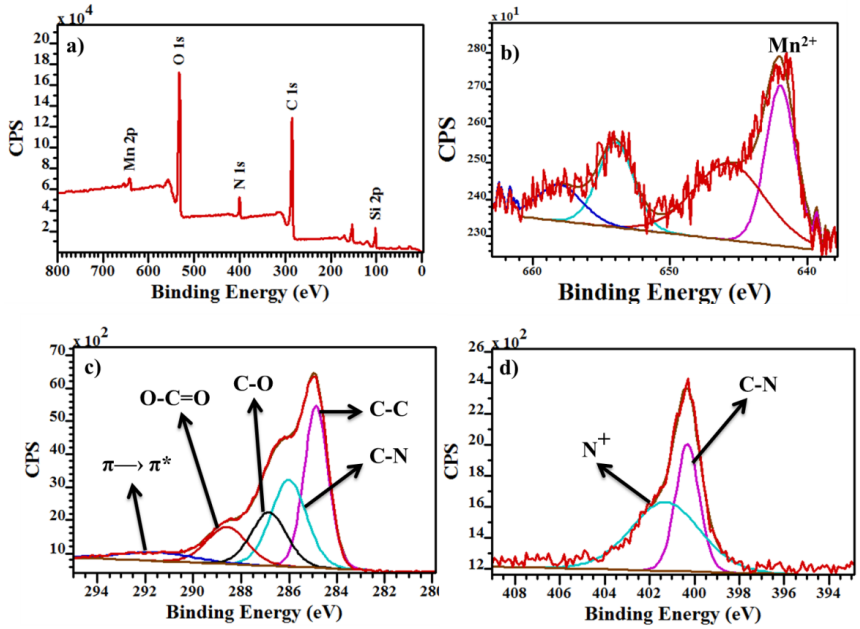


**Fig. S6:** a) A wide scan XPS spectra of L-DOPA coated MONPs; b) high resolution XPS spectra of Mn2p; c) high resolution XPS spectra of C1s and d) high resolution XPS spectra N1s.

We have collected XPS spectra from two weeks old solution of L-DOPA coated MONPs, and no significant difference was noticed in a wide scan spectra and C1s (Fig. S6a,c). The presence of second component (~401.4 eV) at higher binding energy in N1s spectra indicate the protonation of amine group (Fig. S6d). Furthermore, the disappearance of $Mn^{3+}$ components from $Mn2p_{3/2}$ peaks suggests that $Mn^{3+}$ ions are unstable in deionized water (pH~6), and reduced into $Mn^{2+}$.[10] This further suggests the aqueous degradation of the MONPs.

***Ex vivo* degradation of MONPs**

In order to monitor the T1 and T2 effects of MONPs as a function of time, pig eyes were injected with MONPs and scans were performed continuously for 34 hours. Fig. S.7 show scans of one pig eye which was injected with L-DOPA coated MONPs, and one non-injected control eye. An additional eye injected with PEG-coated iron oxide NPs ($Fe_3O_4$) was scanned in order to compare the *T2** contrast.

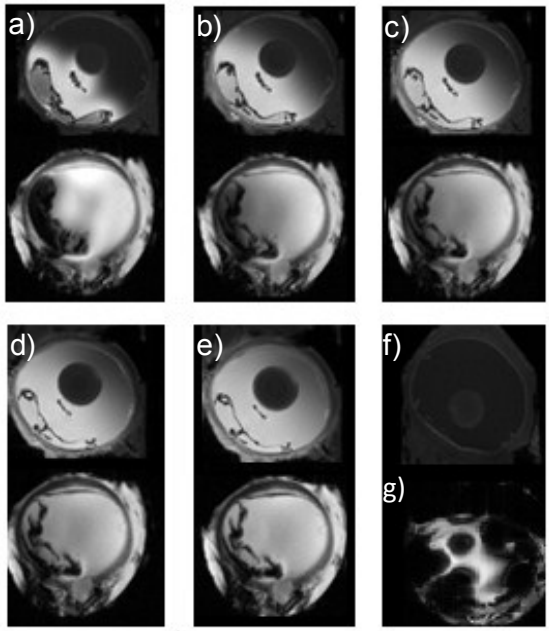


**Fig. S.7: Time-resolved *T1* weighted and *T2** weighted images of pig eyes injected with MONPs.** The *T1w* (top) and *T2w* (bottom) images show how diffusion of $Mn^{2+}$ ions cause *T1* contrast, and how the MONPs give *T2** contrast. a) 1 hour, b) 3 hours, c) 4 hours d) 8 hours and e) 12 hours after injection. Images f) and g) show the *T1w* image of the control eye, and of a pig eye injected with iron oxide NPs.

With time, the region in the injection site becomes less hypointense, with a concomitant hyperintensity observed in the *T1w* images (Fig. S.7a). The initial burst of *T1* contrast is most likely due to $Mn^{2+}$ ions already present in the suspension, and this high concentration of $Mn^{2+}$ ions may also give *T2** contrast (Fig. S.7 b). The final *T1* contrast is evenly distributed throughout the pig eye, and shows the same intensities both at the central part of the pig eye and the lateral side from injection. For both the *T2** and *T1* times, the changes in the lateral part of the eye are delayed compared with the central region, and this is explained by the time of diffusion of $Mn^{2+}$ ions.

The *T1* and *T2* relaxation rate is the inverse of the T1 and T2 time, respectively. Fig. S.8 shows the inverse *T1* and *T2* times as a function of degradation time, *ex vivo* in pig eyes. The T1 and T2 relaxation rates increase with time *ex vivo,* and the highest rate is calculated for the 1/T2 at the
central part of the pig eye.

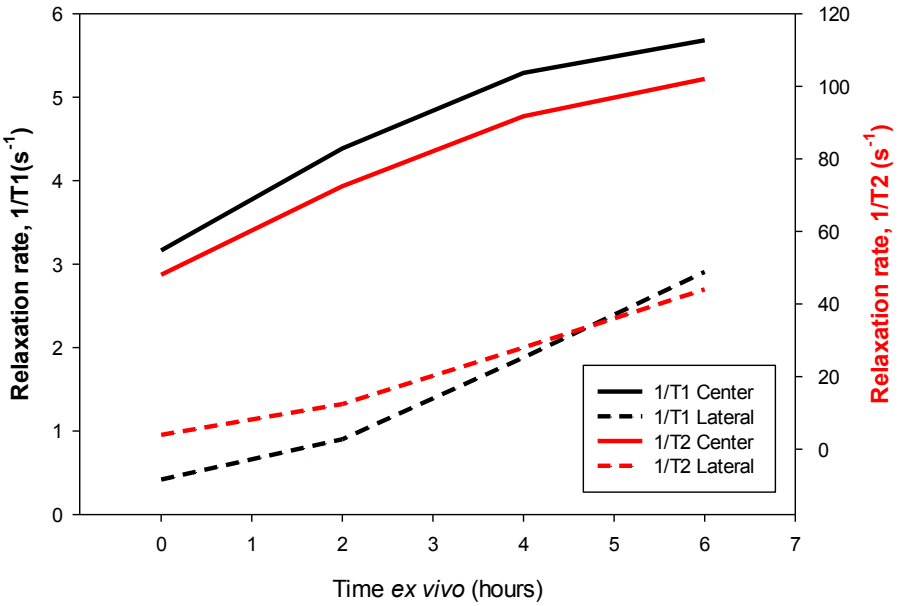


**Fig. S.8: Relaxation rates as a function of time, *ex vivo*.** Beyond 6 hours, curve fitting was not achieved because the T1 andT2 times became too short.

**In vivo degradation of MONPs**

Fig. S.9 shows an example of determining the region of interest (ROI) for quantification of contrast in the optic nerve using ImageJ.

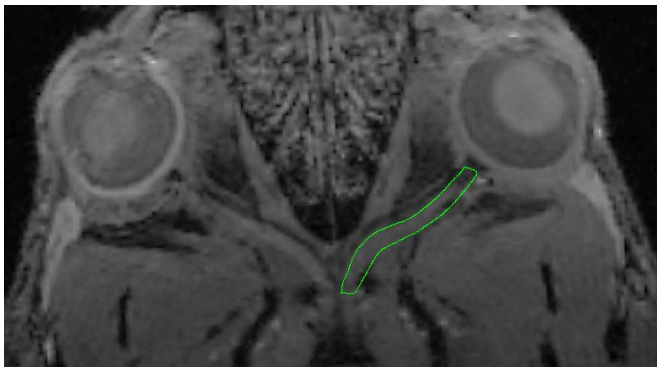

**Fig. S.9: Drawing ROI's defining the optic nerve using image J**

The contrast in the retina and the vitreous body was determined using MatLab 2012a, and an example of an ROI is shown in Fig. S.10.

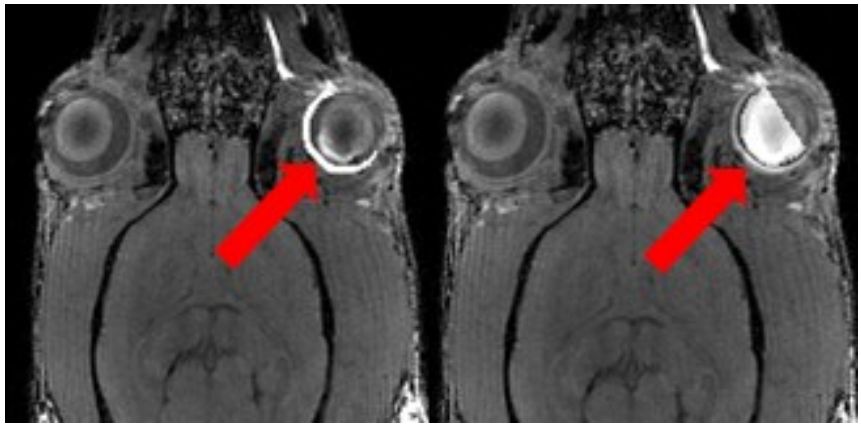

**Fig. S.10: ROI for rats injected with manganese nanoparticles, T1-weighted image.** The ROI for the vitreous body was chosen to be two thirds of the eye. The reason for this being that the outer part of the eye has some presence of artifacts, due to susceptibility at the eye/air interface. The ROI of the retina is chosen to lie outside of the vitreous body ROI in the same half circle.

From these ROIs (Fig S.9 and S.10) the mean intensities and standard deviations were measured. 3 rats (n=3) injected with the same amount of MONPs suspension were used to determine the change in the contrast.

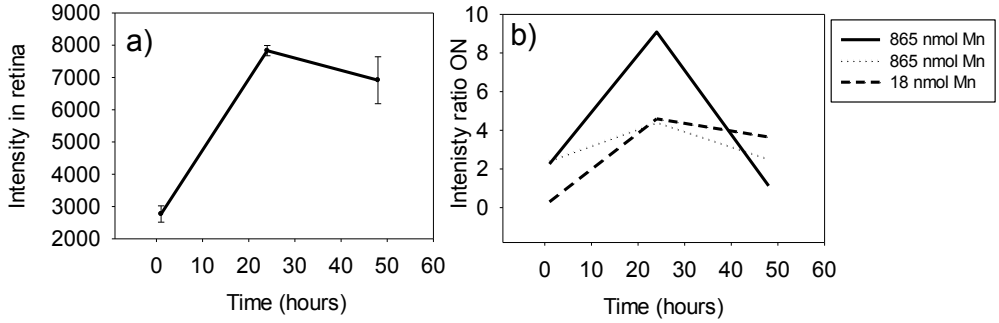


**Fig. S.11: Intensity in retina and ON in rodent model** Graph **a)** shows the intensity in the retina as a function of time (n=3), and graph **b)** shows the intensity ratio in the ON corrected with respect to the intensity in the contralateral control eye.

Fig. S.12 shows the retina and ON 48 hours post injection of MONPs. No intensity differences were found when compared to the lateral control ON.

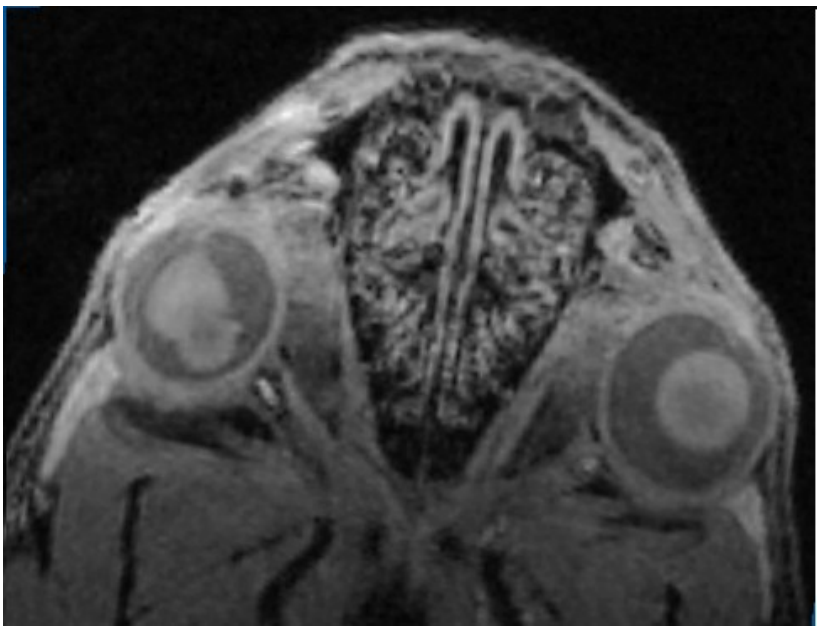

**Fig. S.12: Visualization of the ON, 48 hours after intravitreal injection.**
Iron oxide NPs ($Fe_3O_4$) surface coated with PEG were used as control *T2* contrast agents. Compared to the MONPs, the $Fe_3O_4$ NPs did not show the same movement towards the retina. This is probably a combination of the larger surface molecule, and that the $Fe_3O_4$ NPs do not dissolve in aqueous media. Fig. S.13 show *T2* weighted images of a rat brain after intravitreous injection of $Fe_3O_4$ NPs.

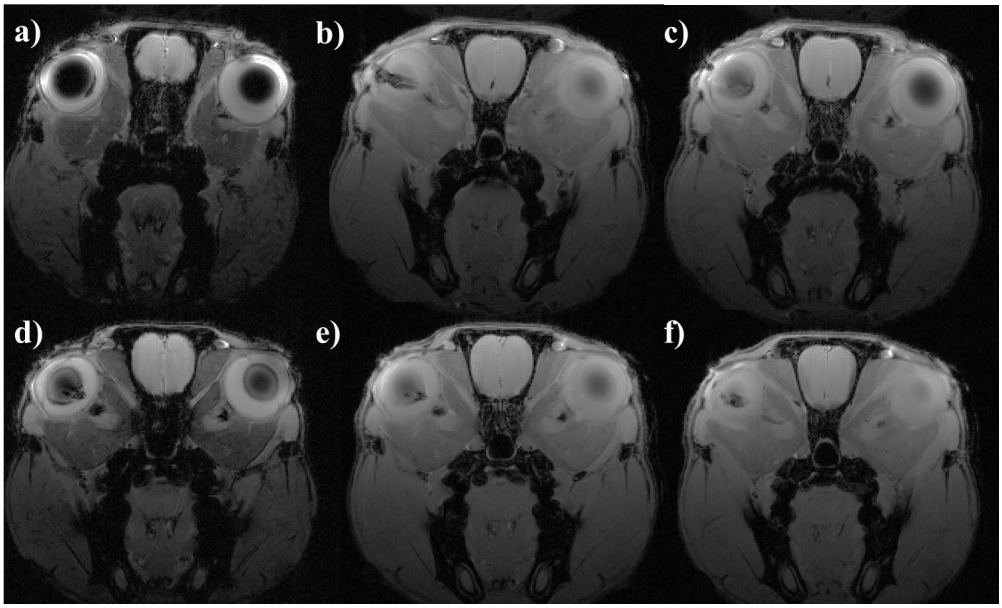


**Fig. S.13: $Fe_3O_4$ NPs as *T2* contrast agents.** Images a)-c) show *T2*w* images 24 hours after injection. Images d)-f) were acquired 48 hours after injection.

**References**

[1.] Ridelman, Y.; Singh, G.; Popovitz-Biro, R.; Wolf, S. G.; Das, S.; Klajn, R., Metallic nanobowls by galvanic replacement reaction on heterodimeric nanoparticles. *Small* **2012,** *8* (5), 654-660.
[2.] Chen, W.; Lu, F.; Chen, C. C. V.; Mo, K. C.; Hung, Y.; Guo, Z. X.; Lin, C. H.; Lin, M. H.; Lin, Y. H.; Chang, C.; Mou, C. Y., Manganese-enhanced MRI of rat brain based on slow cerebral delivery of manganese(II) with silica-encapsulated MnxFe1-xO nanoparticles. *NMR Biomed.* **2013,** *26* (9), 1176-1185; Schladt, T. D.; Graf, T.; Tremel, W., Synthesis and characterization of monodisperse manganese oxide nanoparticles-evaluation of the nucleation and growth mechanism. *Chem. Mater.* **2009,** *21* (14), 3183-3190.
[3.] Xie, J.; Chen, K.; Huang, J.; Lee, S.; Wang, J.; Gao, J.; Li, X.; Chen, X., PET/NIRF/MRI triple functional iron oxide nanoparticles. *Biomaterials* **2010,** *31* (11), 3016-3022.
[4.] Peddis, D.; Rinaldi, D.; Ennas, G.; Scano, A.; Agostinelli, E.; Fiorani, D., Superparamagnetic blocking and superspin-glass freezing in ultra small [small delta]-(Fe0.67Mn0.33)OOH particles. *PCCP* **2012,** *14* (9), 3162-3169.
[5.] Gittleman, J. I.; Abeles, B.; Bozowski, S., Superparamagnetism and relaxation effects in granular Ni-Si${\mathrm{O}}_{2}$ and Ni-${\mathrm{Al}}_{2}$${\mathrm{O}}_{3}$ films. *Physical Review B* **1974,** *9* (9), 3891-3897.
[6.] Si, P. Z.; Li, D.; Choi, C. J.; Li, Y. B.; Geng, D. Y.; Zhang, Z. D., Large coercivity and small exchange bias in Mn3O4 / MnO nanoparticles. *Solid State Commun.* **2007,** *142* (12), 723-726.
[7.] Si, P. Z.; Li, D.; Lee, J. W.; Choi, C. J.; Zhang, Z. D.; Geng, D. Y.; Brück, E., Unconventional exchange bias in oxide-coated manganese nanoparticles. *Appl. Phys. Lett.* **2005,** *87* (13), 1-3; Belviso, C.; Agostinelli, E.; Belviso, S.; Cavalcante, F.; Pascucci, S.; Peddis, D.; Varvaro, G.; Fiore, S., Synthesis of magnetic zeolite at low temperature using a waste material mixture: Fly ash and red mud. *Microporous Mesoporous Mater.* **2015,** *202* (C), 208-216.
[8.] Li, F.; Zhang, L.; Evans, D. G.; Duan, X., Structure and surface chemistry of manganese-doped copper-based mixed metal oxides derived from layered double hydroxides. *Colloids Surf. Physicochem. Eng. Aspects* **2004,** *244* (1–3), 169-177; Ahn, S.; Kang, S. M.; Lee, S. H.; Park, J. B., Facile synthesis of graphene-supported MnO, Mn3O4, and MnO2 nanocomposites by controlling gas environment. *Bull. Korean Chem. Soc.* **2014,** *35* (10), 2889-2890.
[9.] Singh, G.; Pillai, S.; Arpanaei, A.; Kingshott, P., Highly Ordered Mixed Protein Patterns Over Large Areas from Self-Assembly of Binary Colloids. *Adv. Mater.* **2011,** *23* (13), 1519-1523.
[10.] Giri, A.; Goswami, N.; Pal, M.; Zar Myint, M. T.; Al-Harthi, S.; Singha, A.; Ghosh, B.; Dutta, J.; Pal, S. K., Rational surface modification of Mn3O4 nanoparticles to induce multiple photoluminescence and room temperature ferromagnetism. *Journal of Materials Chemistry C* **2013,** *1* (9), 1885-1895.